Volcanic history and magmatic evolution of Mocho-Choshuenco Volcano, Southern Chile

Harriet Rawson

University College

Thesis submitted to the University of Oxford

for the degree of Doctor of Philosophy

in Earth Sciences

Department of Earth Sciences

University of Oxford

Trinity Term, 2015

Supervised by Prof. David Pyle, Prof. Tamsin Mather

and Dr. José Naranjo

View of Volcán Mocho-Choshuenco from the west looking across Lago Riñihue

Declaration

The contents of this thesis are all my own work, except where otherwise stated. The views and opinions expressed herein are mine and not necessarily those of any other person or body unless so attributed.

Citation: Rawson, H.L. (2015), Volcanic history and magmatic evolution of Mocho-Choshuenco Volcano, Southern Chile, D.Phil. Thesis, University of Oxford, Department of Earth Sciences, Oxford, UK.

This thesis has been typeset using LaTeX 2_ε.

Printed in the United Kingdom.

Abstract

Volcanic history and magmatic evolution of Mocho-Choshuenco Volcano, Southern Chile

Harriet L. Rawson
University College, Oxford
Doctor of Philosophy in Earth Sciences

Trinity Term, 2015

Active volcanoes pose a significant natural hazard. In order to evaluate the hazard it is important to reconstruct the history of such volcanoes to understand the frequency, style of eruption and the areas typically affected by the explosive eruptions.

This thesis focuses on deciphering the volcanic and magmatic record for one of the most productive volcanoes in southern Chile, Volcán Mocho-Choshuenco. Work presented in the thesis establishes a detailed record of the explosive activity during the last 18 kyrs, constructed using field observations and geochemical analyses of the eruption deposits. Using a multi-technique approach Mocho-Choshuenco is shown to be one of the most explosive, frequently active and hence hazardous volcanoes in Chile.

This high-resolution eruptive record provides new constraints on the underlying causes of spatial and temporal variability in arc volcanism. Temporally, the record gives new understanding into the response of arc volcanoes to deglaciation; clear temporal variation in eruption flux, eruption size and magma composition are observed. This time-varying behaviour is hypothesised to reflect changes in the crustal plumbing system, and magma storage timescales in response to removal of an ice-load. It demonstrates that deglaciation can drive changes in eruption behaviour at arc volcanoes; however the response is more complex and subtle than settings where decompression melting dominates.

Spatially, Mocho-Choshuenco has a high number and density of scoria cones that have erupted relatively primitive magmas but nonetheless with a wide range of magma compositions. For some of the 'classical' slab and mantle geochemical tracers the erupted magmas span the complete range seen in this part of the arc. The tight temporal and spatial constraints provided by the analysed samples, coupled with recent advances in numerical modelling of magma transport through subduction zones, enable new hypotheses for interpreting the signatures of mafic arc magmas to be defined.

Extended Abstract

Volcanic history and magmatic evolution of Mocho-Choshuenco Volcano, Southern Chile

Harriet L. Rawson
University College, Oxford
Doctor of Philosophy in Earth Sciences

Trinity Term, 2015

Volcán Mocho-Choshuenco (39°55'S 72°2'W) is considered one of the most explosive and hazardous volcanoes in Chile's Southern Volcanic Zone (SVZ), yet has been little studied in the past. Although 400,000 people live within 100 km of the volcano, the eruptive history, even for historical times, is poorly understood. New work presented in this thesis defines the high-resolution history of explosive eruptions for the past 18,000 years. The eruption record established in this work provides new constraints on the tempo of post-glacial volcanism, notably on how arc volcanoes respond to deglaciation, something prior studies have had insufficient data to assess. In addition, the new age model and compositional data for the deposits allows the chemical and physical plausibility of conceptual models of melting processes to be tested.

Volcán Mocho-Choshuenco has been frequently active in the Late Quaternary, and has produced some of the largest, known explosive eruptions in the SVZ. A high-resolution eruption history, the most detailed to date for a volcano in Chile, is reconstructed from detailed field observations and geochemical analyses. Mocho-Choshuenco has experienced ca. 75 post-glacial (<18 ka) explosive eruptions, including three large (volume $\geq$1 km^3) Plinian eruptions (Neltume, Pirehueico and Huilo) and a large pyroclastic density current and associated sub-Plinian event (Enco). Poor preservation and lack of exposure made it difficult to distinguish between medial to distal deposits solely on field observations. Instead, deposits have been correlated using a combination of glass chemistry and Fe–Ti oxide compositions. New radiocarbon dates were obtained and integrated with existing

dates in a Bayesian age model (OxCal) to constrain the tempo of the volcanism. Based on preserved deposits, a post-glacial eruptive frequency of one explosive eruption every ∼220 years is derived with the youngest, confirmed eruption from Mocho-Choshuenco in 1864. The total post-glacial volume of tephra erupted is estimated at ≥20 km^3 (ca. 50% with a dacitic or rhyolitic glass composition) with ≥4 km^3 erupted from the monogenetic cones on the flanks, making Mocho-Choshuenco one of the most productive (ca. 1 km^3/kyr) and active volcanoes in the SVZ during post-glacial times. Many tephra deposits from Mocho-Choshuenco could be preserved in one or more lakes in the region, and have the potential to form regional tephra markers. In particular the Neltume deposits, which are dispersed to the NNE, are found interbedded with tephra deposits from the Villarrica – Quetrupillán – Lanín chain and should be preserved around Sollipulli and Llaima (∼140 km NNE of Mocho-Choshuenco). This thesis highlights how a multi-technique approach enables a complicated tephrostratigraphy to be unravelled allowing more robust estimates of the past eruptive frequency and size to be determined.

The reconstruction of high-resolution eruption histories at volcanoes like Mocho-Choshuenco allow us to test hypotheses about how volcanoes interact with the broader Earth system. Volcanism has influenced Earths atmosphere and surface environments throughout its history. Arc volcanoes account for 90% of subaerial eruptions and are the most significant sources of volcanic gases and tephra to the atmosphere. Understanding the drivers of significant change in the average rates or styles of volcanic activity in subduction zones is of particular importance for understanding the interactions between volcanism and the environment over Earth's history. In plate-tectonic settings where magmatism is driven by decompression melting there is compelling evidence that activity is modulated by changes in ice- or water-loading across glacial/interglacial cycles. In contrast, the response of subduction-related volcanoes, which are dominated by flux melting, remains unclear. Utilising this rare high-resolution post-glacial eruption record from Mocho-Choshuenco provides new insight into the magmatic response to removal of an ice load; variation in eruptive flux, eruption size and magma composition are observed and divided into three distinct phases based on style of activity and erupted composition. Phase 1, shortly after deglaciation, was dominated by large explosive eruptions of dacite and rhy-

olite. During Phase 2 (7.3 – 2.9 ka) eruption rates and eruptive fluxes were lower, and activity was dominated by moderate-scale basaltic-andesite eruptions. Since 2.4 ka (Phase 3) eruptive fluxes have been elevated, and dominated by explosive eruptions of more intermediate magmas. This time-varying behaviour reflects changes in crustal plumbing systems, and magma storage timescales. During glaciations, magmas stall and differentiate to form large, evolved crustal reservoirs. After the load is removed, much of this stored magma is erupted (Phase 1). Subsequently, less-differentiated melts infiltrate the shallow crust (Phase 2). Then, as storage timescales increase, volcanism returns to more evolved compositions (Phase 3). On short (<10 kyr) timescales these variations are unlikely to result from changes in mantle melt flux. Instead, the phenomena likely reflect changes in the crustal stress field due to unloading. This tripartite pattern of evacuation, relaxation and recovery may be a general feature of both previously-glaciated arc volcanoes.

The unusual spatial resolution of the Mocho-Choshuenco dataset allows for the testing of the chemical and physical plausibility of conceptual models of melting processes. Mocho-Choshuenco has a high number and density of scoria cones that have erupted relatively primitive magmas but nonetheless with a wide range of magma compositions. Arc magma genesis is complex, and interpreting the underlying causes of major and trace element diversity in erupted mafic magmas is challenging and often non-unique. This complexity is heightened when comparing magma compositions over large temporal and spatial scales, where the number of potential variables increases. Despite this, few prior studies have investigated mafic magma diversity using samples which are both well-constrained temporally and spatially and span short scales. This is the approach taken in this thesis. Young deposits (< 18 kyrs) are analysed from the central Southern Volcanic Zone, Chile (37°S-45°S). This region spatially has uniform subduction inputs and parameters (e.g., convergence angle and sediment thickness), reducing the number of potential variables at play. This study focusses on one volcano, which has a high density of scoria cones (up to 15 km from the central vent), that have erupted relatively primitive magmas with a wide range of magma compositions. For some of the 'classical' slab and mantle geochemical tracers (e.g., Ce/Pb, Zr/Nb) the erupted magmas in this relatively small geographical area span the complete range seen in this part of the arc (37°S-45°S).

The tight temporal and spatial constraints provided by the analysed samples helps with assessing the chemical and physical plausibility of the conceptual models of melting processes that may play a role in driving the observed mafic magma diversity. The analysis, is also guided by recent advances in numerical modelling, which have improved our understanding of how melts are transported and focussed within the mantle and interact with it. Through this approach it is hypothesised that variable mantle enrichment, as a result of melt focussing, causes significant diversity in mafic magma compositions. Further, it is expected that there may be a relationship between the depth of the inherited compositional signature and the lateral distance over which the signature might be observed. This has implications for the potential of detecting short wavelength slab heterogeneities at arc volcanoes.

Overall, the comprehensive dataset gathered in this thesis has identified and characterised a large number of new explosive eruptions. Locally this has improved understanding of the nature of potential future hazards. Regionally, deposits from the explosive eruptions (tephra) from Mocho-Choshuenco are now invaluable marker beds. As the chemical compositions are well constrained distal deposits can now be correlated to known, well-dated events from Mocho-Choshuenco. This will provide invaluable age constraints to other studies; for example, palaeoenvironmental studies of lake cores and archaeology excavations. More generally the high-resolution record enables new insights into the underlying causes of spatial and temporal variability in arc volcanism. By additionally considering the products of medium to large explosive eruptions the record gives new understanding into the response of arc volcanoes to deglaciation. The response is shown to be more complex and subtle than settings where decompression melting dominates; this has wider implication for the potential positive feedback between deglaciation and volcanic activity. Finally, approaching arc magma genesis from both a physical and geochemical angle enabled new insights into arc mafic magma genesis and interpreting the underlying causes of major and trace element diversity.

Acknowledgements

In researching this thesis I have benefited enormously from the help and encouragement offered by a large number of people in the UK and Chile.

Firstly, for giving me this wonderful opportunity and guiding me through my DPhil I would like to thank my supervisors David Pyle and Tamsin Mather. This thesis would not have achieved its present form without your continuous and invaluable advice, ideas and suggestions on all aspects of this project. My thanks also go to José Naranjo for the sharing of his field data and endless enthusiasm for Chilean volcanism. Our long discussions in Chile and over many an email helped enormously with the work on constructing the eruption history. A special thank you to Vicki Smith, Karen Fontijn and Stefan Lachowycz for helping so readily and frequently with my wide-ranging problems and questions; from sharing your expertise in the field and laboratory, to tireless encouragement and support throughout my DPhil.

My thanks to Lars Hansen and Steve Sparks for examining my thesis, Tobias Keller for the sharing of his figures and useful discussions regarding the work in Chapter 4, Madeleine Humphreys for help with the Fe–Ti oxides and Martin Airey and Pete Davis for their help with LaTeX and Matlab.

I gratefully acknowledge funding from NERC, who funded my studentship, fieldwork in Chile, analytical work and conferences, as well as to the old Members Trust (University College, Oxford), Santander Academic Travel Award and VMSG workshop grant.

This project involved a large amount of laboratory work and so would not have been possible without the advice and experience of a large number people. I am particularly grateful to Norman Charnley, Phil Holdship, Jeremy Hyde and Steve Wyatt in Oxford. Further, Nick Marsh at the XRF laboratory in Leicester and Steve Moreton and the

laboratory staff at the NERC Radiocarbon Facility in East Kilbride, UK. Also I would like to thank the administrative teams in Oxford Earth Sciences for their support.

In Chile I am grateful to José Barrientos, Monse Cascante and Rebecca Neely for invaluable assistance and boundless enthusiasm in the field. Monse additionally for her warm hospitality in Santiago and treating me like one of the family. Huilo-Huilo Biological Reserve, in particular Tania Altamirano, for enabling vital access to the reserve to carry out essential field work and for helping to spread my findings to the local communities. The best campsite in the world for making my stay in Neltume so special and memorable.

Finally, I am grateful to all my family and friends for always being so supportive, encouraging and a welcome distraction throughout my DPhil.

Contents

List of Figures

List of Tables

Chapter 1

Introduction

Volcanic eruptions are significant natural hazards, which can cause loss of life and livelihoods to impacted communities. Globally almost one in nine people are estimated to live within 100 km of an active volcano (Brown et al., 2015). Despite this there are significant gaps in the past eruption histories of many volcanoes, and hence much uncertainty in the nature of potential future eruptions and hazards (e.g., Siebert and Simkin, 2002-; Fontijn et al., 2014; Loughlin et al., 2015). Explosive activity is particularly important to constrain as it is responsible for much of the threat to life (Brown et al., 2015). Continental arc volcanoes represent the dominant source of explosive volcanism on Earth and hence are one of the most significant hazards (e.g., Perfit and Davidson, 2000; Siebert and Simkin, 2002-). The style and magnitude of explosive eruptions here can vary enormously, resulting in impacts from a local to a global scale (e.g., Simkin and Siebert, 2000; Pyle, 2015). Understanding past activity holds the key to better assessing the style, frequency and size of potential future eruptions and hence hazards. Further, volcanic deposits record evidence of how different geological processes may be influencing magma composition and volcanic behaviour. When the deposits additionally have tight temporal and spatial constraints they can give invaluable insights into arc magma genesis and potential coupling with other natural phenomena, such as glaciation (e.g., Watt et al., 2013a). In this thesis I explore such ideas through the post-glacial explosive eruption record in southern Chile, with particular focus on Volcán Mocho-Choshuenco.

Mocho-Choshuenco is a major, twin peaked volcanic complex in southern Chile. It is just one of many active volcanoes in the southern Andean Volcanic zone, and is cur-

rently partially glaciated. Little is known of the eruptive history or evolution, of this volcano (for example, the Smithsonian Catalogue[1] lists only two Holocene eruptions; the LaMEVE database[2], just one), and there have been no modern studies of its products. What is known is it has a complex history with multiple large (volume $\geq$ 1 km^3), early Holocene explosive eruptions, however, the timing and size of these are poorly constrained compared to the other large Holocene eruptions from the region (Moreno and Lara, 2007; Fontijn et al., 2014). Large Holocene eruptions are relatively rare in southern Chile, so it is important to study and characterise both for hazard assessment and for their potential as regional stratigraphic marker beds (e.g., Shane, 2000; Lowe, 2011; Fontijn et al., 2014). In explosive eruptions tephra can be dispersed for 100s of kilometres and enable sedimentary sequences across a wide geographical area and in different environmental settings to be correlated, thereby giving invaluable age constraints. Further, Mocho-Choshuenco is frequently active and was extensively glaciated during the last glacial period; therefore it is an ideal case study to explore the potential influence deglaciation had on volcanic behaviour in an arc setting. Finally, it has the highest density, and abundance of scoria cones associated with a stratovolcano in southern Chile. Thus, there is potential to investigate spatial variability in mafic magma composition and gain valuable insights into arc mafic magma genesis.

The following sections give a background to the volcanic activity, tectonics and geochemistry of southern Chile and Volcán Mocho-Choshuenco.

1.1 Southern Andean Volcanism

Plate convergence along the western side of South America has led to the >7500 km long, continuous Andean Cordillera and coincident, almost continuous, volcanic arc. The Andean-Arc lies parallel to the western margin of South America and is divided into four main zones (Stern, 2004); the Northern Volcanic Zone (NVZ; 5°N-2°S), Central Volcanic Zone (CVZ; 14-27°S), Southern Volcanic Zone (SVZ; 33-47°S) and Austral Volcanic Zone (AVZ; 49-55°S). The SVZ, CVZ and NVZ arise from the subduction of the Nazca Plate

[1] http://volcano.si.edu
[2] http://www.bgs.ac.uk/vogripa/index.cfm

beneath the South American continent. The AVZ, to the south of the SVZ, arises from the subduction of the Antarctic Oceanic Plate beneath the South American Continent (∼49-53°S) and Scotia Microplate (∼53-55°S; e.g., Stern, 2004).

1.1.1 The Southern Volcanic Zone (SVZ)

The Southern Volcanic Zone (SVZ), the focus of this study, is a 1400 km long, continuous volcanic arc that comprises approximately 60 volcanic centres that have been active during the late Quaternary (e.g., Stern, 2004; Fontijn et al., 2014); volcanic centres range from clusters of (monogenetic) cones to stratovolcanoes and large volcanic complexes. The SVZ is further divided into four sub-zones distinguished by along-arc changes in the geochemical characteristics (summarised in section 1.3; e.g., Stern et al., 1984a, Hildreth and Moorbath, 1988, Naranjo and Stern, 2004); the Northern (NSVZ; 33.3-34.4°S), Transitional (TSVZ; 34.4-37°S), Central (CSVZ; 37-42°S) and Southern (SSVZ; 42-46°S; Fig. 1.1).

The major zones of arc volcanism in Chile and Argentina are separated by significant gaps in volcanism. The SVZ extends from Tupungatito (33.4°S) in the north to Hudson (45.9°S) in the south. The SVZ is bounded north of 33.4°S by the Pampean Flat Slab Segment and south of 45.9°S by the Patagonian Volcanic Gap, which also marks the northern limit of the AVZ (e.g., Stern, 2004; Espinoza et al., 2005). The Pampean Flat Slab Segment (27-33°S) is a region of shallow subduction (<10°) thought to arise from the subduction of the Juan Fernández Ridge, an east-west seamount chain with thicker and more buoyant oceanic crust. This current slab geometry is thought to have prevailed for the last 5-6 Ma; consequently, no Pleistocene or Holocene magmatic activity has been recognised in this area (Kay and Mpodozis, 2002; Kay et al., 2005). The Patagonian Volcanic Gap (46-49°S) arises from the subduction of the Chile Rise, an oceanic ridge separating the Nazca and Antarctic Plates. There is no evidence of arc volcanism in this region for the last 12 Ma, however there has still been back-arc volcanic activity (Gorring et al., 1997; Stern, 2004; Espinoza et al., 2005). Late Quaternary back-arc volcanism occurs up to 250 km east of the main volcanic arc, principally in Argentina. This back-arc activity is dominated by alkaline basaltic volcanism from small monogenetic spatter

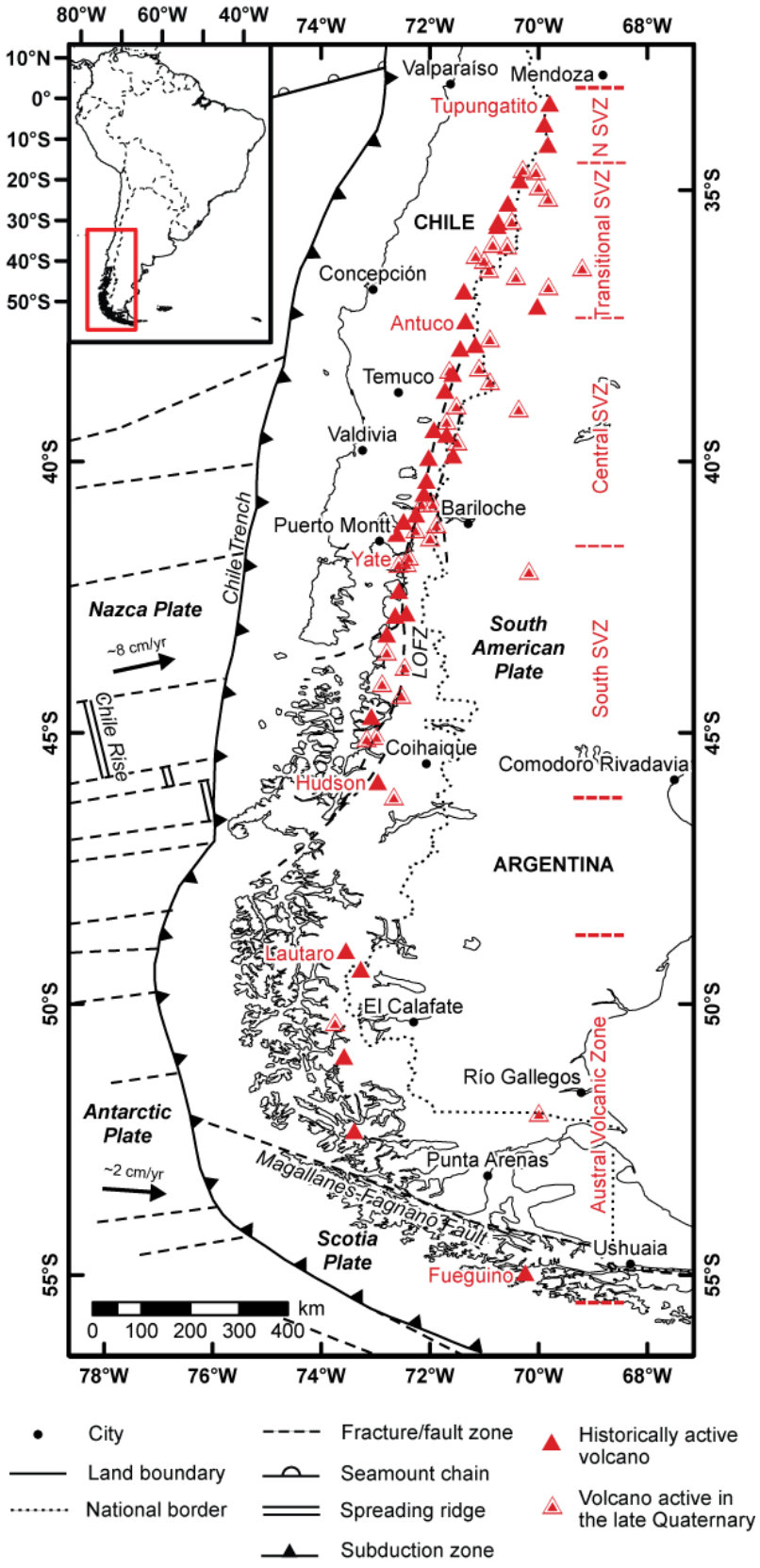

Figure 1.1: Map of southern Chile and Argentina showing the volcanoes of the Andean Southern Volcanic Zone (SVZ) and Austral Volcanic Zone (AVZ) for which there is clear evidence of post-glacial activity and some regional tectonic features. Figure from Fontijn et al. (2014).

and scoria cones with associated lava flows. Examples include the Huanquihue Group (∼39.9°S) and the Payenia volcanic province (∼34.5°–37.5°S; Søager et al., 2013).

The active arc front has migrated over geological time. Presently it is located at the eastern edge of the Andean Cordillera, which runs along the Chilean-Argentine boarder. Consequently the majority of the volcanoes within the SVZ lie in Chile. The SVZ spans the same latitudes as >70% of the Chilean population (e.g., Stern, 2004), with the greatest population density at the northern end within the Central Valley region. Eruptive explosivity and hazards are also elevated in this region by the presence of substantial ice and snowpack. Approximately half of the SVZ volcanoes active in post-glacial times host summit glaciers, or ice-filled summit craters or calderas (Siebert et al., 2010; Rivera and Bown, 2013). At the peak of the the last glacial maximum (LGM), at ca. 25-16 ka in this region (Hulton et al., 2002; Glasser et al., 2008; Kaplan et al., 2008), all the edifices in the SVZ and AVZ south of ∼38°S were covered by ice, possibly >1 km thick (Hulton et al., 2002; Glasser et al., 2008). The lateral extent of the ice sheet, ∼100-150 km and ∼250-300 km wide north and south of ∼42°S respectively (Hulton et al., 2002), greatly restricted terrestrial preservation of tephra from eruptions during glacial periods in the Pleistocene. It has been proposed that ice retreat after the LGM caused a significant increase in global volcanic activity in previously glaciated regions (Huybers and Langmuir, 2009), but evaluation of the post-glacial explosive eruption history of the central and southern sectors of the SVZ by Watt et al. (2013a) found no statistically significant increase in the early post-glacial period here compared to the later Holocene. However, recognition and accurate quantification of such potential changes in eruption rate in the southern Andes are difficult without a more comprehensive tephrostratigraphic record (Chapter 3).

1.1.1.1 Late Quaternary explosive activity

The SVZ has produced some of the largest explosive eruptions in recent history, most notably the 1932 eruption of Quizapu (Cerro Azul; >9.5 km^3 tephra; Hildreth and Drake, 1992) and 1991 eruption of Cerro Hudson (4-7 km^3 tephra; Naranjo et al., 1993). Even larger eruptions are known to have occurred in the SVZ during the Pleistocene (e.g., the

Diamante caldera-forming event at Maipo erupted ∼270-350 km^3 of tephra; Sruoga et al., 2005; Stern et al., 1984b). The SVZ is one of the most active volcanic arcs globally, and includes two of the most active South American volcanoes, Villarrica and Llaima; these lie in the centre of the SVZ and have had over 100 historic eruptions between them, fortunately with relatively limited regional impact (Dzierma and Wehrmann, 2010; Van Daele et al., 2014). In the late Quaternary (ca. the last 25 ka, i.e., the period for which terrestrial tephrostratigraphic records exist), there have been at least 25 large ($\geq$ 1 km^3 of tephra) explosive eruptions generating widespread fall deposits from 18 different SVZ volcanoes. An additional 4 large ignimbrite-forming eruptions have been recognised (e.g., Fontijn et al., 2014). However, despite the high explosivity and frequent activity within the SVZ few were regularly monitored until recently, and only Lonquimay, Llaima, Villarrica, Mocho-Choshuenco, Osorno and Calbuco were monitored on a permanent basis. The unexpected Chaitén eruption in 2008 led to a significant investment in volcano monitoring and enabled a substantial increase in the number of Chilean volcanoes permanently monitored to 43, of which 33 are within the SVZ (SERNAGEOMIN[3]). The benefits of this were evident in the recent March 2015 eruption at Villarrica, where signs of unrest were detected two days before the eruption. The larger, sub-Plinian eruption of Calbuco in April 2015 only showed increased signs of unrest a few hours before eruption, but successful evacuation, rapid-response monitoring and clean up proved effective in the management of this volcanic crisis. There are however still many gaps that exist in our knowledge of the eruptive histories of these volcanoes, even from historical times (e.g., Fontijn et al., 2014).

Records of eruptions in historical times are still confused as few written accounts exist prior to the 19^{th} century, and those that do are mostly secondary sources (e.g., Vidal Gormaz, 1869). This confusion is exacerbated by the fact that some volcanoes have multiple names, which in many cases may be shared with neighbouring volcanoes, making determination of historical activity from written sources problematic (e.g., Vidal Gormaz, 1869; Sepúlveda, 2004); for example, Mocho-Choshuenco Volcano has in the past been referred to as Quetrupillan; while Quetrupillan Volcano (∼55 km to the northeast) has

[3]http://www.sernageomin.cl/volcanes.php

been referred to as Mocho (e.g., Sepúlveda, 2004). As well as this ambiguity concerning the source of eruptions, there is also potential for confusion from the existence of multiple names for single events (see Chapter 2).

Since the historical records of eruptions are short, geological fieldwork provides the most useful tool for establishing longer timescale eruptive records. In southern Chile most prior work has relied on field observations (relative stratigraphic position of identified layers, their physical measurements and mapping their geometry) and limited whole-rock geochemical data to correlate tephra deposits (e.g., Stern, 1991a). Correlating using only field observations is challenging in this region of Chile; the temperate and humid climate means weathering rates are high so often tephra deposits are commonly poorly preserved, or exposed. This can make it difficult to distinguish between the medial to distal deposits of eruptions of magmas of similar composition solely from field observations. As whole-rock chemistry may vary with distance from the vent (as crystal content decreases with distance from the vent), is susceptible to the effects of weathering and tends not to vary much between units it is not a very robust technique for correlating tephra deposits. These problems are further discussed by Fontijn et al. (2014), who concludes that the inadequate characterisation of individual deposits has led to significant gaps and ambiguities in the tephrostratigraphic record.

Having a well constrained and characterised tephra record is valuable not just for understanding the tempo and magnitude of eruptions, but also as 'fingerprints' and age-markers, which other disciplines can utilise (e.g., palaeoclimatological, palaeoseismological and archaeological studies: e.g., Davies et al. 2012; Prieto et al., 2013; Moernaut et al. 2014). Tephra layers represent (quasi-) isochronous marker horizons that can be used to correlate over a vast geographical area and in different environmental settings (e.g., terrestrial outcrops and lacustrine and marine cores). Further, they are invaluable time markers, sometimes helping to date sequences where other chronometers might fail; for example, lake cores often rely heavily on radiocarbon ages, which can be difficult to calibrate due to reservoir effects (e.g., Yu et al., 2007). For tephrochronology to be used to its maximum potential requires tephra layers to be well characterised in terms of glass and/or mineral chemical composition, componentry and physical characteristics such as

colour, grain size and texture (e.g., Lowe, 2011). Tephra horizons are of greatest value when they can be correlated to well-dated volcanic events, enabling more accurate age models of the sediment cores to be constructed; therefore constructing detailed eruptive records from volcanoes is essential.

1.2 Chilean Tectonics (∼33-46°S)

The Chilean basement records the evolution of the Andes Cordillera and magmatic arc since the Late Proterozoic. During most of this time there has been an active plate margin although the convergence rate, angle and subducting plate inputs (e.g., age of oceanic crust, sediment thickness) have all varied. The Late Proterozoic to Late Palaeozoic is described by Charrier et al. (2007) as a "collisional history"; the evolution is characterised by accretion of metamorphic complexes (e.g., Western Coastal series) and westward arc migration. The period is divided into three cycles with the youngest, the Gondwana tectonic cycle (Late Devonian-Early Permian), being best recorded in the rocks; this cycle occurred as continental assembly of Gondwana took place and convergence rates were high leading to the development of a magmatic arc (cf. Charrier et al., 2007). During the final consolidation of the Gondwana megacontinent (Late Permian-Early Jurassic) convergence rates slowed and then finally ceased. These conditions led to the melting of the lower crust. As a consequence magmatism was dominated by silica magmas in the high Chilean Andes and on the Argentinian side of the Andes (cf. Charrier et al., 2007). Along the continental margin extensional basins formed; evidence of this is preserved in the Formation Panguipulli (Upper Triassic), which is found around Volcán Mocho-Choshuenco (Moreno and Lara, 2007).

In the early Jurassic this plate reshuffling came to an end (the assembling of Gondwana was complete) and subduction was reestablished. This renewed subduction led to the development of a new magmatic arc, which has been active almost continuously up to the present date (e.g., Stern, 2004). However, since the Early Jurassic the convergence and subduction parameters have varied so the position of the arc has changed. Early on, until the Early Cretaceous, the Phoenix plate was obliquely (towards the south-east) subducted under the South American Continent causing the magmatic arc to be positioned along the

present-day Coastal Cordillera. Following this there was plate reorganisation on a global scale and consequently in the late Early Cretaceous the convergence conditions changed; the Farallon oceanic plate was obliquely (towards the north-east) subducted and led to the formation of the Liquiñe-Ofqui fault Zone (LOFZ; cf. Charrier et al., 2007). During the early Cenozoic (∼27 Ma) the Farollon plate broke up into the Cocos and Nazca plate, that latter of which is still subducted beneath the Chilean continent. This fragmentation led to a change from oblique to nearly orthogonal convergence and a more than two fold increase in the convergence rate (e.g., Stern, 2004; cf. Charrier et al., 2007). As a result of this there was both an increase in magmatic activity and greater crustal shortening and thickening in Chile. This change led to the onset of Andean uplift, however the Andean Cordillera only had a moderately low elevation until the Early Miocene. The greatest rate of uplift occurred in the Mid Miocene with estimates of 0.3-0.25 mm uplift per a year since 10 Ma (cf. Charrier et al., 2007). During the Mid Miocene the magmatic arc moved westwards, returning approximately to its current location in the Main Cordillera (Stern, 2004); however, most of the current volcanic edifices within the SVZ formed within the last 0.35 Ma.

1.2.1 Present day tectonics within the SVZ

Presently Chilean volcanoes account for ca. 10% of the volcanoes within the Pacific Ring of Fire. These arise from the subduction of the Nazca plate beneath the South American Continent. The angle and rate of convergence varies along the Andean-Arc. In the SVZ the motion of the Nazca Plate is typically 7-9 cm/year at 20-30° from orthogonal to the trench. This oblique convergence is accommodated both by the eastward motion of the subducting Nazca Plate and north-south slip along the arc-parallel Liquiñe-Ofqui Fault Zone (LOFZ). The LOFZ is a major dextral, strike-slip fault system that extends 1000 km from 38°S to 47°S (e.g., López-Escobar et al., 1995, Cembrano 2000). The LOFZ is an important structure in the SVZ as it controls the location of many of the large volcanic centres and minor eruptive centres (MECs). Furthermore, the angle of the subducting Nazca Plate varies along the SVZ. In the NSVZ and TSVZ the slab steepens from ∼20° (33°S) to 25-30° (37°S). Further south, in the CSVZ and SSVZ, the dip is

constant at ∼25-30°. As well as variations along the arc in the configuration of the plates the continental crustal thickness, beneath the arc, also varies. Beneath the SVZ crustal thicknesses are estimated at ∼55-60 km at the northern limit (33°S) gradually decreasing to ∼30-35 km at 37°S. South of 37°S crustal thicknesses remain constant at ∼30-35 km (e.g., Lowrie and Hey, 1981).

Along strike the subduction inputs are relatively uniform. The sediment thickness, lithology (dominated by turbidites of silty clays and sandy silt) and composition are found to be relatively homogenous both spatially and temporally (e.g., Lucassen et al., 2010). The oceanic crust is relatively uniform in thickness and is formed along the >1000 km long Chile rise, which marks the southern end of the SVZ; the oceanic crust presently being subducted is 0-45 Ma and youngs to the south (e.g., Stern, 2004). The northern limit of the SVZ is marked by the Juan Fernández ridge, a chain of seamounts formed by the Juan Fernández hot spot. The only other site of heterogeneities in the subduction inputs are from the fracture zones. Fracture zones are long, linear, large topographic features in the oceans that form beyond transform faults that originate from offsets in a Mid-Ocean Ridge. These offsets juxtapose different aged oceanic lithosphere causing a step in the depth of the seabed and flexure (Watt, 2001). Within the SVZ there are three volcanoes that lie above the projected trace of major fracture zones; Nevado de Longaví (36.2°S) above the Mocho Fracture Zone, Mocho-Choshuenco (39.9°S) above the Valdivia Fracture Zone and Calbuco (41.5°S) above the Chiloé Fracture Zone.

1.3 SVZ Geochemistry

The geochemistry of the SVZ is very diverse, with picrites and tholeiitic basalts though to rhyolites and andesitic adakites. This large variability means it is not possible to classify a typical chemistry or general geochemical trend for the SVZ. Instead, it is better to consider each subdivision of the SVZ separately where general trends are observed.

The volcanoes in the NSVZ (33.3-34.4°S) have erupted rocks with a composition from basaltic-andesite through to dacites. The predominant rock types are 2-pyroxene and olivine-clinopyroxene andesites, although the more silicic rocks (>57% SiO_2) commonly contain hornblende and rare biotite (e.g., at Tupungato Volcano; Hildreth and Moorbath

1988). The volcanic products, from the NSVZ, have relatively high K, Rb, Sr, La/Yb, $^{87}Sr/^{86}Sr$ and lower $^{143}Nd/^{144}Nd$ compared to similarly evolved rocks from other parts of the SVZ (Stern et al., 2007). There are two main theories on the cause of this signature: (1) crustal contamination, as a result of the thicker continental crust, and (2) higher rates of subduction erosion, caused by the subduction of the Juan Fernández Ridge (Hildreth and Moorbath, 1988; Stern, 1991a).

In the TSVZ (34.4-37°S) andesites and dacites dominate, although basalts through to rhyolites are erupted. This large compositional range is also observed within individual complexes, such as Laguna del Maule (basalts to rhyolites: Hildreth et al., 2010) and Planchón-Peteroa (basalts to dacites: Torney et al., 1995). Isotopic and trace element studies indicate that rhyolites from the TSVZ have a significant contribution from crustal partial melts, whilst the more mafic magmas are dominated by a slab-derived component (Hildreth et al., 1999). The source of back-arc magmas is considered to be predominately sub-continental lithospheric mantle (e.g., Jacques et al., 2013). This complexity in the source of the melts is reflected in the large geochemical variation of the volcanic products.

In the CSVZ (37-42°S) and SSVZ (42-46°S), basalts through to rhyolites are erupted, with a predominance of basalts and basaltic-andesites. An important difference between the two segments is the relative lack of hydrous phases in the CSVZ: in evolved rocks (>59% SiO_2) from the SSVZ, amphibole is commonly found and biotite may be present (although it has only been reported in rhyolites from Chaitén: Amigo et al., 2013), whereas amphibole is rare and biotite is absent in the CSVZ (Stern et al., 2007; Gilbert et al., 2014). Isotopic and trace element studies suggest that the mantle is the primary source of melts, but that there is also a (relatively minor) slab-derived component (e.g., Hickey-Vargas et al., 1989; Stern 2004). The evolved melts typically have a similar isotopic signature to more primitive melts; therefore only a minor crustal contribution, or a contribution from young, isotopically similar crust, is inferred (e.g., McMillan et al., 1989; Singer et al., 2008).

In addition to along-arc geochemical trends, across-arc trends have also been identified: more easterly centres typically have a lower Ba/La, La/Nb and Ba/Nb and a higher concentration of K, compared to similarly evolved rocks at more westerly centres (e.g.,

Hickey-Vargas et al., 1989; Jacques et al., 2013). This trend has been interpreted to reflect smaller degrees of partial melting in the mantle wedge, and a decreasing slab-derived contribution towards the east (Hickey-Vargas et al., 1989; Jacques et al., 2013). Watt et al. (2013b), however infer that increasing slab-surface temperatures results in less hydrous parental melts further eastward in the arc, giving rise to the observed geochemical variations.

Within the crust the degree of differentiation (how evolved the melts become) appears to be strongly controlled by tectonics. Volcanic centres controlled by NE-trending fractures and faults, for example the volcanic chain of Osorno-Puntiagudo-Cordón Cenizos, commonly erupt more mafic rocks than centres controlled by NW-trending fractures and faults, for example Puyehue–Cordón Caulle (e.g., López-Escobar et al., 1995; Lara et al., 2006a; Cembrano and Lara, 2009). In addition to the stratovolcanoes the site of the minor eruptive centres (MEC; e.g., scoria cones) is often strongly tied to the tectonics. Many of the MECs are aligned along the Liquiñe-Ofqui Fault Zone (LOFZ); for example, between Calbuco and Osorno there are a large number of cones including La Viguería, Cayutué-Cabeza de Vaca group and Pichilaguna etc. (López-Escobar et al., 1995) and further north the MECs between Villarrica and Quetrupillan are aligned with the LOFZ (Hickey-Vargas et al., 1989).

The apparent sensitivity to the subducting slab and/or crustal tectonics in controlling geochemical trends means that each volcano produces magmas with a distinct geochemistry. This is invaluable in tephrochronology when assigning a tephra deposit to a source volcano. For example, within the CSVZ most volcanoes have a distinct K_2O vs. SiO_2 composition enabling deposits to confidently be assigned a source volcano and/or eruption (Fig. 1.2)

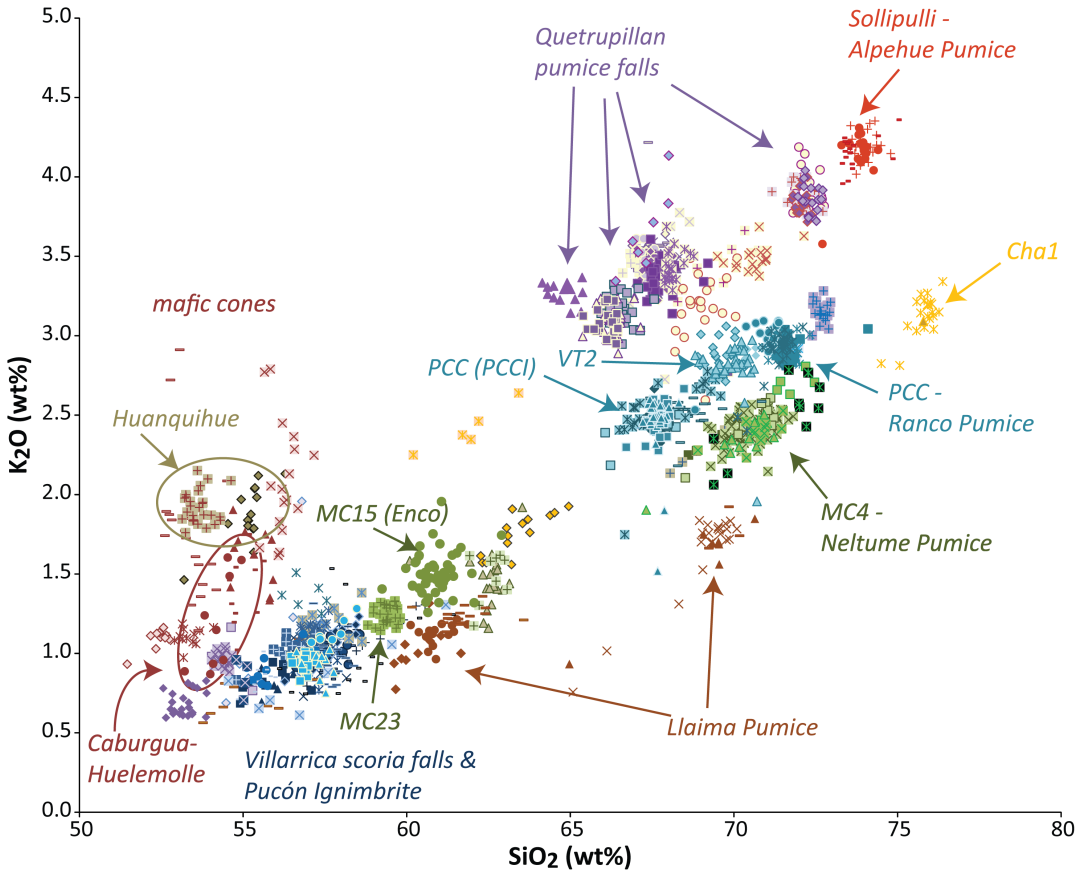

Figure 1.2: Glass analyses of volcanoes within the SVZ collated within Fontijn et al. (submitted). Different coloured symbols are used for different volcanoes and a few key eruptions are labelled. Figure illustrates how different volcanoes and/or eruptions often have a unique geochemical signature. Puyehue-Cordón Caulle (PCC), Mocho-Choshuenco (MC), Chaitén (Cha).

1.4 Regional interest

The SVZ is a region of particular interest not only for its frequent volcanic activity, but also because of the potential for investigating the (pre-) historical regional record of large earthquakes (similar to the 1960 Mw 9.5 Valdivia earthquake) using turbidite deposits in lakes (Arnaud et al., 2006; Moernaut et al., 2007; Bertrand et al., 2008). In addition to being volcanically and tectonically active, southern South America is the only landmass to cross the southern westerly wind belt, which is a significant control on global ocean circulation and so climate (Kilian and Lamy, 2012). High-resolution palaeoenvironmental archives have therefore been sought from the many fjords, lakes, and areas of peatland in southern Chile and Argentina (Kilian and Lamy, 2012). The predominantly post-glacial records obtained have provided significant insights into, for

example, interhemispheric climatic linkages and the dynamics of both Holocene climate and the regional deglaciation (e.g., Lamy et al., 2010; Moreno et al., 2012; Hall et al., 2013). At the Last Glacial Maximum (LGM; ca 25-16 ka within the SVZ; Hulton et al., 2002; Glasser et al., 2008; Kaplan et al., 2008) the SVZ was largely glaciated, so this region is a good case study to investigate the potential coupling between deglaciation and volcanism, namely a possible increase in eruption rates during deglaciation and early post-glacial times (Chapter 3: Huybers and Langmuir, 2009; Watt et al., 2013a; Rawson et al., in review).

1.5 Mocho-Choshuenco

Mocho-Choshuenco is a late Quaternary volcanic complex located at 39°55'S 72°02'W in the SVZ (33°–46°S; Fig. 1.3) of southern Chile. It lies between Volcán Villarrica, 55 km to the north, and the Puyehue-Cordón Caulle volcanic complex, 70 km to the south. The surrounding region is popular with tourists and close to several major population centres (over 400,000 people live within 100 km of the volcano), and presents a moderate level of volcanic hazard to the region. Mocho-Choshuenco is a glacially-capped complex that is interpreted as a compound volcano: Volcán Mocho has a 4 km wide caldera, infilled by a glacier, with a young scoria cone in the centre, called Mocho; Volcán Choshuenco, which forms part of the north-western rim of the caldera, has only been partially affected by the collapse so retains its conical form. Additionally there are circa (ca.) 40 minor scoria cones on the flanks (Moreno and Lara, 2007). During the Llanquihue glaciation, the last glacial period in southern Chile, Mocho-Choshuenco would have been extensively glaciated until ca. 18 ka, when deglaciation began at these latitudes (Hulton et al., 2002; Glasser et al., 2008; Kaplan et al., 2008).

1.5.1 Basement

The basement around Mocho-Choshuenco comprises primarily metasediments and intrusives, which record the geological history of the region from the Palaeozoic to the Lower Pleistocene (Moreno and Lara, 2007). The plutonic rocks are mainly tonalites

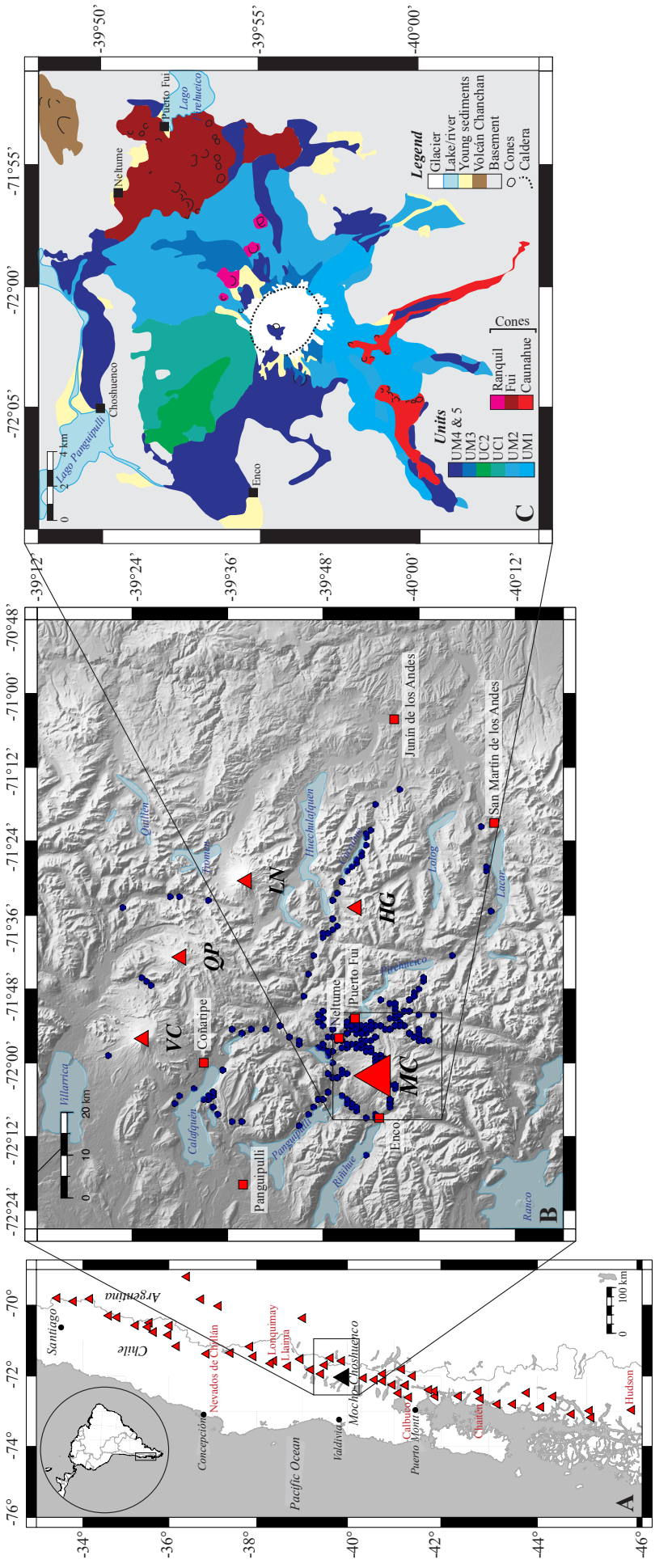

Figure 1.3: A: Map of the Southern Volcanic Zone (SVZ). Volcanoes that have been active in the Holocene are marked with red triangles. Mocho-Choshuenco is marked by the black triangle. B: The region around Mocho-Choshuenco (MC). Localities where deposits from MC are found are marked with a dark-blue circle, other volcanoes are marked with a red triangle (Villarrica (VC), Quetrupillán (QP), Lanín (LN), Huanquihue Group (HG)) and towns are labelled and marked with a red square. C: Simplified geological map adapted from Moreno and Lara (2007). Units are labelled as in Table 2.1 in Chapter 2.

(with biotite and hornblende) and granites, which include Pluton Panguipulli (ca. 140-180 Ma) and Pluton Choshuenco (ca. 135 Ma); Pluton Choshuenco is associated with the re-establishment of the magmatic arc during the Cretaceous and the development of LOFZ (e.g., Cembrano et al., 2000). The metasediments consist of metasandstones, slates, green phyllites and conglomerates. They are associated to Complejo Metamorfico Trafun (Devonian-Carboniferous) and Formation Panguipulli (Upper Triassic); the later, along with Pluton Panguipulli, record the initial fragmentation of Gondwana in the Triassic and the development of a rift basin along its eastern margin (e.g., Ramos and Kay, 1991). There are also minor amounts of volcanic breccias, conglomerates, tuffs and lavas that correspond to remnants of old stratovolcanoes worn away by intense glacial erosion. These are mainly basaltic-andesite to andesite in composition, although rare dacites have been found. Their age has been placed at between 20 Ma and 1 Ma. The influence of the basement on erupted magmas is evident in the geochemistry (e.g., isotopes, trace composition) and in the field at outcrops; one study focussing on magma composition estimated contributions of ∼5 wt% of assimilated crustal rocks in andesites and ∼15% for dacites (McMillan et al., 1989); in the field crustal xenoliths (primarily granites) are preserved in juvenile deposits from some explosive eruptions (e.g., MC15 and MC4).

1.5.2 Volcanic activity

Moreno and Lara (2007) present an overview of the geology of Mocho-Choshuenco. This study uses new and unpublished field observations and geochronological dates (^{14}C, K-Ar and ^{40}Ar/^{39}Ar) to summarise the geological units and basement structure of the complex. They find evidence of effusive activity since 350 ka. Despite the long period of time the style and composition of the activity appears not to have varied temporally; Lavas (often of type aa) are commonly interbedded with volcanic conglomerates and breccias; compositionally andesites are dominant but magmas range from basaltic andesites to dacites (52-69 wt. % SiO_2; whole rock; Fig 1.4). Spatially the activity has moved around the complex with time; this is most clearly seen on the geological map (Fig. 1.3), where the main shift is seen between the UM (Unidad Mocho) and UC (Unidad Choshuenco) formations. Erosion by glaciers mean only the last ∼18 ka of explosive activity is preserved

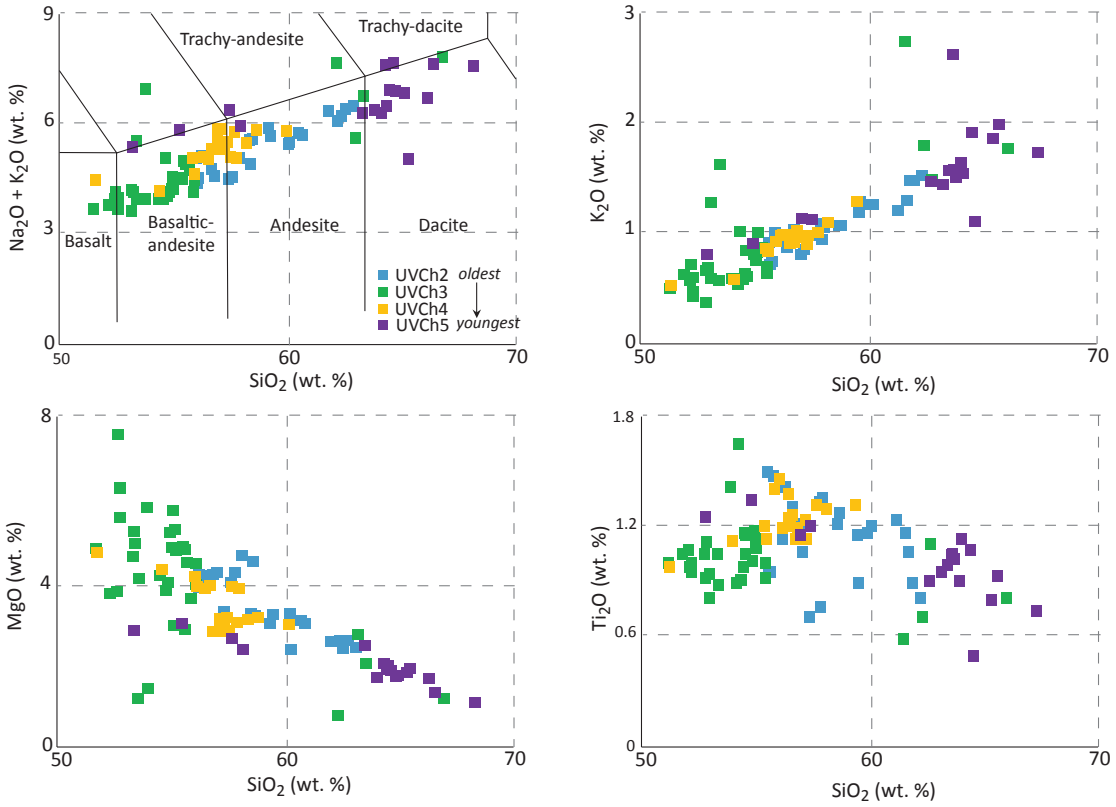

Figure 1.4: Selection of harker plots of geochemical analyses presented in Echegaray, 2004. Different colours represent different formations identified in the study. The oldest (UVCh2) are estimated to have erupted in the Mid Pleistocene and the youngest (UVCh5) during the Holocene. Unfortunately there is insufficient detail to update to the classification defined by Moreno and Lara, 2007, which is built on in this thesis.

in the geological record. Moreno and Lara (2007) recognise seven explosive eruptions of varying size (magnitude 2 to 5) and composition (basaltic-andesite to dacite) but, as presented in Chapter 2, this is a significant underestimate of the true explosive activity.

In addition to activity at the central vent there are circa (ca.) 40 minor scoria cones on the flanks (Moreno and Lara, 2007). The cones are subdivided into three groups: Fui (ca. 25 cones to the north-east and east of the edifice), Caunahue (ca. 10 cones on the south-west flank), and Ranquil (four cones on the north-east flank; Fig. 1.3). These cones are aligned NE-SW and are thought to be directly related to the current dextral transpressional regime (as a result of oblique convergence) and represent tension or extensional-shear fractures (Cembrano and Lara, 2009). Most volcanoes within the SVZ have scoria cones associated with their main stratovolcano but the abundance and density found at Mocho-Choshuenco is unique (Chapter 4).

1.6 Thesis structure

This thesis seeks to contribute to further understanding of the explosive activity at Volcán Mocho-Choshuenco, and by compiling a large comprehensive data set of new and published data shed new light onto broader geological arc volcanic processes. This thesis is divided in five chapters. In Chapter 2 a detailed study of the post-glacial tephra deposits from Volcán Mocho-Choshuenco is used to reconstruct the explosive eruptive history and both physically and geochemically characterise the deposits. This is based on my new field observations, geochemistry (glass and Fe–Ti oxides) and radiocarbon analyses combined with my compilation of unpublished data from collaborators. The chapter is split into three sections: field stratigraphy (section 2.3), tephra correlations (section 2.4) and eruption sizes (section 2.5). In Chapter 3, this high resolution eruption record is used to explore evidence for temporal variability in arc volcanism relating to deglaciation. The observed post-glacial temporal patterns in magma composition, eruption size and eruptive flux lead to the development of a model for how formerly ice-covered arc volcanoes respond to the removal of an ice load. Chapter 4 focuses on mafic magma diversity, particularly within the scoria cones. Major and trace element whole rock analyses are presented in the context of the arc to explore causes of diversity over short temporal and spatial periods. Finally in Chapter 5 a summary of the key findings will be presented and future work discussed. Further results from my analyses from Mocho-Choshuenco are included as an Appendix.

Chapter 2

The frequency and magnitude of post-glacial explosive eruptions at Volcán Mocho-Choshuenco, southern Chile

The work in this Chapter has been published in Rawson, H., Naranjo, J.A., Smith, V.C., Fontijn, K., Pyle, D.M., Mather, T.A., Moreno, H., (2015), The frequency and magnitude of post-glacial explosive eruptions at Volcan Mocho-Choshuenco, southern Chile, *Journal of Volcanology and Geothermal Research.* v. 299, p.103-129, doi:10.1016/j.jvolgeores.2015.04.003

2.1 Introduction

Active volcanoes pose a significant natural hazard, and in order to evaluate the likelihoods of future scenarios it is necessary to understand the frequency, scale and impact of past eruptions. In particular, there is a pressing need to better understand the products of medium to large magnitude explosive events. This requires detailed work in both proximal and distal localities to construct the stratigraphic framework of significant events. Identifying and correlating the deposits of explosive eruptions is also important to enable their potential use as regional chronostratigraphic markers in palaeoenvironmental records (e.g., Naranjo and Stern, 1998; Watt et al., 2013c; Fontijn et al., 2014).

Tephra deposits are commonly poorly preserved, or exposed. This is most problematic in temperate and humid climates where weathering rates are high, such as southern Chile (e.g., Fontijn et al., 2014); or in very arid regions, such as northern Chile or eastern Patagonia, where the lack of vegetation enables tephra to be easily eroded (e.g., Fontijn et al., 2014). Poor preservation and lack of exposure can make it difficult to distinguish between the medial to distal deposits of eruptions of magmas of similar composition solely on field observations. Scarcity of outcrops is also problematic at volcanoes with a complex tephrostratigraphy as a result of high eruptive frequencies, such as at Mocho-Choshuenco. Microanalysis of glass and mineral components provides a tool to fingerprint these deposits as the products of different eruptions typically have distinct glass and/or mineral compositions (e.g., Fierstein, 2007; Lowe, 2011; Smith et al., 2011a), and only small amounts of sample are needed for analysis.

In southern Chile most prior work has relied on field observations (relative stratigraphic position of identified layers, their physical measurements and mapping their geometry) and limited whole-rock geochemical data to correlate tephra deposits (e.g., Stern, 1991b). As whole-rock chemistry may vary with distance from the vent (as crystal content decreases with distance from the vent), is susceptible to the effects of weathering and tends not to vary much between units, it is not a very robust technique for correlating tephra deposits. Increasingly tephra studies use the analysis of glass shards to fingerprint and correlate deposits (e.g., see Lowe, 2011 for a review). In southern Chile, the high weathering rates and rapid degradation of pumice samples pose a significant challenge to the use of glass for chemical correlation.

Mineral chemistry is another less commonly used tool for correlating tephra. Biotite, hornblende, pyroxenes and Fe–Ti oxides have all previously been used for tephra correlation (e.g., Lowe, 1988; Froggatt and Rogers, 1990; Shane, 1998; Shane, 2000; Shane et al., 2003; Fierstein, 2007; Smith et al., 2011a). The Fe–Ti oxides offer an excellent and underexploited potential for use as a discriminant between the deposits of different eruptions. Fe–Ti oxides are almost ubiquitous in tephra samples, they equilibrate rapidly with the melt (e.g., Bacon and Hirschmann, 1988; Venezky and Rutherford, 1999; Devine et al., 2003) and their compositions are sensitive to magmatic conditions, such as temper-

ature and oxygen fugacity (Carmichael and Nicholls, 1967; Ghiorso and Evans, 2008). As a result, Fe–Ti oxides can be sensitive tracers of individual eruptive events (e.g., Shane, 1998; Fierstein, 2007; Marcaida et al., 2014).

Volcán Mocho-Choshuenco is a large compound stratovolcano in the Southern Volcanic Zone (SVZ) of Chile (Fig. 2.1). It lies in a region which is popular with tourists and close to several major population centres (over 400,000 people live within 100 km of the volcano), and presents a moderate level of volcanic hazard to the region. Nonetheless, the eruptive history of Mocho-Choshuenco is still poorly known, though it is clear that it that has experienced multiple large explosive eruptions during the Holocene whose timing and size remain poorly constrained (Moreno and Naranjo, 2006; Moreno and Lara, 2007; Fontijn et al., 2014). In this study we use field observations and major element chemistry of glass and Fe-Ti oxides to correlate the deposits of explosive eruptions from Mocho-Choshuenco between different locations in the region. This enables us to confidently correlate numerous deposits, despite variable preservation and distance from the eruptive source. This multi-technique approach also enables us to recognise many units for the first time, including a Plinian eruption (Huilo, MC9). Consequently the new event stratigraphy includes more eruptive units, and more quantitative details on the ages and sizes of past eruptions, than prior work. Our new high resolution stratigraphy of post-glacial explosive eruptions allows us to better constrain the past explosive activity, and reveals Mocho-Choshuenco to be one of the most productive and active volcanoes, in terms of explosivity, in the SVZ of Chile.

We present the work in three main sections; field stratigraphy (Section 2.3), tephra correlations (Section 2.4) and eruption size (Section 2.5). Section 2.3 focuses on the physical characteristics of the deposits, dispersal and their relative stratigraphic positions. Section 2.4 presents the geochemical data used to chemically fingerprint and correlate deposits, along with new radiocarbon dates and an age model to constrain eruption ages. Finally, in Section 2.5 we use these correlations to estimate the size of the eruptions. Although separate, all three sections are intrinsically linked; for example, units described in Section 2.3 could not have been identified without the chemical analyses presented in Section 2.4.

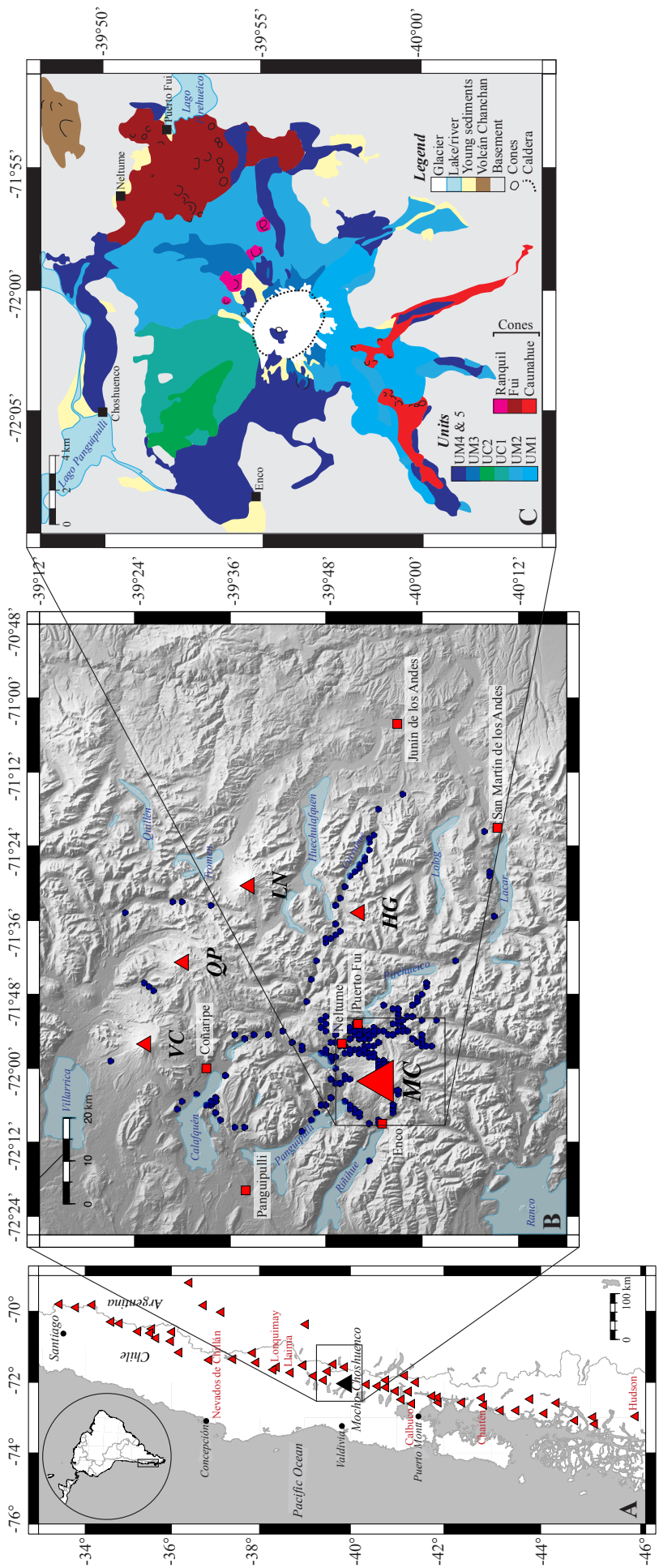

Figure 2.1: A: Map of the Southern Volcanic Zone (SVZ). Volcanoes that have been active in the Holocene are marked with red triangles. Mocho-Choshuenco is marked by the black triangle. B: The region around Mocho-Choshuenco (MC). Localities where deposits from MC are found are marked with a dark-blue circle, other volcanoes are marked with a red triangle (Villarrica (VC), Quetrupillán (QP), Lanín (LN), Huanquihue Group (HG)) and towns are labelled and marked with a red square. C: Simplified geological map adapted from Moreno and Lara (2007). Units are labelled as in Table 2.1.

2.2 Geological setting

Mocho-Choshuenco is a late Quaternary volcanic complex located at 39°55'S 72°02'W in the SVZ (33°46°S; Fig.2.1) of southern Chile. It lies between Volcán Villarrica, 55 km to the north, and the Puyehue-Cordón Caulle volcanic complex, 70 km to the south. Mocho-Choshuenco is a glacially-capped complex that is interpreted as a compound volcano: Volcán Mocho has a 4 km wide caldera, infilled by a glacier, with a young scoria cone in the centre, called Mocho; Volcán Choshuenco, which forms part of the north-western rim of the caldera, has only been partially affected by the collapse so retains its conical form. Additionally there are circa (ca.) 40 minor scoria cones on the flanks (Moreno and Lara, 2007). The cones are subdivided into three groups: Fui (ca. 25 cones to the north-east and east of the edifice), Caunahue (ca. 10 cones on the south-west flank), and Ranquil (four cones on the north-east flank; Fig. 2.1). During the Llanquihue glaciation, the last glacial period in southern Chile, Mocho-Choshuenco would have been extensively glaciated until ca. 18 ka, when deglaciation began at these latitudes (Hulton et al., 2002; Glasser et al., 2008; Kaplan et al., 2008).

2.2.1 Previous work

Moreno and Lara (2007) grouped the volcanic deposits from the Mocho-Choshuenco edifice into eight units, classified by age and source. Deposits from the Volcán Choshuenco peak are labelled Unidad Choshuenco (UC) and those from Volcán Mocho are labelled Unidad Mocho (UM). Additionally units are grouped by age from oldest UM1 to youngest UM5 (illustrated in Table 2.1). The eighth unit, Secuencia Piroclástica, comprises all the deposits from explosive eruptions preserved within the other seven units. As glaciers often erode down to the 'bedrock', the only tephra deposits that are widely preserved in proximal and medial locations are those that post-date the most recent deglaciation (i.e., UM4 and UM5). This study focuses on these post-glacial tephra deposits. The base of unit UM4 is placed at ca. 18 ka, the present estimate of when deglaciation began (e.g., Watt et al., 2013a). The boundary between UM4 and UM5 is marked by an eruption called 'Enco' and is placed at ca. 1.7–1.5 cal. ka BP using newly calibrated and modelled

radiocarbon ages (see Section 2.4.2.2).

In their previous work, Moreno and Lara (2007) presented evidence for three large post-glacial eruptions. Two formed widespread dacitic pumice fall deposits, Neltume and Pirehueico (Table 2.2), which are named after the village closest to the edifice that lies on the dispersal axis. The Neltume deposits are considered to be the oldest and largest preserved Plinian fall deposits from Mocho-Choshuenco and were first described by Echegaray et al. (1994). The Pirehueico deposits are the products of another major Plinian eruption, first identified by Pérez (2005) and are considered to be the second oldest and second largest preserved Plinian fall deposits from Mocho-Choshuenco. The third is a scoria fall deposit overlain by a pyroclastic density current (PDC; interpreted in previous studies as an ignimbrite), which is called Enco after the village where the thickest PDC deposits are found (Moreno and Lara, 2007; Table 2.2). This unit is the youngest of the three major eruptions. Further, possible historic events are summarised in Table 2.2 including 1864, the youngest confirmed eruption from Mocho-Choshuenco. Our work draws on seven field seasons at Mocho-Choshuenco between 1998 and 2014, focusing on the post-glacial tephra deposits. This work reveals the presence of many previously undescribed tephra deposits and expands our knowledge of the late Quaternary eruption record of this major volcanic centre.

	Units	Sub-units	Category
Unidad Mocho 5 (ca. 1.7 cal. ka BP-present)	MC25 (Riñihue)		β
	MC24		γ
	MC23 (Arauco)		β
	MC22		γ
	MC21 (Pilmaiquén)		β
	MC20	MC20B	β
		MC20A	
	MC19		γ
	MC18 (Hua-hum)	MC18C	α
		MC18B	
		MC18A	
	MC17		γ
	MC16		γ
Unidad Mocho 4 (ca. 18-1.7 cal. ka BP)	MC15 (Enco)	MC15 E	α
		MC15D	
		MC15C	
		MC15B	
		MC15A	
	MC14		γ
	MC13		β
	MC12		β
	MC11		γ
	MC10 (Grupo Fui Tephra)	MC10H	α
		MC10G	
		MC10F	
		MC10E	
		MC10D	
		MC10C	
		MC10B	
		MC10A	
	MC9 (Huilo)	MC9B	α
		MC9A	
	MC8		β
	MC7		γ
	MC6		γ
	MC5 (Pirehueico)	MC5F	α
		MC5E	
		MC5D	
		MC5C	
		MC5B	
		MC5A	
	MC4 (Neltume)	MC4C	α
		MC4B	
		MC4A	
	MC3		β
	MC2		γ
	MC1		γ
Unidad Choshuenco 2 (ca. 80-20 ka)			
Unidad Mocho 3 (ca. >60 ka)			
Unidad Choshuenco 1 (ca. >100 ka)			
Unidad Mocho 2 (ca. <200-130 ka)			
Unidad Mocho 1 (ca. >350-200 ka)			

Table 2.1: Stratigraphic summary and proposed nomenclature of the volcanic deposits from Mocho-Choshuenco. The seven formations are taken from Moreno and Lara (2007). Units, and sub-units, are ordered by stratigraphic position with the oldest at the base. Units are given a name from MC1 (oldest) to MC25 (youngest); MC26 and MC27 have poor stratigraphic constraint so are not included. Some units have an additional name (given in brackets). The units are assigned to a category: Category α, Category β, and Category γ depending on their distribution and preservation (see text for more details). Age estimates for the formations are given in brackets. All, apart from Unidad Mocho 4 and 5 (UM4 and UM5), are the values given in Moreno and Lara (2007). UM4 and UM5, the focus of this study, include updated ages from newly calibrated and modelled radiocarbon ages within this study.

Eruption name	Other names in literature	Description	Dispersal	Volume (km^3)	VEI	Date/Age (uncalibrated yrs)	Reference
MC25 (Riñihue)	1864, FP4	Pyroclastic flows, surges, lahars	SW		2	1-3 (± 1day) November 1864 AD	1,2,3
1822		Possible small historic eruption			2	1822 AD	3
1777		Possible small historic eruption			2	1777 AD	3
1759		Possible small historic eruption			2	1775 AD	3
MC15 (Enco)	FPPJB, OPFUY, OPL, FP3	Ignimbrite and scoria fall	Radial			1700 BP	1,4,5
MC5(Pirehueico)	Pp2	Andesitic pumice fall	E and NE	∼1		8200-6700 BP	1,4
MC4 (Neltume)	PpCh1, PpN	Dacitic pumice fall	NNE	2.5-2.9	5	10,700-9700	1,4,5,6
Previous names for Volcán Mocho-Choshuenco	Valdivia, Rauco, Lajara, Penguipulli, Panguipulli, Riñihue, Quetrupillan, Renihue, Shoshuenco						3

Table 2.2: Summary of previous knowledge of the post-glacial explosive history of Mocho-Choshuenco. Volcanic Explosivity Index (VEI) devised by Newhall and Self (1982). References: [1] Moreno and Lara (2007), [2] Vidal Gormaz (1869), [3] Sepulveda (2004), [4] Pérez (2005), [5] Echegaray (2004), [6] Echegaray et al. (1994).

2.3 Field stratigraphy

Late Quaternary tephra deposits from Mocho-Choshuenco are found in scattered exposures around the edifice as far north as Volcán Quetrupillán (ca. 70 km) and as far east as San Martín de Los Andes (ca. 65 km; Fig. 2.1). Approximately 400 localities were visited during fieldwork. Outcrops at these localities were predominantly road-cuttings where tephra layers were preserved either bounded by well-developed palaeosols or draped over glacially eroded basement or the post-glacial scoria cones that also form part of the Mocho-Choshuenco Complex. Outcrop exposure varies considerably in scale (1–20 m), as does unit thickness (from $<$ 5 cm to 8 m) and soil thickness (from a few cm to 60 cm). Dense vegetation, temperate climate and high annual rainfall contribute to the often poor exposure and preservation, making stratigraphic markers difficult to distinguish; even deposits from reasonably large explosive events (VEI $\sim$ 4) may only be preserved in very few localities (e.g., MC3, 3 localities). The best exposures were found in road-cuttings. However, few localities preserve multiple tephra units, and there is no known outcrop that preserves the complete stratigraphy. Many localities visited in early field seasons (by José Naranjo and Hugo Moreno) no longer exist or are no longer accessible due to changes in the road network.

Field work in proximal locations revealed tephra deposits from numerous eruptions. Each tephra deposit bounded by a palaeosol is attributed to a separate eruption, however we acknowledge that there may be insufficient time between two eruptions for soils to develop. Hence what we interpret as a 'single eruption' could still represent multiple events, or events sustained over an extended period of time. This has potential consequences for

the predicted frequency, intensity and scale of explosive eruptions. We describe deposits from 34 explosive eruptions in the post-glacial succession. These we assign to 27 eruptive units, which we label from oldest (MC1) to youngest (MC25; relative stratigraphic position illustrated in Table 2.1). Additionally we categorise these 27 units by their relative distribution and preservation. Units widely distributed and well preserved are assigned to Category 'α', those moderately distributed and preserved to Category 'β' and finally those that have limited distribution and poorly preservation to Category 'γ'. As there is an inherent bias in the rock record these categories do not always directly correlate to eruption size. For example, older deposits have a greater likelihood of being deeply buried and hence require deeper road cuts to be exposed. Therefore older units are not always exposed at the surface and hence may appear poorly distributed and preserved relative to younger units formed by eruptions of comparable size. Equally, the products of eruptions with narrow or uni-directional dispersal axes may be undersampled, compared to the products of eruptions of equivalent size that had a more even distribution.

Of the 27 eruption units identified we confirm the recognition of the previously identified pumice fall deposits of Neltume (MC4) and Pirehueico (MC5) and the large scoria fall and PDC unit of Enco (MC15). In addition to these 27 units, we identify numerous scoria fall deposits interbedded with the pumice fall deposits and palaeosols. These typically are nondescript, black-red, well sorted, fine-medium lapilli scoria fall deposits with microlite-rich glass and rare Fe–Ti oxides, which are rarely possible to chemically fingerprint and correlate. Most of these scoria deposits are likely to record small Strombolian eruptions originating from one of the many scoria cones that can be found on the flanks of Mocho-Choshuenco (ca. 40 cones). However, unless there are associated lava flows (e.g., column I, Fig. 2.2) or the clasts are very large and clearly have a proximal origin (e.g., column K, Fig. 2.2) it is not possible to confidently assign the origin of most deposits to a specific scoria cone or to the main edifice (central vent). To avoid duplication, these deposits were only labelled if they could be chemically fingerprinted (e.g., MC1). Consequently only 34 of the ca. 75 post-glacial eruptions are described and assigned a unit name. Furthermore since the palaeoenvironments are highly variable, it has not yet proved possible to correlate palaeosols, and we make no attempt to formalise

their stratigraphy.

2.3.1 Field sampling

Samples and measurements were taken of the tephra deposits preserved in both proximal and distal locations. Measurements of deposit thickness and maximum clast size of pumice, scoria, lithics and, if present, ballistic bombs, were made where possible. Any evidence of slumping, avalanche bedding, fragmented clasts and bombs was noted and taken into account when constructing the isopach and isopleth maps (see Section 2.5). Maximum clast size was determined from the geometric mean of the three axes of each of the five largest clasts at an outcrop. The geometric mean of these five measurements gives the maximum clast estimate. In early field seasons (1998 to 2006), we determined maximum clast size by measuring only the maximum diameter of the five largest, most spherical clasts. This difference in method is taken into account when drawing isopleth maps of maximum clast size. However, it is unlikely to be significant compared to the effects of post- depositional compaction and weathering.

Bulk samples of tephra and samples of individual pumice, scoria or lithic clasts were taken at ca. 175 sites, providing a set of more than 275 samples. Preliminary correlations in the field were made based on stratigraphic position and physical characteristics such as colour, lithic abundance, lithic type and grain size.

2.3.2 Field descriptions

We identify 27 volcanic deposits that are described below and in Table 2.3. We interpret each unit to be the products of a separate explosive eruption. Sub-units are labelled with a letter after the name (e.g., MC15A). Within the text we describe the units assigned to preservation categories α, β and γ, as defined in Table 2.1. Within each category we describe the units from oldest to youngest. Deposit and clast descriptions, type localities and deposit interpretations are described in Table 2.3. Key field photos (Fig. 2.3 & 2.4) and SEM images of typical glass shards (Fig. 2.5) are also included for units in categories α and β. The notation of maximum pumice (MP), maximum scoria (MS) and maximum lithic (ML) is used. Key localities, not illustrated in Fig. 2.2, are

presented in the text with their locality name (e.g., 120114-13) and GPS co-ordinates (latitude, longitude; WGS84 datum). All distances (km) from summit are measured from the centre of the Mocho scoria cone within the caldera of Mocho-Choshuenco.

2.3.2.1 Category α

These units are the most widely dispersed and preserved from the Mocho-Choshuenco Volcanic Complex. Typically deposits are found at more than 10 localities up to at least 15 km from the summit. Four pumice fall deposits, one scoria fall and PDC unit, and a scoria package are assigned to this category: MC4 (Neltume), MC5 (Pirehueico), MC9 (Huilo), MC10 (Grupo Fui Tephra), MC15 (Enco) and MC18 (Hua-Hum).

2.3.2.1.1 MC4 (Neltume Pumice)

The Plinian-style Neltume eruption produced a major pumice fall deposit, dispersed to the NNE and normally found resting conformably on top of a well-developed palaeosol and/or glacially eroded basement (typically either the Jurassic Tonalite of the Plutón Panguipulli, or the Triassic metasediments of the Formación Panguipulli, Moreno and Lara, 2007). In some proximal localities Neltume Pumice deposits overlie pumice deposits of MC3 and/or minor scoria fall deposits (e.g., MC1) that likely originate from nearby scoria cones (e.g., columns A, C, Fig. 2.2).

Internally, MC4 is a tripartite unit (e.g., column B, Figs. 2.2, 2.3B): at its base is a fine grey ash, interpreted as a vent clearing event (MC4A); This is overlain by a minor, fine-lapilli sized, orange-weathered pumice deposit (MC4B); and capped by the main sub-unit, an orange-weathered, well-sorted, lithic-poor pumice deposit (MC4C). In distal localities (when total thickness ca. <15 cm) the main sub-unit appears zoned as a result of variations in componentry (Fig. 2.3D). This is clearly seen at 030114-4 (39°30'S 71°33'W; MP of 0.4 cm and thickness of 11 cm) where the bottom two thirds (bottom 7 cm; Fig. 2.3D) weathers orange, as in more proximal localities, and changes sharply to dark-grey-yellow weathering in the upper third. This main unit, and underlying finer pumice unit, are interpreted as the deposits of a Plinian-style eruption as they are widely dispersed and thicknesses greater than 1 m are commonly preserved.

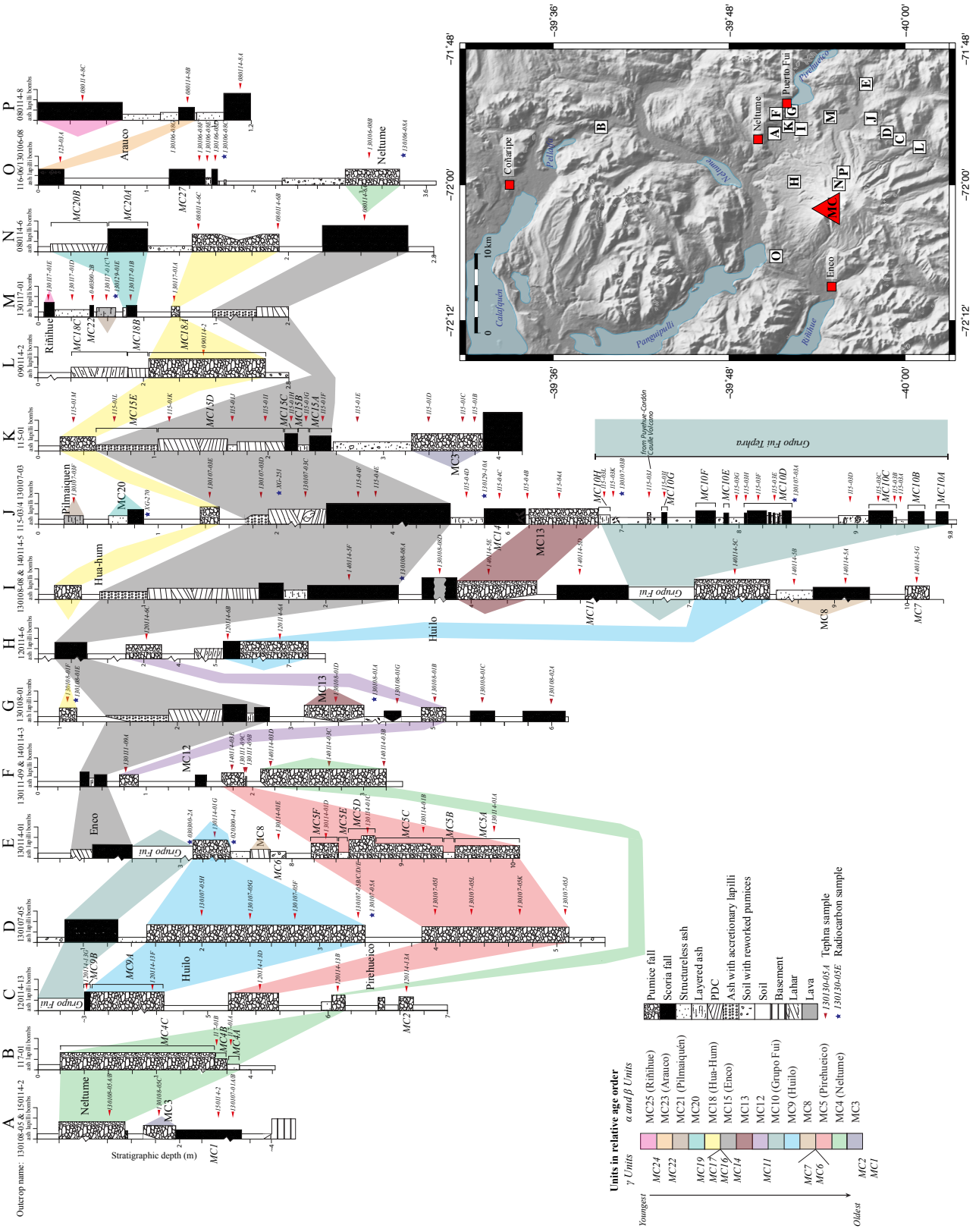

Figure 2.2: Sixteen key localities that preserve Mocho-Choshuenco pyroclastic units. Locations of tephra (red triangles) and carbon (blue star) samples are marked. Correlations between sites are based on stratigraphic position and physical and chemical characteristics (glass and Fe–Ti oxide compositions) of the deposits. The units, and most sub-units, are labelled on the columns. Only units that comprise categories α and β are correlated between multiple localities and assigned a colour. All of these columns are labelled on the map, to the right. The vertical scale is in metres with a tick every 0.2 m.

Deposits from the Neltume unit (MC4) are abundant and narrowly dispersed to the NNE. The thickest deposits of this unit are found NNE of the edifice, along the dispersal axis mid-way between the villages of Neltume and Choshuenco (Fig. 2.1). Here fallout deposit thicknesses (MC4C) reach 8 m and bombs up to 19 cm are preserved (e.g., 160114-1 at 39°50'S 72°3'W, 12 km from summit). The most continuous deposits are found along Ruta 203, along the eastern shore of Lago Panguipulli. The most distal localities with confirmed Neltume deposits are on the northern flank of Volcán Villarrica (63 cm thick, locality 030113-1 at 39°21'S 71°59'W, 65 km north of summit), near the town of Curarrehue (7 cm thick, 310100-3 at 39°21'S 71°36'W, 75 km NNE of summit) and on the northern flank of Volcán Lanín (27 cm thick, CLD163 at 39°34'S 71°32' W, 60 km north-east of summit).

The Neltume deposits are typically capped by a well-developed palaeosol that commonly includes reworked pumice clasts. This palaeosol separates the Neltume deposits from those of the overlying Pirehueico unit (MC5), described next.

2.3.2.1.2 MC5 (Pirehueico Pumice)

The Plinian-style Pirehueico eruption produced a major pumice fall deposit that typically rests conformably on top of a well-developed soil and, in places, MC4 (Neltume) deposits (e.g., 130207-01 at 39°49'S 71°39'W). In a few outcrops, a thin (<2 cm) fine-lapilli scoria fall unit is found at the base of MC5, with no clear palaeosol horizon between (e.g., column F, Fig. 2.2).

The Pirehueico Pumice is the most complex of the large pumice units from Mocho-Choshuenco with 6 distinct beds preserved (e.g., column E, Fig. 2.2; Table 2.3; Fig. 2.3E-G). The deposits, dispersed to the east, are primarily orange weathered, well to moderately sorted, pumice-rich, with variable lithic and clast sizes between the sub-units. Two minor, grey-brown, fine-medium ash layers (MC5B and MC5E) are inter- bedded within the sequence. The deposits are interpreted as the result of a Plinian-style pumice fall with possible interbedded minor PDC deposits. Alternatively these fine ash layers (MC5B, E) could represent the time between eruption pulses, during which finer ash, from within the main fallout, was able to settle.

Deposits from this event are best preserved along the road parallel to the southern shore of Lago Curruhué, 30 km due west of Junín de los Andes, Argentina. The thickest fall deposits of Pirehueico Pumice are found east of the edifice, along the dispersal axis and within the Huilo-Huilo Biological Reserve. Here thicknesses up to 3 m and bombs up to 25 cm are preserved (e.g., 130117-06 at 39°56'S 71°50'W, 16 km east of summit). The most distal locality where Pirehueico deposits are confirmed is near Junín de Los Andes (27 cm thick, 170399- 11 at 39°58'S 71°16'W, 66 km east of summit).

The Pirehueico deposits are capped by a well-developed palaeosol, commonly with pumice clasts and charcoal pieces. At one locality (column E, Fig. 2.2) there is a pumice-rich horizon within the palaeosol, which we interpret as a reworked pumice fall (MC6) based on geochemical data (see Section 2.4).

2.3.2.1.3 MC9 (Huilo Pumice)

The Plinian-style Huilo eruption produced a major pumice fall deposit that typically rests conformably on top of a well-developed palaeosol and deposits from the Neltume (MC4) eruption (e.g., 130120-02, 39°49'S 71°58'W). At rare outcrops to the east it sits above, separated by a palaeosol, the Pirehueico (MC5) deposits (e.g., column D, Fig. 2.2) and the scoria fall and flow MC8 (e.g., 130131-03, 39°55'S 71°55'W; MC8 described in Section 2.3.2.2).

Internally two distinct beds are preserved. The main, lower bed (MC9A) is an orange-weathered, well-sorted, massive, lithic-poor (ca. $< 5\%$) pumice deposit (e.g., column D, Fig. 2.2), interpreted as the deposits of a Plinian-style eruption. At rare outcrops, where the thickest Huilo Pumice deposits are preserved, a second, upper bed (MC9B) is visible (e.g., column C, Fig. 2.2). Here the pumice deposit has a sharp upper contact (i.e., no gradation between beds) with a thin continuous scoria layer (Fig. 2.3G, H) resting conformably on top. This layer is often <10 cm thick and oxidised red. Its limited preservation and presence only to the east of the edifice suggests that this scoria unit may originate from a nearby scoria cone, which erupted immediately after the Plinian-style eruption.

Deposits are relatively abundant and quite broadly dispersed to the east. The thickest

fallout deposits (MC9A) are found east of the edifice, just south of the dispersal axis, which trends east, and within the Huilo- Huilo Biological Reserve. Here thicknesses up to 3.3 m are preserved (e.g., 100114-5 at 39°5'S 71°52'W, 15 km east of summit). The most distal locality where Huilo deposits are confirmed is near Lago Huechulafquen (20 cm thick, 130207-04 at 39°49'S 71°37'W, 38 km ENE of summit).

The Huilo deposits are overlain by a well-developed palaeosol commonly with reworked pumice clasts from MC9A. This palaeosol separates the Huilo deposits from those of the Grupo Fui Tephra package (MC10), described next. At one locality (column H, Fig. 2.2), immediately above the Huilo unit, a light-grey, 95 cm thick laminated succession of fines-depleted layers (each 1–10 cm thick), which are primarily planar bedded although some preserve cross bedding, is interpreted as a reworked ash deposit with some characteristic lahar features (e.g., matrix supported and sub-angular clasts; Fig. 2.2H).

2.3.2.1.4 MC10 (The Grupo Fui Tephra)

The Grupo Fui Tephra comprises multiple coarse-ash to medium-lapilli sized, scoria and ash deposits separated by palaeosols (Fig. 2.3IK); we define 8 sub-units in Table 2.3. Preservation of this unit is poor. Most of the scoria is moderately vesicular, weathers orange, and often has little to no fresh glass preserved. The deposits are predominantly preserved to the east and ENE of the main edifice in the area between the volcano and Lago Pirehueico (Fig. 2.1). This area is also where the greatest concentration of scoria cones is found, and it is inferred that the majority of these deposits, most of which are falls, originate from the cones, rather than from the main edifice. A poorly dispersed scoria unit (MC11; e.g., column I, Fig. 2.2) overlies the Grupo Fui Tephra deposits. This is bound by a palaeosol, which is overlain in turn by deposits from MC12 and MC13 (Section 2.3.2.2).

2.3.2.1.5 MC15 (Enco)

The Enco eruption produced a sub-Plinian scoria fall and a major scoriaceous PDC unit. Deposits typically rest conformably on top of a well-developed palaeosol and, separated by the palaeosol, the deposits of Neltume (MC4), Huilo (MC9) or the Grupo Fui

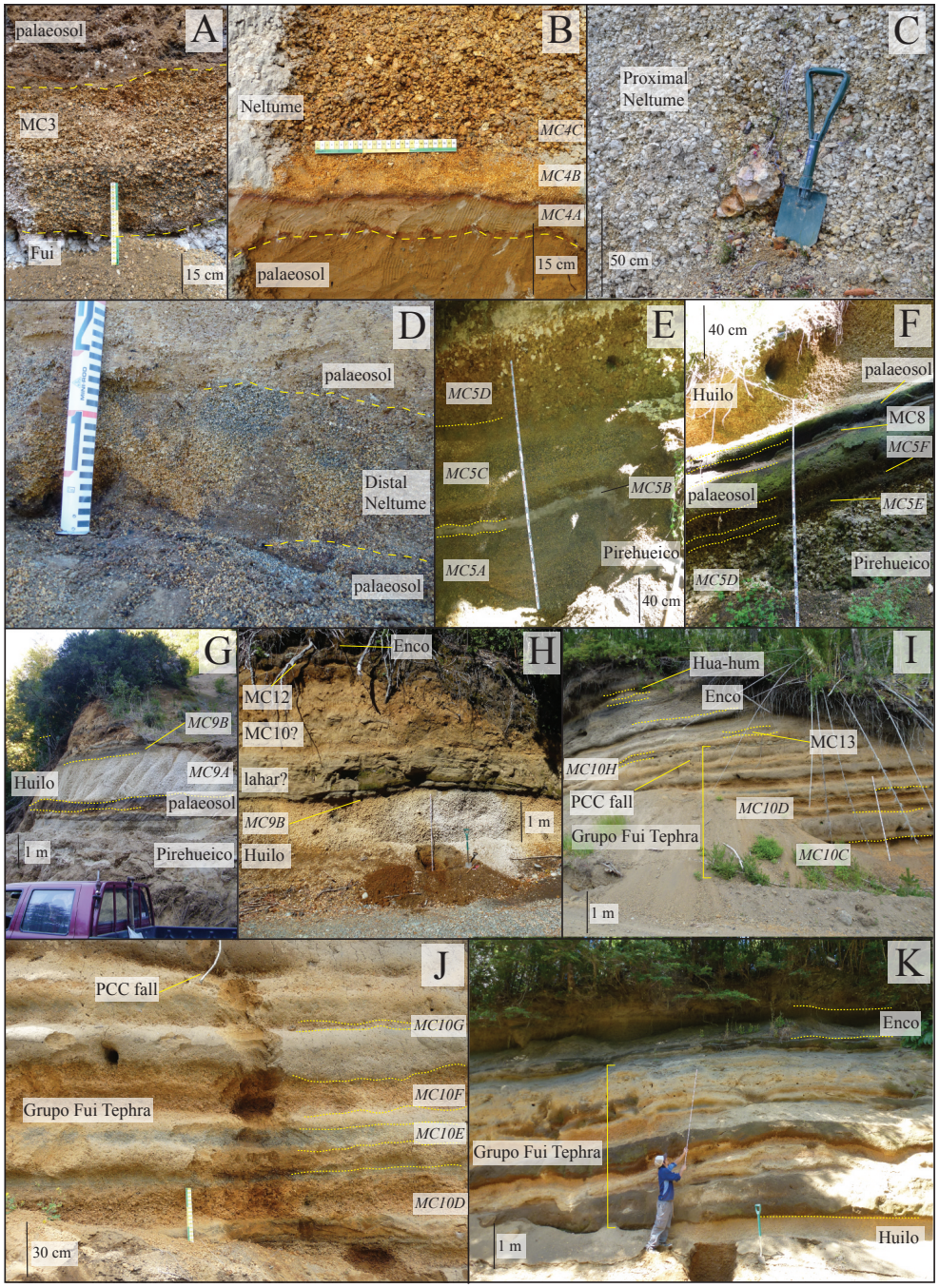

Figure 2.3: Field photos of deposits around Mocho-Choshuenco. Photos included are just of units comprising Category α and β. GPS coordinates of localities (given by codes in the caption) listed are given in Appendix A.1. A: MC3 taken at site 115-01 (column K, Fig. 2.2); B: the three beds of Neltume (MC4) at 117-01 site (column B, Fig. 2.2); C: proximal Neltume (MC4) fall deposit, with bombs, at site 302-01; D: distal Neltume (MC4) at site 030114-4 between Quetrupillán and Lanín; E: lower sub-units of Pirehueico (MC5) at site 130114-1 (column E, Fig. 2.2); F: upper sub-units of Pirehueico (MC5) and lower part of Huilo (MC9) at site 130114-1 (column E, Fig. 2.2); G: Huilo (MC9) with characteristic scoria band (MC9B) at site 060406-7; H: Huilo with overlying lahar or reworked ash deposit at site 120114-6 (column H, Fig. 2.2); I: the Grupo Fui Tephra (MC10) with a thin pumice layer from Puyehue-Cordón Caulle (PCC) interbedded within the group at site 115-03 (column J, Fig. 2.2); J: close-up of the mid-part of MC10 at site 115-03 (column J, Fig. 22.2); K: Grupo Fui Tephra deposits bounded by Huilo (MC9) and Enco (MC15) deposits at site 130114-1 (column E, Fig. 2.2). The yellow and green ruler is 30 cm long, the tape measure has 10 cm intervals labelled and notches on a 1 cm scale.

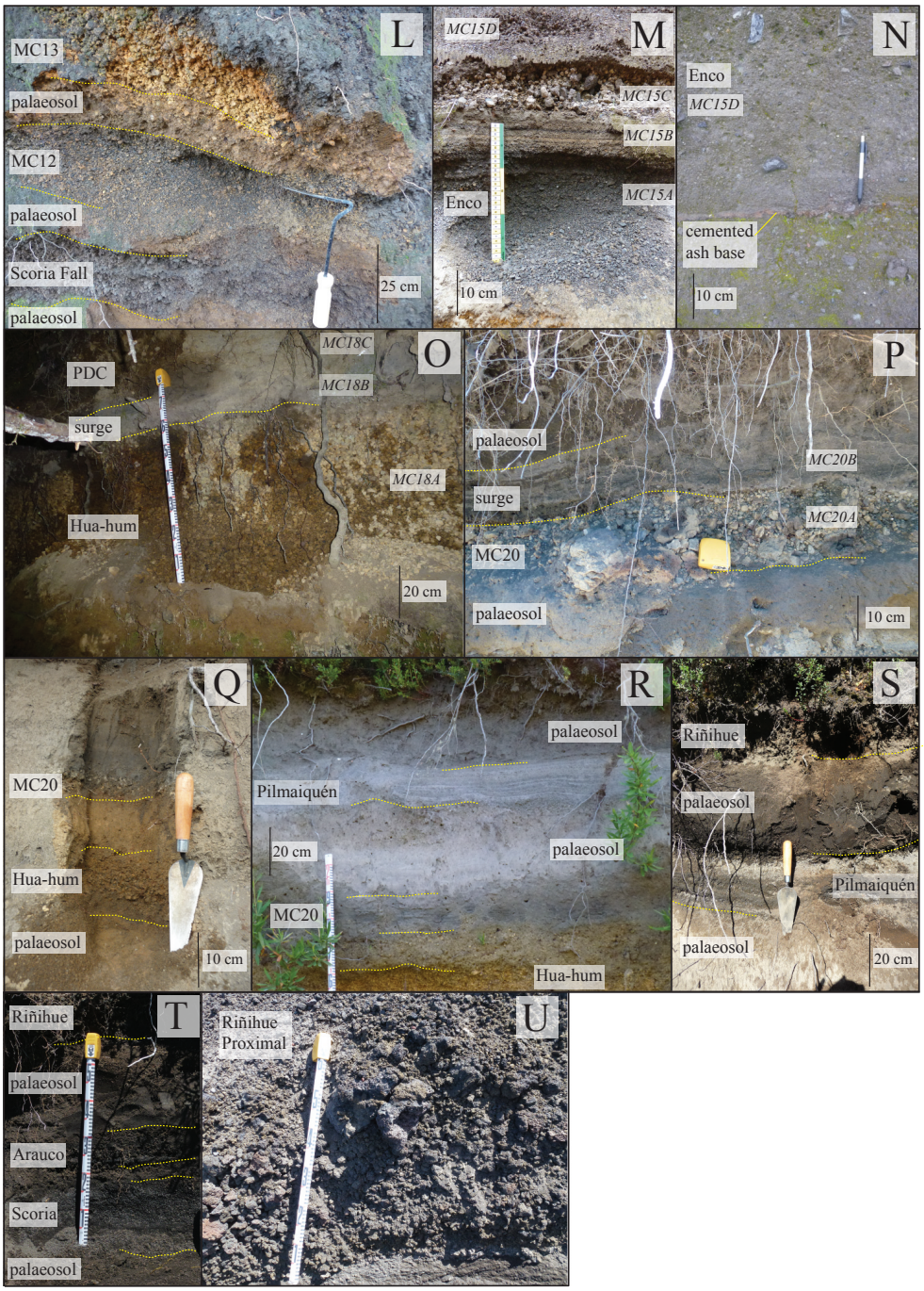

Figure 2.4: Field photos of deposits around Mocho-Choshuenco. Photos included are just of units comprising Category α and β. GPS coordinates of localities (given by codes in the caption) listed are given in Appendix A.1. L: Deposits of MC12 and MC13 at site 130108-1 (column G, Fig. 2.2). Scoria fall is probably from a nearby cone; M: sub-units of Enco (MC15) preserved at site 115-01 (column K, Fig. 2.2); N: close-up of the packages within MC15D preserved near the Refugio at site 113-01; O: Hua-Hum (MC18) deposits at site 080114-2 (column L, Fig. 2.2); P: proximal deposits of MC20 at site 080114-6 (column N; Fig. 2.2); Q: more distal appearance of MC20 and MC18 at site 130129-1; R: Pilmaiquén (MC21) overlying MC20 and within the overlying soil there is scoria from MC25 at site 150114-4; S: Pilmaiquén (MC21) and Riñihue (MC25) at site 130117-1E (column M, Fig. 2.2); T: Arauco (MC23) and Riñihue (MC25) near the summit at site 070114-8; U: proximal Riñihue (MC25) on the surface of the edifice at site 080114-8 (column P, Fig. 2.2). The yellow and green ruler is 30 cm long, the tape measure has 10 cm intervals labelled and notches on a 1 cm scale.

Tephra (MC10). The base of the Enco deposit is not exposed to the west (e.g., 130106-01 at 39°56'S 72°06'W), while few Enco deposits have been found to the south due to limited road access. Here, deposits typically infill the palaeotopography such that the base of the deposit is not exposed (e.g., 050300-2 at 40°0'S 72°7'W)

Internally five separate sub-units are preserved (detailed descriptions in Table 2.3): MC15A is a well sorted, black scoria fall, which rests conformably on top of a well-developed palaeosol; MC15B deposits comprise mm-scale, grey-black-yellow, parallel bands of ash, which have a diffuse, gradational basal contact with MC15A; MC15C is a moderately-well sorted, black scoria fall that rests conformably on top of MC15B; MC15D is a poorly sorted, cross-bedded, grey-weathered PDC deposit that sharply erodes MC15C; and finally MC15E is a grey, ash deposit containing ash pellets and rare accretionary lapilli, with a diffuse, gradational contact with MC15D.

A grey ash (MC15E) at the top of the Enco sequence typically grades into a well-developed palaeosol, which separates the Enco deposits from those of the overlying Hua-Hum event (MC18). At one outcrop (130106-03 at 39°56'S 72°06'W) the PDC deposits of MC15D are sharply eroded by another scoriaceous PDC deposit (MC26), which is thought to originate from the lateral collapse of the Tumba Buey Scoria cone, a large collapsed scoria cone on the western flank of Mocho-Choshuenco 3 km east of this locality. Substantial lahar deposits, with thicknesses <10 m, are also associated with the Enco units. These are principally found to the north-west, along the road between the villages of Enco and Choshuenco (e.g., 150114-11 at 39°53'S 72°09'W), and to the south, in Pampa-Pilmaiquén along the valley of the Pillanleufú River (e.g., 090114-3 at 40°1'S 71°57'W), where they clearly postdate the main PDC deposits of the Enco eruption. The lahar deposits are a succession of grey beds that can be divided into three main levels; the base (<2.5 m thick) is a fine-depleted, densely laminated deposit with scarce, sub-angular lithic fragments of lavas <20 cm; the middle deposit (<2 m thick) is characterised by abundant lava blocks (<50 cm) in a sandy matrix; and the top level reaches <6 m thick and contains imbricated blocks immersed in a predominantly sand-rich matrix that shows diffuse bedding. These deposits possibly represent the interstratification of lahar flood-plain, transition and lahar-runout facies (Scott, 1988).

The Enco deposits are widespread radially around the volcano. The thickest fall deposits are found east of the edifice, along the dispersal axis and mid-way between the edifice and Lago Pirehueico. Here thicknesses of 2.1 m and bombs of 13 cm are preserved (e.g., 130129-10 at 39°57'S 71°54'W, 11 km east of summit). The thickest PDC deposits are found to the west, near the Refugio Universidad Austral, with thicknesses up to 70 m and clasts up to 30 cm (e.g., 130106-01 at 39°56'S 72°06'W, 6 km west of summit). On the eastern flank, just above the tree line, bombs >1 m are preserved (e.g., 070114-8 at 39°55'S 71°59'W, 4.5 km east of summit).

Field descriptions, interpretations and type localities for the post-glacial tephra deposits

Unit		Field Description		Interpretation	Type Locality					Photo in Fig. 2.3 & 2.4	SEM in Fig. 2.5
Name	Subunits	Deposit appearance	Clasts		Column in Fig. 2		MP/MS (cm)	ML (cm)	Th (cm)		
MC25 (Riñihue)		Well-moderately-sorted, black, fine to coarse-lapilli size scoria deposit. On edifice bombs up to 20 cm are found.	Black, vesicular, iridescent, scoria	Scoria fall	P	36°56'S 72°0'W			47	T,U	Q
*MC*24		Black, fine-medium-lapilli sized scoria deposit	Black, vesicular scoria	Scoria fall		39°55'S 71°59'W					
MC23 (Arauco)		Well-sorted, ungraded, scoria deposit. On edifice bombs are preserved (<25 cm)	Medium-lapilli sized, vesicular, black, iridescent scoria	Scoria fall	O	39°51'S 72°6'W			25	T	P
*MC*22		Thin, well-sorted, dense, fine-lapilli scoria deposit	Black, dense, vesicular scoria.	Scoria fall	M	39°55'S 71°53'W					
MC21 (Pilmaiquén)		Indurated, cm-scale thickness, well-sorted, parallel bands comprising grey, medium-ash to fine-lapilli sized clasts. Coarser layers are more loosely consolidated, particularly the top layer, which is not always preserved. The well-sorted top layer weathers grey, is ca. 75% the total thickness of lower bands and comprises fine-lapilli-sized, scoria clasts. Deposits commonly drape over topography and have a roughly uniform thickness over distances of 10s of metres. Rare localities preserve cross-bedding.	Fine-lapilli sized, vesicular, black, scoria	Wet scoria fall. Bands may record pulsating. Flow-like features may be secondary and arise from reworking	100 m south of M	39°55'S 71°54'W	1.4		31	R,S	O
MC20	MC20B	Well-moderately-sorted, grey, fine ash to fine-lapilli sized deposits. Sorting is poorer in more proximal localities where cm-scale, low-angle, cross bedding structures are preserved.		PDC (*surge*)	N	39°54'S 71°58'W			30	P,Q,R	
	MC20A	Moderate-poorly-sorted yellow weathered scoria deposit. In proximal localities fine-coarse lapilli sized clasts with abundant bombs (up to 20 cm).	Yellow weathered, very vesicular, crystal poor, scoria clasts. Large clasts (>10 cm) retain their black appearance in the cores. In more distal localities the scoria appears less vesicular and has a pumice-like appearance.	Scoria fall			20 (bombs)		23	P,Q,R	N
*MC*19		Grey-brown ash with yellow weathered pumice clasts	Weathered, yellow, vesicular, crystal poor pumice clasts.	Pumice fall		39°53'S 71°58'W			258	O	
MC18 (Hua-Hum)	MC18C	Sub-rounded lithic-rich and pumice-rich deposit with a bubble-rich ashy matrix		PDC only preserved at one locality	L	39°53'S 71°58'W	1.1		28	O	
	MC18B	Moderately-poorly-sorted, grey, coarse ash to fine-lapilli sized deposit		PDC (*surge*) only preserved at one locality					13	O	
	MC18A	Well-sorted, ungraded, orange-brown weathered, lithic-poor, medium-lapilli sized pumice deposit.	Orange-brown weathered, very vesicular and crystal poor pumice. Lithics are rare (ca. <5%), black, angular, glassy, poorly vesicular clasts.	Subplinian pumice fall			7.1	3.6	40	O,Q,R	M
*MC*17		Moderately-well-sorted, dark-grey-brown, medium-lapilli sized scoria deposit. Comprises rare small bombs (up to 6 cm).	Grey-brown, vesicular scoria	Scoria fall		39°54'S 71°58'W			18		
*MC*16		Well-sorted, brown-black weathered, fine-lapilli sized scoria deposit	Brown-black, slightly vesicular scoria	Scoria fall		39°54'S 71°58'W			15		

Field descriptions, interpretations and type localities for the post-glacial tephra deposits

Unit		Field Description		Interpretation	Type Locality					Photo in Fig. 2.3 & 2.4	SEM in Fig. 2.5
Name	Subunits	Deposit appearance	Clasts		Column in Fig. 2		MP/MS (cm)	ML (cm)	Th (cm)		
MC15 (Enco)	MC15E	Normally graded, grey, medium-ash, rich, particularly near the contact with MC15D, in both coated ash pellets and, more rarely, accretionary lapilli (typically <2 cm). Top usually grades into a well-developed palaeosol.	Heterogeneous ash with no modal glass morphology and abundant xenoliths of country rock and glass shards of older tephra units.	PDC	K	39°52'S 71°55'W			<55		
	MC15D	Poorly-sorted, indurated, cross-bedded (low-angle, 10's cm-scale), grey-weathered deposit with abundant lithics supported in a medium-coarse ash matrix. Separate flow packages distinguishable in proximal localities. Each package is typically 1–2 m thick and inversely graded. The base is a well-sorted cemented ash, 10–20 cm thick, with red–brown oxidised top and base. The top is marked by a scoria rich layer, or pinching lens, or a thin layer of black glassy clasts. Typically the lithic component decreases up the package.	Lithics are predominantly grey-black, pitted, sub-angular, lava clasts, red-orange hydrothermally altered clasts and chalky-weathered clasts of a felsic intrusive rock. Brown-weathered, medium lapilli sized, black, sub-rounded, vesicular scoria and fine lapilli sized, black, glassy clasts mark the top of the flow packages	PDC (*ignimbrite*) with multiple different flow packages					110	M,N	
	MC15C	Moderately-well-sorted, black scoria deposit with a moderate amount of lithics and abundant bombs. No grading or shower-bedding preserved.	Medium-coarse-lapilli sized, black, vesicular, crystal poor, commonly iridescent scoria, which typically has a fresh appearance. Lithics (ca. 5-10%) are heterogeneous. Most are dense grey or black, angular glassy lava fragments or, more rarely, red-orange coloured (hydrothermal alteration), slightly iridescent, non-vesicular clasts.	Subplinian scoria fall			3		12	M	L
	MC15B	mm-scale grey, black and yellow, parallel bands of medium ash to fine lapilli.	Heterogeneous clasts with no modal glass morphology and abundant xenoliths of glass shards of older tephra units.	Recording pulsating plume activity					9	M	
	MC15A	Well-sorted, black scoria deposit with rare lithics. Inverse grading, in top fifth preserved only in proximal localities.	Medium-lapilli sized, black, crystal poor, angular, glassy scoria with small vesicles. Lithics (ca. 5%) are weathered, milky white, medium-grained, crystalline clasts, probably diorite.	Scoria fall			2		21	M	K
*MC*14		Orange-brown weathered, medium-lapilli sized, scoria deposit. Charcoal at base. In one locality cut by a minor, black, lava flow from a nearby cone.	Orange-brown weathered, black-brown, crystal poor, vesicular scoria	Scoria fall from nearby cone	G	39°52'S 71°53'W			100		
MC13		Moderately-well-sorted, massive, orange-white weathered, lithic-poor medium-lapilli sized pumice deposit.	Orange weathered, very vesicular, crystal poor pumice	Pumice fall	I	39°53'S 71°55'W	4.8	1.9	20-50	L	J
MC12		Well-sorted, ungraded, yellow-brown weathered, medium-fine-lapilli sized pumice deposit.	Clasts have a bimodal appearance. Both weather yellow-brown but one type is more angular, less vesicular, darker and typically smaller than the second pumice type, which has a more pumice, rather than scoria, appearance.	Pumice fall	G	39°52'S 71°53'W	1.3		20	L	I

Field descriptions, interpretations and type localities for the post-glacial tephra deposits

Unit		Field Description		Interpretation	Type Locality					Photo in Fig. 2.3 & 2.4	SEM in Fig. 2.5
Name	Subunits	Deposit appearance	Clasts		Column in Fig. 2		MP/MS (cm)	ML (cm)	Th (cm)		
*MC*11		Brown weathered, lithic-rich (particularly in bottom fifth), medium-lapilli sized scoria deposit.	Black, very vesicular scoria	Scoria fall	I	39°53'S 71°55'W			100		
MC10 (Grupo Fui Tephra)	MC10H	Well-sorted, indurated, dark-grey, coarse-ash with fine laminations, comprising slightly finer layers. Some oxidation	Ash is heterogeneous in composition and microlite rich. Abundant xenolits of country rock	Wet ash fall	J	39°58'S 71°54'W			10	I,K	
	MC10G	Well-sorted, orange weathered, fine-lapilli sized, scoria deposit that grades into overlying palaeosol.	Same as MC10A	Scoria fall			<0.5		6		
	MC10F	Moderately-well-sorted, orange-weathered, medium-lapilli sized deposit	Same as MC10A	Scoria fall			1		15		
	MC10E	Well sorted, orange weathered, medium-lapilli sized scoria deposit.	Same as MC10A	Scoria fall			0.5		4		
	MC10D	Banded, cm-scale thickness, well-sorted, grey-orange-yellow weathered, medium-ash to medium-lapilli sized ash and scoria deposit.	Same as MC10A	Scoria and ash falls			1.5		45	I,J,K	G
	MC10C	Indurated, dark-grey coarse-ash, overlain by a well sorted, orange-weathered, lithic-poor, medium-lapilli sized scoria deposit.	Same as MC10A	Scoria fall			2.4		25		H
	MC10B	Well-sorted, orange weathered, fine-lapilli sized, scoria deposit	Same as MC10A	Scoria fall					10		
	MC10A	Well-sorted, orange weathered, fine-lapilli sized, scoria deposit.	Orange-yellow weathered, vesicular scoria. Very weathered with little to no glass preserved that has not altered to clay.	Scoria fall					15	I,K	
MC9 (Huilo)	MC9B	Thin, continuous, black, medium-lapilli sized, scoria deposit that is often oxidised. Sharply cuts MC9A	Black, vesicular scoria	Scoria fall	C	40°0'S 71°56'W	4.5		10	G,H	F
	MC9A	Well-sorted, massive, orange-white weathered, lithic-poor pumice deposit	Orange weathered, very vesicular, crystal poor pumice with red-pink cores. At rare localities they retain original white appearance. Minor amounts of both grey and banded, vesicular, crystal poor pumice (ca. <5%) of a similar size to the dominant white pumice. Lithics are black-grey, sub-rounded, slightly-vesicular dense clasts (ca. <5%) and dense, grey, angular lava fragments (ca. <5%	Plinian-style pumice fall	C		7.5		166	F,G,H,K	E
MC8		Moderately-sorted, black-red weathered, coarse-ash to fine-lapilli sized scoria rich deposit. Some localities preserve cross-bedding. In the thickest deposits shower-bedding is preserved.	Black-red, weathered, vesicular scoria	Scoria fall and PDC from nearby cone	O	39°55'S 71°55'W			>100	F	D
*MC*7		Moderately-well-sorted, brown weathered, coarse-ash to fine-lapilli sized pumice deposit	Brown weathered, crystal poor, vesicular pumice	Pumice fall	I	39°53'S 71°55'W			13		

Field descriptions, interpretations and type localities for the post-glacial tephra deposits

Unit		Field Description		Interpretation	Type Locality					Photo in Fig. 2.3 & 2.4	SEM in Fig. 2.5
Name	Subunits	Deposit appearance	Clasts		Column in Fig. 2		MP/MS (cm)	ML (cm)	Th (cm)		
MC6		Moderately-sorted, orange weathered, medium-lapilli sized pumice held in a fine-ash sized, brown-grey matrix with charcoal.	Yellow-pink weathered, crystal poor, vesicular pumice	Palaeosol with reworked clasts from a potential pumice fall	E	39°57'S 71°52'W	2.8		12	F	
MC5 (Pirehueico)	MC5F	Moderately-sorted, orange-weathered, fine-coarse-lapilli sized pumice deposit.	Same as MC5D	Plinian-style pumice fall with possible interbedded minor PDCs (*surges*?; i.e., MC5B and MC5E)	E	39°57'S 71°52'W	5		18	F,G	
	MC5E	Grey-brown, medium-fine ash layer containing a moderate amount of, possibly reworked, pumice clasts. Sharp contact with MC3D and MC3F	Yellow-weathered, crystal poor, vesicular pumice.						9	F	
	MC5D	Moderately-well-sorted, orange-red weathered, moderate lithics, medium-lapilli to bomb-size pumice deposit. High concentration of bombs (up to 25 cm), particularly in bottom 75% of the deposit. Sharp contact with MC3C and MC3E.	Same as MC5A.				>7.5 (bombs <25 cm)	4.5	80	F	
	MC5C	Well-sorted, yellow-weathered, lithic-rich, fine-medium-lapilli sized, pumice deposit. The base is slightly finer; fine-lapilli sized clasts.	Same as MC5A				4		62	E	C
	MC5B	Fine, grey ash with no internal structures. Sharp contact with MC5A and MC5B.	Very weathered, heterogeneous ash, with glass having a devitrified appearance on the edges where it has altered to clay.				4		10	E	
	MC5A	Moderately-sorted, yellow-weathered, coarse-ash to medium-lapilli sized pumice deposit. Pumice are set in a lithic-rich (ca. 30%) and grey, ash-rich matrix.	Yellow-weathered, crystal poor, vesicular pumice, some with a mingled appearance. Lithics are predominately black-grey, angular, glassy, non-vesicular clasts and minor amounts of black-grey scoria.				3.3		60	E	
MC4 (Neltume)	MC4C	Well-sorted, orange-yellow-weathered, lithic-poor pumice deposit. Normal grading in the upper quarter observed at rare localities. Typically at distal localities (when thickness ca. <15 cm) the bottom two-thirds, of the deposit, weathers orange, as in more proximal localities, and this sharply changes to dark-grey-yellow weathering in the upper part.	Primarily, orange-yellow weathered, crystal poor, vesicular pumice with, at rare localities, white cores. Moderate amounts (ca. 5%) of grey and banded vesicular, crystal poor pumice and dense cauliform-shaped clasts (<5%) are uniformly distributed through the deposit and more abundantly preserved in proximal localities. Some proximal pumice preserve tuffsite veins and cauliform shaped black clasts trapped within vesicles.	Plinian-style pumice fall	B	39°39'S 71°55'W	2.5	0.7	300	B,C,D	B
	MC4B	Very-well sorted, orange-yellow weathered, lithic-poor, fine-lapilli sized, pumice deposit that is typically <15 cm.	Fine-lapilli sized, orange-yellow-weathered, vesicular, pumice that only have small patches of glass not altered to clay	Pumice fall			0.7		10	B	

Field descriptions, interpretations and type localities for the post-glacial tephra deposits

Unit		Field Description		Interpretation	Type Locality					Photo in Fig. 2.3 & 2.4	SEM in Fig. 2.5
Name	Subunits	Deposit appearance	Clasts		Column in Fig. 2		MP/MS (cm)	ML (cm)	Th (cm)		
	MC4A	Well-sorted, grey, fine ash bounded by red-brown oxidised layers and typically <10 cm	Ash is heterogeneous in composition and only small patches of glass not altered to clay. Abundant xenoliths of country rock and glass shards of older tephra units.	Phreatomagmatic, vent-clearing event			fine ash		9	B	
MC3		Well-sorted, orange-yellow weathered, fine-medium-lapilli sized, pumice deposit. Lithic content changes sharply from ca. 40%, in the bottom half of the deposit, to ca. 15%	Orange-yellow weathered, vesicular, crystal poor pumice, sometimes with a mingled appearance. Two lithic types: black, angular, non-vesicular lava-like clast and a black, vesicular scoria.	Pumice fall	K	39°52'S 71°55'W	3	3	75	A	A
MC2		Orange-weathered, fine-lapilli sized pumice deposit	Orange-weathered, vesicular, crystal poor pumice	Pumice fall	C	40°00'S 72°0'W	2.6		12		
MC1		Moderately-sorted, slight reverse grading, non-welded, black-red weathered, fine-lapilli to coarse-bombs sized clasts (up to 35 cm) scoria deposit.	Black, dense, vesicular scoria.	Scoria fall from nearby cone	K	39°52'S 71°55'W	35		>200		
MC26		Poorly-moderately-sorted, black, medium-lapilli to bombs sized scoria deposit.	Black, vesicular scoria with abundant xenoliths of a milky-white, medium-grained, crystalline, felsic intrusive rock.	Scoriaceous PDC		39°56'S 72°6'W	>20		>180		
MC27	MC27D	Well-sorted, brown-black weathered scoria deposit	Brown-black, vesicular, microlite rich scoria	Scoria fall. Sub-units may record pulsating activity of the plume	O	39°51'S 72°6'W			33		
	MC27C	Thin, coarse, grey ash with fine laminations. Sharp contact with MC27B and MC27D	Heterogeneous clasts with no modal glass morphology and abundant xenoliths of country rock.						5		
	MC27B	Well-sorted, brown-black weathered, medium-lapilli scoria rich deposit.	Brown-black, slightly vesicular scoria, which is often altered to clay, and xenoliths of country rock.						5		
	MC27A	Thin, fine, grey ash with a sharp contact with MC27B							2		

Table 2.3: Units are ordered in stratigraphic order from youngest (MC25; at the top) to oldest (MC1; at the base). MC26 and MC27, described last, have a poor age constraint so are not included within the stratigraphy. Units in Category α, are in bold, those in Category β are unformatted and those pertaining to Category γ are in italics. The letters correspond to the stratigraphic column label in Fig. 2.2, the associate field photos in Fig. 2.3 & 2.4 and SEM images in Fig. 2.5. The maximum pumice (MP), maximum scoria (MS), maximum lithic (ML) and thickness (Th) of the deposit at the type locality are given.

2.3.2.1.6 MC18 (Hua-Hum)

These pumice deposits typically sit conformably on top of a well-developed palaeosol and deposits from the Enco (MC15) eruption (e.g., column K, Fig. 2.2). To the north-east, where often they constitute the youngest unit preserved, MC18 deposits commonly grade into the overlying palaeosol. However, to the east between the summit and Lago Pirehueico, they normally sit beneath, separated by a palaeosol, deposits from MC20 and Pilmaiquén (MC21). The deposits, dispersed to the north-east and south-east, vary in thickness from 80 cm, 10.4 km south-east of the summit, to 15 cm, 23.8 km ESE and 48 cm thick at 6.7 km to 30 cm at 12.9 km to the north-east of the summit.

Internally unit MC18 comprises three sub-units (Fig. 2.4O): a basal orange-brown pumice deposit inferred to be a sub-Plinian fall deposit (MC18A); a grey, moderately sorted, fine-ash unit interpreted as a PDC (surge; MC18B) deposit; and a sub-rounded, lithic-rich and pumice-rich deposit with a vesicular ashy matrix that could be interpreted as a wet PDC deposit (MC18C). MC18B and MC18C (column L, Fig. 2.2) are only preserved at one locality; this is near the mouth of one of the deepest flank valleys to the south-east of the summit. The Hua-Hum deposits are overlain by a well-developed palaeosol. At rare localities, to the SSE, deposits are interbedded with deposits from Puyehue-Cordón Caulle (e.g., CLD153, 40°14'S 71°57'W).

2.3.2.2 Category β

Deposits assigned to Category β are moderately dispersed and preserved, and typically found at 5-10 localities at distances less than 15 km from the summit. Eight units are assigned to this category: three pumice falls (MC3, MC12 and MC13), four scoria falls (MC8, MC21, MC23 and MC25) and one scoria fall and PDC unit (MC20). A short description of each is given below and in Table 2.3.

MC3 is a pumice fall deposit found between the villages of Neltume and Puerto Fui. The deposit, dispersed to the north-east, varies in thickness from 75 cm at 12 km ENE of the summit, to 26 cm at 12.5 km north-east of the summit. At some localities it can be identified by the high lithic abundance and/or sharp change in lithic content from ca. 40%, at the base, to ca. 15% above (e.g., Fig. 2.3A). Locally, MC3 deposits sit

conformably on top of a scoria deposit MC1 and below a palaeosol (Fig. 2.3A), which is in turn overlain directly by MC4 (Neltume) deposits. At the type locality (column K, Fig. 2.2) the overlying palaeosol contains many reworked pumice, scoria and lithic clasts.

MC8 is a red and black scoria deposit found around Pampa- Pilmaiquén. The deposit, probably dispersed to the east, varies in thickness from 15 cm, 10.3 km south-east of the summit, to 90 cm, 11 km north-east. Deposits are intercalated between the pumice deposits of Pirehueico (MC5) and Huilo (MC9; e.g., column E, Fig. 2.2). The highly oxidised appearance, especially in the lower part of the deposit, may suggest that water was involved in its genesis. The deposits unusually preserve both flow (e.g., cross-bedding) and fall (e.g., rhythmic bedding) features (see Table 2.3).

MC12 is a pumice fall with deposits dispersed to the north-east where thicknesses of 28 cm, 13.2 km from the summit, and 15 cm, 14.5 km from the summit are preserved., Deposits are always bedded within a palaeosol sequence, and overlying deposits from the Huilo Unit (MC9, e.g., column F, Fig. 2.2). At a few localities MC12 overlies multiple scoria fall deposits (e.g., column G, Fig. 2.2) that may comprise part of the Grupo Fui Tephra (MC10) sequence. Typically, MC12 lies beneath deposits from the Enco (MC15) eruption (e.g., column H, Fig. 2.2). The juvenile clasts in this deposit characteristically have a bimodal appearance; both weather yellow–brown but one is more angular, less vesicular, darker and typically smaller than the second pumice type.

MC13 is an orange-weathered pumice fall deposit, confirmed at four localities, dispersed to the ENE and preserved 11.5 km ENE (64 cm thick) and 11 km ESE (60 cm thick) of the summit. The deposits look very similar to MC9 (Huilo), and are indistinguishable in the field unless the distinctive scoria bed of MC9B is preserved, or the tephra deposit is greater than 1 m thick, in which case it must be part of the MC9 unit; inferred from relative thicknesses preserved at outcrops with both MC9 and MC13 deposits. MC13 deposits lie between deposits from MC10 (The Grupo Fui Tephra) and MC15 (Enco; e.g., column G, J, Fig. 2.2).

MC20 is a distinctive bi-partite unit comprising two beds, whose appearance differs with proximity to the source (Fig. 2.4P, Q; described in Table 2.3). The lower bed, a scoria fall (MC20A), often weathers yellow and is only black in very proximal localities. The

upper bed, a PDC (surge; MC20B), is typically a grey, medium ash and only preserves characteristic PDC features, such as low-angle cross-bedding, in very proximal sites. Deposits of MC20 are dispersed to the NNE and preserved up to 11 km ESE (10 cm thick) of the summit and 6.2 km ENE (22 cm thick) in Pampa- Pilmaiquén where they overlie the Hua-Hum Unit (MC18), separated by a palaeosol.

MC21 (Pilmaiquén) is a grey, indurated, parallel bedded unit comprising medium ash to fine-lapilli sized clasts (Table 2.3; columns J and M, Fig. 2.2; Fig. 2.4R, S). Beds are continuous, parallel-bedded, well-sorted and often indurated, so we infer that MC21 is the deposit of a wet scoria fall eruption. MC21 deposits commonly overlie MC20, and lie below those from Arauco (MC23) and, more rarely, Riñihue (MC25), all of which are separated by palaeosols. The deposits of MC21 are dispersed to the east and vary in thickness from 18 cm, 11 km ESE of the summit, to 13 cm, 11 km ENE of the summit.

MC23 (Arauco) deposits comprise a well-sorted, massive, scoria deposit (Fig. 2.4T). At localities on the edifice (e.g., column P, Fig. 2.2) iridescent scoria bombs (<25 cm) with a black to grey glassy texture are preserved. At the base a thin, grey, coarse lithic-rich ash is sometimes preserved. MC23 deposits typically overlie deposits from Pilmaiquén (MC21) and lie beneath deposits from Riñihue (MC25), all of which are normally separated by palaeosols. The deposits of MC23 are dispersed to the north and vary in thickness from 25 cm, 11.2 km north-east of the summit, to 5 cm, 10.3 km east of the summit.

MC25 (Riñihue) is a scoria fall unit (Fig. 2.4SU; Fig. 2.2, column P) and the youngest deposit found from Mocho-Choshuenco. It lies on the surface of the edifice (thicknesses up to 47 cm are observed) and at rare outcrops to the east (dispersal direction) where it is preserved up to 11 km from the summit (8 cm thick). Deposits are inferred to have formed during the last known eruption from Mocho-Choshuenco in 1864; a thin soil and no other tephra deposits overly these deposits. This fatal eruption reportedly lasted for many days with “corrientes de fuego” (“streams of fire”) flowing down the valleys mournfully illuminating the elevated waters of Lago Riñihue (Vidal Gormaz, 1869). Local stories describe how the waters of Rio Enco boiled as a result of the eruption, causing the death of a young Mapuche man trying to flee by a canoe (Bernales, 1990). These historic accounts coupled with the preserved deposits comprising well-sorted, vesicular

scoria clasts and, on the edifice, bombs (<20 cm diameter) imply that this was probably a Strombolian event.

2.3.2.3 Category γ

Category γ units are poorly dispersed and preserved. Typically deposits are found at fewer than 5 localities and at distances <15 km from the summit. This group comprises thirteen units, described in Table 2.3. Primarily units in this group are dark coloured scoria falls (e.g., MC11 and MC22), many of which are likely to originate from one of the many monogenetic cones. However a few units are white-yellow weathered, pumice falls (e.g., MC2 and MC7), which may originate from the main edifice (central vent). Although poorly preserved, MC2 and MC7 may record significant past eruptions as lapilli-size deposits are preserved over 10 km from the Mocho cone. For example, a 12 cm thick, MP of 2.6 cm deposit of MC2 is observed 11 km south-east of the summit (column C, Fig. 2.2). As these units have limited preservation it is not possible to infer, with any certainty, the dispersal direction or quantify their size.

2.3.3 Petrography

Most tephra produced at Mocho-Choshuenco is crystal-poor with variable microlite contents and vesicularity. In general the chemically more evolved units (e.g., MC9 (Huilo); ca. 66.7 wt.% SiO_2 ; Fig. 2.5E) have a more skeletal morphology with larger (<100 μm) and less spherical vesicles than the more mafic samples. The more mafic samples (e.g., MC25 (Rinihue); ca. 55.5 wt.% SiO_2 ; Fig. 2.5Q) tend to have a higher concentration of microlites. The mineralogical assemblage comprises plagioclase, orthopyroxene ± clinopyroxene ± olivine ± magnetite ± ilmenite ± apatite. Rare crystals of chromite and pyrite are also observed.

2.3.4 Summary of units

We recognise three major pumice fall deposits (MC4 (Neltume), MC5 (Pirehueico) and MC9 (Huilo)) and a large scoria fall and scoriaceous PDC unit (MC15). The MC15 (Enco) unit is very distinctive in the field as it is the only widespread scoria fall deposit

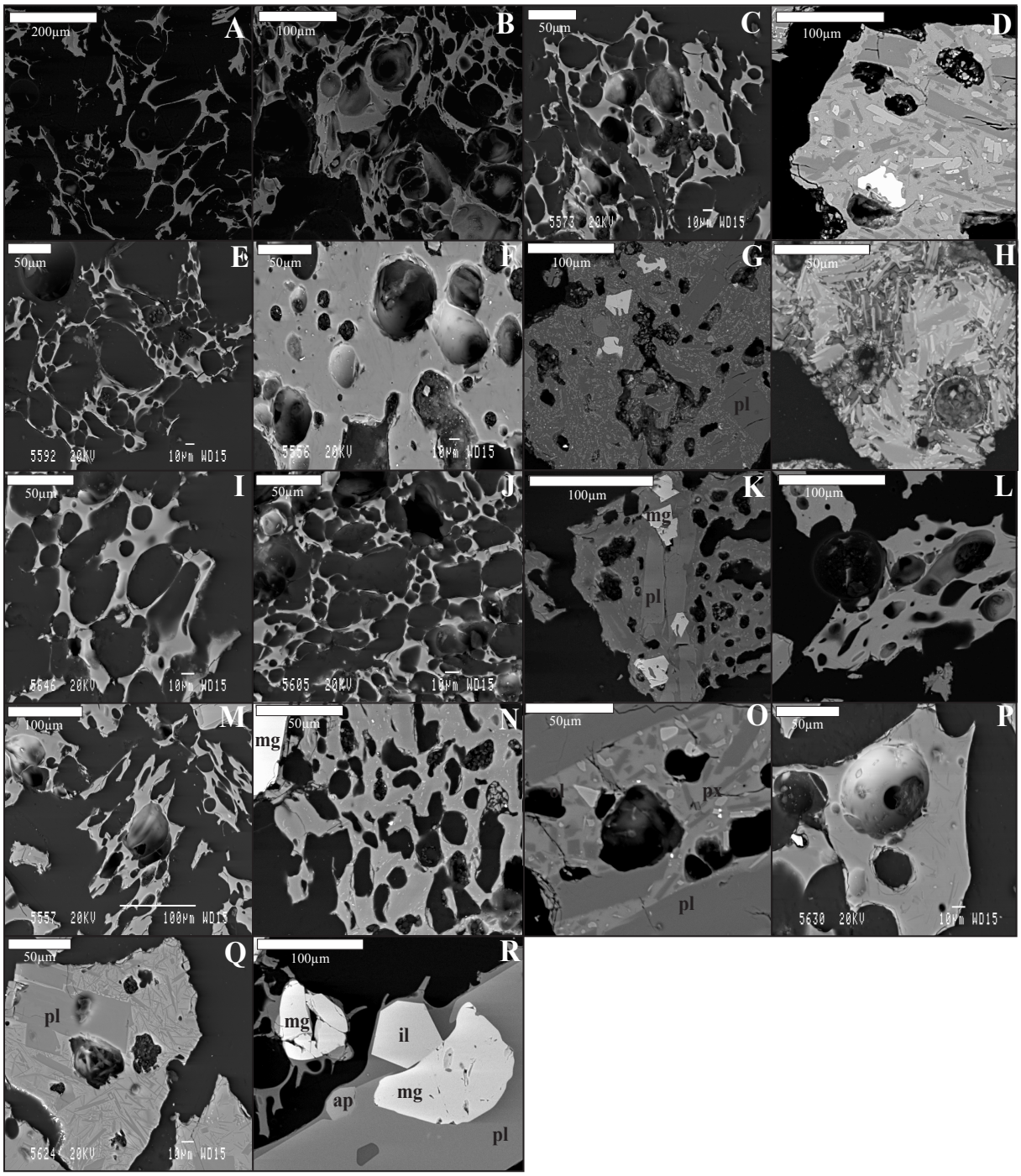

Figure 2.5: Backscattered electron images of typical glass shards for the tephra units that comprise Categories α and β and an example of touching Fe–Ti oxide pairs. A: MC3 pumice; B: MC4B (Neltume) pumice; C: MC5 (Pirehueico) pumice; D: MC8 scoria; E: MC9A (Huilo) pumice; F: MC9B (Huilo) scoria; G: MC10D (Group Fui Tephra) microlite-rich glass; H: MC10C (Grupo Fui Tephra) altered scoria clast; I: MC12 pumice; J: MC13 pumice; K: MC10A (Enco) scoria; L: MC10C (Enco) scoria; M: MC18A (Hua-Hum) pumice; N: MC20A scoria; O: MC21 (Pilmaiquén) scoria; P: MC23 (Arauco) scoria; Q: MC25 (Riñihue) scoria; R: touching Fe–Ti oxide pair in MC4B pumice. Magnetite (mg), ilmenite (il), apatite (ap), plagioclase (pl), pyroxene (px), olivine (ol).

from Mocho-Choshuenco, and commonly multiple beds are preserved. The three pumice fall deposits, on the other hand, all have a very similar appearance in the field: orange-weathered, lithic-poor, pumice fall deposits with few other characteristic features. There are few localities where more than one large tephra unit is preserved.

In addition, there are nine further pumice fall deposits (MC1, MC3, MC6, MC7, MC12, MC13, MC18 and MC19), a scoria fall package (MC10), two combined scoria fall and PDC deposits (MC8 and MC20) and a PDC deposit (MC26). The remaining ten units are all scoria fall deposits. The predominance of fall deposits could be due to preservation. Many of the tephra units are overlain by brown-black deposits that include clasts of variable size and composition, which we interpret as palaeosols. High eruptive frequencies, rapid weathering, poor preservation and common reworking mean that it is sometimes difficult to confidently distinguish between palaeosols/weathering horizons, and primary volcanic units, particularly PDCs. Hence it is likely that, despite the high-resolution stratigraphy developed here, we underestimate the scale and frequency of moderate to large eruptions from Mocho-Choshuenco.

The temperate climate and dense vegetation of the region results in exposures often limited to road-cuttings, which makes tracing the deposits from a single event challenging. Measurements of thickness and maximum clast size can help when compared to nearby outcrops where the deposits have been confidently assigned to an event. However, although this approach helps in places (e.g., north of Mocho-Choshuenco and near Coñaripe where only MC4 (Neltume) deposits are preserved), in most areas this is not possible where multiple deposits of a similar appearance are found. This is often the case for MC5 (Pirehueico) and MC9 (Huilo) fall deposits, which are deposits of similar scale that both extend east from the edifice and have similar field parameters in this region. Hence, unless both deposits are preserved in the same locality it is difficult to assign an event to a particular deposit. However, as we show in Section 2.4, these units are clearly distinguishable chemically.

Pumice samples from the three large eruptions have the same crystal phases: plagioclase, orthopyroxene, clinopyroxene, magnetite, ilmenite and apatite. They are all crystal- and microlite-poor and highly vesicular. Consequently, petrographic observations

cannot be used as a diagnostic tool to correlate units. Therefore, to verify stratigraphic correlations, geochemical analyses of glass and Fe–Ti oxides were required.

2.4 Tephra correlations

2.4.1 Methods

The deposits were correlated using a combination of field observations (relative stratigraphic position of identified layers, their physical measurements and mapping their geometry) and their composition (glass and mineral chemistry). Outcrops with multiple tephra units preserved (Fig. 2.2 e.g., columns C, D and F), were chemically analysed first to check whether each unit had a distinct chemical composition, both in terms of glass and Fe–Ti oxides. Outcrops where units had been sub-sampled were analysed next to check for possible internal chemical variability (Fig. 2.2 e.g., columns D and H). Once units at these key localities had been well characterised, chemically and physically, and the relative ages determined, the remaining tephra samples were correlated. This was done by using the geochemical characteristics of the units to correlate deposits, which were complemented and verified with field observations (e.g., checking whether the thickness and grain size was consistent with nearby outcrops). At outcrops where samples were not taken, the units were deduced by relative stratigraphic order and physical characteristics (e.g., grain size, thickness and colour).

2.4.1.1 Chemical analysis

Major element glass compositions of ca. 275 samples were determined with a JEOL JXA-8600 wavelength-dispersive electron microprobe (EMP), equipped with four spectrometers, at the Research Laboratory for Archaeology and the History of Art, University of Oxford. To reduce alkali loss in the glass during analyses, an accelerating voltage of 15 kV, a low beam current (6 nA), and a defocused (10 μm) beam were used. For a few highly vesicular samples a narrower beam (5 μm) was needed and therefore the beam current was reduced (4 nA). Continuity between data from the two beam conditions was checked by analysing a few samples using both setups; no difference within error was

found. Na was analysed first to minimise the effect of possible Na migration. Counts for each element were collected on the peak for 30s (Si, Ca, K, Al, Ti, Fe, Mg), except for Na (10s), P (60s), Mn (40s) and Cl (50s), and background counts were collected for half the time on either side of the peak. The EMP was calibrated using a suite of mineral standards. This calibration was verified using a range of secondary glass standards, which for all runs were within 2 standard deviations of the preferred values (Jochum et al., 2006). Approximately 2150 glass analyses were obtained for which a threshold of 91% was used but totals were mostly >95%. These were normalised to 100% to account for variable secondary hydration (see Appendix A.2 for raw data and Table 2.4 for average values). Glass analyses were only possible for ca. 135 samples (i.e., half of those crushed) because of alteration and/or the glass being either too skeletal or microlite-rich.

Magnetite and ilmenite were analysed for ca. 275 samples by EMP with an accelerating voltage of 15 kV, a beam current of 20 nA and a focussed beam. Element counts were collected for 30s (on-peak; Fe, Mg, Al, Si, Ca, Ti) or 40s (Mn). This calibration was verified using a range of secondary mineral standards, which for all runs were within 2 standard deviations of the preferred values (Jarosewich et al., 1980). Approximately 2700 analyses were obtained (data presented in Table 2.5 and Appendix A.2) for which totals were typically >94 wt.%, >98.5 wt.% after accounting for the Fe oxidation state so that the stoichiometry is correct (Droop, 1987). All the Fe–Ti oxide pairs presented in this paper (except those noted in 2.4.2.1.2), are in equilibrium (determined using the method of Bacon and Hirschmann, 1988). Over 600 temperature and oxygen fugacity estimates were calculated using the method of Ghiorso and Evans (2008). As with glass, it was not possible to get Fe–Ti oxide analyses for all samples due to limited abundance and/or size.

2.4.1.2 Radiocarbon dating

The ages of the explosive eruptions from Mocho-Choshuenco have been constrained through a combination of ^{14}C dating and Bayesian age modelling (e.g., using OxCal; Bronk-Ramsey, 2009a). 48 samples have been ^{14}C-dated, of which 29 were previously published by Lara and Moreno (2007) and 19 new samples were analysed at the NERC Radiocarbon Facility and SUERC AMS laboratory in East Kilbride using the same methodology

outlined in Watt et al., (2011).

Full details of these results including uncalibrated and calibrated ages, can be found in Appendix A.3. The ages are calibrated with OxCal 4.2.3 (e.g., Bronk-Ramsey, 2009a) using the Southern Hemisphere ShCal13 curve (Hogg et al., 2013). The dated carbon samples are typically organic-rich palaeosols or small pieces of charcoal within palaeosols bounding the tephra deposits. Most samples are collected below the tephra deposit within the top 5 cm of the palaeosol (Fig. 2.3 & 2.4; Appendix A.3). Only three charcoal samples (within MC15 and MC18; XG-251, 100303-2B and Ch-3; Appendix A.3) were recovered from within the deposits themselves. Hence, as most of these samples date the palaeosols that seal, or are sealed by, the eruptive deposits, rather than the eruptions themselves, we create an age model (code included in Appendix A.3) to constrain eruption ages. The age model uses a Bayesian statistical approach to combine multiple radiocarbon ages for sequences of events along with constraints provided from field stratigraphy. The approach is outlined by Bronk-Ramsey (2009a, b) and Blockley et al. (2008).

The Bayesian model takes uncalibrated radiocarbon dates as input values. An outlier function was included to identify any radiocarbon analyses that were inconsistent with the age model (e.g., analyses of more modern or reworked older carbon). Three (from 48) radiocarbon dates were found to be outliers, a further three had a <95% probability range and 17 could not be included in the model as they could not be confidently placed within the stratigraphy, and were instead just calibrated. The results from this model are presented in the Appendix A.3 and Table 2.6.

2.4.2 Results

2.4.2.1 Unit chemistry

Glass and Fe–Ti oxide analyses were attempted for all units (MC1–MC27; Table 2.3) to aid correlation of the units. The glass geochemistry is plotted in Fig. 2.6 and summarised in Table 2.4. The Fe–Ti oxide data and estimated temperature and oxygen fugacity are plotted in Fig. 2.7 and summarised in Table 2.5. Raw geochemical data are presented in Appendix A.2.

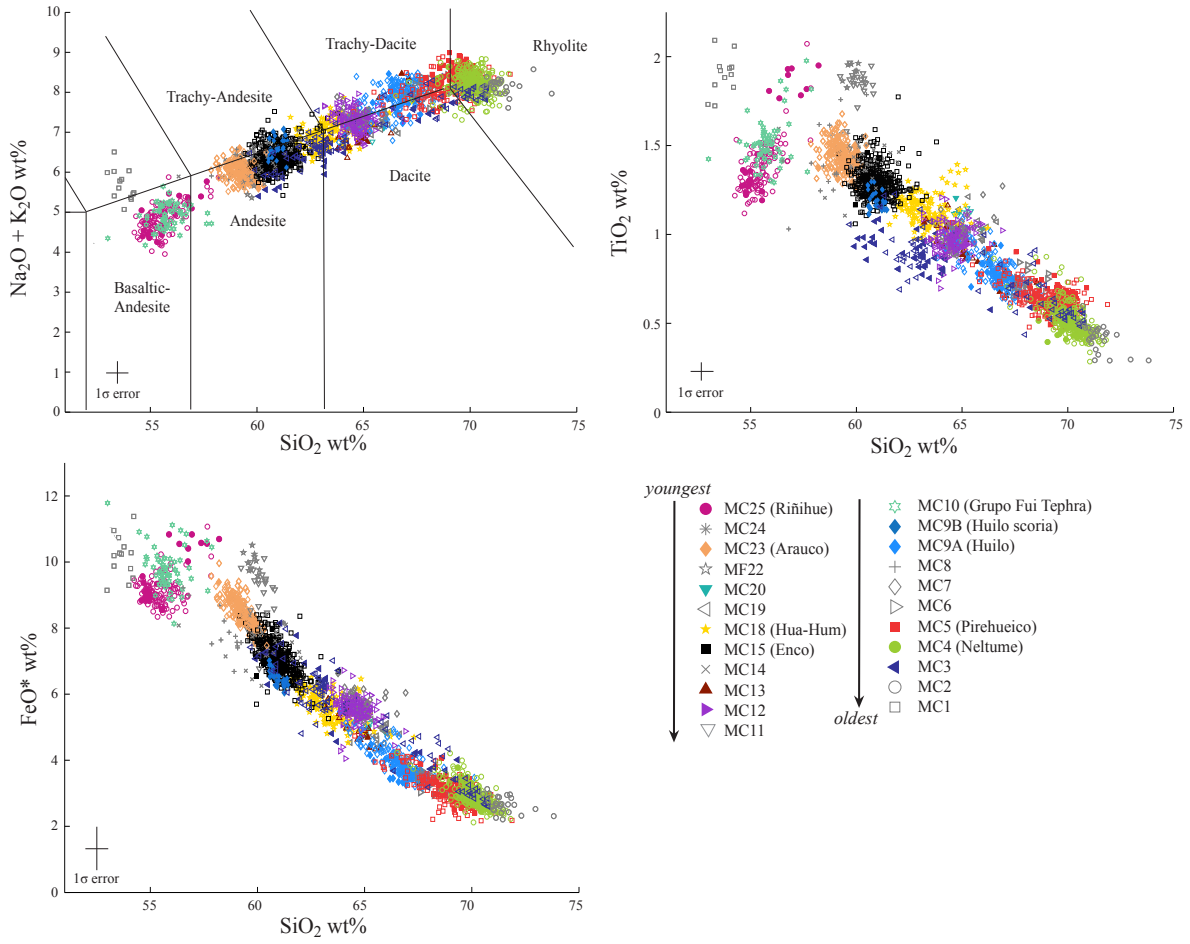

Figure 2.6: Major element composition for the matrix glass (anhydrous) for the different tephra units from Mocho-Choshuenco. The different colours and/or symbols represent the data from different units, as labelled in the legend. The filled symbols represent data from the type localities for Category α and β units, as defined in Table 2.3. All the units that form part of Categories α and β are given coloured symbols whereas units in Category γ are grey. The error bars are calculated from the relative percentage errors on the compositionally similar secondary standards.

Eruption	MC25 (Riñihue)		MC24		MC23 (Arauco)		MC22		MC20		MC19		MC18B (Hua-Hum)		MC15C (Enco)		MC14		MC13		MC12		MC11	
SiO_2	55.5	*0.78*	60.19	*0.49*	59.27	*0.47*	59.78	*0.24*	65.02	*0.38*	65.31	*1.35*	63.43	*0.96*	60.94	*0.68*	60.28	*1.14*	65.46	*1.40*	64.34	*2.17*	60.11	*0.42*
TiO_2	1.40	*0.18*	1.38	*0.06*	1.44	*0.08*	1.90	*0.05*	1.09	*0.06*	1.04	*0.10*	1.13	*0.09*	1.29	*0.08*	1.37	*0.14*	0.90	*0.14*	0.98	*0.19*	1.81	*0.13*
Al_2O_3	16.13	*0.73*	15.67	*0.31*	15.60	*0.27*	13.56	*0.28*	15.56	*0.30*	15.44	*0.44*	16.15	*0.47*	16.11	*0.49*	16.35	*0.85*	16.09	*0.29*	15.97	*0.57*	14.22	*0.87*
FeO*	9.19	*0.54*	7.84	*0.35*	8.51	*0.41*	10.03	*0.30*	5.17	*0.27*	5.09	*0.68*	5.59	*0.47*	7.06	*0.49*	7.45	*0.57*	4.53	*0.74*	5.67	*1.04*	9.15	*0.78*
MnO	0.18	*0.04*	0.17	*0.04*	0.19	*0.04*	0.20	*0.06*	0.17	*0.03*	0.14	*0.05*	0.16	*0.05*	0.18	*0.05*	0.18	*0.04*	0.15	*0.05*	0.17	*0.06*	0.19	*0.06*
MgO	4.55	*0.46*	2.69	*0.16*	2.79	*0.11*	2.46	*0.14*	1.49	*0.15*	1.45	*0.23*	1.73	*0.24*	2.30	*0.33*	2.15	*0.42*	1.46	*0.41*	1.36	*0.62*	2.42	*0.43*
CaO	7.86	*0.50*	5.42	*0.26*	5.78	*0.18*	5.74	*0.21*	3.86	*0.11*	4.00	*0.62*	4.30	*0.40*	5.24	*0.30*	5.43	*0.63*	3.77	*0.59*	3.74	*0.99*	5.39	*0.41*
Na_2O	3.83	*0.26*	4.59	*0.26*	4.75	*0.20*	4.23	*0.27*	5.40	*0.17*	5.41	*0.19*	5.34	*0.25*	5.00	*0.30*	4.97	*0.27*	5.59	*0.47*	5.46	*0.45*	4.40	*0.30*
K_2O	1.00	*0.17*	1.62	*0.11*	1.27	*0.06*	1.59	*0.08*	1.77	*0.08*	1.70	*0.15*	1.65	*0.17*	1.40	*0.16*	1.38	*0.17*	1.66	*0.17*	1.90	*0.25*	1.73	*0.13*
P_2O_5	0.26	*0.06*	0.33	*0.03*	0.34	*0.03*	0.41	*0.03*	0.34	*0.02*	0.30	*0.04*	0.39	*0.06*	0.37	*0.05*	0.35	*0.05*	0.25	*0.06*	0.37	*0.08*	0.45	*0.06*
Cl	0.06	*0.02*	0.09	*0.02*	0.06	*0.05*	0.11	*0.02*	0.13	*0.02*	0.12	*0.02*	0.14	*0.03*	0.10	*0.03*	0.10	*0.03*	0.15	*0.03*	0.14	*0.04*	0.12	*0.02*
H_2O**	0.20	*0.93*	-0.02	*0.48*	0.84	*0.90*	0.53	*0.28*	2.43	*1.13*	2.381	*0.90*	0.06	*1.65*	0.82	*1.36*	1.15	*0.59*	0.31	*1.74*	-0.10	*1.39*	-0.04	*0.65*
N	124		29		140		9		13		19		156		340		26		31		183		21	

Eruption	MC10 (Grupo Fui Tephra)		MC9B (Huilo)		MC9A (Huilo)		MC8		MC7		MC6		MC5 (Pirehueico)		MC4C (Neltume)		MC3		MC2		MC1	
SiO_2	55.80	*0.74*	60.93	*0.29*	66.69	*0.96*	58.70	*0.91*	64.84	*0.71*	68.01	*0.55*	69.13	*1.06*	70.12	*0.69*	64.78	*3.31*	71.46	*0.69*	53.69	*0.40*
TiO_2	1.51	*0.13*	1.20	*0.05*	0.78	*0.09*	1.45	*0.19*	1.01	*0.09*	0.72	*0.06*	0.63	*0.08*	0.51	*0.08*	0.81	*0.18*	0.42	*0.07*	1.88	*0.13*
Al_2O_3	15.55	*0.63*	16.47	*0.15*	16.04	*0.30*	16.35	*0.87*	15.42	*0.47*	15.97	*0.30*	15.55	*0.45*	15.29	*0.31*	15.92	*0.79*	14.85	*0.37*	15.02	*0.58*
FeO*	9.78	*0.61*	6.51	*0.25*	3.88	*0.47*	8.04	*0.69*	5.77	*0.35*	3.36	*0.28*	3.03	*0.40*	2.89	*0.35*	5.33	*1.47*	2.65	*0.24*	10.16	*0.64*
MnO	0.19	*0.04*	0.18	*0.03*	0.15	*0.05*	0.17	*0.05*	0.18	*0.05*	0.14	*0.04*	0.12	*0.05*	0.12	*0.04*	0.14	*0.05*	0.09	*0.05*	0.18	*0.04*
MgO	4.14	*0.42*	2.40	*0.07*	1.09	*0.19*	2.28	*0.82*	1.23	*0.16*	0.84	*0.11*	0.71	*0.19*	0.56	*0.09*	1.56	*0.65*	0.40	*0.08*	4.33	*0.28*
CaO	7.79	*0.47*	5.15	*0.15*	3.12	*0.39*	6.39	*0.56*	3.67	*0.30*	2.57	*0.20*	2.26	*0.41*	2.01	*0.22*	4.22	*1.33*	1.71	*0.18*	8.36	*0.40*
Na_2O	3.81	*0.26*	5.24	*0.22*	6.07	*0.30*	4.94	*0.34*	5.46	*0.17*	6.06	*0.19*	5.97	*0.27*	5.84	*0.25*	5.10	*0.40*	5.60	*0.18*	3.89	*0.37*
K_2O	1.10	*0.12*	1.37	*0.07*	1.81	*0.12*	1.13	*0.18*	1.93	*0.15*	1.99	*0.12*	2.26	*0.16*	2.37	*0.10*	1.86	*0.39*	2.54	*0.12*	1.80	*0.26*
P_2O_5	0.28	*0.03*	0.43	*0.03*	0.20	*0.05*	0.48	*0.07*	0.34	*0.04*	0.16	*0.03*	0.15	*0.04*	0.10	*0.04*	0.14	*0.04*	0.07	*0.03*	0.60	*0.06*
Cl	0.06	*0.01*	0.11	*0.02*	0.18	*0.03*	0.08	*0.02*	0.15	*0.03*	0.18	*0.03*	0.20	*0.03*	0.19	*0.03*	0.13	*0.04*	0.20	*0.02*	0.09	*0.02*
H_2O**	1.76	*0.73*	0.19	*0.66*	0.31	*1.79*	0.80	*0.83*	-0.13	*0.54*	-0.16	*0.64*	0.84	*1.73*	1.12	*2.06*	1.14	*1.43*	0.19	*0.69*	0.36	*0.56*
N	64		26		179		19		34		21		262		282		110		28		13	

Table 2.4: Average and standard deviations (*italics*) for tephra deposits. Compositions in weight percent (wt.%) were determined using a wavelength-dispersive EMP (see Section 2.4.1). N = number of analyses, **H_2O by difference. See Appendix A.2 for the ca. 2150 raw analyses. Glass analysis was not possible for all samples. For the more evolved samples (i.e., the dacites and rhyolites) this was as a result of extensive weathering (e.g., the deposits in Argentina) or the material being too highly vesicular, which is often the case with MC9 (Huilo) pumice (vesicle walls commonly thinner than 1 *mu*m). For the more mafic samples (i.e., basaltic andesites and basalts; particularly the scoria from the cones) the microlite density was often too high (e.g., Fig. 2.5G) for glass analysis to be possible. Therefore the melt chemistry is likely to be biased towards the more silicic compositions.

Eruption		MC27		MC26		MC24		MC23 (Arauco)		MC21 (Pilmaiquén)		MC20		MC19		MC18B (Hua-Hum)		MC17		MC16		MC15C (Enco)	
Magnetite	SiO_2	0.08	*0.02*	0.06	*0.05*	0.06	*0.02*	0.07	*0.02*	0.11	*0.13*	0.05	*0.02*	0.06	*0.06*	0.05	*0.02*	0.05	*0.02*	0.14	*0.14*	0.07	*0.05*
	TiO_2	12.59	*0.35*	11.97	*2.92*	13.01	*1.10*	11.52	*0.19*	12.05	*2.82*	13.12	*0.33*	14.54	*0.28*	13.54	*0.79*	15.71	*0.34*	12.79	*1.76*	13.57	*4.90*
	Al_2O_3	3.54	*0.13*	3.17	*0.87*	3.12	*0.38*	3.81	*0.09*	3.48	*0.83*	2.91	*0.11*	2.77	*0.08*	3.15	*0.23*	2.87	*0.16*	3.69	*0.55*	3.39	*0.63*
	FeO*	73.81	*0.85*	75.83	*3.57*	74.31	*0.45*	74.62	*0.49*	74.47	*3.57*	74.72	*0.92*	73.76	*0.37*	74.17	*1.16*	72.39	*0.63*	73.06	*1.58*	73.68	*4.07*
	MnO	0.44	*0.04*	0.54	*0.20*	0.46	*0.07*	0.40	*0.03*	0.38	*0.05*	0.65	*0.04*	0.57	*0.03*	0.56	*0.05*	0.59	*0.03*	0.42	*0.05*	0.48	*0.06*
	MgO	3.41	*0.34*	2.96	*0.92*	3.30	*0.28*	3.60	*0.08*	3.12	*0.66*	2.85	*0.18*	3.15	*0.19*	3.29	*0.24*	2.80	*0.20*	3.29	*0.16*	3.48	*0.40*
	CaO	0.08	*0.03*	0.04	*0.04*	0.02	*0.02*	0.02	*0.01*	0.12	*0.06*	0.03	*0.02*	0.03	*0.03*	0.03	*0.04*	0.02	*0.01*	0.11	*0.06*	0.05	*0.05*
	Total	93.95	*0.75*	94.56	*1.74*	94.28	*0.63*	94.03	*0.55*	93.72	*1.34*	94.32	*1.12*	94.89	*0.48*	94.78	*0.88*	94.44	*0.82*	93.50	*0.67*	94.71	*1.31*
	FeO	37.08	*0.71*	37.30	*2.35*	37.68	*1.41*	36.02	*2.11*	37.02	*2.11*	38.23	*0.68*	39.27	*0.63*	38.20	*0.73*	40.65	*0.53*	37.38	*1.65*	37.50	*1.75*
	Fe_2O_3	40.82	*0.94*	42.81	*5.63*	40.70	*1.59*	42.89	*0.43*	41.61	*5.74*	40.55	*0.64*	38.33	*0.48*	39.97	*1.60*	35.28	*0.67*	39.65	*3.46*	40.21	*4.72*
	Total	97.96	*0.82*	98.81	*1.57*	98.30	*0.54*	98.26	*0.58*	97.78	*1.21*	98.34	*1.16*	98.67	*0.48*	98.74	*0.91*	97.97	*0.85*	97.33	*0.99*	98.68	*1.11*
	N	18		50		18		39		26		53		18		402		17		13		182	
Ilmenite	SiO_2			0.00	*0.01*							0.00	*0.01*			0.00	*0.01*	0.00	*0.00*				
	TiO_2			45.02	*1.40*							44.77	*0.39*			45.42	*0.69*	47.02	*0.27*				
	Al_2O_3			0.24	*0.11*							0.35	*0.03*			0.34	*0.03*	0.36	*0.03*				
	FeO*			47.31	*1.20*							48.31	*0.46*			46.96	*0.80*	45.35	*0.04*				
	MnO			1.47	*1.07*							0.68	*0.05*			0.63	*0.05*	0.58	*0.06*				
	MgO			2.87	*0.99*							3.78	*0.30*			4.16	*0.34*	4.40	*0.42*				
	CaO			0.06	*0.02*							0.05	*0.04*			0.07	*0.11*	0.10	*0.09*				
	Total			96.96	*1.53*							97.96	*0.68*			97.57	*0.73*	97.81	*0.01*				
	FeO			33.83	*1.50*							32.78	*0.67*			32.74	*0.76*	33.73	*0.82*				
	Fe_2O_3			14.98	*2.15*							17.26	*0.65*			15.80	*1.05*	12.91	*0.86*				
	Total			98.46	*1.44*							99.68	*0.70*			99.15	*0.72*	99.10	*0.07*				
	N			8								28				27		2					
Temperature (°C)												963	*9*			955	*12*	954	*11*				
$\log_{10}(fO_2)$												0.55	*0.04*			0.38	*0.08*	0.03	*0.13*				

Eruption		MC13		MC12		MC9B (Huilo)		MC9A (Huilo)		MC7		MC6		MC5 (Pirehueico)		MC4 (Neltume)		MC3		MC2	
Magnetite	SiO_2	0.04	*0.02*	0.05	*0.02*	0.04	*0.02*	0.04	*0.03*	0.05	*0.02*	0.04	*0.01*	0.05	*0.08*	0.05	*0.09*	0.04	*0.02*	0.03	*0.01*
	TiO_2	12.20	*0.21*	17.24	*0.32*	13.40	*6.67*	12.31	*0.20*	17.14	*0.29*	12.56	*0.12*	11.44	*0.38*	13.21	*1.53*	14.17	*3.46*	14.15	*0.28*
	Al_2O_3	2.64	*0.09*	2.67	*0.07*	2.90	*0.88*	2.65	*0.10*	2.67	*0.04*	2.49	*0.07*	2.40	*0.10*	2.07	*0.21*	2.11	*0.21*	1.98	*0.16*
	FeO*	75.98	*0.47*	72.06	*0.54*	74.13	*5.80*	75.98	*0.77*	72.57	*0.34*	75.79	*0.52*	76.91	*1.13*	76.57	*1.68*	76.03	*3.13*	76.52	*0.37*
	MnO	0.79	*0.04*	0.65	*0.03*	0.71	*0.15*	0.78	*0.04*	0.66	*0.03*	0.77	*0.03*	0.83	*0.04*	0.85	*0.08*	0.79	*0.05*	0.83	*0.05*
	MgO	2.74	*0.10*	2.61	*0.09*	3.07	*0.52*	2.74	*0.11*	2.64	*0.06*	2.56	*0.07*	2.35	*0.10*	1.84	*0.24*	2.06	*0.17*	1.60	*0.02*
	CaO	0.03	*0.05*	0.05	*0.10*	0.05	*0.12*	0.03	*0.05*	0.04	*0.06*	0.02	*0.02*	0.03	*0.04*	0.02	*0.03*	0.02	*0.03*	0.03	*0.04*
	Total	94.43	*0.58*	95.33	*0.65*	94.29	*0.79*	94.54	*0.83*	95.76	*0.42*	94.25	*0.52*	94.01	*1.31*	94.61	*0.85*	95.22	*1.02*	95.15	*0.34*
	FeO	37.45	*0.04*	42.45	*0.50*	36.59	*1.81*	37.59	*0.41*	42.48	*0.40*	37.98	*0.28*	37.18	*0.67*	39.63	*1.15*	40.02	*0.86*	41.41	*1.56*
	Fe_2O_3	42.82	*0.34*	32.90	*0.58*	41.65	*5.11*	42.67	*0.55*	33.44	*0.49*	42.01	*0.42*	44.15	*0.85*	41.05	*2.93*	40.02	*2.82*	39.02	*1.74*
	Total	98.70	*0.59*	98.58	*0.66*	98.42	*0.48*	98.78	*0.87*	99.06	*0.43*	98.41	*0.55*	98.39	*1.37*	98.68	*0.82*	99.19	*0.98*	99.02	*0.41*
	N	81		122		23		274		17		11		250		446		88		13	
Ilmenite	SiO_2	0.01	*0.03*	0.00	*0.01*	0.00	*0.00*	0.01	*0.02*	0.00	*0.00*	0.00	*0.00*	0.00	*0.01*	0.00	*0.02*	0.00	*0.00*	0.00	*0.00*
	TiO_2	44.67	*0.42*	48.38	*0.35*	44.76	*0.36*	44.80	*0.40*	48.40	*0.26*	45.31	*0.41*	44.90	*0.39*	47.07	*0.46*	47.17	*1.05*	47.64	*0.30*
	Al_2O_3	0.30	*0.02*	0.26	*0.01*	0.30	*0.01*	0.30	*0.03*	0.25	*0.02*	0.27	*0.02*	0.25	*0.02*	0.18	*0.02*	0.20	*0.01*	0.15	*0.02*
	FeO*	47.67	*0.38*	45.40	*0.33*	47.51	*0.26*	47.71	*0.43*	45.46	*0.17*	47.24	*0.31*	47.64	*0.51*	46.77	*0.46*	46.72	*0.59*	46.82	*0.39*
	MnO	0.87	*0.05*	0.72	*0.04*	0.81	*0.06*	0.85	*0.06*	0.73	*0.03*	0.90	*0.04*	0.98	*0.06*	1.09	*0.07*	0.93	*0.06*	1.11	*0.11*
	MgO	4.02	*0.09*	3.73	*0.12*	4.05	*0.05*	3.98	*0.17*	3.68	*0.09*	3.81	*0.18*	3.59	*0.18*	3.06	*0.17*	3.49	*0.35*	2.64	*0.26*
	CaO	0.04	*0.04*	0.04	*0.04*	0.05	*0.05*	0.05	*0.07*	0.04	*0.01*	0.04	*0.03*	0.05	*0.07*	0.03	*0.03*	0.03	*0.02*	0.04	*0.03*
	Total	97.58	*0.62*	98.54	*0.56*	97.47	*0.49*	97.70	*0.63*	98.57	*0.34*	97.57	*0.37*	97.39	*0.54*	98.21	*0.67*	98.54	*1.32*	98.39	*0.30*
	FeO	32.09	*0.45*	36.10	*0.39*	32.17	*0.26*	32.29	*0.51*	36.20	*0.35*	33.01	*0.64*	32.95	*0.46*	35.75	*0.59*	32.24	*0.80*	3.98	*0.57*
	Fe_2O_3	17.31	*0.52*	10.34	*0.54*	17.04	*0.43*	17.14	*0.65*	10.30	*0.22*	15.82	*0.76*	16.32	*0.70*	12.24	*0.80*	12.75	*0.79*	10.94	*1.04*
	Total	99.32	*0.62*	99.57	*0.57*	99.17	*0.49*	99.41	*0.65*	99.65	*0.32*	99.15	*0.35*	99.02	*0.56*	99.43	*0.70*	99.82	*1.27*	99.49	*0.39*
	N	28		40		8		141		3		8		141		128		28		7	
Temperature (°C)		933	*6*	932	*6*	930	*9*	934	*8*	924	*1*	924	*11*	903	*11*	888	*12*	905	*9*	876	*16*
$\log_{10}(fO_2)$		0.54	*0.03*	-0.36	*0.10*	0.51	*0.03*	0.53	*0.05*	-0.37	*0.06*	0.41	*0.06*	0.48	*0.08*	-0.04	*0.11*	0.06	*0.06*	-0.26	*0.19*

Table 2.5: Major element compositions (average and *standarddeviation*) of the Fe–Ti oxides from the Mocho-Choshuenco tephra deposits. Average and standard deviations (*italics*) for tephra deposits. Compositions in weight percent (wt.%) were determined using a wavelength-dispersive EMP (see Section 2.4.1). N = number of analyses. FeO and Fe_2O_3 calculated as in Droop (1987). Temperature (T) and oxygen fugacity (fO_2) calculated as in Ghiorso and Evans (2008). See Appendix A.2 for the ca. 2700 raw analyses.

2.4.2.1.1 Glass geochemistry

A total of ~2150 glass shards were analysed from 22 tephra units (Fig. 2.6). Magmas erupted from Mocho-Choshuenco during the last ca. 18 ka are calc-alkaline and range from basaltic andesite to rhyolite in composition. The average major element glass composition is given for each unit in Table 2.4. The only chemically zoned deposit is MC3, which becomes more evolved up the deposit, from ~60 wt.% SiO_2 at the base to ~70 wt.% SiO_2 towards the top (Fig. 2.6). The remaining sub-sampled units (MC4, MC5, MC9 and MC18) are relatively compositionally homogeneous and typically span 2 to 3 wt.% SiO_2, which is greater than the calculated error.

Robust chemical correlation ideally requires distinct compositional fields with a narrow distribution from each unit, however this is rarely achieved at volcanoes that are frequently active and experience repeated eruptions across a narrow range of magma compositions (e.g., Smith et al., 2011b). The post-glacial tephra from Mocho-Choshuenco show overlap in glass major element composition between several of the units. Seven units have sufficiently unique major element glass compositions to allow discrimination with just a few glass analyses. Unfortunately, the deposits of the three largest pumice eruptions (MC4, MC5 and MC9) cannot be confidently discriminated using major element glass chemistry alone (Fig. 2.6).

2.4.2.1.2 Oxide geochemistry

Analysis of the Fe–Ti oxide compositions of the post-glacial explosive deposits from Mocho-Choshuenco was attempted for all units. A total of ~2700 Fe–Ti oxides were analysed from 19 tephra units (Fig. 2.7; Table 2.5). We observe no systematic changes in Fe–Ti oxide chemistry within any eruptive units. Units with a distinct compositional field typically span 2 to 4 wt.% Fe_2O_3 for both the ilmenite and magnetite chemical composition.

Six of the major Mocho-Choshuenco units can be discriminated from each other by Fe–Ti oxide composition alone: MC3, MC4 (Neltume), MC5 (Pirehueico), MC18 (Hua-Hum), MC20 and MC23 (Arauco). Two further units, MC12 and MC9 (Huilo), have compositional fields that overlap with one other unit; MC12 with MC7 and MC9 (Huilo)

with MC13. In these cases the stratigraphic position and location relative to the edifice, helps us to distinguish between them: MC12 postdates and MC7 predates both MC9 (Huilo) and MC10 (Grupo Fui Tephra) deposits; MC13 deposits are only found in very proximal localities, compared to MC9 (Huilo) and MC13 glasses are slightly more mafic than those of MC9 (Huilo; Fig. 2.6). Of the minor events (Category γ), MC2, MC19, MC27 and MC17 all define distinct compositional fields. Fe–Ti oxide data are not sufficient for distinguishing the remaining units, which are typically andesitic, or more mafic in composition. Most major units (Categories α and β), with the exception of MC9, MC15, MC21, MC23 and MC25, contain both magnetite and ilmenite. There are a further five minor units (MC17, MC19, MC24, MC26, MC27) that also have no Fe–Ti oxide pairs i.e., the ilmenite phase is not found in samples.

2.4.2.2 Chronology

In Table 2.6 we present the first detailed, calibrated chronology for Volcán Mocho-Choshuenco. The earliest post-glacial explosive activity occurred before 14.9–12.2 cal. ka BP (95% confidence level). The four large (volume >1 km^3, see Section 2.5) explosive eruptions occurred at 12.4–10.4 cal. ka BP (MC4, Neltume), 11.5–8.8 cal. ka BP (MC5, Pirehueico), 8.4–8.0 cal. ka BP (MC9, Huilo) and 1.7–1.5 cal. ka BP (MC15, Enco). These ages supersede previous estimates, which used only uncalibrated ^{14}C dates to constrain eruption ages (e.g., Moreno and Lara, 2007). Our new age model, coupled with the high-resolution stratigraphy, gives further constraints on the tempo of volcanism from Mocho-Choshuenco. The geological record preserves, on average, one explosive event every ∼440 years (34 events including the 8 eruptions within Grupo Fui Tephra). However, when taking all the monogenetic cone deposits (ca. 40 eruptions) into account the complex is more active with one explosive event preserved every ∼220 years.

2.4.3 Discussion

By combining field stratigraphy, glass and Fe–Ti oxide compositional data, we are able to identify and chemically fingerprint 27 explosive units (34 eruptions) from Mocho-Choshuenco from post-glacial times, and confirm the existence of three, rather than two

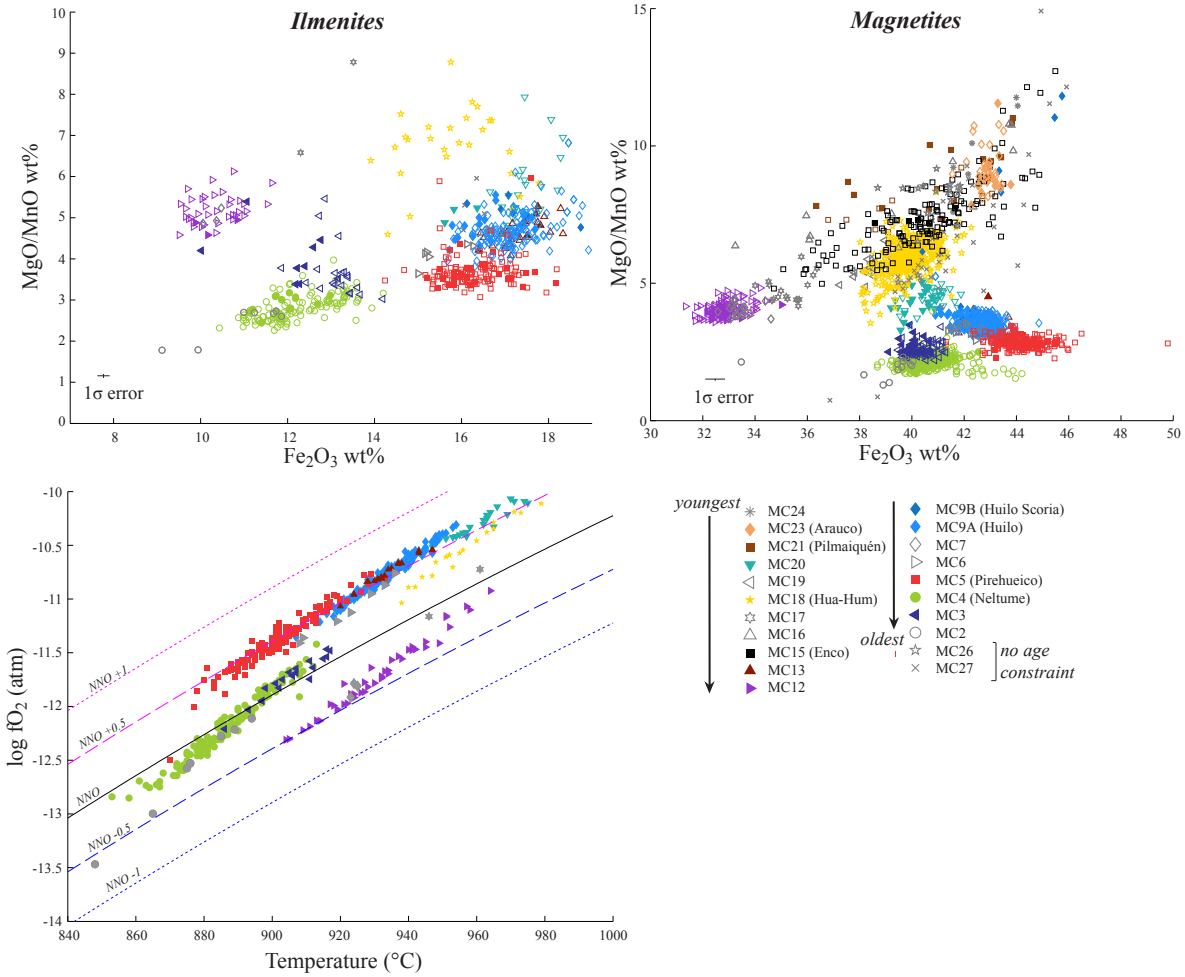

Figure 2.7: Fe–Ti oxide (magnetite and ilmenite) composition of the different Mocho-Choshuenco tephra units. The notation is the same as in Fig. 2.6 with the filled symbols representing data from the type localities for Category α and β units, as defined in Table 2.3. The error bars are calculated from the relative percentage errors on the secondary standards. The bottom left graph is the temperature and log (fO_2) estimates, determined using Ghiorso and Evans (2008) Fe–Ti oxide geothermometer plotted with respect to the Ni–Ni–O (NNO) buffer. All units have filled symbols for temperature and oxygen fugacity estimates.

(Moreno and Lara, 2007), major dacitic pumice fall deposits. In turn, these data provide a more complete picture of the style, frequency, distribution and size of past explosive eruptions. This is invaluable not just for evaluating potential future volcanic hazards, but also for understanding how the system has changed over time and may have been affected by changes in the regional climatic and/or tectonic regimes.

2.5 Eruption sizes

Having established tools to discriminate between the deposits of different eruptions, we now explore constraints on eruption size and frequency from the dispersal and grain size characteristics of the deposits. Measurements of unit thickness, maximum pumice, scoria and lithic sizes enable eruption parameters, such as eruption volume, column height, dispersal and magnitude to be estimated (Carey and Sparks, 1986; Pyle, 1989, 1995, 2000). The eruptive parameters were determined for the five most widely dispersed and well preserved fall units: MC4 (Neltume), MC5 (Pirehueico), MC9 (Huilo), MC15 (Enco) and MC18 (Hua-Hum).

Fall deposit volumes were estimated by constructing isopach maps (Fig. 2.8) and plotting the ln (thickness) against the square root of the isopach area. Deposit volumes were determined with the *AshCalc* tool (Daggitt et al., 2014), using the exponential thickness decay model of Pyle (1989, 1995), with one (MC9A, MC15C, MC18A) or two (MC4C, MC5) segments (Fierstein and Nathenson, 1992). The absence of distal material and post-depositional compaction means that the volume estimates represent minimal values. Total (preserved) deposit mass was determined using an assumed (medial) deposit density of 1000 kg/m^3 for Neltume (MC4), Pirehueico (MC5), Huilo (MC9) and Hua-Hum (MC18), and 1500 kg/m^3 for Enco (MC15) as denser scoria and more abundant lithics are present in the deposit. These assumed density values have been estimated for similar tephra deposits by Scasso et al. (1994) and Cobeñas et al. (2012). The estimates were then used to calculate the approximate magnitude of these eruptions, using the relationship magnitude = $\log_{10}$[erupted mass, kg] – 7 (Pyle, 2000). Eruption column heights were estimated using the Carey and Sparks (1986) model, based on the maximum pumice isopleths (MP and ML measurements included in Appendix A.4). As a result of pumice clasts breaking upon impact and unconstrained pumice density the eruption column heights are considered indicative rather than absolute. Maximum lithic measurements, although taken, unfortunately were too sparse and variable to construct isopleths. Estimates of eruption volume, mass, magnitude and column height are presented in Table 2.6 along with the dispersal direction and modelled ages for the 27 units identified.

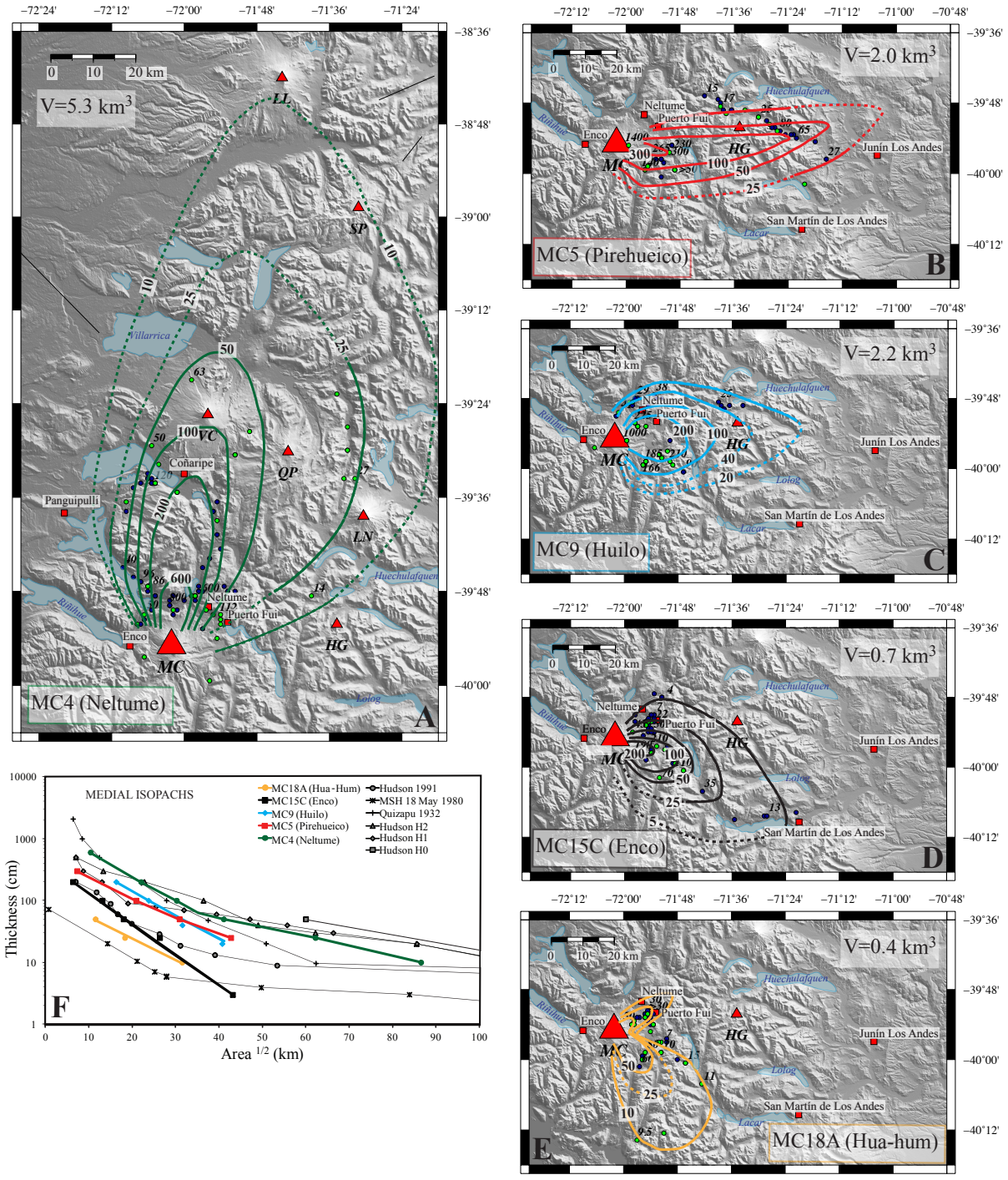

Figure 2.8: Isopach maps (cm) for the five largest fall deposits from Mocho-Choshuenco. The volumes (V; bulk rock) and unit names are shown on the figure. Dashed lines are used instead of solid lines when there is greater uncertainty due to an absence of data. Localities, where the deposits are found, are marked with circles; selected sites have their corresponding thickness (cm) annotated. Green circles are sites where the deposit was additionally confirmed with glass and/or Fe–Ti oxide chemistry and dark-blue circles are sites where just field observations and stratigraphic position is used. Red triangles mark the regional volcanoes: MC = Mocho-Choshuenco, VC = Villarrica, QP = Quetrupillán, LN = Lanín, SP = Sollipulli, LL = LLaima and HG = Huanquihue Group. The towns and villages are labelled and marked with red squares. Graph F shows how the log(thickness) vs. area$^{1/2}$ varies between the different deposits from Mocho-Choshuenco and compared to those estimated from Volcán Hudson (Scasso et al., 1994; Naranjo and Stern, 1998; Weller et al., 2014), Quizapu (Hildreth and Drake, 1992) and Mount St Helens, USA (MSH; Sarna-Wojcicki et al., 1981).

Four deposits exceed magnitude 5: MC4 (Neltume), MC5 (Pirehueico), MC9 (Huilo) and MC15 (Enco). The Neltume unit (MC4) is the largest and oldest of these four events (magnitude ∼5.7). Its deposits are abundant and narrowly dispersed to the NNE (Fig. 2.8A). Enco (MC15), the second largest and youngest of the large units, comprises a sub-Plinian fall and PDC deposit, with a combined magnitude of ∼5.4. The PDC deposit volume was estimated from field thickness measurements and measuring the area of valleys, on Google Earth, where deposits were found. Deposits (PDC and fall) from this event are widespread radially around the volcano (Fig. 2.8D). The Huilo unit (MC9) is the third largest unit preserved (magnitude ∼ 5.3). Deposits are relatively abundant and quite broadly dispersed to the east (Fig. 2.8C). Pirehueico (MC5) is the smallest of the four large units (magnitude ∼ 5.3) with deposits dispersed to the east (Fig. 2.8B).

Deposits are classified as Plinian if their magnitude exceeds 5, the column height estimate is $\gtrsim$ 30 km and they plot within the Plinian field defined in the classification scheme of Pyle (1989; Fig. 2.9). Following these criteria three deposits are classified as Plinian: MC4 (Neltume), MC5 (Pirehueico) and MC9 (Huilo).

As well as four units having a magnitude >5, six units are estimated to have a magnitude ∼4, 19 units (including the 8 within Grupo Fui Tephra) have a magnitude ∼3 and five units have a magnitude $\lesssim$3 (Table 2.6). For units with magnitude <5 these estimates are indicative as they are not based on isopach measurements, due to absence of data, instead they are approximated from comparing their thickness, with distance from the edifice, to well constrained events. The 27 units (34 eruptions) have a combined estimated volume of ∼16 km^3 of pyroclastic material. Using the monogenetic cone dimensions given in Moreno and Lara (2007), i.e., base diameter 1250 m, height 150–250 m and crater diameter of 200–750 m, the cones are estimated to contribute a further ∼4 km^3 of pyroclastic material. Therefore it is estimated that $\geq$ 20 km^3 of pyroclastic material (circa 50% with a dacitic or rhyolitic glass composition) has been erupted from the Mocho-Choshuenco complex during the last ca. 18 ka.

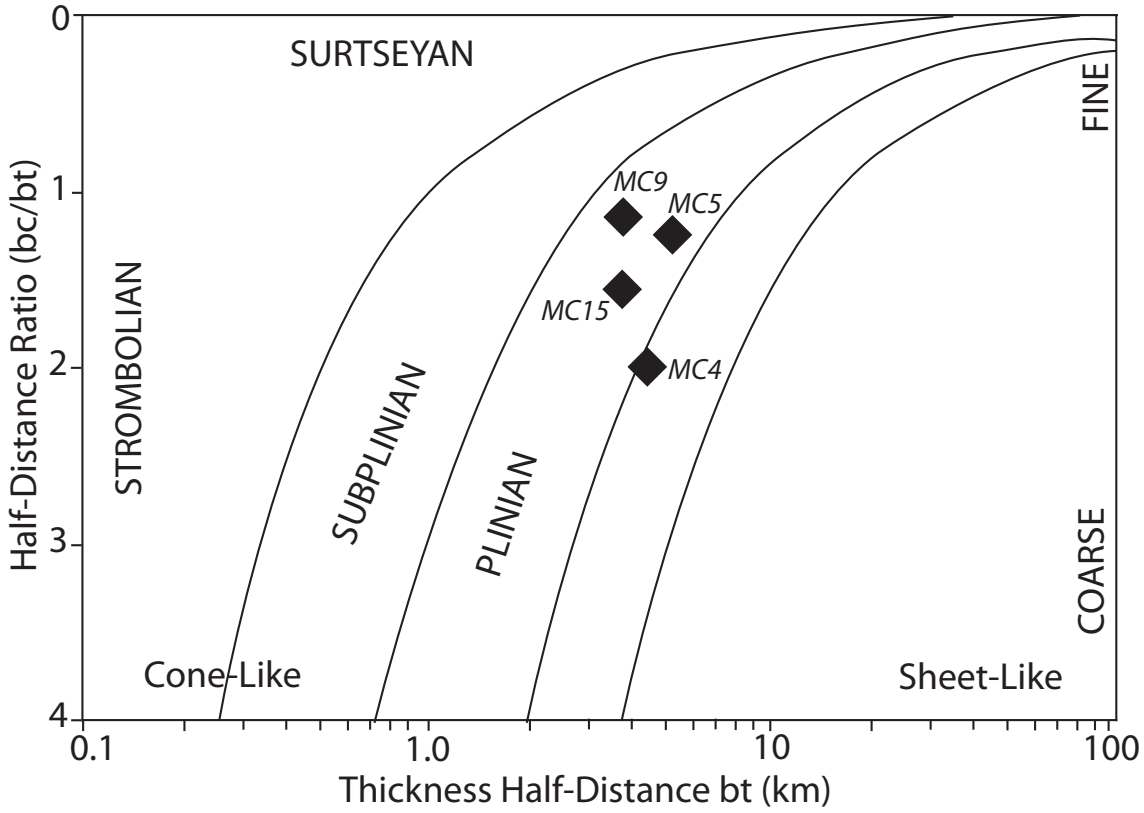

Figure 2.9: Classification scheme for tephra fall deposits from Pyle (1989). Plotted are the fall deposits with a sufficient number of maximum pumice and thickness measurements to construct isopach and isopleth maps. The half-distance ratio represents the total grainsize population and the thickness half-distance represents the dispersal. bc is the maximum clast size half-distance and bt the thickness half-distance. Although MC15 plots within the Plinian field the estimated magnitude is <5, hence it is interpreted as sub-Plinian.

Eruption		Unit type	Chemical Analyses	Dispersal	Volume (km^3)	Mass (kg)	Magnitude	Column Height (km)	Wind Speed (ms^{-1})	Modelled age cal. yrs BP
MC25 (Riñihue)		Basaltic-andesite fall	**Glass**	E			∼3			278–48
MC24		Andesite fall	**Glass** & oxides	E?			∼ <3			374–96
MC23 (Arauco)		Andesite fall	**Glass** & oxides	N			∼3			460–215
MC22		Andesite fall	**Glass**	E?			∼ <3			495–325
MC21 (Pilmaiquén)		Wet scoria fall	**Oxides**	E			∼4			543-365
MC20		Dacitic fall and overlying PDC	Glass & **Oxides**	NEE			∼4			1228–842
MC19		Andesitic-dacitic fall	Glass & **Oxides**	NE?			∼ <3			1328–1061
MC18 (Hua-Hum)		Andesitic-dacitic fall	Glass & **Oxides**	NE & SE	0.4	4.0×10^{11}	4.6	∼30	∼30	1375–1155
MC16		Scoria fall	**Oxides**	NE?			∼ <3			1624–1340
MC17		Scoria fall	**Oxides**	NE?			∼ <3			1490–1303
MC15	MC15D	Andesitic PDC	**Glass** & oxides	Radial	1	1.5×10^{12}	5.0			1695–1465
(Enco)	MC15C	Andesitic fall	**Glass** & oxides	SE	0.7	1.1×10^{12}		∼ <30	∼ <30	
MC14		Andesitic cone eruption	**Glass**	E?			∼3			2083–1594
MC13		Dacitic fall	Glass & **oxides**	ENE			∼4			2324–1806
MC12		Andesite-dacitic fall	Glass & **oxides**	NE			∼4			2832–2158
MC11		Andesite fall	**Glass**	E?			∼3			3494–2302
	MC10H						∼3			3692–2755
	MC10G						∼3			5415–3580
	MC10F						∼3			6053–3770
MC10	MC10E	Scoria fall package	**Glass**	NE, E, SE			∼3			6613–4105
(Grupo Fui	MC10D						∼3			7065–4555
Tephra)	MC10C						∼3			7413–5101
	MC10B						∼3			7628–5685
	MC10A						∼3			8001–6577
MC9 (Huilo)		Dacitic fall	Glass & **oxides**	E	2.2	2.2×10^{12}	5.3	∼30	∼30	8422–7982
MC8		Andesite cone eruption	**Glass**	E?			∼3			8896–8321
MC7		Andesite-dacitic fall	Glass & **oxides**	E?			∼3			9166–8396
MC6		Dacitic fall?	Glass & **oxides**	E?			∼3			9381–8561
MC5 (Pirehueico)		Rhyolite-dacitic fall	Glass & **oxides**	E	2.0	2.0×10^{12}	5.3	∼30–35	∼40	11549–8828
MC4 (Neltume)		Rhyolitic fall	Glass & **oxides**	NNE	5.3	5.3×10^{12}	5.7	∼30–35	∼35	12393–10389
MC3		Zoned fall	**Glass** & oxides	NE			∼4			13208–11999
MC2		Rhyolitic fall	Glass & **oxides**	SE?			∼3			14145–12073
MC1		Basaltic-andesite cone eruption	**Glass**	NE?			∼3			14918–12183
Relative stratigraphy not well constrained										
MC26		Tumba Buey Cone scoria fall and flow	**Oxides**	W						Post-dating MC15
MC27		Scoria fall	**Oxides**	NW?						Between MC4 and MC23

Table 2.6: Summary of stratigraphic relationship and characteristics of the explosive units. Chemical analyses highlights the geochemical analyses that were possible on the deposits with the better phase for correlation in bold. Eruption sizes are estimated using *AshCalc* (Daggit et al., 2014) and the exponential thickness decay mode (e.g., Pyle, 1989; Fierstein and Nathenson, 1992) and magnitude equation of Pyle (2000). For evolved deposits, with a density of 1000 kg/m^3, the VEI and magnitude estimates are identical. For more mafic, dense deposits (e.g., density of 1500 kg/m^3) the magnitude estimates are higher; a VEI 3–4 eruption would have a magnitude of 3.2–4.2. For units with limited exposure magnitudes are estimated by general thickness and grain size and compared to similar units in the literature. Question marks and tildes (∼) are used where there is uncertainty due to limited preservation.

2.5.1 Eruptive frequency and scale

The estimated magnitude and age of the 27 identified units is summarised in Fig. 2.10. The large eruptions are not evenly spaced in time. The three Plinian events all occurred between 12.4 and 8.0 cal. ka BP (maximum modelled range). The most recent large (magnitude >5) event, Enco (MC15), occurred 1.5–1.7 cal. ka BP. Between Enco and Huilo (MC9), the youngest of the Plinian eruptions, deposits from only a few minor eruptions from the main edifice are preserved on the volcano flanks (MC11, MC12 and MC13), with the oldest estimated to have occurred 3.5–2.3 cal. ka BP. Between ca. 3.5 ka and ca. 8 ka (Huilo), the only tephra units that are preserved are the minor scoria fall deposits of the Grupo Fui Tephra (8 sub-units MC10A-H, i.e., 8 eruptions). Most of these deposits are likely to originate from one of the many cones on the flanks inferred from their limited dispersal, proximity to the Fui cones and mafic composition. The geological record therefore suggests that there was a relatively long period (ca. >4.5 ka) of low explosivity from the central vent, apart from possible effusive activity. In contrast, we identify 11 tephra units, including the sub-Plinian Hua-Hum (MC18), eruption that are younger than Enco. This implies an increase in explosive frequency from the central volcano (one eruption every ∼150 years compared to one every ∼550 years prior to the Enco eruption, when the monogenetic cone eruptions are not considered). Given the limited dispersal of deposits associated with the monogenetic cones it is not yet possible to integrate these eruptions within the tephrostratigraphy established for the more explosive eruptions. Thus, the tempo of the monogentic volcanism cannot be constrained.

The apparent temporal variations in central vent eruption frequency and size could reflect changes in the volcanic system or, instead, it may simply be an artefact of preservation due to variations in the regional climate. Pollen and sedimentological studies in Lago Puyehue and Los Mallines peat bog (both ca. 90 km south of Mocho-Choshuenco; Bertrand et al., 2008; Vargas-Ramirez et al., 2008) indicate that the temperature, humidity and vegetation density have varied since deglaciation began (ca. 18 ka; Fig. 2.10). Between 17.4 ka and 15.5 cal. ka BP low pollen concentrations and low carbon contents are found in the Lago Puyehue core (Vargas-Ramirez et al., 2008) suggesting sparse vegetation cover, and presumably poor soil development. This is an unfavourable environment

for tephra preservation (e.g., Fontijn et al., 2014, for further discussion) and could explain why no deposits are found from this period. Between 5.3 ka and 0.52 cal. ka BP the peat core suggests that the climate was highly variable with both warm pulses (e.g., 4.6–4.3 cal. ka BP) and cold-humid periods (e.g., 3.4–2.9 cal. ka BP) recorded. The ca. 3 ka cold-humid period is linked to glacial advances in the central Andes (e.g., Bertrand et al., 2008). One implication of this is that proximal deposits on the flanks may have been eroded by advancing glaciers, removing evidence for older, smaller central vent events (e.g., sub-Plinian, magnitude $\sim$ <4) from the geological record. This could also explain the apparent low explosivity from the central vent between ca. 8–3.5 cal. ka BP where only the lower altitude cone forming eruptions (MC10 Grupo Fui Tephra) are preserved. Consequently, despite the high-resolution stratigraphy, we may still significantly underestimate eruption frequency, particularly for the activity pre-dating the most recent glacier advance (>ca. 2.9 cal. ka BP). We suggest that only central vent eruptions with a magnitude >4, or with a narrow dispersion (and magnitude >3), are expected to be preserved prior to the last glacier advance. Hence the more recent activity (<2.9 ka) is a truer reflection of the eruption behaviour at Mocho-Choshuenco.

Although changes in preservation might account for the apparent heightened eruption frequency in recent times it cannot explain the temporal spacing of the largest, magnitude > 5, events. The three Plinian eruptions all occurred early in the post-glacial period over a relatively short period of time (12.4–8 cal. ka BP). Since Huilo (MC9), the last of the Plinian eruptions, Enco (MC15) is the only magnitude >5 eruption preserved. If there had been younger Plinian eruptions (or magnitude >5 events) they would have been detected. Therefore the geological record implies that there has been a change in eruption behaviour through time, with large eruptions more prevalent prior to 8 cal. ka BP. This may reflect a change in the magmatic system, perhaps as a response to changes in regional ice cover during deglaciation (e.g., Watt et al., 2013a), or to long-term fluctuations in magma supply rates and storage timescales.

Sixty volcanic centres in the SVZ have been active since the last glacial period. However, the published literature suggests only seven volcanoes have had more than 10 eruptions: Nevados de Chillán (12 eruptions), Lonquimay (23), Llaima (11), Villarica (23),

Puyehue-Cordón Caulle (15), Calbuco (28) and Hudson (17) (references within Fontijn et al., 2014). At the majority of the volcanic centres (n = 36) only one to three post-glacial events are identified. Our study shows that Mocho-Choshuenco has had at least 34 eruptions (with magnitude $\gtrsim$3; prior work only identified 4 eruptions) and therefore indicates that it is one of the most active volcanoes in the SVZ. However many volcanoes in the SVZ have an incomplete record as they are still poorly studied or difficult to access. Around Mocho-Choshuenco there is a recently expanded road network (and hence outcrops) enabling easy access to the summit and flanks (east, north and west side). However, at other volcanoes the infrastructure is not as well developed, for example, at Volcán Hudson the nearest road is 30 km from the summit. Therefore finding any evidence of smaller past eruptions (magnitude <5) is highly challenging and consequently many studies focus solely on the largest, widespread events (e.g., Naranjo and Stern, 1998). Furthermore the high number of active volcanoes in the SVZ (60 volcanic centres) means many are still poorly studied (or the work has not yet been published in easily accessible or international literature). Therefore, presently, it is difficult to compare the explosive activity and eruptive frequency estimated for Mocho-Choshuenco to other volcanoes in the region with much certainty.

Only 18 volcanoes within the SVZ since the last glacial maximum have known deposits from a large eruption (magnitude >5; Fontijn et al., 2014), of which just nine, including Mocho-Choshuenco, have had multiple large events according to the published literature (Llaima, Villarrica, Puyehue-Cordón Caulle, Antillanca, Calbuco, Minchinmávida, Chaitén and Hudson). Further large eruptions have been identified but with insufficient published details to critically evaluate eruption parameters (e.g., Naranjo et al., 2001; Fierstein et al., 2013). Hudson is the only other volcano where more than two large units are recognised; Ho, H1, H2 and H3, all of which have Plinian deposits (Naranjo and Stern, 1998; Weller et al., 2014). Plinian eruptions with volumes >1 km^3 are rare in the SVZ (23 eruptions, including this work, are identified in the published literature; references within Fontijn et al., 2014), with only Hudson, Chaitén, Calbuco, Mocho-Choshuenco and Puyehue-Cordón Caulle known to have more than one large fall deposit. Three large Plinian eruptions are identified from Mocho-Choshuenco (MC4 (Neltume), MC5

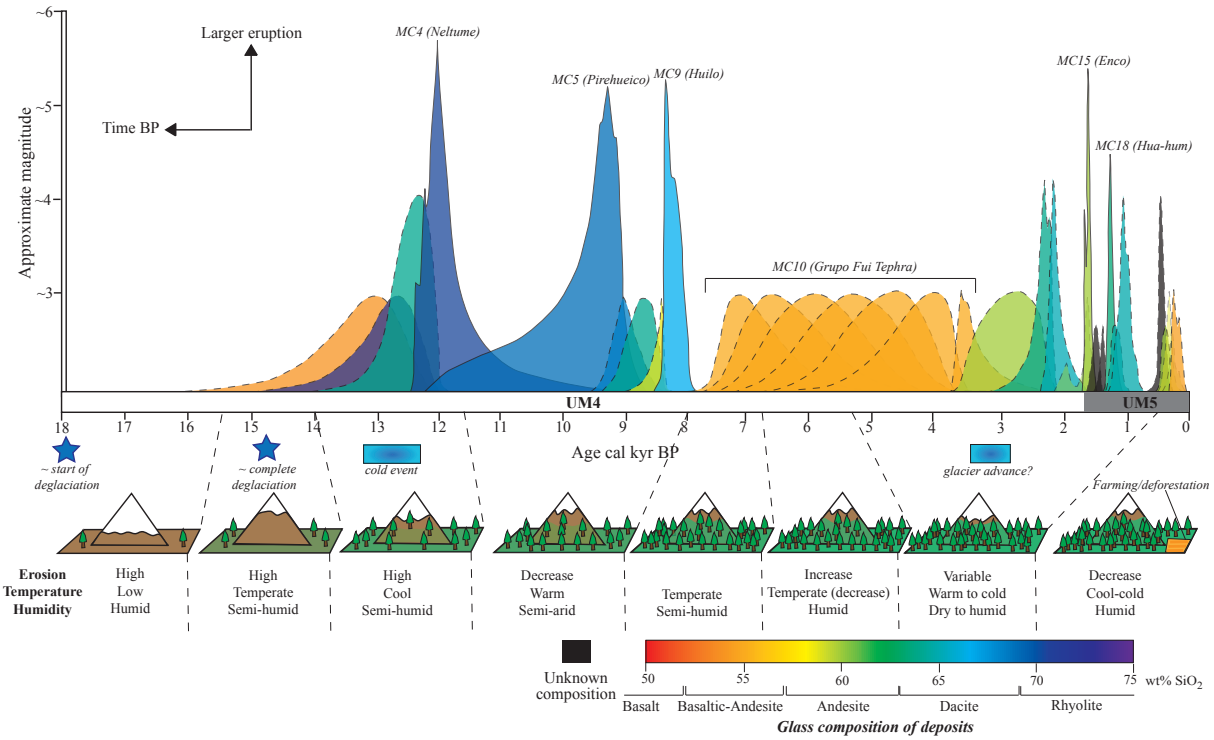

Figure 2.10: Summary of the explosive history from Mocho-Choshuenco since deglaciation (∼8 ka). Each unit is represented by its age probability distribution determined using Bayesian analysis of radiocarbon data, the height corresponds to the approximate magnitude (dashed lines used where magnitude is not well constrained) and the colour corresponds to the average SiO_2 glass composition. Magnitude = $\log_{10}$[eruption mass (kg) – 7] (Pyle, 2000). The erosion rates, temperature, humidity, climate and vegetation densities are inferred from the interpretations made on the Lago Puyehue core (ca. 90 km south of Mocho-Choshuenco; Bertrand et al., 2008; Vargas-Ramirez et al., 2008).

(Pirehueico) and MC9 (Huilo)), all of which have a dacitic melt composition. Therefore Mocho-Choshuenco is unusual in the SVZ in having evidence of four large eruptions, three of which generated by sustained Plinian eruption columns; hence it is potentially one of the most hazardous volcanoes in SVZ in terms of explosivity.

2.5.2 Regional tephra markers

Most deposits from Mocho-Choshuenco are dispersed to the north and east (due to prevailing wind directions, Fig. 2.8). Only two units are found in terrestrial sequences interbedded with deposits from neighbouring volcanoes: Neltume (MC4) and Hua-Hum (MC18). Hence Pirehueico (MC5), Huilo (MC9) and Enco (MC15), the other large and widely dispersed eruptions, are not useful regional markers, probably as their dispersion directions are roughly perpendicular to the volcanic arc. Neltume, the largest preserved

deposits from an explosive eruption from Mocho-Choshuenco, has a NNE dispersion, which is uncommon in this region. Cha1, from Chaitén, is the only other Plinian eruption known to have a NNE dispersal in the SVZ (Watt et al., 2013c; Fontijn et al., 2014); the majority are dispersed east, ENE or ESE. Neltume deposits are confirmed, with chemistry, at more than nine outcrops (north of Lago Calafquén), interbedded with tephra deposits from the Villarrica–Quetrupillán–Lanín chain. The reconstructed isopach map (Fig. 2.8A) suggests that deposits could originally have been deposited around Sollipulli and Llaima too. Hence this unit is an invaluable regional marker.

Hua-Hum (MC18), a smaller and younger deposit than Neltume (MC4), is dispersed to the north-east and south-east. To the south-east, the larger lobe, deposits are found interbedded with deposits from Puyehue-Cordón Caulle (e.g., CLD153, 40°14'S 71°57'W). Unfortunately it has not been possible to assign the Puyehue-Cordón Caulle deposits to known events or correlate to the Puyehue-Cordón Caulle deposit interbedded with deposits from MC10 (Grupo Fui Tephra; Fig. 2.3J) and hence gain further stratigraphic constraints. They are inferred to come from Puyehue-Cordón Caulle as the glass chemistry of the deposits does not correlate to any proximal Mocho-Choshuenco deposit, it lies off the Mocho-Choshuenco compositional trend (particularly for K_2O vs. SiO_2; Appendix A.2) and the glass has a rhyolitic composition similar to that of the Puyehue- Cordón Caulle 2011 eruption (Bertrand et al., 2014). No other rhyolite producing volcano has known eruptions that are likely to have deposits preserved near Puyehue-Cordón Caulle or Mocho-Choshuenco.

Although deposits from Mocho-Choshuenco are found interbedded around the Villarrica–Quetrupillán–Lanín chain there are only three localities around Mocho-Choshuenco where deposits from other volcanoes are observed; CLD153 (40°14'S 71°57'W), 115-03 (Fig. 2.3J) and 130112-3 (40°13'S 71°51'W). All three of these localities lie to the south of the edifice and preserve deposits from Puyehue-Cordón Caulle. This result illustrates two important features of the SVZ, which restricts the number of potential regional tephra marker beds. Firstly, the wind direction is predominantly to the east and consequently most volcanic eruptions in Chile get blown perpendicular to the volcanic arc and into Argentina. Secondly, only large eruptions (i.e., magnitude $\geq$5) are likely to be preserved

at neighbouring volcanoes due to the typical wide spacing (>60 km) of volcanoes along the arc. This scale of eruption is uncommon in Chile (see Section 2.5.1 and Fontijn et al., 2014). Therefore in the SVZ it is rare to find interbedded tephra deposits from more than one volcanic centre preserved in terrestrial sites. On the other hand, preservation of the tephra in lake sediments is significantly better as they are not eroded or weathered in the same way that land deposits are. Consequently lakes in the region form excellent repositories for finer material (from smaller or more distal eruptions) and hence there is a greater potential for finding deposits from more than one volcano in lake cores. However, interpretations may be complicated by the delivery of tephra from run-off, rather than fallout, and from tectonic disturbances (e.g., Juvigné et al., 2008; Van Daele et al., 2014; Bertrand et al., 2014; Moernaut et al., 2014; Van Daele et al., 2015). Since the post-glacial tephra deposits from Mocho-Choshuenco now have well constrained chemistry, dispersion and ages they could be invaluable markers in the regional lake cores, both in Chile and Argentina.

2.6 Conclusions

A detailed study of the post-glacial tephra deposits from Volcán Mocho-Choshuenco has enabled the explosive activity to be accurately reconstructed. This new tephrostratigraphy shows that Mocho-Choshuenco is the source of more than 34 explosive eruptions and ∼40 smaller eruptions forming monogenetic cones during the last 18 ka; this is the highest number of post-glacial explosive eruptions identified from a single volcanic centre in the SVZ. Analysis indicates that the eruptive frequency at Mocho-Choshuenco is one moderate- large (magnitude ≥ 3) eruption every ∼440 years. During the past 1.7 kyrs, radiocarbon dating of formation UM5 suggests an eruptive frequency of one explosive eruption every ∼150 years. This may be a truer reflection of the eruption frequency at Mocho-Choshuenco. This is particularly important to consider as the last known eruption from Mocho-Choshuenco was in 1864. Mocho-Choshuenco is estimated to have erupted ≥20 km^3 of pyroclastic material (ca. 50% with a dacitic to rhyolitic glass composition) during the last 18 ka, making it one of the most productive and active volcanoes in the SVZ since deglaciation.

The large new compositional dataset and eruption chronology means that the major late Quaternary tephra deposits from Mocho-Choshuenco are now well characterised, and may be used as regional stratigraphic marker beds. The Neltume deposits, which have a rare NNE dispersion, are found interbedded with tephra deposits from the Villarrica–Quetrupillán–Lanín chain and are expected to be preserved around Sollipulli and Llaima (∼140 km NNE of Mocho-Choshuenco), which could be used to help constrain the eruption chronology at these volcanoes.

The success of using this multi-phase approach to unravel the complicated volcanic stratigraphy at Mocho-Choshuenco suggests that a similar approach at other SVZ volcanoes could prove worthwhile. This would enable robust comparisons of eruption style and frequency between different volcanic centres, and could be used for hazard assessments in the region.

Chapter 3

The magmatic and eruptive response of arc volcanoes to deglaciation: temporal variability driven by changing crustal stresses

The work in this Chapter has been submitted for publication as: Rawson, H., Pyle, D.M., Mather, T.A., Smith, V.C., Fontijn, K., Lachowycz, S., Naranjo, J.A. (in review) The magmatic and eruptive response of arc volcanoes to deglaciation: temporal variability driven by changing crustal stresses, *Geology*.

3.1 Introduction

Volcanism exerts a major influence on Earth's atmosphere and surface environments (e.g., Schmidt et al., 2015). Understanding feedbacks between climate and long-term changes in rates or styles of volcanism is important, but unresolved. In regions dominated by decompression melting (e.g., oceanic ridges and some continental volcanic fields) there is strong evidence that unloading by both ice-removal and changing sea-level influence the amount of mantle melting, and magmatic fluxes *into* the crust (e.g., Jull and McKenzie, 1996; Nowell et al., 2006; Crowley et al., 2015). Accounting for 90% of subaerial eruptions (Siebert and Simkin, 2014), arc volcanoes are the most significant sources of volcanic gases and tephra to the atmosphere. Huybers and Langmuir (2009) proposed

that from 12 to 7 ka a pulse of activity at once-glaciated volcanoes contributed to increasing atmospheric CO_2 accelerating early Holocene climate change. While this hypothesis may be compelling, empirical data on arc eruption rates through time remain ambiguous, and attempts to identify whether, or how, subduction-related volcanoes responded to the removal of ice loads during deglaciation remains inconclusive (e.g., McGuire et al., 1997; Singer et al., 2008; Watt et al., 2013a).

Modelling the arc-scale volcanic response to unloading is also challenging. In arc settings the crust is typically thicker, and mantle melting is dominated by flux melting (e.g., Grove et al., 2012). Consequently, it has been suggested that ice unloading would primarily affect the crustal stress regime and hence vertical magma movement *within* the crust rather than melt generation itself (e.g., Nakada and Yokose, 1992; Jellinek et al., 2004; Singer et al., 2008; Kutterolf et al., 2013; Watt et al., 2013a).

The sparse nature of current datasets makes it challenging to distinguish whether the lack of evidence for an arc volcanic response to deglaciation reflects incompleteness in the records or the absence of a response (Watt et al., 2013a). Subduction zone volcanoes present particular challenges when compiling regional eruption archives. Records of effusive eruptions from long-lived systems are challenging to obtain, and to date; while deposits from the explosive eruptions that dominate arc records are prone to erosion and reworking (Fontijn et al., 2014). Many prior studies have focussed on changes in eruption frequency, rather than eruption flux. Eruption frequency records, although more readily compiled, are prone to bias via preservation potential (typically worse with time) and assume equal significance independent of eruption size. Detailed characterisation of preserved eruptive products is essential to reconstruct a sufficiently complete eruptive history to investigate arc-scale volcanic responses to deglaciation.

Here, we investigate the response of arc volcanoes to deglaciation via detailed analysis of one representative volcano (Mocho-Choshuenco, Chile). Mocho-Choshuenco is an ideal case study. It is a major stratovolcano that was extensively glaciated, and draped by up to ∼1 km of ice until ∼18 kyr BP (Porter, 1981; Glasser et al., 2008). It has a long eruption history, and has been one of the most active volcanoes in Chile during post-glacial times. The 18 kyr-long post-glacial record of explosive eruptions has been reconstructed through

detailed fieldwork and radiocarbon dating (Rawson et al., 2015). Analysis of erupted glasses and Fe–Ti oxides provide complementary datasets of temporal changes in magma compositions and temperatures. Together, these data provide the critical information on post-glacial eruption fluxes and crustal magma storage that allows us to investigate the 18 kyr volcanic response to the removal of an ice load.

3.2 Results

Analysis of tephra deposits at Mocho-Choshuenco constrains the cumulative erupted magma volume through time (Figure 3.1A; Rawson et al., 2015), showing clearly the magmatic output has varied significantly in post-glacial times. We identify three phases of activity, distinguished by different time-averaged eruptive fluxes, characteristic eruption sizes, distinct magma compositions and temperature ranges (Fig. 3.1): Phase 1 (13.0–8.2 kyr BP), Phase 2 (7.3–2.9 kyr BP), and Phase 3 (2.4 kyr BP to present; age range given by mean eruption ages bounding the phase). Eruption records prior to 13 kyr BP are incomplete, as the glaciers eroded down to bedrock, and tephra deposits may not have been preserved until terrestrial soils had stabilised (e.g., Fontijn et al., 2014; Rawson et al., 2015).

Phase 1 included several large eruptions (magnitude $\geq$5; erupted volumes >1 km^3) of dacite and rhyolite composition, and is characterised by elevated eruptive flux (0.9 km^3/kyr (dense-rock-equivalent; DRE)) but low eruption frequency (1.9 eruptions/kyr; Fig. 3.1). During Phase 1, magma temperatures increased systematically with time (from ~860°C to ~930°C; Fig. 3.1B). During Phase 2 the eruptive flux was lower (0.06 km^3/kyr (DRE); Fig. 3.1A), the eruption frequency was similar to Phase 1 (2.0 eruptions/kyr) but dominated by smaller eruptions (magnitude ~3; erupted volumes ~0.05 km^3) of more mafic melts (basaltic-andesites; Fig. 3.1). Phase 3 is typified by a higher eruptive flux (1.0 km^3/kyr (DRE)) and frequency (6.3 eruptions/kyr). Eruptions spanned a range of sizes (magnitude 3 to 5), dominated by intermediate melt composition (dominantly andesite and dacite), while magmatic temperatures ranged from ~930°C to ~960°C (Fig. 3.1)

Figure 3.1 only captures the flux of magma that erupted explosively. Since there is

little age data for effusive eruptions at Mocho-Choshuenco, we use edifice volume (∼160 km^3) and $^{40}Ar/^{39}Ar$ dates for the oldest exposed lavas (∼350 ka; Moreno and Lara, 2007), to estimate the time-averaged DRE magma flux of ∼0.5 km^3/kyr. Mantle melts that differentiate on their way through the crust beneath arc volcanoes leave plutonic cumulates. We estimated the mass of cumulate rocks retained in the crust during crystallisation by assuming the spectrum of erupted melt compositions was generated dominantly by fractional crystallisation (Rawson et al., 2015). Three different proxies were used to estimate the crystallisation fraction: (1) taking the Mg# [= 100*Mg/(Mg + Fe)] of the primary melts as 50-70 (e.g., Workman and Hart, 2005; Grove et al., 2012) and assuming potassium behaves perfectly incompatibly, (2) taking the SiO_2 of the primary melt as 50 wt.% and assuming Zr behaves perfectly incompatibly, (3) using the experimentally determined melt fraction curve (Nandedkar et al., 2014; Caricchi and Blundy, 2015; see Appendix A.6 for further discussion). By summing the cumulate and extrusive mass (per kyr) and assuming a primary magma density of 2830 kg/m^3, we estimate the approximate magma supply rate required to sustain the eruptive fluxes (see Appendix A.6). Phase 1 has the highest magma supply rate (3-24 km^3/kyr (1); 4.6 km^3/kyr (2); 3.0 km^3/kyr (3)), of which the smallest fraction erupts (<50% (1); 10% (2); 20% (3)); Phase 2 has the lowest magma supply rate (1-6 km^3/kyr(1); 0.8 km^3/kyr (2); 0.8 km^3/kyr (3)) and the largest erupted proportion (<70% (1); 60% (2); 60% (3)); and Phase 3 has the median magma supply rate (2-17 km^3/kyr (1); 2.9 km^3/kyr (2); 2.1 km^3/kyr (3)), of which the median fraction erupts (<65% (1); 20% (2); 25% (3)). For a primary melt with a Mg# of 60 the first proxy gives similar estimates for the primary magma supply rate and erupted proportion as proxy two and three.

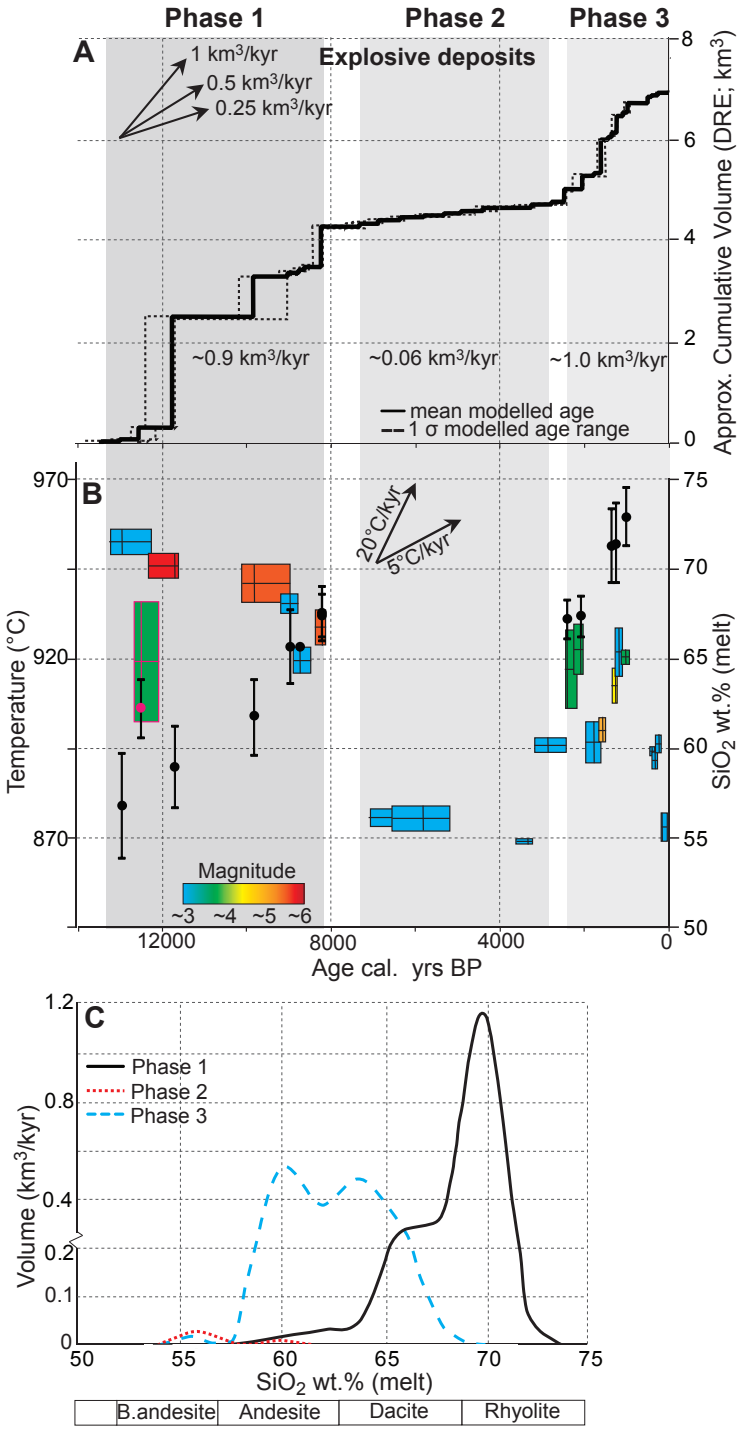

Figure 3.1: Observations and analyses of explosive eruptions of Mocho-Choshuenco Volcano. A) Cumulative dense-rock-equivalent (DRE) erupted volume of tephra through time. The thick line is the mean age; dashed lines show the 1σ uncertainty, from the age model. B) Temporal trends in magmatic temperature (From Fe–Ti oxide pairs, black circle and 1σ error) and mean eruptive melt SiO_2 content (box shows the 1σ range, coloured by eruption magnitude). The pink symbol corresponds to the one unit formed by mixing rather than fractional crystallisation (see Appendix A.6). Fe–Ti oxide pairs were not stable in the magmas erupted during Phase 2 C) Comparison of the ranges of melt compositions during each post-glacial phase of activity, based on glass data for each phase, normalised by eruption volume and phase duration

3.3 Discussion

Significant variations in the observed eruption fluxes (0.06 to 1 km^3/kyr (DRE); Fig. 3.1A) and estimated magma supply rates (6 to 24 km^3/kyr for primary melt Mg# of 70 (1); 0.8 to 4.6 km^3/kyr (2); 0.8 to 3.0 km^3/kyr (3)) between different phases of Mocho-Choshuencos post-glacial eruptive history imply changes either in the magma flux *into* the crust from the mantle, or from the crust to the surface, i.e., timescales of magma storage *within* the crust. Subduction zone arc-front magmatism is dominated by flux melting (e.g., Grove et al., 2012), with melting rates governed primarily by subduction inputs and parameters (e.g., convergence rate and sediment thickness). Changes in these are only detected in erupted magma composition on timescales of 100s kyr (e.g., Turner and Hawkesworth, 1997). It is not known how quickly a mantle-melting response to unloading would be reflected in the erupted magmas because of poor constraints on melt extraction velocities and transport rates through the crust (e.g., Zellmer et al., 2005). Given the relatively short timescales (∼10 kyr) considered here, we make the first order assumption that magma fluxes *into* the crust are (quasi-)constant and consider how the storage timescales *within* the crust might change.

Magma residence time in the crust will depend on the ratio between the stored volume and erupted flux (Fig. 3.2). One major control on the eruptive output flux will be the regional crustal stress field, which influences dyke formation. This will be sensitive to loading and unloading of ice sheets (e.g., Jellinek et al., 2004). At the last glacial maximum, the ice sheet around Mocho-Choshuenco extended ∼100 km perpendicular to the arc and was ∼1 km thick (e.g., Porter, 1981). Considering the lithosphere as an elastic half-space, unloading of this ice sheet alone leads to a maximum decrease in the lithostatic crustal stress, over the entire period of deglaciation, of ∼6 MPa at ∼16 km depth (i.e., in the mid-crust; see Appendix A.6 for details). This stress change is the same order of magnitude as that involved in dyke formation (Rubin, 1995). Thus, ice-unloading during deglaciation might promote dyke formation, promoting increased magma flux and reduced crustal storage times; and vice versa during glacial periods (Jellinek et al., 2004). We suggest that large volumes of magma were able to accumulate, and differentiate, in

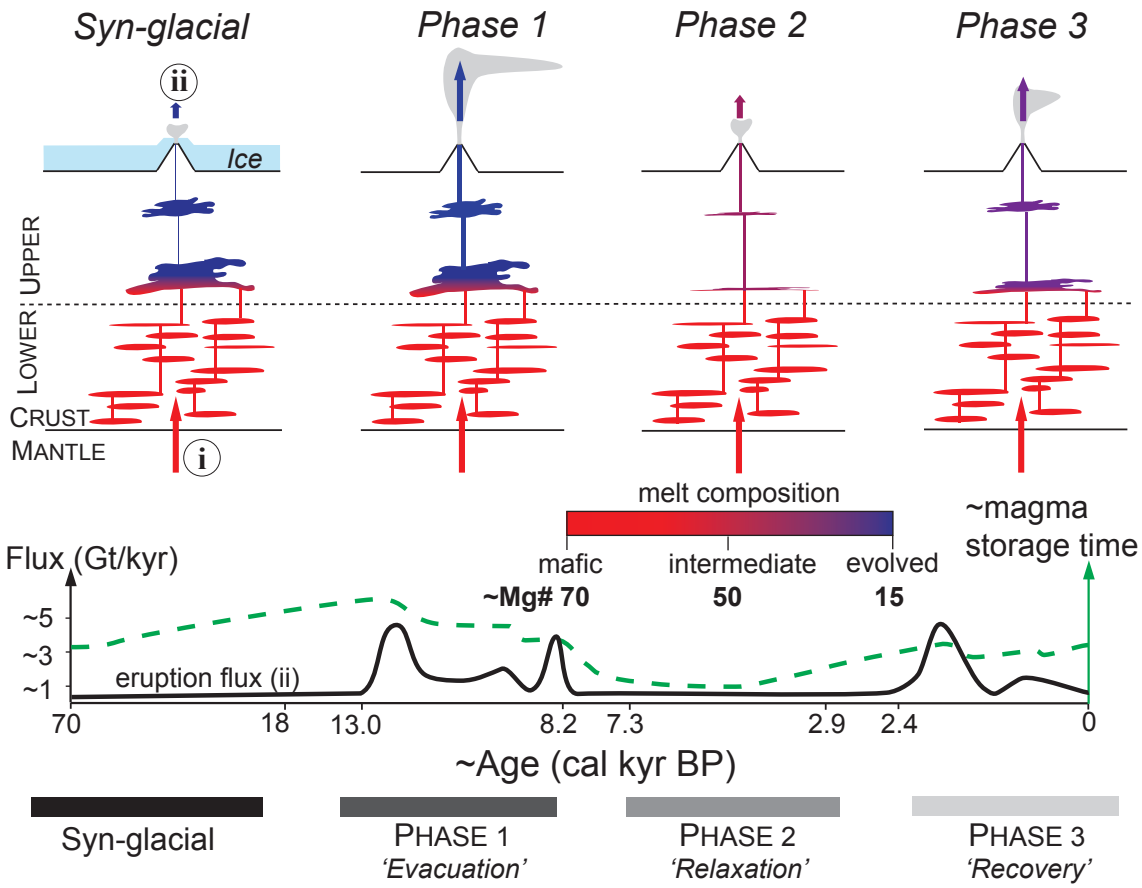

Figure 3.2: Illustration of changes in the magmatic system from syn-glacial times to the present day. During syn-glacial times eruption fluxes (ii) are low, and magma storage times, τ are high (τ, will depend on the ratio between the stored volume, V, and erupted flux (ii), F, so low F leads to large V/F and large τ). Magma accumulates in the crust and evolves. During Phase 1, large eruptions rapidly drain the crust of evolved magma. During phase 2, the system recharges with mafic magmas; eruption fluxes are low. During Phase 3 the system returns to steady-state behaviour as the system has relaxed. The lower panel shows eruption flux, determined by summing the effusive and explosive masses in 0.5 kyr bins, using the deposit volumes and the age probability distribution from the age probability distribution (see Appendix A.6). The magma storage time (shown in green; stored volume (V) will follow the same general trend), represents the average time magma spent in the crust prior to eruption, inferred from the prior eruption fluxes and erupted melt composition (see Appendix A.6). Low prior eruption fluxes (i.e., during syn-glacial period) and evolved melts imply that magma erupted in Phase 1 had a longer magma storage time. The processes governing the change from Phase 2 to 3 are not as yet clear but could be related to factors such as the thermal status of the crust (e.g., Bacon and Lanphere, 2006).

the crust during the last glaciation. Following deglaciation, dyke formation enabled these stored magmas to erupt during the early post-glacial volcanic activity, Phase 1 (Fig 3.1). We note that ice retreat would have been accompanied by a significant increase in physical erosion rates (e.g., Koppes et al., 2015), contributing further to rates of unloading, and local faults may accommodate part of this change in stress (see Appendix A.6).

Our hypothesis that variations in magma storage timescales explain the variable post-

glacial eruption fluxes at Mocho-Choshuenco is consistent with observed trends in magma chemistry. Erupted melt composition vary temporally from evolved (Phase 1) to mafic (Phase 2) and then to intermediate (Phase 3; Fig. 3.1C). Since the compositional diversity of magmas at Mocho-Choshuenco is primarily generated by fractional crystallisation (Rawson et al., 2015), melt composition will also be a proxy for crustal storage time (e.g., Hawkesworth et al., 2004). Hence evolved magmas erupted during Phase 1 have the longest crustal residence time and the lowest magmatic temperatures (Fig. 3.1B). This is consistent with our hypothesis that magmas accumulated, cooled and differentiated in the crust during the glacial period. Large eruptions during Phase 1 drained the crustal storage system, reducing the volume of stored melt. Phase 2 was dominated by mafic melt compositions, reflecting a limited crustal storage time. Then, during Phase 3, as stored magma volumes increased, so did crustal storage times. These changes in the magmatic system from syn-glacial to recent activity can be broadly characterised in terms of three phases, of evacuation, relaxation and recovery (summarised in Fig. 3.2).

3.4 Evidence from other arc volcanoes

We propose that variations in magma storage timescales related to changes in crustal stresses following ice unloading can explain the pattern of post-glacial eruption fluxes at Mocho-Choshuenco. By analogy, similar trends should be observed at other previously-glaciated arc volcanoes. The magnitude and tempo of variations (e.g., in eruption rate and silica composition) may differ between volcanic centres, depending on the local stress regime, edifice size, and the nature of the magmatic plumbing system. In the Andean Southern Volcanic Zone (SVZ) only three other volcanoes — Calbuco, Puyehue-Cordón Caulle and Villarrica (of the ∼60 centres active in the Holocene) — have sufficiently complete datasets to reconstruct the cumulative volume of post-glacial eruptions (Fig. 3.3). Although the records at other SVZ volcanoes are not as complete as for Mocho-Choshuenco, these three volcanoes exhibit similar changes in eruption rate through time (Fig. 3.3). The age of the earliest volcanic activity and timing of later phases decreases with increasing latitude. This may reflect the differential timing of ice retreat with latitude (e.g., Glasser et al., 2008; Watt et al., 2013a) and implies a lag of a few thousand

years (∼5 kyr at Mocho-Choshuenco) between deglaciation and the onset of large-scale explosive post-glacial volcanic activity. This synchronising of erutpion behaviour between these four volcanoes supports our inference that this is a volcanic response to deglaciation; there are no other external forces that could account for this over these spatial (>200 km) and temporal (millennia) scales. There are insufficient published compositional data to establish whether Calbuco, Puyehue-Cordón Caulle and Villarrica also show temporal trends in erupted melt composition. There are hints of similar temporal trends at volcanoes from other formerly-glaciated arcs (e.g., Kamchatka; Watt et al., 2013a) but sparse data on eruption chronologies, magnitudes and compositions hamper comparisons (e.g., Cascades; Hildreth, 2007). While well-studied arc volcanoes, which were not extensively glaciated, do not display similar temporal trends (see Appendix A.6), more work at other previously glaciated arc volcanoes is needed to test the wider applicability of our hypothesis. Records that preserve evidence for syn-glacial activity would offer key new insight. In southern South America only one known such record exists (Potrok Aike lake core at 52°S 70°W); however, this system shows significant reworking and is unsuitable to test our hypotheses (e.g., Wastegård et al., 2013).

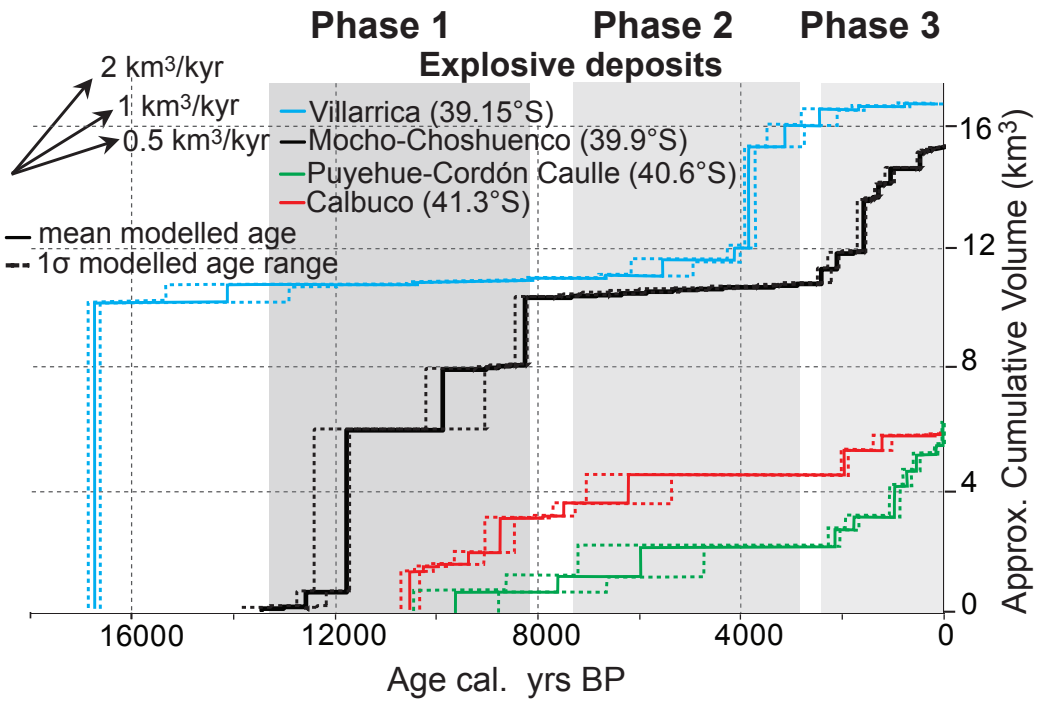

Figure 3.3: Cumulative tephra volume (bulk) estimates from Villarrica, Puyehue-Cordón Caulle and Calbuco compared to Mocho-Choshuenco. These three volcanoes, although with less complete eruption records, appear to exhibit the same three phases as Mocho-Choshuenco. Thick lines are mean ages, and dashed lines show the 1σ uncertainty in age, from Bayesian modelling of published radiocarbon dates (Fontijn et al., 2014 and Appendix A.6).

3.5 Implications and Conclusions

Analysis of high-resolution eruption records from a previously glaciated arc stratovolcano (Mocho-Choshuenco, Chile) reveals the volcanic response to deglaciation over millennial timescales. Mocho-Choshuenco, and some other Southern Andean volcanoes, show significant variations in eruption flux, and the composition and size of eruptions following deglaciation. These observations are consistent with a mechanism by which the unloading of an ice sheet affects the magma storage timescales via changes in crustal stress regime, rather than changing melting rates in the mantle.

This pattern of response to ice unloading may be a general feature of previously glaciated arc volcanoes. These observations have wider implications for the potential impact of post-glacial volcanic activity on the release of tephra and volcanic gas to the atmosphere (e.g., Huybers and Langmuir, 2009; Watt et al., 2013a). As the effect of ice-loading on volcanic activity appears to relax after ∼10 kyrs the observed volcanic response to deglaciation is essentially a 'transient' feature.

Chapter 4

Compositional variability in mafic magmas over short spatial and temporal scales

Arc magma genesis is complex, and interpreting the underlying causes of major and trace element diversity in erupted mafic magmas is challenging and often non-unique. This complexity is heightened when looking across temporal and spatial scales, where the number of potential variables increases. Despite this, few prior studies have investigated mafic magma diversity using sample suites which are both well constrained (age, location and composition) and spanning short temporal and spatial scales. This is the approach we take in this study. We analyse young deposits (< 18 kyrs) from the central Southern Volcanic Zone, Chile (37°S-45°S). This region has uniform subduction inputs and parameters (e.g., convergence angle and sediment thickness), reducing the number of potential variables at play. We focus on one volcano that has a high density of young scoria cones exposed across its flanks (up to 15 km from the central vent) and which have erupted relatively primitive magmas with diverse compositions. For some of the 'classical' slab and mantle geochemical tracers (e.g., Ce/Pb, U/Th, Zr/Nb) the erupted magmas span the complete range seen in this part of the arc (37°S-45°S). The tight temporal and spatial constraints provided by our analysed samples help us to assess the chemical and physical plausibility of the conceptual models of melting processes that may play a role

in driving the observed mafic magma diversity. In our analysis, we are also guided by recent advances in numerical modelling, which have improved our understanding of how melts are transported and focussed within the mantle, and of their interactions. This approach helps us to define some new hypotheses for interpreting the signatures of mafic arc magmas.

4.1 Introduction

Mafic magmas are rare components of the magmatic output at subduction-related volcanoes, but are critically important for our understanding of the origins of arc magmatism. In an arc setting it is widely agreed that mantle melting is dominated by flux melting due to the release of fluids and/or melts from the subducting slab (e.g., Elliott et al., 1997; Grove et al., 2012; Spandler and Pirard, 2013); these primary magmas then differentiate and interact with the mantle and crust as they ascend to the surface. These processes, between the slab and surface, affect the geochemical composition of the magma; however, the relative importance of these processes in causing the chemical diversity in erupted mafic magmas in arc settings remains unresolved.

Ideas regarding the origins of this chemical diversity can be broadly sorted into three groups of hypotheses. These are that magma compositional diversity (i) is inherited in the crust during ascent and differentiation (e.g., Hildreth and Moorbath, 1988; Annen et al., 2006), (ii) is inherited or driven by variations in the subducting slab inputs and/or thermal structure (e.g., Plank and Langmuir, 1988; Watt et al., 2013b; Turner and Langmuir, 2015) and/or (iii) reflects different modes of melt transport within and interactions with the mantle wedge and its heterogeneities (e.g., Kelemen et al., 1997; Reiners, 1998). Hypothesis groups (i) and (ii) are well-established and there is a considerable literature on the topic (e.g., see also McCulloch and Gamble, 1991; Plank and Langmuir, 1998; Wallace and Carmichael, 1999; Elliott, 2003; Grove et al., 2006; Annen et al., 2006). In terms of hypothesis group (iii), although there is a good understanding of melt transport within the mantle at mid ocean ridges (e.g., McKenzie, 1985; Kelemen et al., 1995; Kelemen et al., 1997; Katz et al., 2004) there is still great uncertainty in applying these approaches to arc settings. Recent advances in numerical modelling (e.g., Keller et al., 2013; in prep) have

shown that melt transport in an arc setting may be more complex than initially thought. How the melts are transported (e.g., decompaction or reactive channels), focussed and interact with the mantle are affected by the physical properties of the mantle; the nature of these processes can both affect the magma composition and the distances over which variations are detected at the surface.

Arc magma genesis is complex, and erupted magmas may be chemically and isotopically diverse across a range of temporal and spatial scales. Spatially variations in composition are observed between arcs; along arc (100-1000's km); between volcanoes (<100 km); and within a single volcano (<10 km) (e.g., Carr et al., 1990; Stern, 2004; Watt et al., 2013b; Jacques et al., 2014; Turner and Langmuir, 2015; Fontijn et al., submitted). Temporal variations in compositional parameters can be seen both within and between eruptions; and on timescales from days/weeks to millennia and longer (e.g., Ramos and Kay, 1992; Gertisser and Keller, 2003; Ripepe et al., 2005; Singer et al., 2008; Rawson et al., in review). Understanding the origins of compositional diversity in mafic arc magmas ideally requires sampling of materials on appropriate spatial and temporal scales; this is a challenge which few prior studies have met (e.g., Hildreth and Moorbath, 1988; Plank and Langmuir, 1988; Druitt et al., 1999; Dungan et al., 2001; Dungan and Davidson, 2004; Jacques et al., 2014). For example, some prior studies have used a limited number of samples (typically fewer than 5) per volcano, commonly of unknown age. This can lead to potential biases in the data, such as underestimating the full magma diversity at a single volcanic centre and confusing spatial trends for changing regional tectonics.

Further, the larger the temporal and spatial scales considered, the greater the complexity in deciphering the underlying cause of magma diversity. For example, over long time durations (10's to 100's thousands of years) the potential influences of glaciation and deglaciation, changing subduction parameters (e.g., convergence rate and angle), regional tectonics (e.g., stress regime and arc location) and mantle convection all need to be taken into account (e.g., Wallace and Carmichael, 1999; Nakada and Yokose, 1992; Singer et al., 2008). Over large distances variations in the subduction inputs (e.g., age of oceanic crust, sediment thickness and lithology being subducted) and regional tectonics (e.g., crustal thickness) may all influence magma diversity (e.g., Hickey et al., 1986; Plank

and Langmuir, 1993; Peacock et al., 1994). Here we focus on a region where mafic magma diversity is seen over short temporal (millennia) and spatial (few to tens of kilometres) scales, within an arc where the regional tectonics and arc inputs are relatively uniform along strike. This approach enables us to reduce the number of potential physical and chemical variables that could influence mafic magma diversity

Our particular focus is on the mafic products of post-glacial (<18 kyr) eruptions from Mocho-Choshuenco Volcanic complex (40°), from the Southern Volcanic Zone of Chile (37°S-45°S; SVZ: Fig. 4.1). This part of the SVZ is an ideal case study since the regional tectonics and arc inputs are relatively invariant and typical for an arc setting. The subduction angle (20-30°), dip (25-35°), convergence rate (7-9 cm/yr), sediment thickness, sediment lithology and crustal thicknesses (∼35 km) are all uniform (e.g. Stern 2004; Syracuse and Abers, 2006; Lucassen et al., 2010). Mocho-Choshuenco has the highest number and density of mafic cones within the SVZ (∼40 scoria cones, dispersed up to ∼15 km from the central vent), which have erupted relatively primitive magma with a wide range of magma compositions. Spatially this gives us a high-resolution dataset with the potential to reveal fine-scale melt heterogeneity inherited beneath the crust (e.g., within the mantle or from the subducting slab). This melt-heterogeneity could be lost by under sampling, or by focusing on samples from the major stratovolcanoes, where it may be concealed by the larger fluxes of magma and/or overprinted by processes in magmatic reservoirs en route to the surface. A high resolution post-glacial tephrochonological record that has been reconstructed for Mocho-Choshuenco, provides tight age constraints for the deposits, all of which have erupted within the last 18 kyr (Rawson et al., 2015).

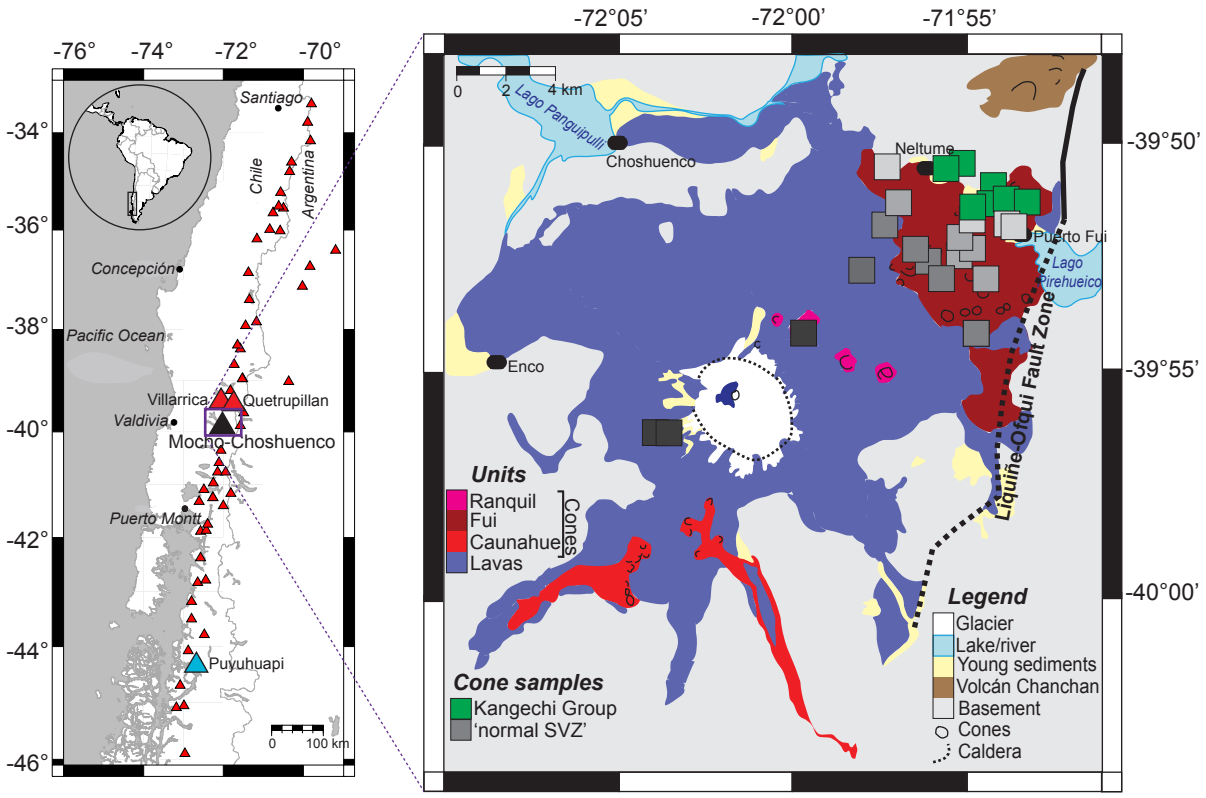

Figure 4.1: left: Map of the Southern Volcanic Zone (SVZ). Volcanoes that have been active during the Holocene are marked with red triangles. Mocho-Choshuenco is marked with a black triangle, Puyuhuapi with a blue triangle and Villarrica and Quetrupillan with a larger red triangle; these are the volcanic centres where the unusual melt composition (Kangechi) is observed. Right: Simplified geological map adapted from Moreno and Lara (2007). Cones samples are marked with a square. These are shaded by distance from the central vent; dark grey samples are closer to the central vent. The Kangechi cones are shaded in green. Previous work subdivided the cones into three geographical groups, which are marked on the figure; Fui (ca. 20 cones to the north-east and east of the edifice), Caunahue (ca. 13 cones on the south-west flank) and Ranquil (four cones on the north-east flank; Moreno and Lara, 2007)

4.2 Methods

Whole rock analyses (major and trace) were carried out on a suite of post-glacial tephra samples from Mocho-Choshuenco. To give regional context these were compared to previous published and unpublished analyses from other volcanic centres within the SVZ. 120 samples from Mocho-Choshuenco were analysed, including 44 scoria cone samples. Majors were analysed by X-ray fluorescence spectrometry (XRF) in the Department of Geology, University of Leicester and trace elements by Inductively Coupled Plasma-Mass Spectroscopy (ICP-MS; solution nebulised on a Thermo Finnigan Element 2 Sector-Field ICP-MS) at the Department of Earth Sciences, University of Oxford. See Appendix A.7

for the detailed methodology and full set of analyses.

To capture the compositional range of the SVZ we compiled whole rock data from the literature. To remove temporal uncertainties only samples known to have erupted in post-glacial times ($\sim$ <18 kyr) are considered. To reduce the number of variables (e.g., variations in slab inputs and crustal composition), only volcanic centres between 37°S and 45°S are plotted; volcanoes within the Northern and Transitional SVZ (33.3°S to 37°S) are excluded due to the thicker continental crust, which could impart a stronger crustal signature in the magmas (e.g., Hildreth and Moorbath, 1988). Volcanoes south of 45°S are excluded because of the potential influence of the Chile Rise, an oceanic ridge that marks the boundary between the Nazca and Antarctic Plates (e.g., Gutierrez et al., 2005). We refer to the filtered dataset as 'SVZ' hereafter. Within this SVZ dataset we distinguish two volcanic groups for further discussion: the Puyuhuapi volcanic group and the satellite cones between Villarrica and Quetrupillan. The Puyuhuapi volcanic group is a chain of Holocene basaltic cinder cones (44°18'S, 72°32'W; about 500 km south of Mocho-Choshuenco). They form on two NE-SW trending fissures, each with four associated cones (e.g., the Smithsonian Catalogue[1]; Watt, 2010). The satellite cones between Villarrica and Quetrupillan ($\sim$39°30'S, 71°50'W) are located up to 35 km east and northeast of Volcán Villarrica (60 km north of Mocho-Choshuenco). They comprise small scoria cones and associated flows of probable post-glacial age. The cones are grouped into five clusters; Huelemolle, Cerro Redondo, Caburga, Pichares and Huilico (e.g., Hickey-Vargas et al., 1989). To also assess how crustal contamination may influence magma composition we compiled the unpublished whole rock data on basement samples taken in the region around Mocho-Choshuenco (Echegaray, 2004). Although the precise location of these samples is not available they are representative of the major basement lithologies found within $\sim$20 km of the volcanic complex (Moreno and Lara, 2007).

[1]http://volcano.si.edu

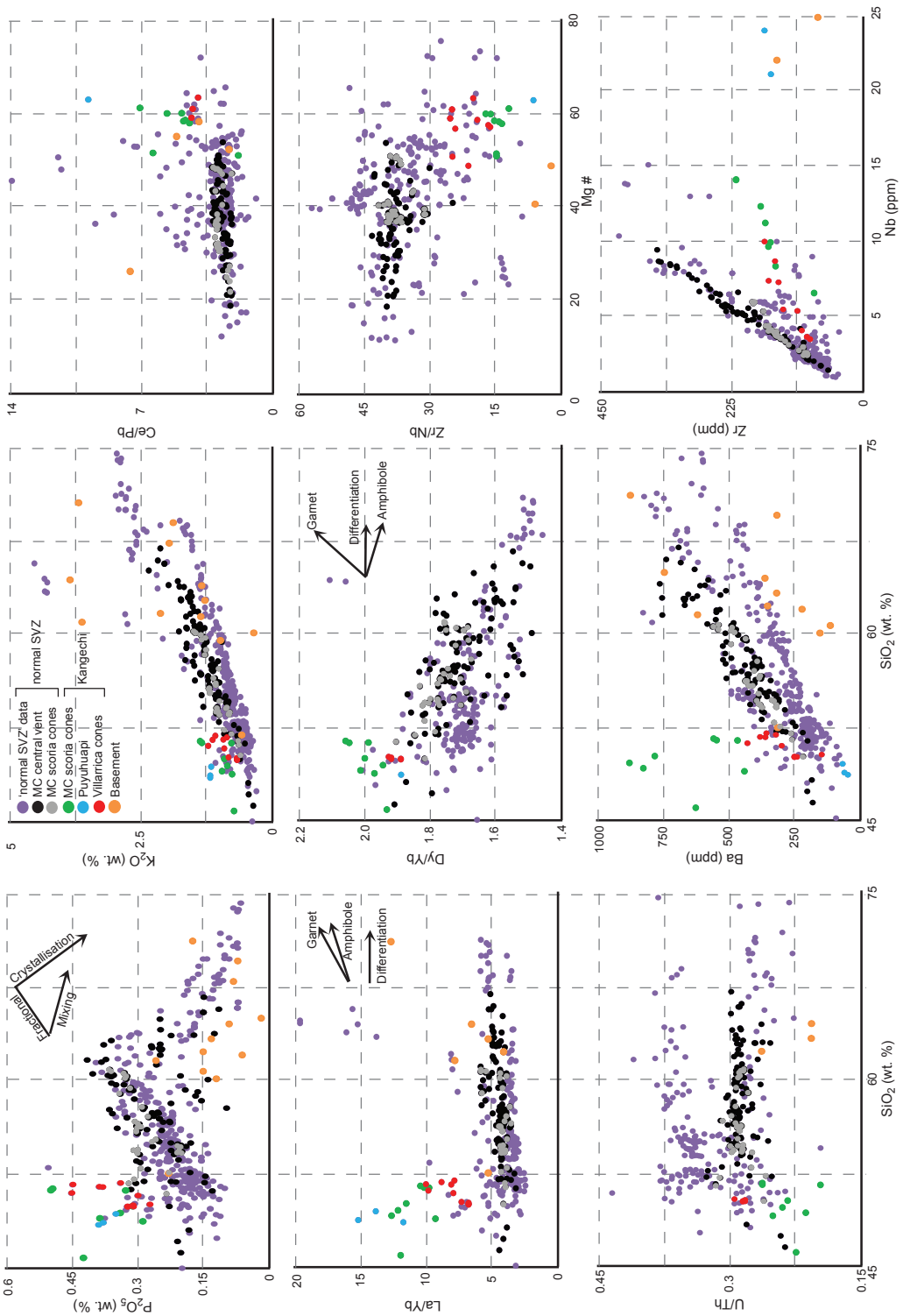

Figure 4.2: Whole rock major and trace element compositions of Mocho-Choshuenco deposits compared to other volcanoes within the SVZ (published and unpublished data: López-Escobar and Moreno, 1981; Hickey-Vargas, et al., 1989; López-Escobar et al., 1993; López-Escobar et al., 1995; Naranjo and Stern, 2004; Witter et al., 2004; Echegaray, 2005; Singer et al., 2008; Watt et al., 2010; Constantini et al., 2011; Reubi et al., 2011; Watt et al., 2011; Bouvet de Maisonneuve et al., 2012; Lohmar et al., 2012; Jacques et al., 2014; Schindlbeck et al., 2014; Fontijn, unpublished). Graphs illustrate how the 'normal SVZ' cones (grey) and central vent (black) deposits from Mocho-Choshuenco plot in the same field as most samples from other volcanoes within the SVZ. The Kangechi composition at Mocho-Choshuenco (green) is different to the main SVZ trend and is similar to the composition of the Puyuhuapi cones (blues) and cones near Villarrica volcano (red; locations marked in Figure 4.1). Country rock samples (orange) are also included. The country rock samples are taken from Echegaray (2004). Mixing between Kangechi and the country rocks cannot reproduce the compositions of 'normal SVZ' deposits.

4.3 Results

Figure 4.2 shows compositions of SVZ volcanic data, for selected major and trace elements. We distinguish six groups: the compiled SVZ data (purple circles), deposits from the Mocho-Choshuenco central vent (black circles), Mocho-Choshuenco scoria cones (grey circles), one cluster of scoria cones at Mocho-Choshuenco (green circles), the Puyuhuapi Volcanic Group (blue circles) and the Villarrica/Quetrupillan cones (red circles). The latter three groups are isolated as they have a distinct composition from the normal SVZ trend; they are enriched in incompatible elements and have an elevated Ce/Pb, La/Yb, Dy/Yb, P_2O_5 and K_2O and depleted U/Th and Zr/Nb compared to the normal SVZ. Hereafter we refer to cones with this signature as 'Kangechi' and volcanic centres without this signature as 'normal SVZ'. This 'Kangechi' signature has additionally been recognised at the Tatara-San Pedro Complex (36°S) within the basaltic-andesite lavas of the gamma episode (Lower Volcán Tatara: Dungan et al., 2001). However, it is not considered in this study as it is both older (∼130–60 kyr; Dungan et al., 2001) and outside the region examined.

4.3.1 Mocho-Choshuenco case study

The Mocho-Choshuenco Volcanic complex (40°S) is the only place in the southern Andean Volcanic Zone where mafic magmas with both the 'normal SVZ' and Kangechi signature are observed in close proximity (< 1 km between cones and < 15 km from the central vent: Fig. 4.1), and where the magmas are erupted effectively contemporaneously. The tephra-stratigraphic record implies that eruptions of normal SVZ compositions have occurred every ∼ 220 years in post-glacial times at Mocho-Choshuenco (<18 kyr; from both the central vent and flank cones). The Kangechi magmas were first erupted around 13.5 cal. kyr BP and most recently between ∼1.7-1.2 cal. kyr BP at Mocho-Choshuenco. The age of the most recent Kangechi magmas is bounded by the age estimates for the overlying and underlying tephra deposits (Chapter 2), which are of 'normal SVZ' composition. This constraint implies that magmas with a Kangechi signature were erupted within 500 years of 'normal SVZ' magma.

In post-glacial times Mocho-Choshuenco has erupted a wide range of magma compositions (basalt to dacite; Fig. 4.2). From whole rock major elemental signatures (e.g., P_2O_5 vs. SiO_2) as well as glass data presented in Rawson et al. (2015), we infer that the 'normal SVZ' chemical trends at Mocho-Choshuenco is primarily driven by fractional crystallisation. There is a distinct kink at ∼63 wt. % SiO_2 on the P_2O_5-SiO_2 plot which appears to mark the onset of apatite crystallisation. Apatite can have a strong influence on melt composition as many trace elements are compatible within its crystal structure (e.g., the REEs, Sr, U, Th), however their compatibility is sensitive to temperature, pressure and melt composition (e.g., Watson and Green, 1981). This complexity in the more evolved melts, coupled with the greater extent of crustal assimilation for evolved magmas inferred from isotopic analysis by McMillan et al. (1989) (they estimate the andesite and dacitic magmas assimilated 5% and ∼15% crustal rocks, respectively), mean that hereafter we focus on samples with $SiO_2 < 63$ wt. % (i.e., andesites or more mafic), for which our assumption is that they have primarily evolved by fractional crystallisation.

In total, 87 samples from Mocho-Choshuenco have $SiO_2 < 63$ wt. %. This includes 37 samples from the central vent and 40 samples from the scoria cones; the scoria cones form chains that are aligned predominantly in the direction northeast-southwest (Fig. 4.1) with the LOFZ marking the north-east limit. The scoria cones have basal diameters of up to 1250 m, heights of 150-250 m, crater diameters of 200-750 m and comprise black-red scoria of fine-lapilli to bombs that are up to 2 m across. Ejecta often have rare phenocrysts of plagioclase, olivine ± orthopyroxene ± clinopyroxene ± Fe-Ti oxides. The glass is very microlite rich, with the same crystal phases as the phenocrysts, and only small areas (<5 μm) of fresh glass. Microlites and phenocrysts are rarely euhedral, while the Fe–Ti oxides have highly irregular edges. Zoning is rare and normally only the olivine phenocrysts and pyroxene microlites preserve a thin, compositionally different rim.

4.3.1.1 Spatial variations

Cones with chemical signatures that overlap with the 'normal SVZ' trend have erupted effectively contemporaneously (i.e., within hundreds of years) with the central vent over the past 15 ka (Rawson et al., 2015). Their compositions plot in the same major and

trace element fields as deposits from the central vent and the normal SVZ trend (Fig. 4.2). Figure 4.1 shows the location of the samples and cones on a simplified geological map. Figure 4.3 and 4.4 are a selection of geochemical plots illustrating how major and trace elements vary with distance from the central vent. Within the cones there is a general trend to more mafic magmas with increasing distance from the central vent; slightly higher MgO, lower SiO_2 and lower incompatible elemental contents (e.g., LREE and Nb) with distance from the central vent (Fig. 4.3 and 4.4). Trace element ratios that are considered to be unaffected by crustal processes for mafic melts (U/Th, Zr/Nb and Ce/Pb: e.g., McCulloch and Gamble, 1991; Lee and Bachmann, 2014), plot within the central vent range and do not significantly vary spatially (Fig. 4.3). These trace element ratios are different from the country rock compositions, implying that crustal assimilation is not driving the geochemical trend (Fig. 4.2).

4.3.1.2 Kangechi signature

The cones with the Kangechi signature form a cluster near the town of Puerto Fui (Fig. 4.1); they occur <1 km from the next nearest cone and <15 km from the central vent (Fig. 4.1). These cones are the most mafic samples analysed from Mocho-Choshuenco; their Mg#'s (51-61) are higher (normal SVZ composition cones ∼Mg# <51) and SiO_2 values are lower (47-52 wt. %) than the other cones (51-61 wt. %; Fig. 4.2, 4.3). Despite being more mafic in composition the Kangechi cones are enriched in incompatible elements. For example, they have higher LREE, Zr, Ba and Nb concentrations relative to the other cones (Fig. 4.2 and 4.4). The Kangechi cones also have a distinct REE profile, which is most clearly seen for La/Yb (LREE/HREE) and Dy/Yb (MREE/HREE; Fig. 4.2); unlike the normal SVZ trend both these ratios are elevated (Fig. 4.2). The Kangechi cones also have a distinct U/Th, Ce/Pb and Zr/Nb signature, which significantly differ from the normal SVZ trend (Fig. 4.2, 4.3).

As trace and major element compositions may be affected by fractional crystallisation processes we normalise to a constant index of fractionation to verify the compositional differences between the Kangechi cones and Mocho-Choshuenco 'normal SVZ' composition. We normalise key major and trace elemental values to MgO 6.0 wt. % (determined

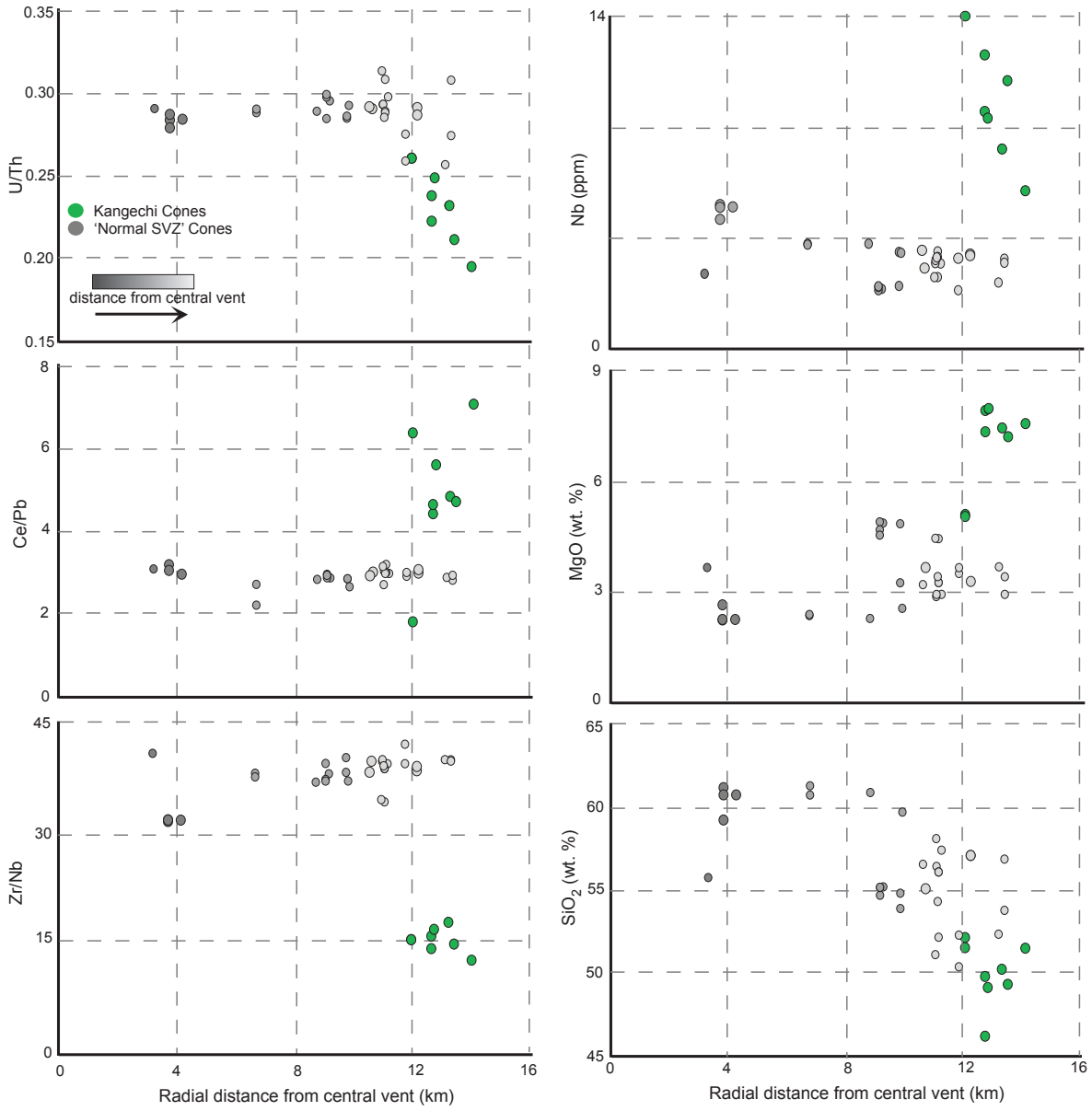

Figure 4.3: Whole rock analyses of the samples of the cones on the flanks of Mocho-Choshuenco. Composition is plotted against radial distance from the central vent. 'Normal SVZ' cones are shaded in grey with darker colours for cones closer to the central vent. As in Figure 4.1 the Kangechi cones are shaded in green

by back projection as in Plank and Langmuir, 1988). The results are summarised in Table 4.1. Kangechi magmas have higher K_2O, P_2O_5, Zr, Nb, La/Yb, Dy/Yb, Ce/Pb and Ba but lower Na_2O, Zr/Nb, U/Th at MgO of 6.0 wt. % than 'normal SVZ' magmas.

	'Normal SVZ' composition cones/Central vent	Kangechi
K_2O (wt. %)	0.7	1.2
P_2O_5 (wt. %)	0.2	0.4
Na_2O (wt. %)	3.7	3.3
Zr (ppm)	70.1	188.9
Nb (ppm)	1.9	12.3
Zr/Nb	37.4	15.4
La/Yb	4.0	11.1
Dy/Yb	1.8	2.0
U/Th	0.3	0.2
Ce/Pb	2.7	4.5
Ba (ppm)	271.9	619.9
Ba/La	∼15-30	∼15-30

Table 4.1: A selection of major and trace elemental concentrations and ratios normalised to MgO of 6 wt. % determined by back projection as in Plank and Langmuir, 1988

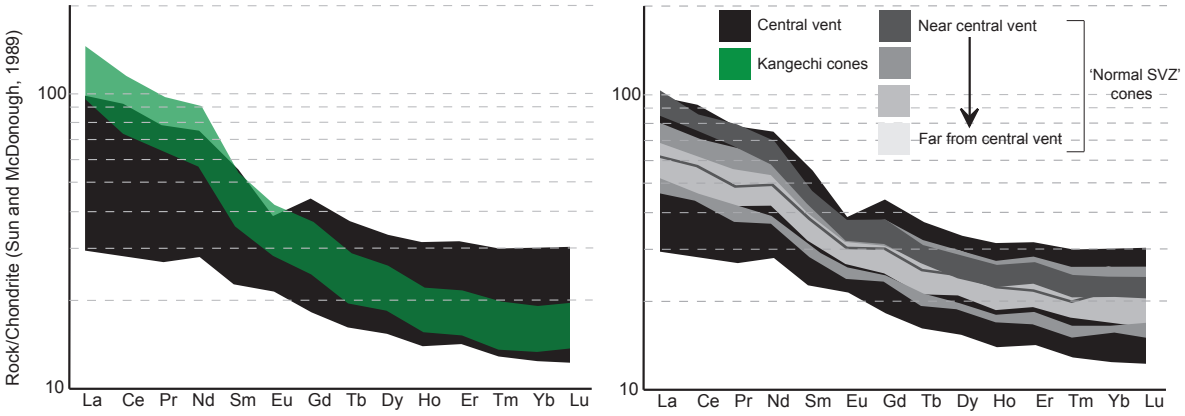

Figure 4.4: Whole rock REE composition of 'normal SVZ' cones, Kangechi cones and mafic central vent deposits from Mocho-Choshuenco. Left: the Kangechi cones (green) have an elevated LREE composition and a steeper REE profile compared to the central vent (black). Right: The 'normal SVZ' cones (grey) fall in the same REE range as samples from the central vent (black). There is a slight trend to elevated REE concentrations for cones closer to the central vent.

4.4 Discussion

During post-glacial times the Mocho-Choshuenco complex has erupted relatively primitive magmas with a wide range of magma compositions. For some of the 'classical' slab and mantle geochemical tracers the erupted magmas span almost the complete range seen in this part of the arc (Fig. 4.2). However, these variations are seen over short temporal (< 15 ka) and spatial (< 15 km) scales; such tight constraints are rare and have often been overlooked in prior studies (e.g., Hildreth and Moorbath, 1988; Dungan et al., 2001; Singer et al., 2008; Jacques et al., 2014). For example, Dungan et al. (2001) reconstructed a detailed eruption history of the effusive activity at the Tatara-San Pedro volcanic complex (36°S; SVZ), using $^{40}Ar/^{39}Ar$ measurements to constrain the age of the deposits. When dating effusive deposits this is often the best available technique, however it is challenging to get tight temporal constraints as often the uncertainty in the age estimate is 10's of thousands of years (e.g., Dungan et al., 2001). By focussing on young tephra deposits, although a shorter record is obtained, precise ^{14}C dating can yield tighter age constraints for the deposits.

As presented in the introduction ideas regarding the origins of this chemical diversity in arc magmas can be broadly grouped into three principal hypotheses. These are that magma compositional diversity (i) is inherited in the crust during ascent and differentia-

tion, (ii) is inherited or driven by variations in the subducting slab inputs and/or thermal structure and/or (iii) reflects different modes of melt transport within and interactions with the mantle wedge and its heterogeneities. We discuss these different hypotheses below with reference to the geochemical observations within the SVZ. We focus not on whether these processes impart a geochemical signature onto the magmas, but whether they could plausibly influence magma diversity over short length scales ($<$ 15 km) and timescales ($<$ 500 years) and thus account for the differences observed in these samples. In other words, are melts of differing compositions inherited at depth sufficiently isolated to be preserved at the surface, a consideration few prior studies have addressed.

4.4.1 Slab effects and crustal contamination

As the slab descends, it heats up, causing the release of fluids and melts into the overlying mantle. Changes in the rate, angle and dip of the subducting slab as well as the nature, age and thickness of the sediment and oceanic crust can all affect the flux and composition of the fluids and melts released, which in turn can affect the magma chemistry (e.g., Carr et al., 1990; Stern and Kilian, 1996). However, over such short scales we assume that subduction parameters and inputs remain constant. Variations down dip caused by increasing slab-surface temperatures and/or cracks on the slab providing a pathway for the slab-fluids could vary the flux of water and melts into the overlying mantle wedge (e.g., Hermann and Spandler, 2008; Watt et al., 2013b). However, the across-arc length scales over which these variations are thought to be significant are greater than the distances considered in this study (e.g., Watt et al., 2013b). Therefore although we cannot rule out hypothesis (ii) it seems a less probable cause for the magma diversity observed at Mocho-Choshuenco (see section 4.4.2.3 for further discussion).

Compositions of continental arc magmas may be influenced by crustal contamination. Whilst quantifying this effect often requires isotopic data (e.g., McMillan et al., 1989; Reubi et al., 2011), the trace elemental geochemistry is sufficient to indicate whether crustal assimilation is driving the compositional diversity. Figure 4.2 shows how the country rock samples have a lower Zr/Nb, Ba and P_2O_5 than all samples from Mocho-Choshuenco, but a La/Yb similar to 'normal SVZ' composition. Therefore as the Mocho-

Choshuenco 'normal SVZ' magma compositions show no systematic trend towards the country rock end member compositions, we infer that crustal assimilation cannot account for the divergence in composition between the 'normal SVZ' composition and Kangechi magmas nor the spatial variation within the 'normal SVZ' cones.

4.4.2 Kangechi signature

The plausibility of fractional crystallisation within the crust (i) and different modes of melt transport within the mantle wedge (iii) causing the Kangechi signature are discussed below. The nature of melt channelization is strongly controlled by the heat profile within the mantle. Above the thermal boundary layer (TBL) heat transfer is predominantly conductive, whereas below convection is important. One implication of this is that above the TBL melt transport is dominated by decompaction channels and dykes, whereas below reactive melt channelization are prevalent (e.g., Keller et al., 2013). Understanding how the physical properties of the mantle control the nature of melt transport is a recent advancement, and has not been previously considered for natural samples in an arc setting. To account for this we additionally subdivide hypothesis (iii) into two stages: (1) reactive melt channelization and (2) decompaction channels and dykes.

4.4.2.1 Reactive melt channelization

In arc settings, melting is dominated by flux melting (e.g., Grove et al., 2012). These initial melts move upwards within the mantle wedge primarily by reactive porous flow (Keller et al., 2013). Reactive porous flow occurs when melt ascends adiabatically, becomes undersaturated in a crystal phase and so reacts with the surrounding mantle causing the dissolution of one crystal phase and the precipitation of another more compatible phase plus melt (Fig. 4.5). As additional melt is produced, this will cause local increases in porosity and permeability, which in turn results in a larger flux of undersaturated melt (e.g., Kelemen et al., 1997). Due to the presence of dunite channels in ophiolite sequences (e.g., in Oman; Kelemen et al., 1995) it is often assumed that pyroxene breaks down and olivine is precipitated; however in arc settings, it is likely that other crystal phases would also be involved in the reaction (e.g., spinel, garnet, amphibole). Further, modelling

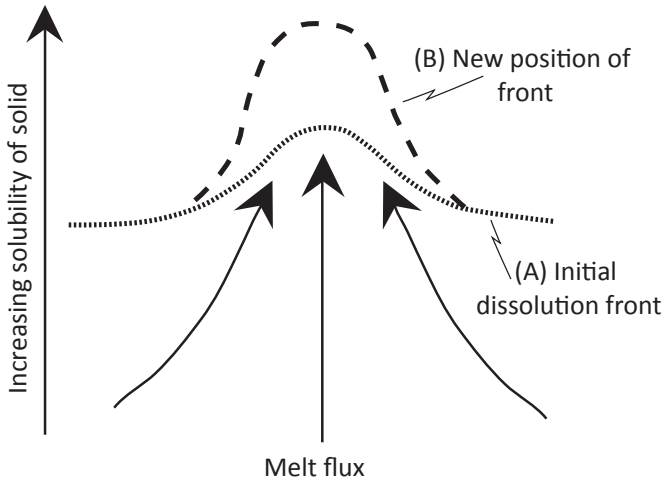

Figure 4.5: Schematic illustration of reaction infiltration instability (Ortoleva et al., 1987), which leads to reactive porous flow. Solid black arrows indicate the direction of melt flux. The dashed lines represent contours of constant dissolution at different times. As melt rises it reacts with and dissolves the mantle rock. This leads to the dissolution of one crystal phase and the precipitation of another more compatible phase plus melt. The centre of the initial dissolution front (A) has a slightly higher melt flux, which will lead to a greater rate of dissolution and hence increase in melt flux. This positive feedback leads to focussing of the melt into channels (B).

by Liang et al., (2010) suggested that dunite channels may be shallow features, and at greater depths harzburgite and lherzolite channels would preferentially form. For a homogeneous garnet lherzolite, modelled by Spiegelman and Kelemen, (2003) reactive melt channels cannot reproduce the compositional difference between Kangechi and 'normal SVZ'. Their models predict that although you can get a large diversity in melt composition a melt depleted in LREE would have a higher U/Th and lower Ba/La than an enriched melt; the normal SVZ composition is depleted, relative to Kangechi, but has a higher U/Th and similar Ba/La.

A lherzolite composition mantle will mainly comprise olivine > orthopyroxene > clinopyroxene. Although mantle xenoliths and ophiolites have shown that the mantle is dominated by this composition they also indicate that the mantle is heterogeneous and comprises centimetre to meter scale veins and/or lenses of more fusible material (e.g., metasomatised and/or pyroxenite veins; e.g., Hirschmann and Stolper, 1996). For example, there is evidence of metasomatised veins comprising amphibole ± clinopyroxene ± apatite ± garnet ± mica (e.g., phlogopite), all of which can significantly alter the trace elemental composition of the melt (e.g., Ionov et al., 1997; Pilet et al., 2008). However,

how the melt is modified during ascent and reaction will depend on the stability, composition and modal abundance of these different crystal phases, which is sensitive to the mantle condition, such as the pressure, temperature and water content. For example, the depth to which pargasitic amphibole is stable is sensitive to the temperature and water content of the mantle; and compositions are also dependent on pressure and temperature (e.g., Niida and Green, 1999). Experiments on natural samples have shown how mantle heterogeneities could affect melt composition. Pilet et al. (2008) carried out experiments on a hornblendite, taken from a metasomatised lithospheric mantle vein that formed at ~45 km. They showed that partial melting could produce a melt enriched in incompatible elements with an elevated La/Yb, Dy/Yb and Ce/Pb but depleted in U/Th and Zr/Nb (particularly enriched in Nb). This is geochemically consistent with the divergence in magma composition between Kangechi and 'normal SVZ' and we suggest that this is a plausible mechanism to account for the diversity in primitive magmas produced beneath Mocho-Choshuenco.

Computational simulations show that reactive melt channels can both nucleate within or interact with more fusible mantle material to varying degrees. Within the mantle only ~100 ppm of water is needed for these channels to form (e.g., Keller et al., in prep). Therefore, the erupted Kangechi magmas may have reacted with a more enriched mantle (i.e., with more fusible material) than the melts supplying volcanic centres with a 'normal SVZ' signature. Alternatively, the Kangechi melts could be fed from melt channels that nucleated from this more enriched rock. Therefore these channels could have formed at shallower depths than those feeding volcanic centres erupting magmas of a 'normal SVZ' composition. This model also offers a viable way to produce this unusual geochemical signature at different locations along the arc as well as in the same place at different times (see section 4.4.2.3 for further discussion).

4.4.2.2 Decompaction channels and dykes

Above the thermal boundary layer there is a change in the primary mode of melt transport (e.g., Keller et al., 2013; in prep). As the mantle is cooler and mechanically stronger reactive melt channels are inefficient at transporting melts as they are hindered by

crystallisation. Instead melt is thought to be predominantly transported by decompaction channels, which arise due to rock weakening at high fluid pressures (e.g., Connolly and Podladchikov, 2007; Keller et al., 2013); the presence of an overpressurised melt forces the opening of crystal grain boundaries enabling the melts to move upwards. However, the surrounding material is cooler than the melt, which causes it to crystallise and drives the melt to more evolved compositions.

The strength profile of the lithosphere, for example where the brittle-ductile transition occurs, will ultimately control whether melts reach the base of the crust in decompaction melt channels or whether dykes form. When the rock has a higher viscosity and lower tensile strength, dykes form preferentially to decompaction melt channels (e.g., Keller et al., 2013). In their numerical models, Keller et al. (2013) indicate that established dykes were able to transport large volumes of melt, even crystal-bearing magma, rapidly both within the mantle and crust; the initial size and orientation of these dykes would be controlled by the stress state. When these melts reach the base of the crust the crustal tectonics will control which melts reach the surface and their ascent rate. The presence of a large fault can act as a pathway for the melts enabling both rapid ascent to the surface and the ability for small volumes of melts to reach the surface.

Compositionally melt transported within decompaction channels and dykes will be affected by the extent of crystallisation and phases involved; for example, garnet, amphibole, olivine and clinopyroxene are all phases that could crystallise and would significantly change both the major and trace composition of the melt (e.g., Davidson et al., 2007; Smith, 2014). The only known mechanism that could account for the differences in REE magma composition between the Kangechi and normal SVZ is the fractionation of garnet (Fig. 4.2). Crystallisation and removal of garnet would drive the melts towards higher La/Yb (i.e. LREE/HREE) and Dy/Yb (i.e. MREE/HREE) with increasing SiO_2. However, garnet crystallisation would also drive the melts to lower Ce/Pb (Fig. 4.2; e.g., Hauri et al., 1984; Salters et al., 2002). This is not consistent with observed melt compositions at Mocho-Choshuenco as Kangechi has a *higher* La/Yb, Dy/Yb and Ce/Pb than 'normal SVZ'. Therefore we suggest that the distinct Kangechi signature cannot be generated by fractional crystallisation from a parental 'normal SVZ' magma at this stage

or within the crust (i).

4.4.2.3 Spatial constraints and likelihood of signature preserved.

The distinct Kangechi composition is erupted near to magmas of the 'normal SVZ' composition (< 15 km from central vent; < 1 km from a 'normal SVZ' cone). Preservation of this magma diversity from depth requires the two melts to be isolated from each other in the mantle over short lateral distances; if channels coalesce then the melts will mix and homogenise any variations that may be presence. The spacing and width of melt channels is primarily controlled by the melt flux and mantle permeability. Reactive melt channels have been suggested to be spaced on scales of 1-100 m (e.g., Kelemen et al., 2000) and decompaction channels on the order of ∼10 km (e.g., Keller et al., in prep.). In simulations melt channels often coalesce thus focussing the melts and reducing the channel spacing; in particular decompaction channels often form root-like structures in numerical models (e.g., Kelemen et al., 1995; Keller et al., in prep.; Fig. 4.6). Ophiolite studies show that coalescence of melt channels can focus melts from a ∼100 km wide region of partial melting to a ∼5 km wide zone (e.g., Kelemen et al., 2000). This observation is directly relevant for melt focussing at mid ocean ridges and highlights how this process could greatly increase the spacing between isolated melt channels. If this is the case in the SVZ, then the deeper the signature is inherited, the wider the area across which it should be observed at the surface. Since there is considerable magma diversity over short distances at Mocho-Choshuenco it seems less probable that variations in the subducting slab (ii) would be observed.

In section 4.4.2.1 we propose the Kangechi signature may have been inherited by reacting with a more enriched mantle or fed from melt channels that nucleated from more enriched material below the TBL. Variations in the mantle enrichment could occur as a result of melt focussing. Focussing of melt means that successive melt batches will pass through the same regions of mantle, increasingly leaching more incompatible elements (e.g., Reiners, 1998). Therefore the signature from any metasomatised mantle material will become more dilute with time. Larger fluxes of melt, potentially as a result of coalescing of melt channels, would cause a more rapid dilution of this signature. In

contrast, the mantle away from this primary melt network will remain comparatively enriched. Stratovolcanoes along the volcanic arc are relatively long lived (100's kyrs to millions of years) and large (>100 km^3; e.g., Völker et al., 2011) this implies that large fluxes of melt have passed through the mantle below. We propose that the Kangechi melts are fed by a separate, less extensive network with a lower melt flux. Therefore the mantle that the Kangechi melt network passes through may have been less depleted by earlier batches of melt and hence the resultant melts inherit a greater geochemical signature from the metasomatised mantle material. The Kangechi melt network may have formed either near the subducting slab and is just less extensive due to the geometry of the mantle wedge; or the melt network formed at a shallower depth by nucleating from more fusible material. Considering how extensive these melt networks can be from ophiolite studies, and the small spatial distances over which the signature is preserved (∼15 km), we favour the latter hypothesis (Fig. 4.6). The less extensive melt channel, with a lower melt flux is also supported by the rarity and small volume of the Kangechi magmas within the SVZ.

The only two other volcanic centres within this part of the SVZ where the Kangechi signature is observed is the Villarrica/Quetrupillan cones (∼60 km north of Mocho-Choshuenco) and Puyuhuapi volcanic group (∼500 km south of Mocho-Choshuenco). Although spatially and temporally their deposits are less tight than Mocho-Choshuenco, they are also of post-glacial age (<18 kyrs) and to the east of the main volcanic arc (over 15 km). Therefore physically the mechanism proposed for Mocho-Choshuenco is additionally plausible for these volcanic centres. Further, all three cone groups (including Mocho-Choshuenco) are in close proximity to the trace of the Liquiñe-Ofqui Fault Zone (LOFZ; Fig. 4.1), a major, dextral transform fault, which is thought to propagate through the entire crust (e.g., Cembrano et al., 1996). Potentially this fractured crust may be aiding the melt transport to the surface of these small melt fractions. Additionally it could account for the absence of this signature at the surface further to the east and/or west of the main volcanic arc where there are no large faults. However, 'normal SVZ' magmas are erupted at other volcanic groups that lie close to the LOFZ, for example the Palena Volcanic group (43°47'S, 72°28'W) and Carrán-Los Venados (40°21'S, 72°04'W). Therefore whether the Kangechi signature reaches the surface may also be controlled by

the geometry and size of the melt network in the mantle.

4.4.3 Spatial trend within 'normal SVZ' cones

As inferred in section 4.3.1 the 'normal SVZ' chemical trends at Mocho-Choshuenco is primarily driven by fractional crystallisation. Within the 'normal SVZ' cones there is a systematic trend to more mafic magmas, with a lower concentration of incompatible elements (e.g., LREE) with distance from the central vent; this is consistent with decreasing extents of crystal fractionation. This is further supported by the fractionation of the REEs (Fig. 4.2); the trend to higher La/Yb (i.e. LREE/HREE) and lower Dy/Yb (i.e., MREE/HREE) with increasing SiO_2 is consistent with amphibole fractionation. Although no phenocrysts of amphibole are found in erupted magmas at Mocho-Choshuenco it has been proposed that in an arc setting most amphibole fractionation is 'cryptic' as it accumulates in the mid-lower crust (Davidson et al., 2007). There is no clear evidence of garnet fractionation (e.g., an increase in La/Yb and Dy/Yb with increasing SiO_2) within the 'normal SVZ' magmas. As experiments suggest garnet would be stable at $>$ 16 kbar $\sim$50 km (e.g., Rapp and Watson, 1995) this implies the compositional trend is associated with shallow processes. Therefore, we propose that spatial variations reflect the compositional diversity of melts that are present in the crust, and more distal cones tap a more primitive, less fractionated melt. Further, as these cones plot in the same major and trace element fields, and follow the same evolutionary trends as deposits from the central vent these cones are likely to be parasitic and tapping the same melt source. This has been observed and modelled at other volcanoes, for example, Mount Mazama (e.g., Karlstrom et al., 2015).

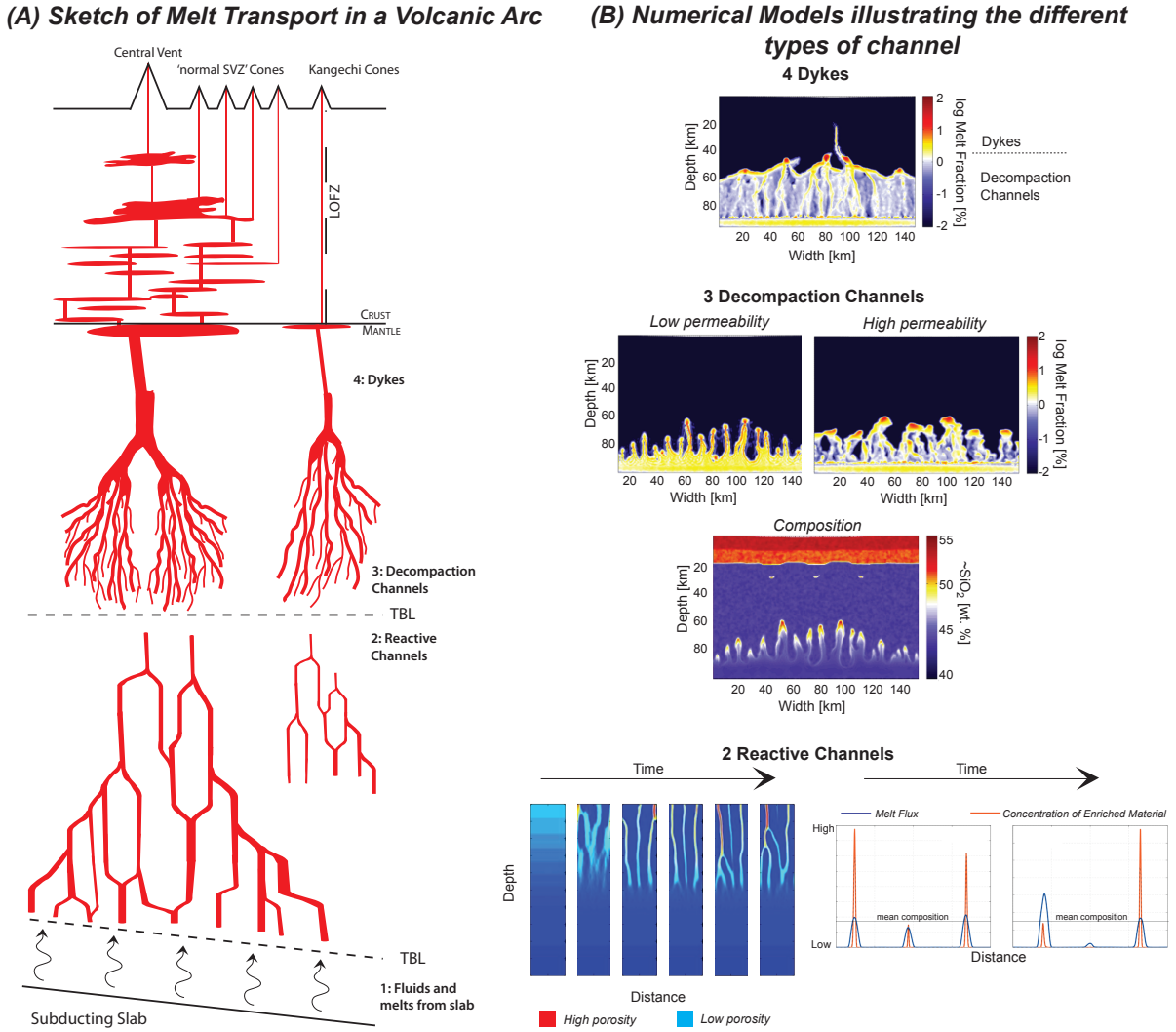

Figure 4.6: Schematic model of melt transport in a subduction zone illustrating some of the processes described in Section 4.4 . (a) Schematic of a hypothesis of how the two compositional trends are inherited at Mocho-Choshuenco over small spatial distances. Within the 'normal SVZ' cones a more primitive melt is tapped with distance from the central vent. The Kangechi cones inherit their distinct melt composition within the mantle wedge, where the melt channel is isolated from the main melt network feeding the central vent and 'normal SVZ' cones. The melt flux is lower beneath the Kangechi cones hence the small volume of melt is only able to reach the surface as the LOFZ offers a direct pathway. (b) Numerical models that illustrate some of the key features of melt channels. 4) Dykes: This figure is from Keller et al., (in prep.) and illustrates how dykes can nucleate from decompaction channels when the mantle is sufficiently viscous, permeable and the tensile strength is sufficiently low. It illustrates how decompaction channels often quickly coalesce to form tree-like structures. 3) Decompaction Channels: The three images are from numerical models run by Keller et al., (in prep.). The top two images show how an increasing permeability leads to an increased melt flow and the formation of fewer, but larger, melt channels. The bottom image illustrates how the melt composition within the channels is zoned, with more evolved melts towards the top where the melt experiences greater extents of crystal fractionation. 2) Reaction channels: images from numerical models run by Spiegelman and Kelemen (2003). These images show how the morphology and melt composition can vary temporally and spatially. For example, the left most channel changes significantly over time as it becomes connected to three other channels, which leads to an increase in the melt flux of more depleted material from depth.

4.5 Conclusions

Major and trace element compositions were analysed for a large number of mafic samples from the SVZ, Chile. Two main compositional trends were identified. Firstly, the composition of the magmas erupted from the cones on the flanks erupt becomes more mafic with distance from the central vent. This is attributed to fractional crystallisation processes within the crust and it is speculated that the spatial trend arises from more distal cones tapping a deeper, more primitive melt reservoir. Secondly there are three clusters of cones within the SVZ, which have a distinct major and trace element composition; for example, they are enriched in incompatible elements and have an elevated Ce/Pb and depleted Zr/Nb and U/Th compositions relative to the central vent; cones with this signature we attribute the name Kangechi.

The underlying cause of this distinct Kangechi geochemical signature is not unique when considering just the geochemistry; geochemically this signature could be inherited from the subducting slab or within the mantle wedge. However, unlike most prior studies we focus on deposits erupted over short timescales (< 18 kyrs) and distances (< 15 km). With these extra considerations we suggest one mechanism is physically and geochemically more plausible. We propose the distinct Kangechi composition arises as a result of melt focussing in the mantle leading to variations in mantle enrichment. Compared to other volcanic centres in the SVZ the melt channels feeding the Kangechi cones are less extensive and form at shallower levels, probably nucleating off more fusible material. They have a lower melt flux passing through them and appear to require tectonic support to get to the surface (i.e., the LOFZ). Therefore, the Kangechi magmas are likely to give greater insights into mantle heterogeneities. Further, as a result of melts focussing in the mantle wedge, there is a relationship between the depth of the inherited compositional signature and the lateral distance over which is it is observed on the surface, with deeper signatures being observed over greater distances.

Chapter 5

Summary and Future Directions

This thesis presents a detailed study of the post-glacial tephra deposits from Volcán Mocho-Choshuenco, Chile. Physical and chemical analysis of the deposits and eruptive products has allowed the development of a high resolution eruption record and provided new information on the past explosive behaviour, the influence of deglaciation on the tempo of arc volcanism, and helped to define some new hypotheses for interpreting the geochemical signatures of mafic arc magmas.

By combining field stratigraphy with glass and Fe–Ti oxide compositional data and new radiocarbon determinations, it was possible to identify and chemically fingerprint 27 units (and 34 eruptions) from Mocho-Choshuenco from post-glacial times, and confirm the existence of three major dacitic pumice fall deposits. In turn, these data provide a more complete picture of the style, frequency, distribution and size of past explosive eruptions during the post-glacial period. This reveals a volcano that is one of the most explosive (four eruptions magnitude > 5), productive ($> 1.3 km^3/kyr$), and frequently active (recent activity suggests one eruption on average every 150 years) in Chile during the Late Quaternary (e.g., Stern et al., 2007; Fontijn et al., 2014; Rawson et al., 2015). This improved understanding will be invaluable not just for evaluating potential future volcanic hazards, but also for understanding how the system has changed over time, and how it may have been affected by changes in the regional climate and/or tectonic regime.

Mocho-Choshuenco now has the most detailed and complete post-glacial eruption record for a volcano in Chile (e.g., Stern et al., 2007; Fontijn et al., 2014). This has allowed investigation of how a continental arc volcano responds to the combined climatic and

tectonic processes induced by deglaciation. Analysis of the high-resolution eruptive record shows clear evidence for a time-dependent volcanic response to deglaciation over millennial timescales. The response was more complex and subtle than the few prior examples documented for volcanoes in settings controlled by decompression melting (e.g., Iceland; Jull and McKenzie, 1996; Maclennan et al., 2002). A tripartite pattern of evacuation, relaxation and recovery was observed. Evacuation (early post-glacial) was characterised by an elevated eruptive flux, large eruptions and evolved melt compositions; relaxation by a low eruptive flux, small eruptions and mafic melt compositions; recovery (most recent activity) by a high eruptive flux, range of eruption sizes and intermediate melt compositions. This time-varying behaviour provided new insights into the magmatic response to removal of an ice load. It is proposed that the pattern reflects changes in the crustal stress field due to unloading, and the subsequent recovery of the the entire magmatic plumbing system towards a new steady-state, and may be a general feature of previously-glaciated arc volcanoes.

The unusual high density of young scoria cones on the flanks of Mocho-Choshuenco enabled a dataset of mafic magmas to be constructed over short temporal and spatial scales. This approach made it possible to reduce the number of potential variables that might be influencing mafic magma diversity. Two main compositional trends were identified. The first is a general trend to more mafic compositions, with distance from the central vent. This is attributed to fractional crystallisation processes within the crust and it is speculated that the spatial trend arises from more distal cones tapping a deeper, more primitive melt reservoir. The second, a cluster of cones with an unusually enriched (in incompatible elements) melt composition was proposed to arise from melt channelisation and focussing processes within the mantle. As a result of melt focusing, it is expected that there may be a relationship between the depth of the inherited compositional signature and the lateral distance over which the signature might be observed; deeper signatures are expected to be observed over greater distances. This has implications for the potential of detecting short wavelength slab heterogeneities at arc volcanoes.

Mocho-Choshuenco and Southern Chile are ideal places to explore many key questions in volcanology. This thesis has shown that detailed studies on past volcanic behaviour

have the ability to offer a wealth of information regarding arc magma genesis and the influence of external systems (e.g., deglaciation) on volcanic processes. It has also raised several questions. A few of these I discuss briefly below.

5.1 Potential coupling between glaciation and volcanic activity

The eruption record at Mocho-Choshuenco showed clear time-varying behaviour in the eruption flux, eruption size and magma composition (Chapter 3). This I hypothesised reflected changes in the crustal plumbing system, and magma storage timescales in response to removal of an ice-load. As arc volcanoes account for 90% of subaerial eruptions and are the most significant source of volcanic gases and tephra to the atmosphere this has important implications for the potential coupling between volcanism and deglaciation.

Coupling between volcanism and deglaciation was previously explored on a global scale by Huybers and Langmuir (2009), but relied on global eruption databases (Siebert and Simkin, 2002; Bryson et al., 2006) to evaluate the changes in the global volcanic eruption frequency over the last 40 kyr. One of the main challenges with using these databases, is knowing how to compare between different regions and timescales (e.g., Brown et al., 2014; Kiyosugi et al., 2015). For example, in the LaMEVE database, although Japanese volcanoes account for ca. 3.4 % of the volcanoes their eruptions account for ca. 40% (Brown et al., 2014). In addition to geographical biases there is a tendency for studies to focus on the largest eruptions as well as on the youngest activity. These biases mean global eruption records must be used cautiously and the under-recording of events must be corrected for when identifying and interpreting any global changes in volcanic activity through time (e.g., Kiyosugi et al., 2015). A further complexity that was overlooked in the approach taken by Huybers and Langmuir (2009) is that the underlying mechanisms modulating the response of individual volcanoes to deglaciation may be different leading to systematic differences in their behaviour (e.g., Maclennan et al., 2002; Chapter 3). In regions dominated by decompression melting observations suggest higher eruption rates occurred rapidly (within 2 kyrs of deglaciation in Iceland) as a result of ice-unloading

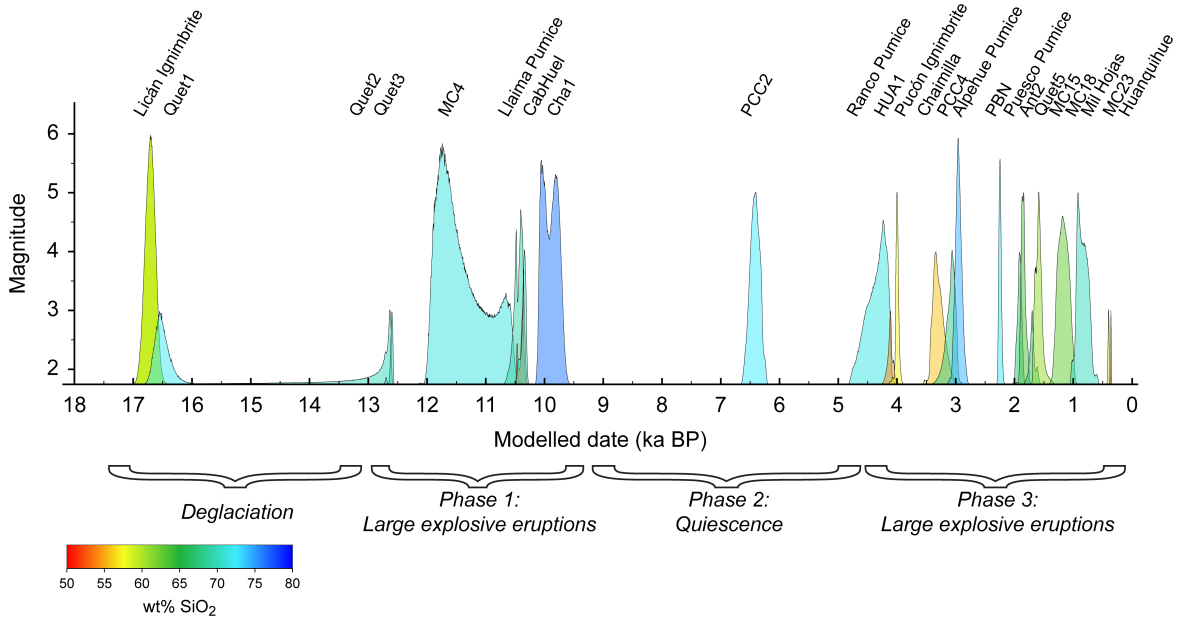

Figure 5.1: Summary of explosive history from the Chilean Lake district. Each unit is represented by its age probability distribution determined using Bayesian analysis of radiocarbon data, the height corresponds to the approximate magnitude and the colour corresponds to the average SiO_2 content of the glass: most units are dacitic to rhyolitic in composition. The temporal spacing of marker horizons in the Lake District is seemingly skewed towards the earlier postglacial ($\sim$ 17 – 9.5 ka) and the last 4.5 kyr. Figure from Fontijn et al., (submitted)

driving an increase in the rate of melt generation within the mantle (e.g., Maclennan et al., 2002). In contrast in arc settings observations imply high eruption rates occurred after a delay of a few thousand years ($\sim$5 kyrs at Mocho-Choshuenco between the start of deglaciation and onset of high eruption rates; Chapter 3) and were driven by changes in the crustal stress regime, rather than changing melting rates in the mantle. This has important implications for potential temporal variability in the global volcanic gas fluxes. In an arc setting, long-term changes in volcanic gas fluxes in response to deglaciation may not be significant as there appears to be no long-term changes in the magma flux into the crust. As arc volcanoes account for 90% of subaerial eruptions (Siebert and Simkin, 2002) this has important consequences for the extent to which there may be a feedback between deglaciation and volcanic activity. To address this requires volatile measurements and similar records to be constructed at other arc volcanoes in order to better quantify their response.

Success in obtaining high resolution eruption records from terrestrial sections is partly dependent on the accessibility of the volcano. Around Mocho-Choshuenco there is a re-

cently expanded road network (and hence outcrops) enabling easy access to the summit and flanks. However, at other volcanoes the infrastructure is not as well developed. For example, at Volcán Hudson, $\sim$ 750 km further south and thought to be a frequently active and highly explosive volcano as well, the nearest road is 30 km from the summit. Therefore finding evidence of smaller past eruptions (magnitude < 5) and hence reconstructing high resolution records from terrestrial sections is highly challenging. One way to overcome this is to integrate data from lakes sections, and other environmental records (e.g., peat bogs). Lakes have the potential to preserve tephra, both as discrete units, or as 'invisible' cryptotephra horizons, and may contain a more complete record of past eruptions (e.g., Lowe, 2011; Fontijn et al., 2014; Fontijn et al., submitted). This combined approach in Southern Chile has enabled higher resolution records to be reconstructed and demonstrated that other arc volcanoes possibly have a similar response to deglaciation as Mocho-Choshuenco. Fontijn et al. (submitted) constructed a detailed tephrostratigraphic record for the region between ca. 38° and 42°S. They report a similar general temporal trend in recorded eruption rate and size (highest in the early post-glacial and recent period) impacting the region (Fig. 5.1). Further, at Volcán Hudson (45°54'S 72°59'W) by compiling all the regional terrestrial and lacustrine sections Lachowycz et al. (in prep) observes a similar temporal trend in melt composition: during the early post-glacial period evolved compositions are erupted, followed by mafic and then more intermediate melts (Fig. 5.1). Therefore, similar trends might be expected at other previously glaciated arc volcanoes. Undertaking more detailed tephra studies on these volcanoes should give better constraints on the timings and magnitude of these changes globally in arc settings other than the SVZ. This will enable a more rigorous assessment of the potential coupling and feedbacks between deglaciation and volcanic activity.

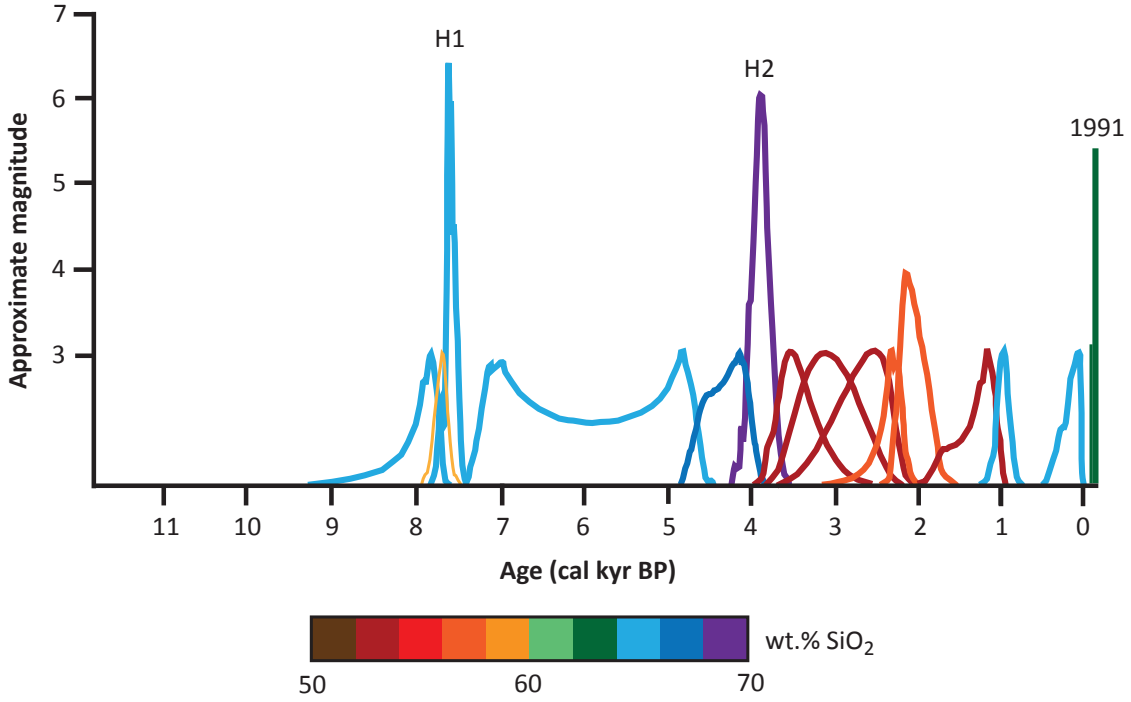

Figure 5.2: Summary of explosive history from Volcán Hudson since deglaciation. Each unit is represented by its age probability distribution determined using Bayesian analysis of radiocarbon data, the height corresponds to the approximate magnitude and the colour corresponds to the average SiO_2 content of the glass. Figure is taken from Lachowycz et al. (in prep)

5.2 Fe–Ti oxide trends

In order to fingerprint and correlate the tephra deposits at Mocho-Choshuenco a large amount of Fe–Ti oxide geochemical data was collected. In addition to being a valuable tephrochronological (correlation) tool these data also permit quantitative estimation of the temperature and oxygen fugacity of the erupted magmas for multiple eruptions (Chapter 2; e.g., Shane, 1998; Ghiorso and Evans, 2008). This reveals four main oxygen-fugacity trends (Fig. 5.2): across the NNO 0 buffer (MC2 to MC4), along the NNO +0.5 buffer (e.g., MC5 and MC9), between the NNO -0.5 and NNO 0 buffer (e.g., MC12 and MC17) and across the NNO +0.5 buffer. What causes these changes in oxygen fugacity is still poorly understood.

In an arc setting variations in the oxygen fugacity trends could be related to the fluid composition and oxidation state of elements given off the subducting plate (e.g., Kelly and Cottrell, 2009), H_2 exchange with the country rocks (e.g., Humphreys et al., 2015) and the

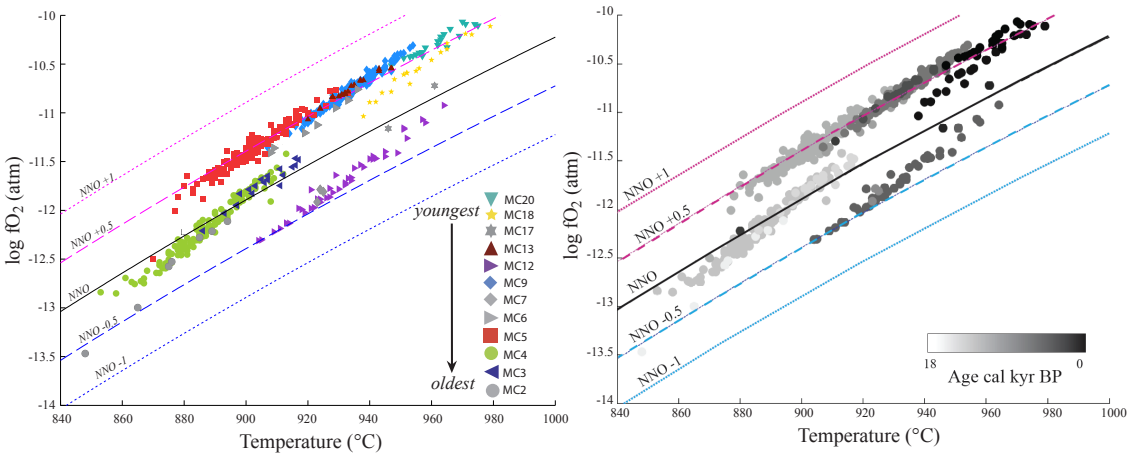

Figure 5.3: Temperature and oxygen fugacity (fO_2) estimates, determined using Fe–Ti oxide (magnetite and ilmenite) compositions and Ghiorso and Evans (2008). Fe–Ti oxide geothermometer plotted with respect to the Ni–Ni–O (NNO) buffer. Different colours and/or symbols represent the data from different units, as labelled in the legend. On the right the data is shaded by age from oldest (light grey) to youngest (black).

storage, ascent and fractionation of magmas in crustal resevoirs influencing the degassing of C-O-S-H volatile species (e.g., Fiege et al., 2014; Humphreys et al., 2015). Experiments have shown these processes can all control oxygen fugacity, but untangling these processes in natural samples is challenging. For example, in natural magmas multiple volatile species are present, and their differing behaviour can significantly affect the oxidation state of the magma (e.g., Fiege et al., 2014; Humphreys et al., 2015). Magma degassing can be strongly influenced by the temperature, pressure, initial oxygen fugacity and mode of degassing (open or closed system). Quantifying these variables (e.g., volatile contents, storage depths) should therefore help to untangle the underlying drives of different oxygen fugacity trends.

In the published literature oxygen fugacity and temperature estimates for multiple deposits at a single volcano are rare and often have poor temporal constraints (e.g., Shane, 1998; Selles et al., 2004; Sparks et al., 2008). The dataset at Mocho-Choshuenco includes estimates from 12 deposits with a wide range in oxygen fugacity-temperature trends over short timescales (<15 kyr). Further, changes in the oxygen fugacity trends happen sequentially with multiple deposits, of similar age, plotting along the same buffer, before a significant change in the system occurs around once every few thousand years. These significant changes in buffer could represent fresh batches of magma entering the system from depth; however, without further constraints on the system (e.g., volatile

contents, storage depths) it is challenging to interpret these trends. Therefore further analyses (e.g., geobarometry on clinopyroxenes; Nimis, 1999) to better constrain the system, Mocho-Choshuenco could be an interesting case study to explore the controls on the oxygen fugacity trends in natural samples.

5.3 Fracture Zones

In Chapter 4 I explored the possibility that melt focussing in the mantle means that there is a relationship between the depth of the inherited compositional signature and the lateral distance over which it is observed on the surface, with deeper signatures being observed over greater distances. One potential test for this hypothesis is whether we detect a geochemical signature from subducting fracture zones and if so over what lateral distances.

Fracture Zones are long, linear, large topographic features in the oceans that form beyond transform faults that originate from offsets in a Mid-Ocean Ridge. These offsets juxtapose different aged oceanic lithosphere causing a step in the depth of the seabed and flexure. This can produce high ridges ($<$ 3 km) relative to the surrounding ocean floor and deep troughs ($<$1 km; Watts, 2001). Within the SVZ there are three volcanoes that lie above the projected trace of major fracture zones: Nevado de Longaví (36.2°S) above the Mocho Fracture Zone, Mocho-Choshuenco (39.9°S) above the Valdivia Fracture Zone and Calbuco (41.5°S) above the Chiloé Fracture Zone. The influence these may have on magma composition is still poorly constrained and relatively few studies of this have been published (e.g., Jicha et al., 2004; Selles et al., 2004; Singer et al., 2007; Manea et al., 2014). Previous studies have used variations in the along-arc geochemical and isotopic compositions to propose that there is a higher degree of partial melting and greater flux of water-rich material beneath volcanoes that lie above fracture zones (e.g., the Amlia Fracture Zone in the Aleutians; Jicha et al., 2004).

Higher volumes of sediment, higher degrees of hydration in the oceanic crust and mantle and thinner oceanic crust would be expected at fracture zones compared to the surrounding subducting oceanic slab (e.g., Morgan and Forsyth, 1988; White et al., 1992; Detrick et al., 1993; Watt, 2001). Using traditional geochemical arguments, if slab het-

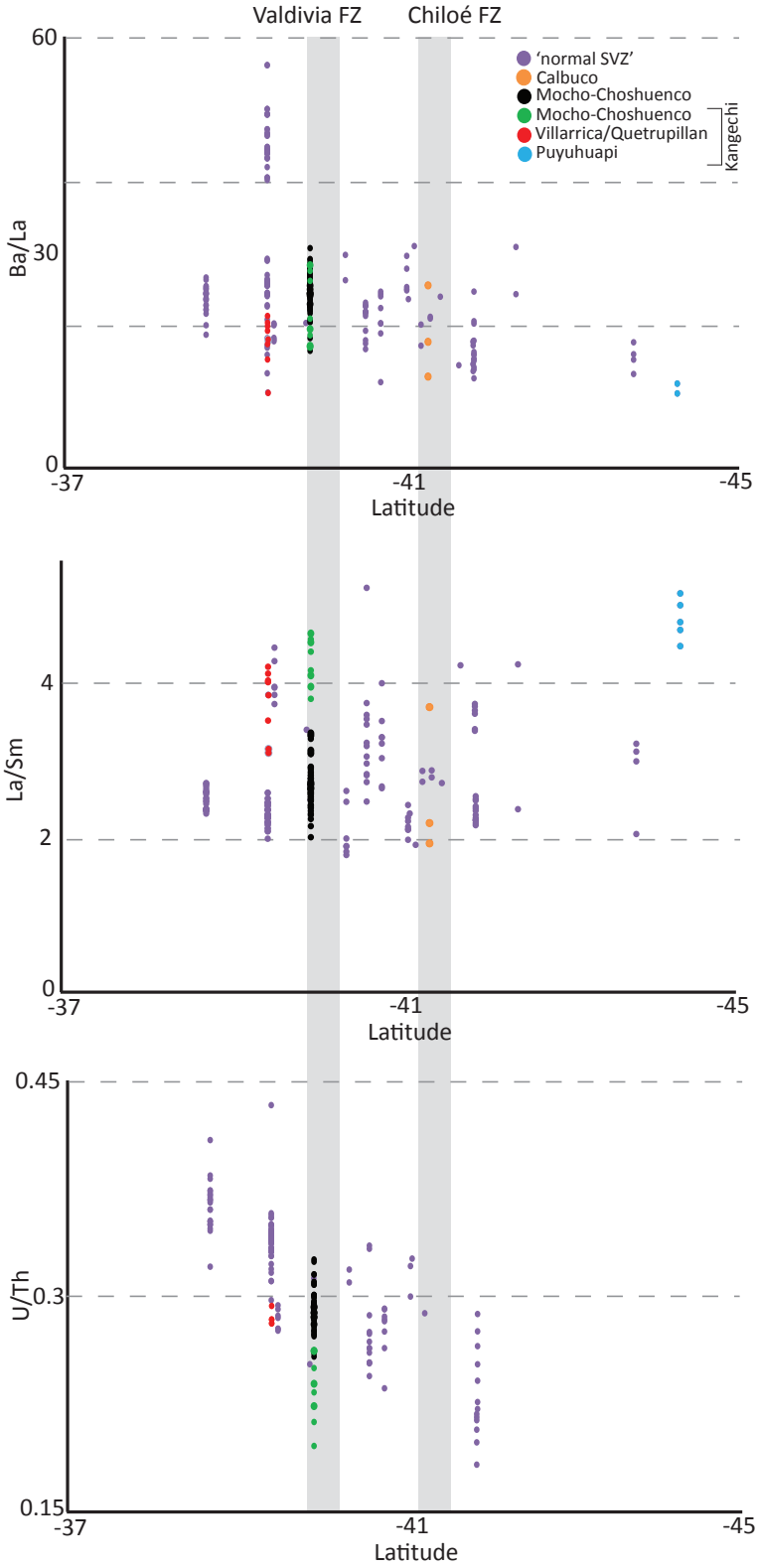

Figure 5.4: A selection of trace element ratios for whole rock data presented in Chapter 4. Deposits from volcanoes that lie above the trace of a fracture zone (Calbuco and Mocho-Choshuenco) and have the 'Kangechi' signature are distinguished, as labelled in the legend. The shaded area represents the section of the arc above the trace of the subducting fracture zones.

erogeneities are detectable at the surface then volcanoes overlying the trace of a fracture zone would be expected to have: (1) a stronger sediment signature (e.g., elevated Th/La, Zr/Nb, La/Sm), (2) a greater fluid signature (e.g., elevated Ba/La, U/Th), and (3) evidence of greater extents of mantle melting (e.g., depleted La/Yb, elevated Ba/La; e.g., McCulloch and Gamble, 1991; Plank and Langmuir, 1998; Jicha et al., 2004; Plank, 2005).

Considering the central Southern Volcanic Zone, Chile (37-45°S) and the assumptions presented in section 4.2, a selection of trace elemental ratios are plotted along this segment of the arc (Fig. 5.4). Deposits from Mocho-Choshuenco and Calbuco are distinguished as they lie above the trace of a fracture zone. Further magmas with the 'Kangechi' signature are also differentiated as part of their distinct composition may be inherited from mantle heterogeneities (Chapter 4). Focussing in on the 'normal SVZ' data there does not appear to be any systematic change in erupted magma composition, along strike, as a result of the subduction of fracture zones; Ba/La, U/Th, and La/Sm are not elevated at Mocho-Choshuenco and Calbuco compared to neighbouring volcanoes. This apparent absence of a geochemical signature from the subducting fracture zones may suggest that short wavelength slab heterogeneities are not possible to detect at arc volcanoes, when using major and trace element whole rock data. However, this absence of a signature could also be a result of the sparse resolution in the dataset. Presently in the published literature (and applying filters described in Chapter 4) there are a number of volcanoes with no data (e.g., Sollipulli); sparse data (e.g., one analysis at Yate), or only partial data (e.g., no U or Th for Puyuhuapi or Calbuco). Therefore potential along-arc variations may be lost by under sampling spatially and by not fully characterising the breadth of magma compositions erupted at each volcanic centre. Systematic collection and analysis of young mafic volcanic deposits in this region is a necessary step forward to help to better assess the influence of the slab in driving magma diversity and the extent of across-arc mixing during magma transport through the mantle wedge.

Bibliography

Amigo, A., Lara, L.E., and Smith, V.C., (2013). Holocene record of large explosive eruptions from Chaitn and Michinmahuida Volcanoes, Chile. *Andean Geology*, 40, 227-248. doi:10.5027/andgeoV40n2-a03.

Annen, C., Blundy, J.D., and Sparks, R.S.J. (2006). The genesis of intermediate and silicic magmas in deep crustal hot zones. *Journal of Petrology*, 47(3), 505-539 doi:10.1093/petrology/egi084

Arnaud, F., Magand, O., Chapron, E., Bertrand, S., Bos, X., Charlet, F., Mélières, M.A., (2006). Radionuclide dating (^{210}Pb, ^{137}Cs, ^{241}Am) of recent lake sediments in a highly active geodynamic setting (Lakes Puyehue and Icalma-Chilean Lake District). *Science Total Environment*, 366, 837-850. doi:10.1016/j.scitotenv. 2005.08.013.

Bacon, C. R., and Hirschmann, M. M. (1988). Mg/Mn partitioning as a test for equilibrium between coexisting Fe-Ti oxides. *American Mineralogist*, 73(1-2), 57-61.

Bacon, C.R., and Lanphere, M.A. (2006). Eruptive history and geochronology of Mount Mazama and the Crater Lake region, Oregon. *Geological Society of America Bulletin*, 118(11-12), 1331-1359. doi: 10.1130/B25906.1

Bernales, (1990). Toponimia de Valdivia, Temuco, *Ediciones Universidad de la Frontera*

Bertrand, S., Charlet, F., Charlier, B., Renson, V., and Fagel, N. (2008). Climate variability of southern Chile since the Last Glacial Maximum: a continuous sedimentological record from Lago Puyehue (40°S). *Journal of Paleolimnology*, 39(2), 179-195. doi: 10.1007/s10933-007-9117-y

Bertrand, S., Daga, R., Bedert, R., and Fontijn, K. (2014). Deposition of the 20112012 Cordón Caulle tephra (Chile, 40°S) in lake sediments: Implications for tephrochronology and volcanology. *Journal of Geophysical Research: Earth Surface*, 119, 2555-2573. doi: 10.1002/2014JF003321

Blockley, S. P., Ramsey, C. B., and Pyle, D. M. (2008). Improved age modelling and high-precision age estimates of late Quaternary tephras, for accurate palaeoclimate reconstruction.

Journal of Volcanology and Geothermal Research, 177(1), 251-262. doi: 10.1016/ j.jvolgeores.2007.10.015

Bronk-Ramsey, C. B. (2009a). Bayesian analysis of radiocarbon dates. *Radiocarbon*, 51(1), 337-360.

Bronk-Ramsey, C. B. (2009b). Dealing with outliers and offsets in radiocarbon dating. *Radiocarbon*, 51(3), 1023-1045

Brown, S.K., Crosweller, H.S., Sparks, R.S.J., Cottrell, E., Deligne, N.I., Guerrero, N.O., Hobbs, L., Kiyosugi, K., Loughlin, S.C., Siebert, L., and Takarada, S. (2014). Characterisation of the Quaternary eruption record: analysis of the Large Magnitude Explosive Volcanic Eruptions (LaMEVE) database. Journal of Applied Volcanology, 3(1), 5. doi:10.1186/2191-5040-3-5

Brown, S.K., Auker, M.R., and Sparks, R.S.J. (2015). Populations around Holocene volcanoes and development of a Population Exposure Index. *Global Volcanic Hazards and Risk* (Loughlin et al., (eds)), 223-232.

Bryson, R.U., Bryson, R.A., and Ruter, A. (2006). A calibrated radiocarbon database of late Quaternary volcanic eruptions. *eEarth Discussions*, 1(2), 123-134.

Carey, S., and Sparks, R.S.J. (1986). Quantitative models of the fallout and dispersal of tephra from volcanic eruption columns. *Bulletin of Volcanology*, 48(2-3), 109-125. doi: 10.1007/BF01046546

Caricchi, L., and Blundy, J. (2015). The temporal evolution of chemical and physical properties of magmatic systems. *Geological Society, London, Special Publications*, 1-15. doi: 10.1144/SP422.11

Carmichael, I. S. E., and Nicholls, J. (1967). Irontitanium oxides and oxygen fugacities in volcanic rocks. *Journal of Geophysical Research*, 72(18), 4665-4687. doi: 10.1029/JZ072i018p04665

Carr, M.J., Feigenson, M.D., and Bennett, E.A. (1990). Incompatible element and isotopic evidence for tectonic control of source mixing and melt extraction along the Central American arc. *Contributions to Mineralogy and Petrology*, 105(4), 369-380 doi: 10.1007/BF00286825

Castro, J.M., Schipper, C.I., Mueller, S.P., Militzer, A.S., Amigo, A., Parejas, C.S., and Jacob, D., 2013, Storage and eruption of near-liquidus rhyolite magma at Cordón Caulle, Chile. *Bulletin of Volcanology*, 75, 1-17, doi: 10.1007/s00445-013-0702-9

Cembrano, J., Hervé, F., and Lavenu, A. (1996). The Liquiñe Ofqui fault zone: a long-lived intra-arc fault system in southern Chile. *Tectonophysics*, 259(1), 55-66 doi: 10.1016/0040-1951(95)00066-6

Cembrano, J., Schermer, E., Lavenu, A., and Sanhueza, A. (2000). Contrasting nature of deformation along an intra-arc shear zone, the Liquiñe-Ofqui fault zone, southern Chilean Andes. *Tectonophysics*, 319, 129-149.

Cembrano, J., and Lara, L. (2009). The link between volcanism and tectonics in the southern volcanic zone of the Chilean Andes: a review. *Tectonophysics*, 471(1), 96-113. doi:10.1016/j.tecto.2009.02.038

Charrier, R., Pinto, L., and Rodríguez, M. P. (2007). Tectonostratigraphic evolution of the Andean Orogen in Chile. *The Geology of Chile* (Moreno, T., and Gibbons, W. (eds)). The Geological Society, 21-114.

Clavero, J. and Moreno, H., (2004). Evolution of Villarrica Volcano, *Servicio Nacional de Geología y Minería Boletín*, 61, 5-12

Cobeñas, G., Thouret, J. C., Bonadonna, C., and Boivin, P. (2012). The c. 2030 yr BP Plinian eruption of El Misti volcano, Peru: Eruption dynamics and hazard implications. *Journal of Volcanology and Geothermal Research*, 241, 105-120. doi: 10.1016/j.jvolgeores.2012.06.006

Connolly, J.A.D., and Podladchikov, Y.Y. (2007). Decompaction weakening and channeling instability in ductile porous media: Implications for asthenospheric melt segregation. *Journal of Geophysical Research: Solid Earth*, 112(B10). doi: 10.1029/2005JB004213

Costantini, L., Pioli, L., Bonadonna, C., Clavero, J., and Longchamp, C., (2011). A Late Holocene explosive mafic eruption of Villarrica volcano, Southern Andes: the Chaimilla deposit, *Journal of Volcanology and Geothermal Research*, 200, 143-158, doi: 10.1016/j.jvolgeores.2010.12.010

Crowley, J.W., Katz, R.F., Huybers, P., Langmuir, C.H., and Park, S.H., (2015). Glacial cycles drive variations in the production of oceanic crust. *Science*, 347, 1237-1240, doi:10.1126/science.1261508

Daggitt, M. L., Mather, T. A., Pyle, D. M., and Page, S. (2014). *AshCalc*–a new tool for the comparison of the exponential, power-law and Weibull models of tephra deposition. *Journal of Applied Volcanology*, 3(1), 7. doi:10.1186/2191-5040-3-7

Davidson, J., Turner, S., Handley, H., Macpherson, C., and Dosseto, A. (2007). Amphibole "sponge" in arc crust? *Geology*, 35(9), 787-790 doi: 10.1130/G23637A.1

Davies, S.M., Abbott, P.M., Pearce, N.J.G., Wastegård, S., Blockley, S.P.E., (2012). Integrating the INTIMATE records using tephrochronology: rising to the challenge. *Quaternary Science Reviews* 36, 11-27. doi:10.1016/j.quascirev.2011.04.005.

Darwin, G.H., (1907-16), Scientific papers, Cambridge, Cambridge University Press

Detrick, R.S., White, R.S., and Purdy, G.M. (1993). Crustal structure of North Atlantic fracture zones. Reviews of Geophysics, 31(4), 439-458.

Devine, J. D., Rutherford, M. J., Norton, G. E., and Young, S. R. (2003). Magma storage region processes inferred from geochemistry of Fe–Ti oxides in andesitic magma, Soufrière Hills Volcano, Montserrat, WI. *Journal of Petrology*, 44(8), 1375-1400. doi: 10.1093/petrology/44.8.1375

Droop, G. T. R. (1987). A general equation for estimating Fe^{3+} concentrations in ferromagnesian silicates and oxides from microprobe analyses, using stoichiometric criteria. *Mineralogical magazine*, 51(361), 431-435.

Druitt, T. H., Edwards, L., Mellors, R. M., Pyle, D. M., Sparks, R. S. J., Lanphere, M., Davies, M., and Barreirio, B. (1999). Santorini volcano. *Geological Society Memoir*, 19.

Dungan, M.A., Wulff, A., and Thompson, R. (2001). Eruptive stratigraphy of the TataraSan Pedro complex, 36°S, Southern Volcanic Zone, Chilean Andes: reconstruction method and implications for magma evolution at long-lived arc volcanic centers. *Journal of Petrology*, 42(3), 555-626. doi: 10.1093/petrology/42.3.555

Dungan, M. A., and Davidson, J. (2004). Partial assimilative recycling of the mafic plutonic roots of arc volcanoes: An example from the Chilean Andes. *Geology*, 32(9), 773-776. doi: 10.1130/G20735.1

Dzierma, Y., Wehrmann, H., (2010). Eruption time series statistically examined: probabilities of future eruptions at Villarrica and Llaima Volcanoes, Southern Volcanic Zone, Chile. *Journal of Volcanology and Geothermal Research.* 193, 82-92. doi:10.1016/j.jvolgeores.2010.03.009.

Echegaray, J. (2004). Evolución geológica y geoquímica del Centro Volcánico Mocho-Choshuenco, Andes del Sur. Master Thesis, Universidad de Chile, Chile

Echegaray, J, Moreno, H., and Lopez-Escobar, L. (1994). El Deposito de Pomez Pliniana del Grupo Volcanico Mocho-Choshuenco, Andes del Sur (40°S), Chile. Congreso Geologico Chileno 1:269-272.

Elliott, T., Plank, T., Zindler, A., White, W., and Bourdon, B. (1997). Element transport from slab to volcanic front at the Mariana arc. *Journal of Geophysical Research: Solid Earth*, 102(B7), 14991-15019 doi: 10.1029/97JB00788

Elliott, T. (2003). Tracers of the slab. Inside the subduction factory, 23-45. doi:10.1029/138 GM03

Espinoza, F., Morata, D., Pelleter, E., Maury, R.C., Suárez, M., Lagabrielle, Y., Polvé, M., Bellon, H., Cotton, J., De la Cruz, R., Guivel, C., (2005). Petrogenesis of the Eocene and Mio-Pliocene alkaline basaltic magmatism in Meseta Chile Chico, southern Patagonia, Chile: evidence for the participation of two slab windows. *Lithos*, 82, 315-343. doi:10.1016/j.lithos.2004.09.024.

Fiege, A., Behrens, H., Holtz, F., and Adams, F. (2014). Kinetic vs. thermodynamic control of degassing of $H_2OS\pm Cl$-bearing andesitic melts. *Geochimica et Cosmochimica Acta*, 125, 241-264. doi:10.1016/j.gca.2013.10.012

Fierstein, J. (2007). Explosive eruptive record in the Katmai region, Alaska Peninsula: an overview. *Bulletin of volcanology*, 69(5), 469-509. doi: 10.1007/s00445-006-0097-y

Fierstein, J., and Nathenson, M. (1992). Another look at the calculation of fallout tephra volumes. *Bulletin of Volcanology*, 54(2), 156-167. doi: 10.1007/BF00278005

Fierstein, J., Sruoga, P., Amigo, A., Elissondo., M., and Rosas, M. (2013). Tephra in Argentina establishes postglacial eruptive history of Laguna del Maule volcanic field in Chile: IAVCEI 2013 Scientific Assembly (abstract 3A2_3FO11, 23 July)

Fontijn, K., Lachowycz, S. M., Rawson, H., Pyle, D. M., Mather, T. A., Naranjo, J. A., and Moreno, H. (2014). Late Quaternary tephrostratigraphy of southern Chile and Argentina. *Quaternary Science Reviews*, 89, 70-84. doi: 10.1016/j.quascirev.2014.02.007

Fontijn, K., Rawson, H., Van Daele, M., Moernaut, J., Abarzua, A.M., Heirman, K., Bertrand, S., Pyle, D.M., Mather, T.A., De Batist, M., Naranjo, J.A., and Moreno, H. (submitted). Synchronisation of sedimentary records using tephra: A postglacial tephrochronological model for the Chilean Lake District. *Quaternary Science Reviews*.

Froggatt, P. C., and Rogers, G. M. (1990). Tephrostratigraphy of high-altitude peat bogs along the axial ranges, North Island, New Zealand. New Zealand journal of geology and geophysics, 33(1), 111-124. doi: 10.1080/00288306.1990.10427577

Geirsdóttir, Á., Hardardóttir, J., and Sveinbjörnsdóttir, Á.E., (2000). Glacial extent and catastrophic meltwater events during the deglaciation of Southern Iceland, *Quaternary Science Reviews*, 19, 1749-1761, doi:10.1016/S0277-3791(00)00092-5

Gertisser, R., and Keller, J. (2003). Temporal variations in magma composition at Merapi Volcano (Central Java, Indonesia): magmatic cycles during the past 2000 years of explosive activity. *Journal of Volcanology and Geothermal Research*, 123(1), 1-23. doi:10.1016/S0377-0273(03)00025-8

Geyer, A., and Bindeman, I., (2011), Glacial influence on caldera-forming eruptions, *Journal of Volcanology and Geothermal Research*, 202, 127-142, doi:10.1016/j.jvolgeores.2011.02.001

Ghiorso, M. S., and Evans, B. W. (2008). Thermodynamics of rhombohedral oxide solid solutions and a revision of the Fe–Ti two-oxide geothermometer and oxygen-barometer, *American Journal of Science*, 308(9), 957-1039. doi: 10.2475/09.2008.01

Gilbert, D., Freundt, A., Kutterolf, S., Burkert, C., (2014). Post-glacial time series of explosive eruptions and associated changes in the magma plumbing systems of Lonquimay volcano, south central Chile, *International Journal of Earth Sciences*, doi:10.1007/s00531-012-0796-x.

Glasser, N. F., Jansson, K. N., Harrison, S., and Kleman, J. (2008). The glacial geomorphology and Pleistocene history of South America between 38°S and 56°S, *Quaternary Science Reviews*, 27(3), 365-390. doi: 10.1016/j.quascirev.2007.11.011

González-Ferrán, O., (1995), Volcanes de Chile: Instituto Geogrfico Militar.

Gorring, M.L., Kay, S.M., Zeitler, P.K., Ramos, V.A., Rubiolo, D., Fernandez, M.I., and Panza, J.L., (1997). Neogene Patagonian plateau lavas: continental magmas associated with ridge collision at the Chile Triple Junction, *Tectonics*, 16, 1-17. doi:10.1029/96TC03368.

Grove, T.L., Till, C.B., and Krawczynski, M.J., (2012), The role of H_2O in subduction zone magmatism, *Annual Review of Earth and Planetary Sciences*, 40, 413-439, doi:10.1146/annurev-earth-042711-105310

Grove, T. L., Chatterjee, N., Parman, S. W., and Médard, E. (2006). The influence of H_2O on mantle wedge melting, *Earth and Planetary Science Letters*, 249(1), 74-89. doi:10.1016/j.epsl.2006.06.043

Gutiérrez, F., Gioncada, A., Ferran, O.G., Lahsen, A., and Mazzuoli, R. (2005). The Hudson Volcano and surrounding monogenetic centres (Chilean Patagonia): an example of volcanism associated with ridge–trench collision environment, *Journal of Volcanology and Geothermal Research*, 145(3), 207-233 doi: 10.1016/j.jvolgeores.2005.01.014

Hall, B.L., Porter, C.T., Denton, G.H., Lowell, T.V., and Bromley, G.R.M., (2013). Extensive recession of Cordillera Darwin glaciers in southernmost South America during Heinrich Stadial 1, *Quaternary Science Reviews*, 62, 49-55. doi:10.1016/j. quascirev.2012.11.026.

Hauri, E.H., Wagner, T.P., and Grove, T.L. (1994). Experimental and natural partitioning of Th, U, Pb and other trace elements between garnet, clinopyroxene and basaltic melts, *Chemical Geology*, 117(1), 149-166 doi: 10.1016/0009-2541(94)90126-0

Hawkesworth, C., George, R., Turner, S., and Zellmer, G., (2004). Time scales of magmatic

processes, *Earth and Planetary Science Letters*, 218, 1-16, doi:10.1016/S0012-821X(03)00634-4

Hermann, J., and Spandler, C.J. (2008). Sediment melts at sub-arc depths: an experimental study, *Journal of Petrology*, 49(4), 717-740, doi: 10.1093/petrology/egm073

Hickey, R. L., Frey, F. A., Gerlach, D. C., and LópezEscobar, L. (1986). Multiple sources for basaltic arc rocks from the southern volcanic zone of the Andes (34–41°S): trace element and isotopic evidence for contributions from subducted oceanic crust, mantle, and continental crust, *Journal of Geophysical Research: Solid Earth*, 91(B6), 5963-5983. doi:10.1029/JB091iB06p05963

Hickey-Vargas, R., Moreno Roa, H., López-Escobar, L., Frey, F.A., (1989). Geochemical variations in Andean basaltic and silicic lavas from the Villarrica-Lanin volcanic chain (39.5°S): an evaluation of source heterogeneity, fractional crystallization and crustal assimilation. *Contributions to Mineralogy Petrology*, 103, 361-386. doi:10.1007/BF00402922.

Hildreth, W., (2007), Quaternary magmatism in the Cascades-geologic perspectives (No. 1744): Geological Survey (US).

Hildreth, W., and Moorbath, S., (1988). Crustal contributions to arc magmatism in the Andes of Central Chile, *Contributions to Mineralogy Petrology*, 98, 455-489. doi:10.1007/BF00372365.

Hildreth, W., and Drake, R. E. (1992) Volcán Quizapu, Chilean Andes. *Bulletin of Volcanology*, 54 (2), 93125. doi: 10.1007/BF00278002

Hildreth, W., Godoy, E., Fierstein, J., and Singer, B., (2010). Laguna del Maule Volcanic Field: Eruptive History of a Quaternary Basalt-to-rhyolite Distributed Volcanic Field on the Andean Range Crest in Central Chile. In: Servicio Nacional de Geología y Minería Boletin 63, SERNAGEOMIN, Chile, 143.

Hirschmann, M. M., and Stolper, E. M. (1996). A possible role for garnet pyroxenite in the origin of the "garnet signature" in MORB. *Contributions to Mineralogy and Petrology*, 124(2), 185-208, doi: 10.1007/s004100050184

Hogg, A.G., Hua, Q., Blackwell, P.G., Niu, M., Buck, C.E., Guilderson, T.P., Heaton, T.J., Palmer, J.G., Reimer, P.J., Reimer, R.W., Turney, C.S.M., and Zimmerman, S.R. (2013). SHCal13 Southern Hemisphere calibration, 0–50,000 cal yr BP. *Radiocarbon*, 55(4), 1889-1903. doi: 10.2458/azu_js_rc.55.16783

Hulton, N. R., Purves, R. S., McCulloch, R. D., Sugden, D. E., and Bentley, M. J. (2002). The last glacial maximum and deglaciation in southern South America, *Quaternary Science Reviews*, 21(1), 233-241, doi: 10.1016/S0277-3791(01)00103-2

Humphreys, M.C.S., Brooker, R.A., Fraser, D.G., Burgisser, A., Mangan, M.T., and McCam-

mon, C. (2015). Coupled Interactions between Volatile Activity and Fe Oxidation State during Arc Crustal Processes. *Journal of Petrology*, 56(4), 795-814.doi: 10.1093/petrology/egv017

Huybers, P., Langmuir, C., (2009). Feedback between deglaciation, volcanism, and atmospheric CO_2., *Earth Planetary Science Letters*, 286, 479-491, doi:10. 1016/j.epsl.2009.07.014.

Ionov, D.A., Griffin, W.L., and O'Reilly, S.Y. (1997). Volatile-bearing minerals and lithophile trace elements in the upper mantle. *Chemical Geology*, 141(3), 153-184 doi: 10.1016/S0009-2541(97)00061-2

Jacques, G., Hoernle, K., Gill, J., Hauff, F., Wehrmann, H., Garbe-Schnberg, D., van den Bogaard, P., Bindeman, I., and Lara, L.E., (2013). Across-arc geochemical variations in the Southern Volcanic Zone, Chile (34.5-38.0°S): constraints on mantle wedge and slab input compositions, *Geochimica et Cosmochimica Acta* 123, 218-243, doi:10.1016/j.gca.2013.05.016.

Jarosewich, E., Nelen, J. A., and Norberg, J. A. (1980). Reference Samples for Electron Microprobe Analysis. *Geostandards Newsletter*, 4(1), 43-47. doi:10.1111/j.1751-908X.1980.tb00273.x

Jellinek, A.M., Manga, M., and Saar, M.O., (2004), Did melting glaciers cause volcanic eruptions in eastern California? Probing the mechanics of dike formation, *Journal of Geophysical Research: Solid Earth*, 109, doi:10.1029/2004JB002978

Jicha, B.R., Singer, B.S., Brophy, J.G., Fournelle, J.H., Johnson, C.M., Beard, B.L., Lapen, T.J., and Mahlen, N. J. (2004). Variable impact of the subducted slab on Aleutian island arc magma sources: evidence from Sr, Nd, Pb, and Hf isotopes and trace element abundances. *Journal of Petrology*, 45(9), 1845-1875. doi:10.1093/petrology/egh036

Jochum, K. P., Stoll, B., Herwig, K., Willbold, M., Hofmann, A. W., Amini, M., Aarburg, S., Abouchami, W., Hellebrand, E., Mocek, B., Raczek, I., Stracke, A., Alard, O., Bouman, C., Becker, S., Dücking, M., Brätz, H., Klemd, R., de Bruin, D., Canil, D., Cornell, D., de Hoog, C., Dalpé, C., Danyushevsky, L., Eisenhauer, A., Gao, Y., Snow, J. E., Groschopf, N., Günther, D., Latkoczy, C., Guillong, M., Hauri, E., Höfer, H. E., Lahaye, Y., Horz, K., Jacob, D. E., Kasemann, S. A., Kent, A. J. R., Ludwig, T., Zack, T., Mason, P. R. D., Meixner, A., Rosner, M., Misawa, K., Nash, B. P., Pfänder, J., Premo, W. R., Sun, W. D., Tiepolo, M., Vannucci, R., Vennemann, T., Wayne, D., Woodhead, J. D., (2006). MPIDING reference glasses for in situ microanalysis: New reference values for element concentrations and isotope ratios. *Geochemistry, Geophysics, Geosystems*, 7(Q02008). doi: 10.1029/2005GC001060

Jull, M., and McKenzie, D., (1996), The effect of deglaciation on mantle melting beneath Iceland: *Journal of Geophysical Research: Solid Earth*, 101, 21815-21828, doi:10.1029/96JB01308

Juvigné, E., Bertrand, S., Heuschen, B. and Tallier, E. (2008). Téphrostratigraphie de sediments lacustres situés en context géodynamique actif: exemple des sediments du lac Icalma, (Chili, zone volcanique sud, 38°S). *Quaternaire*, 19, 175-189. doi: 10.4000/quaternaire.3532

Kaplan, M.R., Fogwill, C.J., Sugden, D.E., Hulton, N.R.J., Kubik, P.W., and Freeman, S.P.H.T. (2008). Southern Patagonian glacial chronology for the Last Glacial period and implications for Southern Ocean climate, *Quaternary Science Reviews*, 27(3), 284-294. doi: 10.1016/j.quascirev.2007.09.013

Katz, R. F., Spiegelman, M., and Carbotte, S. M. (2004). Ridge migration, asthenospheric flow and the origin of magmatic segmentation in the global midocean ridge system. *Geophysical research letters*, 31(15). doi:10.1029/2004GL020388

Kay, R.W., Kay, S.M. and Arculus, R.J., (1992), Magma genesis and crustal processing, in: *Continental Lower Crust* (Fountain, D.M., Arculus, R. and Kay, R.W. (eds)), Amsterdam: Elsevier, 423-445

Kay, S.M., Mpodozis, C., (2002). Magmatism as a probe to the Neogene shallowing of the Nazca plate beneath the modern Chilean flat-slab. *Journal of South American Earth Scences*, 15, 39-57. doi:10.1016/S0895-9811(02)00005-6.

Kay, S.M., Godoy, E., Kurtz, A., (2005). Episodic arc migration, crustal thickening, subduction erosion, and magmatism in the south-central Andes, *Geological Society of America Bulletin*, 117, 67-88. doi:10.1130/B25431.1.

Karlstrom, L., Wright, H. M., and Bacon, C. R. (2015). The effect of pressurized magma chamber growth on melt migration and pre-caldera vent locations through time at Mount Mazama, Crater Lake, Oregon, *Earth and Planetary Science Letters*, 412, 209-219 doi: 10.1016/j.epsl.2014.12.001

Kelemen, P.B., Shimizu, N., and Salters, V.J. (1995). Extraction of mid-ocean-ridge basalt from the upwelling mantle by focused flow of melt in dunite channels, *Nature*, 375(6534), 747-753 doi: 10.1038/375747a0

Kelemen, P.B., Hirth, G., Shimizu, N., Spiegelman, M., and Dick, H.J. (1997). A review of melt migration processes in the adiabatically upwelling mantle beneath oceanic spreading ridges. *Philosophical Transactions of the Royal Society of London A: Mathematical, Physical and Engineering Sciences*, 355(1723), 283-318 doi: 10.1098/rsta.1997.0010

Kelemen, P.B., Braun, M., and Hirth, G. (2000). Spatial distribution of melt conduits in the mantle beneath oceanic spreading ridges: Observations from the Ingalls and Oman ophiolites,

Geochemistry, Geophysics, Geosystems, 1(7) doi: 10.1029/1999GC000012

Keller, T., May, D. A., and Kaus, B. J. (2013). Numerical modelling of magma dynamics coupled to tectonic deformation of lithosphere and crust. *Geophysical Journal International*, 195(3), 1406-1442. doi: 10.1093/gji/ggt306

Kilian, R., Lamy, F., 2012. A review of Glacial and Holocene paleoclimate records from southernmost Patagonia (49-55°S). *Quaternary Science Reviews*, 53, 1-23. doi:10.1016/j.quascirev. 2012.07.017.

Kiyosugi, K., Connor, C., Sparks, R. S. J., Crosweller, H. S., Brown, S. K., Siebert, L., Wang, T., and Takarada, S. (2015). How many explosive eruptions are missing from the geologic record? Analysis of the quaternary record of large magnitude explosive eruptions in Japan. *Journal of Applied Volcanology*, 4(1), 1-15. doi:10.1186/s13617-015-0035-9

Koppes, M., Hallet, B., Rignot, E., Mouginot, J., Wellner, J. S., and Boldt, K. (2015). Observed latitudinal variations in erosion as a function of glacier dynamics. *Nature*, 526(7571), 100-103. doi: 10.1038/nature15385

Kutterolf, S., Jegen, M., Mitrovica, J.X., Kwasnitschka, T., Freundt, A., and Huybers, P.J., (2013). A detection of Milankovitch frequencies in global volcanic activity, *Geology*, 41, 227-230, doi:10.1130/G33419.1

Lamy F, Kilian R, Arz HW, Francois J-P, Kaiser J, Prange M, Steinke T (2010). Holocene changes in the position and intensity of the southern westerly wind belt. *Nature Geoscience*, 3(10), 695- 699

Lara, L., (2004). Overview of Villarrica Volcano, *Servicio Nacional de Geología y Minería Boletín*, 61, 5-12

Lara, L.E., Lavenu, A., Cembrano, J., Rodríguez, C., (2006a). Structural controls of volcanism in transversal chains: resheared faults and neotectonics in the Cordón Caulle-Puyehue area (40.5°S), Southern Andes, *Journal of Volcanology and Geothermal Research*, 158, 70-86. doi:10.1016/j.jvolgeores.2006.04.017.

Lara, L.E., Moreno, H., Naranjo, J.A., Matthews, S., and de Arce, C.P, (2006b), Magmatic evolution of the Puyehue–Cordón Caulle Volcanic Complex (40°S), Southern Andean Volcanic Zone: from shield to unusual rhyolitic fissure volcanism, *Journal of Volcanology and Geothermal Research*, 157, 343-366, doi: 10.1016/j.jvolgeores.2006.04.010

Lara, L.E., Cembrano, J., and Lavenu, A. (2008). Quaternary vertical displacement along the Liquiñe-Ofqui fault Zone: differential uplift and coeval volcanism in the Southern Andes?.

International Geology Review, 50(11), 975-993. doi: 10.2747/0020-6814.50.11.975

Lee, C.T.A., and Bachmann, O. (2014). How important is the role of crystal fractionation in making intermediate magmas? Insights from Zr and P systematics. *Earth and Planetary Science Letters*, 393, 266-274 doi: 10.1016/j.epsl.2014.02.044

Liang, Y., Schiemenz, A., Hesse, M.A., Parmentier, E.M., and Hesthaven, J.S. (2010). High-porosity channels for melt migration in the mantle: Top is the dunite and bottom is the harzburgite and lherzolite. *Geophysical Research Letters*, 37(15) doi: 10.1029/2010GL044162

Lohmar, S., Robin, C., Gourgaud, A., Clavero, J., Parada, M. ., Moreno, H., Ersoy, O., López-Escobar, L., and Naranjo, J. A., (2007). Evidencias de interacción magma-agua durante el ciclo eruptivo explosivo de la Ignimbrita Licán (13.800 años AP), volcán Villarrica (sur de Chile), *Revista geológica de Chile*, 34, 233-247, doi: 10.4067/S0716-02082007000200004

Lohmar, S., Parada, M., Gutiérrez, F., Robin, C., and Gerbe, M.C., (2012). Mineralogical and numerical approaches to establish the pre-eruptive conditions of the mafic Licán Ignimbrite, Villarrica Volcano (Chilean Southern Andes), *Journal of Volcanology and Geothermal Research*, 235, 55-69, doi:10.1016/j.jvolgeores.2012.05.006

López-Escobar, L. L., and Moreno, H. (1981). Eruption in 1979 of the Mirador volcano, Southern Andes; geochemical characteristics of the lavas and granitic inclusions. *Revisata Geología de Chile*, 13, 17-33.

López-Escobar, L., Kilian, R., Kempton, P. D., and Tagiri, M. (1993). Petrography and geochemistry of Quaternary rocks from the Southern Volcanic Zone of the Andes between 41°30' and 46°00'S, Chile. *Andean Geology*, 20(1), 33-55 doi: 10.5027/andgeoV20n1-a04

López-Escobar, L., Cembrano, J., and Moreno, H., (1995). Geochemistry and tectonics of the Chilean Southern Andes basaltic Quaternary volcanism (37-46°S). *Revista Geología de Chile*, 22, 219-234. doi:10.5027/andgeoV22n2-a06.

Loughlin, S., Sparks, R.S.J, Brown, S.K., Jenkins, S.F., Vye-Brown, C. (Eds.) (2015). Global Volcanic Hazards and Risk. Cambridge University Press.

Lowe, D.J. (1988). Stratigraphy, age, composition, and correlation of late Quaternary tephras interbedded with organic sediments in Waikato lakes, North Island, New Zealand. *New Zealand journal of geology and geophysics*, 31(2), 125-165, doi: 10.1080/00288306.1988.10417765

Lowe, D. J. (2011). Tephrochronology and its application: a review. *Quaternary Geochronology*, 6(2), 107-153. doi: 10.1016/j.quageo.2010.08.003

Lowrie, A., and Hey, R., (1981). Geological and geophysical variations along the western

margin of Chile near lat. 33 to 36°S and their relation to Nazca plate subduction. *Geological Society America Memoirs* 154, 741-754. doi:10.1130/ MEM154-p741.

Lucassen, F., Wiedicke, M., and Franz, G. (2010). Complete recycling of a magmatic arc: evidence from chemical and isotopic composition of Quaternary trench sediments in Chile (36-40°S). *International Journal of Earth Sciences*, 99(3), 687-701. doi:10.1007/s00531-008-0410-4

Maclennan, J., Jull, M., McKenzie, D., Slater, L., and Grönvold, K., (2002). The link between volcanism and deglaciation in Iceland, *Geochemistry, Geophysics, Geosystems*, 3, 1-25, doi:10.1029/2001GC000282

Marcaida, M., Mangan, M. T., Vazquez, J. A., Bursik, M., and Lidzbarski, M. I. (2014). Geochemical fingerprinting of Wilson Creek formation tephra layers (Mono Basin, California) using titanomagnetite compositions. *Journal of Volcanology and Geothermal Research*, 273, 1-14. doi: 10.1016/j.jvolgeores.2013.12.008

McCulloch, M.T., and Gamble, J.A. (1991). Geochemical and geodynamical constraints on subduction zone magmatism. *Earth and Planetary Science Letters*, 102(3), 358-374 doi: 10.1016/0012-821X(91)90029-H

McGuire, W.J., Howarth, R.J., Firth, C.R., Solow, A.R., Pullen, A.D., Saunders, S.J., Steward, I.S., and Vita-Finzi, C., (1997). Correlation between rate of sea-level change and frequency of explosive volcanism in the Mediterranean, *Nature*, 389, 473-476, doi:10.1038/38998

McKenzie, D. (1985). The extraction of magma from the crust and mantle. *Earth and Planetary Science Letters*, 74(1), 81-91. doi:10.1016/0012-821X(85)90168-2

McMillan, N.J., Harmon, R.S., Moorbath, S., López-Escobar, L., and Strong, D.F., (1989). Crustal sources involved in continental arc magmatism: a case study of volcan Mocho-Choshuenco, southern Chile. *Geology*, 17, 1152-1156.

Kelley, K.A., and Cottrell, E. (2009). Water and the oxidation state of subduction zone magmas. *Science*, 325(5940), 605-607. doi:10.1126/science.1174156

Manea, V.C., Leeman, W.P., Gerya, T., Manea, M., and Zhu, G. (2014). Subduction of fracture zones controls mantle melting and geochemical signature above slabs. *Nature communications*, 5. doi:10.1038/ncomms6095

Moernaut J, De Batist M, Charlet F, Heirman K, Chapron E, Pino M, Brümmer R, and Urrutia R (2007) Giant earthquakes in South-Central Chile revealed by Holocene mass-wasting events in Lake Puyehue. *Sedimentary Geology*, 195, 239-256

Moernaut, J., Daele, M. V., Heirman, K., Fontijn, K., Strasser, M., Pino, M., Urrutia, R.,

and De Batist, M. (2014). Lacustrine turbidites as a tool for quantitative earthquake reconstruction: New evidence for a variable rupture mode in south central Chile. *Journal of Geophysical Research: Solid Earth*, 119(3), 1607-1633. doi: 10.1002/2013JB010738

Moreno, H., and Lara, L. (2007). Geologia del Complejo Volcánico Mocho-Choshuenco. *Carta Geológica de Chile, Serie Geología Básica*, No. 107, 1-27.

Moreno, H. and Clavero, J., (2006). Geología del área del volcán Villarrica, Regiones de la Araucanía y de los Lagos. *Servicio Nacional de Geología y Minería, Carta Geológica de Chile, Serie Geología Básica*, 1- 21

Moreno, H., and Naranjo, J.A. (2006) Peligros del Complejo Volcánico Mocho-Choshuenco, Región de los Lagos, escala 1:50.000. *Servicio Nacional de Geologoía y Minería, Carta Geológica de Chile*, Serie Geología Ambiental N°9.

Moreno, P.I., Villa-Martínez, R., Cárdenas, M.L., and Sagredo, E.A., (2012). Deglacial changes of the southern margin of the southern westerly winds revealed by terrestrial records from SW Patagonia (52°S). *Quaternary Science Reviews*, 41, 1-21. doi:10.1016/j.quascirev.2012.02.002.

Morgan, J. P., and Forsyth, D. W. (1988). Threedimensional flow and temperature perturbations due to a transform offset: Effects on oceanic crustal and upper mantle structure. *Journal of Geophysical Research: Solid Earth*, 93(B4), 2955-2966.

Nakada, M., and Yokose, H., (1992). Ice age as a trigger of active Quaternary volcanism and tectonism, *Tectonophysics*, 212, 321-329, doi:10.1016/0040-1951(92)90298-K

Nandedkar, R.H., Ulmer, P., and Müntener, O. (2014). Fractional crystallization of primitive, hydrous arc magmas: an experimental study at 0.7 GPa. *Contributions to Mineralogy and Petrology*, 167(6), 1-27. doi: 10.1007/s00410-014-1015-5

Naranjo, J.A., Moreno, H., and Banks, N.G., (1993). La erupción del Volcán Hudson 1991 (46°S), Región de Aisén, Chile. In: *Servicio Nacional Geoloía Minería Boletin*, vol. 44. SERNAGEOMIN, Santiago.

Naranjo, J. A., and Stern, C. R. (1998). Holocene explosive activity of Hudson Volcano, southern Andes. *Bulletin of Volcanology*, 59(4), 291-306. doi: 10.1007/s004450050193

Naranjo, J.A., Polanco, E., Lara, L., Moreno, H., and Stern, C.R. (2001). Holocene tephrafall deposits of Southern and Austral Andes Volcanic Zones (33-54∘S): Eruption recurrence. *Comunicaciones* No. 52, 109 (abstract).

Naranjo, J.A. and Stern, C.R. (2004.) Holocene tephrochronology of the southernmost part

(42°30'-45°S) of the Andean Southern Volcanic Zone. *Revista Geológica de Chile*, 31(2), 225-240.

Newhall, C.G., and Self, S. (1982). The Volcanic Explosivity Index (VEI) an estimate of explosive magnitude for historical volcanism. *Journal of Geophysical Research*, 87(C2), 1231-1238. doi: 10.1029/JC087iC02p01231

Niida, K., and Green, D.H. (1999). Stability and chemical composition of pargasitic amphibole in MORB pyrolite under upper mantle conditions. *Contributions to Mineralogy and Petrology*, 135(1), 18-40 doi: 10.1007/s004100050495

Nimis, P. (1999). Clinopyroxene geobarometry of magmatic rocks. Part 2. Structural geobarometers for basic to acid, tholeiitic and mildly alkaline magmatic systems. *Contributions to Mineralogy and Petrology*, 135(1), 62-74.doi:10.1007/s004100050498

Nowell, D.A., Jones, M.C., and Pyle, D.M., (2006), Episodic Quaternary volcanism in France and Germany, *Journal of Quaternary Science*, 21, 645-675, doi:10.1002/jqs.1005

Ortoleva, P., Chadman, J., Merino, E., and Sen, A. (1987), Geochemical self-organization II: The reactive-infiltration instability, *American Journal of Science*, 287, 1008-1040

Pérez, S. (2005). Volcanismo Explosivo Postglacial del Complejo Volcánico Mocho-Choshuenco. Master Thesis, Universidad de Concepción, Facultad de Ciencias Quimicas, Chile

Parejas, C.S., Druitt, T.H., Robin, C., Moreno, H., and Naranjo, J.A., (2010). The Holocene Pucón eruption of Volcán Villarrica, Chile: deposit architecture and eruption chronology, *Bulletin of Volcanology*, 72, 677-692 doi: 10.1007/s00445-010-0348-9

Peacock, S.M., Rushmer, T., and Thompson, A.B. (1994). Partial melting of subducting oceanic crust. *Earth and Planetary Science Letters*, 121(1), 227-244. doi:10.1016/0012-821X(94)90042-6

Perfit, M.R. and Davidson, J.P. (2000). Plate tectonics and volcanism. in: *Encyclopedia of Volcanoes* (Sigurdsson H., et al., (eds)), 89-113. Academic Press, San. Diego.

Petit-Breuilh S., (2004), La Historía Eruptiva de los Volcanes Hisponamericanos (Siglos XVI Al XX) Casa de los Volcanes 8, Huelva

Pilet, S., Baker, M. B., and Stolper, E.M. (2008). Metasomatized lithosphere and the origin of alkaline lavas.*Science*, 320(5878), 916-919 doi: 10.1126/science.1156563

Plank, T. (2005). Constraints from thorium/lanthanum on sediment recycling at subduction zones and the evolution of the continents. *Journal of Petrology*, 46(5), 921-944. doi: 10.1093/petrology/egi005

Plank, T., and Langmuir, C.H. (1988). An evaluation of the global variations in the ma-

jor element chemistry of arc basalts.*Earth and Planetary Science Letters*, 90(4), 349-370 doi: 10.1016/0012-821X(88)90135-5

Plank, T., and Langmuir, C.H. (1993). Tracing trace elements from sediment input to volcanic output at subduction zones. *Nature*, 362(6422), 739-743.

Plank, T., and Langmuir, C.H. (1998). The chemical composition of subducting sediment and its consequences for the crust and mantle. *Chemical geology*, 145(3), 325-394. doi:10.1016/S0009-2541(97)00150-2

Porter, S.C., (1981), Pleistocene glaciation in the southern Lake District of Chile, *Quaternary Research*, 16, 263-292, doi:10.1016/0033-5894(81)90013-2

Prieto, A., Stern, C.R., and Estévez, J.E., (2013). The peopling of the Fuego-Patagonian fjords by littoral hunter-gatherers after the mid-Holocene H1 eruption of Hudson Volcano. *Quaternary International*, 317, 3-13. doi:10.1016/j.quaint.2013.06.024.

Pyle, D. M. (1989). The thickness, volume and grainsize of tephra fall deposits. *Bulletin of Volcanology*, 51(1), 1-15. doi: 10.1007/BF01086757

Pyle, D. M. (2000). Sizes of volcanic eruptions. in: *Encyclopedia of Volcanoes* (Sigurdsson H., et al., (Eds.)), Academic Press, San Diego, 1, 263-269.

Pyle, D. M. (1995). Assessment of the minimum volume of tephra fall deposits. *Journal of Volcanology and Geothermal Research*, 69(3), 379-382. doi: 10.1016/0377-0273(95)00038-0

Ramos, V.A., and Kay, S.M. (1992). Southern Patagonian plateau basalts and deformation: backarc testimony of ridge collisions. *Tectonophysics*, 205(1), 261-282.

Rapp, R.P., and Watson, E.B. (1995). Dehydration melting of metabasalt at 8–32 kbar: implications for continental growth and crust-mantle recycling. *Journal of Petrology*, 36(4), 891-931 doi: 10.1093/petrology/36.4.891

Rawson H, Naranjo J-A, Smith V.C., Fontijn K, Pyle D.M., Mather T.A., Moreno H (2015). The frequency and magnitude of post-glacial explosive eruptions at Volcn Mocho-Choshuenco, southern Chile. *Journal of Volcanology and Geothermal Research*, 299: 103-129. doi:10.1016/j.jvolgeores.2015.04.003

Rawson H., Pyle D.M., Mather T.A., Smith V.C., Fontijn K., Lachowycz S., Naranjo J.A. (in review). The magmatic and eruptive response of arc volcanoes to deglaciation: temporal variability driven by changing crustal stresses. *Geology*.

Reiners, P.W. (1998). Reactive melt transport in the mantle and geochemical signatures of mantle-derived magmas. *Journal of Petrology*, 39(5), 1039-1061 doi: 10.1093/petroj/39.5.1039

Reubi, O., Bourdon, B., Dungan, M.A., Koornneef, J.M., Selles, D., Langmuir, C.H., and Aciego, S. (2011). Assimilation of the plutonic roots of the Andean arc controls variations in U-series disequilibria at Volcán Llaima, Chile. *Earth and Planetary Science Letters*, 303(1), 37-47 doi: 10.1016/j.epsl.2010.12.018

Ripepe, M., Marchetti, E., Ulivieri, G., Harris, A., Dehn, J., Burton, M., Caltabiano, T., and Salerno, G. (2005). Effusive to explosive transition during the 2003 eruption of Stromboli volcano. *Geology*, 33(5), 341-344. doi: 10.1130/G21173.1

Rivera, A., and Bown, F., (2013). Recent glacier variations on active ice capped volcanoes in the Southern Volcanic Zone (37-46°S), Chilean Andes. *Journal of South American Earth Sciences*, 45, 345-356. doi:10.1016/j.jsames.2013.02.004.

Rubin, A.M., (1995), Propagation of magma-filled cracks, *Annual Review of Earth and Planetary Sciences*, 23, 287-336, doi:10.1146/annurev.ea.23.050195.001443

Salters, V. J., Longhi, J. E., and Bizimis, M. (2002). Near mantle solidus trace element partitioning at pressures up to 3.4 GPa. *Geochemistry, Geophysics, Geosystems*, 3(7), 1-23. doi:10.1029/2001GC000148

Sarna-Wojcicki, A. M., Shipley, S., Waitt Jr, R. B., Dzurisin, D., and Wood, S. H. (1981). Areal distribution, thickness, mass, volume, and grain size of air-fall ash from the six major eruptions of 1980. In: *The 1980 eruptions of Mount St Helens* (Lipman P.W., and Mullineaux D.R. (eds.)) , Washington. USGS Prof Paper 1250, 577600

Scasso, R. A., Corbella, H., and Tiberi, P. (1994). Sedimentological analysis of the tephra from the 12–15 August 1991 eruption of Hudson volcano. *Bulletin of Volcanology*, 56(2), 121-132. doi: 10.1007/BF00304107

Schindlbeck, J. C., Freundt, A., and Kutterolf, S. (2014). Major changes in the post-glacial evolution of magmatic compositions and pre-eruptive conditions of Llaima Volcano, Andean Southern Volcanic Zone, Chile. *Bulletin of Volcanology*, 76(6), 1-22 doi: 10.1007/s00445-014-0830-x

Schmidt, A., Fristad, K. and Elkins-Tanton, L. (eds, 2015). Volcanism and global environmental change. Cambridge University Press

Scott, K. M. (1988). Origins, behavior, and sedimentology of lahars and lahar-runout flows in the ToutleCowlitz River system. *U.S. Geological Survey Professional Papers*. 1447-A.

Sellés, D., Rodriguez, A., Dungan, M.A., Naranjo, J.A., and Gardeweg, M. (2004). Geochemistry of Nevado de Longaví Volcano (36.2°S): a compositionally atypical arc volcano in the South-

ern Volcanic Zone of the Andes. *Revista geológica de Chile*, 31(2), 293-315. doi:10.4067/S0716-02082004000200008

Sepulveda, M. E. P. (2004). La historía eruptiva de los volcanes hispanoamericanos (Siglos XV1 al XX): El model Chileno

Shane, P. (2000). Tephrochronology: a New Zealand case study. *Earth-Science Reviews*, 49(1), 223-259. doi: 10.1016/S0012-8252(99)00058-6

Shane, P. (1998). Correlation of rhyolitic pyroclastic eruptive units from the Taupo volcanic zone by Fe–Ti oxide compositional data. *Bulletin of Volcanology*, 60(3), 224-238. doi: 10.1007/s004450050229

Shane, P., Smith, V.C., and Nairn, I. (2003). Biotite composition as a tool for the identification of Quaternary tephra beds. *Quaternary Research*, 59(2), 262-270. doi: 10.1016/S0033-5894(03)00012-7

Siebert, L., and Simkin, T., (2014), Volcanoes of the world: an illustrated catalog of Holocene volcanoes and their eruptions, *Smithsonian Institution, Global Volcanism Program Digital Information Series*, GVP-3

Siebert, L., Simkin, T., and Kimberly, P., (2010). Volcanoes of the World, third ed. University of California Press, Berkeley.

Singer, B.S., Jicha, B.R., Leeman, W.P., Rogers, N.W., Thirlwall, M.F., Ryan, J., and Nicolaysen, K.E. (2007). Alongstrike trace element and isotopic variation in Aleutian Island arc basalt: Subduction melts sediments and dehydrates serpentine. *Journal of Geophysical Research: Solid Earth*, 112(B6). doi:10.1029/2006JB004897

Singer, B.S., Jicha, B.R., Harper, M.A., Naranjo, J.A., Lara, L.E., and Moreno-Roa, H., (2008). Eruptive history, geochronology, and magmatic evolution of the Puyehue-Cordón Caulle volcanic complex, Chile. *Geological Society American Bulletin*, 120, 599-618. doi:10.1130/b26276.1.

Smith, D.J. (2014). Clinopyroxene precursors to amphibole sponge in arc crust. *Nature communications*, 5 doi: 10.1038/ncomms5329

Smith, V.C., Shane, P., and Nairn, I.A. (2005). Trends in rhyolite geochemistry, mineralogy, and magma storage during the last 50 kyr at Okataina and Taupo volcanic centres, Taupo Volcanic Zone, New Zealand. *Journal of Volcanology and Geothermal Research*, 148(3), 372-406. doi:10.1016/j.jvolgeores.2005.05.005

Smith, V.C., Pearce, N.J., Matthews, N.E., Westgate, J.A., Petraglia, M.D., Haslam, M., Lane, C.S., Korisettar, R., and Pal, J.N. (2011a). Geochemical fingerprinting of the widespread

Toba tephra using biotite compositions. *Quaternary International*, 246(1), 97-104. doi: 10.1016/j.quaint.2011.05.012

Smith, V.C., Isaia, R., and Pearce, N.J.G. (2011b). Tephrostratigraphy and glass compositions of post-15 kyr Campi Flegrei eruptions: implications for eruption history and chronostratigraphic markers. *Quaternary Science Reviews*, 30(25-26), 36383660. doi:10.1016/j.quascirev.2011.07.012

Søager, N., Holm, P.M., and Llambías, E.J., (2013). Payenia volcanic province, southern Mendoza, Argentina: OIB mantle upwelling in a backarc environment. *Chemical Geology*, 349-350, 36-53. doi:10.1016/j.chemgeo.2013.04.007.

Spandler, C., and Pirard, C. (2013). Element recycling from subducting slabs to arc crust: a review. *Lithos*, 170, 208-223. doi:10.1016/j.lithos.2013.02.016

Sparks, R.S.J., Folkes, C.B., Humphreys, M.C., Barfod, D.N., Clavero, J., Sunagua, M.C., McNutt, S.R., and Pritchard, M.E. (2008). Uturuncu volcano, Bolivia: Volcanic unrest due to mid-crustal magma intrusion. *American Journal of Science*, 308(6), 727-769. doi: 10.2475/06.2008.01

Spiegelman, M., and Kelemen, P.B. (2003). Extreme chemical variability as a consequence of channelized melt transport. *Geochemistry, Geophysics, Geosystems*, 4(7) doi: 10.1029/2002GC000336

Sruoga, P., Llambías, E.J., Fauqué, L., Schonwandt, D., and Repol, D.G., (2005). Volcanological and geochemical evolution of the Diamante Caldera-Maipo volcano complex in the southern Andes of Argentina (34°10'S). *Journal of South American Earth Sciences* 19, 399-414. doi:10.1016/j.jsames.2005.06.003.

Stern, C.R., (1991a). Role of subduction erosion in the generation of Andean magmas. *Geology*. 19, 78-81. doi:10.1130/0091-7613(1991)019<0078: ROSEIT>2.3.CO;2.

Stern, C. R. (1991b). Mid-Holocene tephra on Tierra del Fuego (54°S) derived from the Hudson volcano (46°S): evidence for a large explosive eruption. *Andean Geology*, 18(2), 139-146. doi: 10.5027/andgeoV18n2-a04

Stern, C.R., (2004). Active Andean volcanism: its geologic and tectonic setting. *Revista Geología de Chile*, 31, 161-206. doi:10.4067/S0716-02082004000200001.

Stern, C.R., Futa, K., and Muehlenbachs, K., (1984a). Isotope and trace element data for orogenic andesites from the Austral Andes. In: *Andean Magmatism* (Harmon, R.S., and Barreiro, B.A. (Eds.)), Birkhäuser, Boston, 31-46. doi:10. 1007/978-1-4684-7335-3_4.

Stern, C.R., Amini, H., Charrier, R., Godoy, E., Herve, F., and Varela, J., (1984b). Petrochemistry and age of rhyolitic pyroclastic flows which occur along the drainage valleys of the Rio Maipo and Rio Cachapoal (Chile) and the Rio Yaucha and Rio Papagayos (Argentina). *Revista Geología de Chile* 23, 39-52. doi:10.5027/ andgeoV11n3-a03.

Stern, C.R., and Kilian, R. (1996). Role of the subducted slab, mantle wedge and continental crust in the generation of adakites from the Andean Austral Volcanic Zone. *Contributions to mineralogy and petrology*, 123(3), 263-281 doi: 10.1007/s004100050155

Stern, C.R., Moreno, H., López-Escobar, L., Clavero, J., Lara, L., Naranjo, J.A., Parada, M.A., Skewes, M.A., (2007). Chilean volcanoes. In: *Geology of Chile* (Moreno, T., and Gibbons, W. (Eds.)), The Geological Society, London, 147-178.

Syracuse, E. M., and Abers, G. A. (2006). Global compilation of variations in slab depth beneath arc volcanoes and implications. *Geochemistry, Geophysics, Geosystems*, 7(5). doi:10.1029/2005GC001045

Tormey, D.R., Frey, F.A., López-Escobar, L., (1995). Geochemistry of the active Azufre–Planchón–Peteroa Volcanic Complex, Chile (35°15'S): evidence for multiple sources and processes in a cordilleran arc magmatic system. *Journal of Petrology.* 36, 265- 298. doi:10.1093/petrology/36.2.265.

Turner, S., and Hawkesworth, C., (1997). Constraints on flux rates and mantle dynamics beneath island arcs from Tonga–Kermadec lava geochemistry, *Nature*, 389, 568-573 doi:10.1038/39257

Turner, S.J., and Langmuir, C.H. (2015). The global chemical systematics of arc front stratovolcanoes: Evaluating the role of crustal processes. *Earth and Planetary Science Letters*, 422, 182-193 doi: 10.1016/j.epsl.2015.03.056

Van Daele, M., Moernaut, J., Silversmit, G., Schmidt, S., Fontijn, K., Heirman, K., Vandoorne, W., De Clercq, M., van Acker, J., Wolff, C., Pino, M., Urrutia, R., Robert, S.J., Vincze, L., and De Batist, M. (2014).The 600 yr eruptive history of Villarrica Volcano (Chile) revealed by annually laminated lake sediments.*Geological Society of America Bulletin*, 126, 481-498. doi: 10.1130/B30798.1

Van Daele, M., Moernaut, J., Doom, L., Boes, E., Fontijn, K., Heirman, K., Vandoorne, W., Hebbeln, D., Pino, M., Urrutia, R., Brümmer, R., and De Batist, M. (2015). A comparison of the sedimentary records of the 1960 and 2010 great Chilean earthquakes in 17 lakes: Implications for quantitative lacustrine palaeoseismology. *Sedimentology*, doi: 10.1111/sed.12193

Vargas-Ramirez, L., Roche, E., Gerrienne, P., and Hooghiemstra, H. (2008). A pollen-based

record of late glacialHolocene climatic variability in the southern lake district, Chile. *Journal of Paleolimnology*, 39(2), 197-217. doi: 10.1007/s10933-007-9115-0

Venezky, D. Y., and Rutherford, M. J. (1999). Petrology and Fe–Ti oxide reequilibration of the 1991 Mount Unzen mixed magma. *Journal of Volcanology and Geothermal Research*, 89(1), 213-230. doi: 10.1016/S0377-0273(98)00133-4

Vidal Gormaz, F. (1869). Esploración del río Calle-Calle, provincia de Valdivia, *Anales de la Universidad de Chile*, tomo XXXII, 34-35

Villarosa, G., Outes, V., Hajduk, A., Montero, E.C., Sellés, D., Fernández, M., and Crivelli, E., (2006), Explosive volcanism during the Holocene in the Upper Limay River Basin: the effects of ashfalls on human societies, Northern Patagonia, Argentina. *Quaternary international*,158, 44-57, doi: 10.1016/j.quaint.2006.05.016

Völker, D., Kutterolf, S., and Wehrmann, H. (2011). Comparative mass balance of volcanic edifices at the southern volcanic zone of the Andes between 33°S and 46°S. *Journal of Volcanology and Geothermal Research*, 205(3), 114-129. doi:10.1016/j.jvolgeores.2011.03.011

Wallace, P.J., and Carmichael, I.S. (1999). Quaternary volcanism near the Valley of Mexico: implications for subduction zone magmatism and the effects of crustal thickness variations on primitive magma compositions. *Contributions to Mineralogy and Petrology*, 135(4), 291-314. doi:10.1007/s004100050513

Watson, E.B., and Green, T.H. (1981). Apatite/liquid partition coefficients for the rare earth elements and strontium. *Earth and Planetary Science Letters*, 56, 405-421. doi: 10.1016/0012-821X(81)90144-8

Watts, A.B. (2001). Isostasy and Flexure of the Lithosphere. Cambridge University Press. 38

Watt, S.F. (2010). Records of volcanism and controls on volcanic processes in southern Chile, DPhil Thesis, University of Oxford, UK

Watt, S.F., Pyle, D.M., Naranjo, J.A., Rosqvist, G., Mella, M., Mather, T.A., and Moreno, H. (2011). Holocene tephrochronology of the Hualaihue region (Andean southern volcanic zone, ∼42°S), southern Chile. *Quaternary International*, 246(1), 324-343. doi:10.1016/j.quaint.2011.05.029

Watt, S. F., Pyle, D. M., and Mather, T. A. (2013a). The volcanic response to deglaciation: Evidence from glaciated arcs and a reassessment of global eruption records. *Earth-Science Reviews*, 122, 77-102. doi: 10.1016/j.earscirev.2013.03.007

Watt, S.F., Pyle, D.M., Mather, T.A., Naranjo, J.A., (2013b). Arc magma compositions

controlled by linked thermal and chemical gradients above the subducting slab. *Geophysical. Research Letters* 40, 2550-2556. doi:10.1002/grl.50513.

Watt, S. F., Pyle, D. M., and Mather, T. A. (2013c). Evidence of mid-to late-Holocene explosive rhyolitic eruptions from Chaitén Volcano, Chile. *Andean Geology*, 40(2), 216-226. doi: 10.5027/andgeoV40n2-a02

Weller, D., Miranda, C.G., Moreno, P.I., Villa-Martínez, R., and Stern, C.R. (2014). The large late-glacial Ho eruption of the Hudson volcano, southern Chile. *Bulletin of Volcanology*, 76(6), 1-18. doi: 10.1007/s00445-014-0831-9

Wastegård, S., Veres, D., Kliem, P., Hahn, A., Ohlendorf, C., Zolitschka, B., and Team, T.P.S. (2013). Towards a late Quaternary tephrochronological framework for the southernmost part of South America–the Laguna Potrok Aike tephra record. *Quaternary Science Reviews*, 71, 81-90. doi: 10.1016/j.quascirev.2012.10.019

Witter, J.B., Kress, V.C., Delmelle, P., and Stix, J., (2004). Volatile degassing, petrology, and magma dynamics of the Villarrica Lava Lake, Southern Chile, *Journal of Volcanology and Geothermal Research*, 134, 303-337, doi: 10.1016/j.jvolgeores.2004.03.002

Workman, R.K., and Hart, S. R., (2005). Major and trace element composition of the depleted MORB mantle (DMM), *Earth and Planetary Science Letters*, 231, 53-72, doi:10.1016/j.epsl.2004.12.005

Yu, S.Y., Shen, J., and Colman, S.M., (2007). Modeling the radiocarbon reservoir effect in lacustrine systems. *Radiocarbon*, 49, 1241-1254. doi:10.2458/azu_ js_rc.v.3016.

Zellmer, G.F., Annen, C., Charlier, B.L.A., George, R.M.M., Turner, S.P., and Hawkesworth, C.J., (2005). Magma evolution and ascent at volcanic arcs: constraining petrogenetic processes through rates and chronologies, *Journal of Volcanology and Geothermal Research*, 140, 171-191, doi:10.1016/j.jvolgeores.2004.07.020

Appendix A

Appendix

Within the Appendix I present:

- Section A.1 GPS locations for the key field localities

- Section A.2 A sample of the raw glass and oxide analyses

- Section A.3 The raw and calibrated radiocarbon dates and OxCal script written to construct the age model

- Section A.4 The thickness and maximum clast size field measurements used to estimate the eruption parameters of the largest eruptions

- Section A.5 Further Fe–Ti oxide methodology and all the temperature and oxygen fugacity estimates

- Section A.6 Extended methodology for Chapter 3

- Section A.7 Further whole rock methodology and all the raw analyses

A.1 GPS for key field localities

In this section the GPS localities are given for the stratigraphic columns of key localities (Fig. 2.2) and field photos of deposits around Mocho-Choshuenco (Fig. 2.3 and 2.4).

Column	Locality	GPS (WGS84 datum)
A	130108-05, 150114-2	39°51'S 71°55'W
B	117-01	39°39'S 71°55'W
C	120114-13	40°00'S 72°00'W
D	130207-05	39°59'S 71°55'W
E	130114-01	39°57'S 71°52'W
F	130111-09, 14014-3	39°51'S 71°54'W
G	130108-01	39°52'S 71°53'W
H	120114-6	39°52'S 71°57'W
I	130108-08, 140114-5	39°53'S 71°55'W
J	115-03/4, 130107-03	39°58'S 71°54'W
K	115-01	39°52'S 71°55'W
L	090114-2	40°01'S 71°57'W
M	130117-01	39°55'S 71°53'W
N	080114-6	39°54'S 71°58'W
O	116-06, 130106-08	39°51'S 72°06'W
P	080114-8	39°56'S 72°00'W

Table A.1: GPS for columns in Fig. 2.2

Column	Locality	GPS (WGS84 datum)
A	115-01	39°52'S 71°55'W
B	117-01	39°39'S 71°55'W
C	302-02	39°51'S 71°57'W
D	030114-4	39°30'S 71°33'W
E	130114-01	39°57'S 71°52'W
F	130114-01	39°57'S 71°52'W
G	060406-7	39°58'S 71°55'W
H	120114-6	39°52'S 71°57'W
I	115-03	39°58'S 71°54'W
J	115-03	39°58'S 71°54'W
K	130114-01	39°57'S 71°52'W
L	130108-01	39°52'S 71°53'W
M	115-01	39°52'S 71°55'W
N	113-01	39°55'S 72°06'W
O	080114-2	40°01'S 71°57'W
P	080114-6	39°54'S 71°58'W
Q	130129-1	39°55'S 71°54'W
R	150114-4	39°57'S 71°54'W
S	130117-1	39°55'S 71°53'W
T	070114-8	39°55'S 71°59'W
U	080114-8	39°56'S 72°00'W

Table A.2: GPS for field photos in Fig. 2.3, 2.4

A.2 Raw glass and oxide data

Within Chapter 2 the major element compositions (average and standard deviation) of the matrix glass (anhydrous; Table 2.4) and Fe–Ti oxides (Table 2.5) from the Mocho-Choshuenco tephra deposits is presented. In this section I present a sample of the raw EMP data from the ca. 275 samples analysed: glass (Table A.3) and Fe–Ti oxides (Table A.4). The full dataset, including all the secondary standard data, is available in the supplementary material from Rawson et al. (2015; 10.1016/j.jvolgeores.2015.04.003) and (http://figshare.com/authors/Harriet_Rawson /663416); both are open access.

Sample	NaO	MgO	Al_2O_3	SiO_2	P_2O_5	Cl	K_2O	CaO	TiO_2	MnO	FeO*	Totals
MC1												
12F6_1	4.05	4.12	16.05	52.17	0.53	0.07	1.85	8.78	1.70	0.15	9.00	98.48
12F6_3	3.47	4.04	13.93	53.80	0.72	0.13	1.97	7.68	2.04	0.14	11.29	99.23
12F6_4	3.92	3.99	15.06	53.84	0.60	0.07	1.50	8.95	1.82	0.17	9.45	99.37
12F6_6	4.07	4.59	15.08	54.13	0.61	0.08	1.98	8.24	1.94	0.19	9.32	100.24
12F6_7	4.27	3.87	14.94	53.27	0.65	0.11	1.74	7.76	2.09	0.28	10.94	99.94
12F6_8	3.30	4.64	14.23	53.47	0.65	0.08	2.30	8.38	1.94	0.18	10.73	99.91
12F6_9	3.51	4.46	15.05	53.97	0.60	0.10	1.85	8.46	1.90	0.12	9.78	99.79
12F6_10	4.03	4.48	14.98	53.17	0.56	0.08	1.74	8.16	1.63	0.11	10.15	99.09
12F6_11	3.82	4.14	15.05	53.89	0.51	0.06	1.49	8.27	1.93	0.21	10.24	99.61
12F6_13	4.58	4.51	14.63	53.23	0.63	0.09	1.92	8.07	1.84	0.20	10.18	99.98
12F6_14	3.82	4.24	14.87	53.74	0.62	0.12	1.98	8.50	1.93	0.20	10.30	100.31
12F6_15	4.10	4.21	15.87	53.50	0.53	0.11	1.33	8.88	1.73	0.19	9.91	100.38
12F6_16	3.41	4.78	14.77	53.26	0.61	0.08	1.61	8.12	1.86	0.18	10.36	99.06
MC2												
2F1_1	5.45	0.43	14.74	72.26	0.11	0.22	2.58	1.59	0.43	0.07	2.98	100.86
2F1_2	5.72	0.22	15.16	70.52	0.07	0.21	2.44	1.74	0.32	0.13	2.18	98.71
⋮	⋮	⋮	⋮	⋮	⋮	⋮	⋮	⋮	⋮	⋮	⋮	⋮

Table A.3: Raw matrix glass EMP analyses (wt.%). There are ca. 2200 analyses so only a selection are included here.

Sample	SiO_2	TiO_2	Al_2O_3	FeO*	MnO	MgO	CaO	FeO (corrected)	Fe_2O_3 (corrected)	Total with FeO*	Total with Fe correction
MC1											
2F1_1	0.00	47.30	0.14	46.91	1.05	2.87	0.02	36.35	11.73	98.29	99.46
2F1_2	0.02	14.02	2.03	76.98	0.78	1.68	0.03	40.91	40.05	95.51	99.50
2F1_3	0.00	47.37	0.16	47.24	1.07	2.77	0.03	36.57	11.86	98.63	99.82
2F1_4	0.04	14.07	2.05	76.29	0.82	1.69	0.00	40.78	39.46	94.96	98.87
2F1_5	0.00	47.71	0.16	46.69	1.04	2.81	0.04	36.80	10.99	98.47	99.57
2F1_6	0.03	13.93	2.07	76.30	0.74	1.71	0.01	40.61	39.66	94.80	98.75
2F1_7	0.00	47.44	0.17	47.25	1.02	2.74	0.01	36.74	11.67	98.62	99.79
2F1_8	0.04	13.88	2.06	76.47	0.86	1.73	0.08	40.47	40.00	95.12	99.08
2F1_9	0.00	48.20	0.12	46.17	1.28	2.28	0.02	37.97	9.11	98.07	98.94
2F1_10	0.00	47.73	0.13	46.51	1.26	2.25	0.06	37.57	9.94	97.95	98.94
⋮	⋮	⋮	⋮	⋮	⋮	⋮	⋮	⋮	⋮	⋮	⋮

Table A.4: Raw Fe–Ti oxide EMP analyses (wt.%). There are ca. 2700 analyses so only a selection are included here.

A.3 Radiocarbon dates and OxCal model

Within this section further details on how the eruption ages were determined for the explosive units defined in Chapter 2 are presented. This includes: (1) a more detailed methodology of how the radiocarbon dates were determined, (2) details of the radiocarbon samples and their corresponding uncalibrated, calibrated and modelled ages (Table A.5), (3) OxCal script written to constrain the tempo of volcanism (Fig. A.1), (4) the outputted probability distributions for the radiocarbon dates and explosive units (Fig. A.2).

A.3.1 Methodology

The ages of the explosive eruptions from Mocho-Choshuenco have been constrained through a combination of ^{14}C dating and Bayesian age modelling (e.g., using OxCal; Bronk-Ramsey, 2009a). 48 samples have been ^{14}C-dated, of which 29 were previously published in the SERNAGEOMIN Mocho-Choshuenco geological field report (by Moreno and Lara, (2007). 19 new samples were analysed at the NERC Radiocarbon Facility-East Kilbride (code SUERC). These were pre-treated to remove potential contamination with 2M HCl (80°C, 8 hours), rinsed (deionised water) and digested in 1M KOH (80°C, 2 hours). This was repeated until no further humics were extracted. Samples were then rinsed (deionised water), digested in 2M HCl (80°C, 2 hours) and rinsed, dried and homogenised. Gases were recovered from the sample by heating at 900°C with CuO in a sealed quartz tube. CO_2 was extracted from the gas mix and part of the CO_2 converted to graphite and analysed by Accelerator Mass Spectroscopy. The remaining CO_2 was analysed for $^{13}C/^{12}C$ to improve the precision and check the purity of the sample.

Radiocarbon dates

Sample	Lab code	Stratigraphic position	Column in Fig. 2.2	Uncalibrated yrs BP	Individual age calibrated ShCal13 cal. yrs BP (95.4% confidence level)		$\delta^{13}C$	Method	Sample Material dated	Reference	Modelled age cal. yrs BP	Outlier?
130292-4		above MC25		140 ± 60	280-0	140 ± 140		Radiometricˆ		1,2	239-0	Date may extend out of range
220198-5	Beta-115243	below MC25		140 ± 60	280-0	140 ± 140	-25.0	Radiometricˆ		3	295-80	Date may extend out of range
130108-08H	SUERC-51920	below MC23	O	376 ± 35	488-318	403 ± 85	-26.8	AMS*	Carbonised twigs in soil at base of tephra deposit	3	464-310	
Ch-4		below MC21		650 ± 80	683-502	593 ± 91		Radiometric		1,4	712-503	
130129-01E	SUERC-51932	below MC21	M	664 ± 37	656-550	603 ± 53	-26/9	AMS*	Carbon flecks in organic rich soil at base of tephra deposit	3	659-548	
XG-272		below MC21 & above MC18		470 ± 50	545-327	436 ± 108		Radiometric		1,4	638-432	
Ch-18		above MC20		1110 ± 70	1173-801	987 ± 186		Radiometric		1,4	1073-773	
XG-270/220198-4/040300-1/etc.		below MC20 & above MC15	J	1340 ± 110	1402-963	1183 ± 220				4	1245-975	
Ch-4		above MC19		1300 ± 80	1304-981	1143 ± 162		Radiometric		1,4	1281-1001	
Ch-3		within MC18		1420 ± 80	1424-1074	1249 ± 175		Radiometric		1,4	1396-1234	
130126-02A	SUERC-51931	below MC18		2831 ± 35	2990-2783	2887 ± 104	-24.8	AMS*	∼1 cm pieces of carbonised branches 3 cm below tephra deposit in soil	3		Yes
130108-03A	SUERC-51922	below MC18		1509 ± 37	1417-1300	1300 ± 59	-26.0	AMS*	small carbonised twigs in soil at base of tephra deposit	3	1406-1301	
100303-2B	Beta-181369	within MC15D		1740 ± 40	1705-1533	1619 ± 86	-24.7	AMSˆ	Partially carbonised wood	3	1692-1544	
XG-251		within MC15D	J	1850 ± 60	1879-1587	1733 ± 146					1696-1557	<59% confidence range
R-5		below MC15		1660 ± 60	1698-1370	1534 ± 164		Radiometric		1,4	1698-1516	
040493-01		below MC15		1820 ± 60	1835-1545	1690 ± 145		Radiometricˆ		1,4	1814-1588	
130292-01		below MC15		1650 ± 90	1704-1320	1512 ± 192		Radiometricˆ		1,2	1744-1575	<53% confidence range
Ch-22		below MC15		1750 ± 70	1811-1430	1621 ± 191		Radiometric		1,4	1786-1578	
R6		below MC15		1680 ± 100	1781-1317	1549 ± 232		Radiometric		1,4	1800-1576	
130108-08A	SUERC-51929	below MC15	I	2067 ± 37	2085-1895	1900 ± 95	-27.9	AMS*	Carbonised twigs in soil at base of tephra deposit	3	2014-1578	<31% confidence range

Radiocarbon dates

Sample	Lab code	Stratigraphic position	Column in Fig. 2.2	Uncalibrated yrs BP	Individual age calibrated ShCal13 cal. yrs BP (95.4% confidence level)		$\delta^{13}C$	Method	Sample Material dated	Reference	Modelled age cal. yrs BP	Outlier?
130129-10A	SUERC-51925	below MC15	J	1807 ± 37	1809-1582	1696 ± 114	-26.6	AMS*	Carbon flecks in organic rich soil at base of tephra deposit	3	1747-1588	
130108-01A	SUERC-51928	below MC13	G	2253 ± 37	2337-2112	2225 ± 113	-27.7	AMS*	Outer part of a large carbonised brance, 50 cm below MC7 deposit within a soil	3	2338-2148	
130108-08C	SUERC-51919	below MC8	O	2532 ± 37	2738-2380	2559 ± 179	-27.1	AMS*	Top 1 cm of an organic rich soil with small pieces of charcoal directly below a fine grey ash	3		Yes
130116-03D	SUERC-51930	below MC12		1384 ± 37	1305-1185	1245 ± 60	-26.3	AMS*	Carbon flecks in organic rich soil at base of tephra deposit	3		Yes
XG-271		below MC13 & within MC10	J	2330 ± 70	2680-2095	2388 ± 293				4	2427-2110	
XG-275/6?		within MC10?		2450 ± 60	2709-2343	2526 ± 183		Radiometric		1,4	not included in model as poor stratigraphic constraint	
130107-03B	SUERC-51927	within MC10	J	3405 ± 37	3699-3478	3589 ± 111	-23.9	AMS*	Top 5 cm of an organic rich soil with small pieces of charcoal directly below tephra layer	3	3708-3467	
130292-02		within MC10?		4560 ± 70	5445-4882	5164 ± 282		Radiometric^		1,2	not included in model as poor stratigraphic constraint	
Ch-8		within MC10?		1830 ± 70	1877-1545	1711 ± 166		Radiometric		1,4	not included in model as poor stratigraphic constraint	
Ch-17		within MC10?		1850 ± 70	1896-1567	1732 ± 165		Radiometric		1,4	not included in model as poor stratigraphic constraint	
Ch-4		within MC10?		1910 ± 70	1997-1612	1805 ± 193		Radiometric		1,4	not included in model as poor stratigraphic constraint	
MC/C-9		within MC10?		2010 ± 100	2298-1629	1964 ± 335		Radiometric		1,4	not included in model as poor stratigraphic constraint	
Ch-9		within MC10?		2260 ± 70	2353-2048	2201 ± 153		Radiometric		1,4	not included in model as poor stratigraphic constraint	
Ch-5		within MC10?		2330 ± 80	2696-2064	2380 ± 317		Radiometric		1,4	not included in model as poor stratigraphic constraint	
Ch-24		within MC10?		2360 ± 60	2685-2154	2420 ± 266		Radiometric		1,4	not included in model as poor stratigraphic constraint	
Ch-10		within MC10?		2940 ± 40	3168-2885	3027 ± 142		AMS		1,4	not included in model as poor stratigraphic constraint	

Radiocarbon dates

Sample	Lab code	Stratigraphic position	Column in Fig. 2.2	Uncalibrated yrs BP	Individual age calibrated ShCal13 cal. yrs BP (95.4% confidence level)		δ^{13}C	Method	Sample Material dated	Reference	Modelled age cal. yrs BP	Outlier?
Ch-1		within MC10?		5780 ± 180	7143-6182	6663 ± 481		Radiometric		1,4	not included in model as poor stratigraphic constraint	
XG-283/220198-5		within MC10?		3720 ± 60	4225-3840	4033 ± 193		Radiometric^	Carbonised small branches	3	not included in model as poor stratigraphic constraint	
300892-02		between MC4 & MC9 deposits		8640 ± 150	10155-9296	9741 ± 445		Radiometric^		1,5	not included in model as poor stratigraphic constraint	
Ch-11		between MC4 & MC9 deposits		10680 ± 90	12732-12414	12573 ± 159		Radiometric		1,4	not included in model as poor stratigraphic constraint	
MC-8		between MC4 & MC9 deposits		9680 ± 170	11599-10440	11020 ± 580		Radiometric		1,4	not included in model as poor stratigraphic constraint	
Ch-12		between MC4 & MC9 deposits		8860 ± 50	10158-9678	9918 ± 240		AMS		1,4	not included in model as poor stratigraphic constraint	
Ch-7		above MC9		6710 ± 90	7687-7420	7554 ± 134		Radiometric		1,4	8010-7338	
030300-2A	Beta-156226	above MC9		7260 ± 70	8183-7879	8031 ± 152	-25.0	Radiometric^	Carbonised small branches	3	8185-7860	
020300-4A/XG-254		below MC9		8160 ± 100	9400-8658	9029 ± 371		Radiometric	Charcoal	3	9453-8775	
020300-2A	Beta-156225	between MC5 & MC9		6940 ± 40	7840-7625	7733 ± 108	-25/6	AMS^	Carbonised small branches	3	9452-8775	
130107-05A	SUERC-51921	between MC5 & MC9	D	7627 ± 41	8514-8320	8417 ± 97	-26.4	AMS*	Top 3 cm of organic rich soil with small pieces of charcoal directly below tephra layer	3	8511-8219	
200892-02		below MC4		10660 ± 140	12744-12056	12400 ± 344		Radiometric^		1,5	12695-11990	
130106-08A	SUERC-51918	below MC4	O	10349 ± 43	12399-11838	12119 ± 281	-27.0	AMS*	Carbonised twigs in soil at base of tephra deposit	3	12404-11847	

Table A.5: Radiocarbon dates for Mocho-Choshuenco post-glacial eruptions. [1] Moreno and Lara (2007); [2] Pérez (2005); [3] This work; [4] Echegaray (2004); [5] Moreno et al (1994). Accelerator Mass Spectroscopy* (AMS*) are ^{14}C analyses performed by the NERC Radiocarbon Facility and SUERC AMS laboratory in East Kilbride, UK. AMS$^{\wedge}$ and Radiometric$^{\wedge}$ are analyses carried out at Beta Analytic Florida. Calibrations and the Bayesian age model were run in OxCal 4.2.3. "Outlier" column highlights the samples identified as outliers in the model, and those which have a lower than 95.4% confidence level. These outliers could be old, reworked material or young rootlets. From the isotope measurements δ^{13}C is calculated. This value is a measure of the samples stable carbon isotope ratio of ^{13}C:^{12}C in respect to a reference standard, in this case the Pee Dee Belemnite (PDB) standard

- Options()
  - Curve="ShCal13.14c"
  - BCAD=FALSE
- Plot()
  - Outlier_Model("General",T(5),U(0,4),"t")
  - Sequence()
    - Sequence("Mochoshuenco")
      - Boundary("MC1")
      - Boundary("MC2")
      - Boundary("MC3")
      - Phase("base_Neltume")
        - R_Date("SUERC-51918", 10349, 43)
          - Outlier(0.05)
        - R_Date("200892-02", 10660, 140)
          - Outlier(0.05)
      - Boundary(Neltume)
      - Boundary("Pirehueico")
      - Phase("in_soil_above_Pirehueico")
        - R_Date("020300-4a", 8160, 100)
          - Outlier(0.05)
      - Boundary("MC6")
      - Boundary("MC7")
      - Boundary("MC8")
      - Phase("below_Huilo")
        - R_Date("SUERC-51921", 7627, 41)
          - Outlier(0.05)
      - Boundary(Huilo)
      - Phase("Top_Huilo")
        - R_Date("Beta-156226", 7260, 70)
          - Outlier(0.05)
        - R_Date("Ch-7", 6710, 90)
          - Outlier(0.05)
      - Boundary("MC10A")
      - Boundary("MC10B")
      - Boundary("MC10C")
      - Boundary("MC10D")
      - Boundary("MC10E")
      - Boundary("MC10F")
      - Boundary("MC10G")
      - Boundary("PCC unit")
      - Phase("below_ MC10H")
        - R_Date("SUERC-51927", 3405, 37)
          - Outlier(0.05)
      - Boundary("MC10H")
      - Boundary("MC11")
      - Boundary("MC12")
      - Phase("Below_MC13")
        - R_Date("SUERC-51928", 2253, 37)
          - Outlier(0.05)
        - R_Date("XG-271", 2330, 70)
          - Outlier(0.05)
      - Boundary("MC13")
      - Boundary("MC14")
      - Phase("below_Enco")
        - R_Date("SUERC-51925", 1807, 37)
          - Outlier(0.05)
        - R_Date("SUERC-51929", 2067, 37)
          - Outlier(0.05)
        - R_Date("ch-22", 1750, 70)
          - Outlier(0.05)
        - R_Date("R6", 1680, 100)
          - Outlier(0.05)
        - R_Date("130292-01", 1650, 90)
          - Outlier(0.05)
        - R_Date("040493-01", 1820, 60)
          - Outlier(0.05)
      - Phase("within_Enco")
        - R_Date("Beta-181369", 1740, 40)
          - Outlier(0.05)
        - R_Date("XG-251", 1850, 60)
          - Outlier(0.05)
        - R_Date("R-5", 1660, 60)
          - Outlier(0.05)
      - Boundary(Enco)
      - Boundary("MC16")
      - Boundary("MC17")
      - Phase("below_Hua-hum")
        - R_Date("SUERC-51922", 1509, 37)
          - Outlier(0.05)
      - Phase("within_Hua-hum")
        - R_Date("Ch-3", 1420, 80)
          - Outlier(0.05)
      - Boundary("Hua-hum")
      - Boundary("MC19")
      - Phase("above_MC19")
        - R_Date("Ch-14", 1300, 80)
          - Outlier(0.05)
      - Phase("below_MC20")
        - R_Date("XG-270", 1340, 110)
          - Outlier(0.05)
      - Boundary("MC20")
      - Phase("above_MC20")
        - R_Date("Ch-18", 1110, 70)
          - Outlier(0.05)
      - Phase("Below_Pilmaiquen")
        - R_Date("SUERC-51932", 664, 37)
          - Outlier(0.05)
        - R_Date("XG-272", 470, 50)
          - Outlier(0.05)
        - R_Date("ch-4", 650, 80)
          - Outlier(0.05)
      - Boundary(Pilmaiquen)
      - Boundary("MC22")
      - Phase("Arauco")
        - R_Date("SUERC-51920", 376, 35)
          - Outlier(0.05)
      - Boundary("Arauco")
      - Boundary("MC24")
      - Phase("Below_Rinihue")
        - R_Date("Beta-115243", 140, 60)
          - Outlier(0.05)
      - Boundary("Rinihue")
      - Phase("above_Rinihue")
        - R_Date("130292-4", 140, 60)
          - Outlier(0.05)
    - Boundary("upper level")

Figure A.1: OxCal 4.2.3 script to model the radiocarbon dates and constrain the tempo of volcanism. Boundary (volcanic unit name), R_date (labcode/sample name, conventional radiocarbon age, 1σ value). Ordered from oldest (top) to youngest (base)

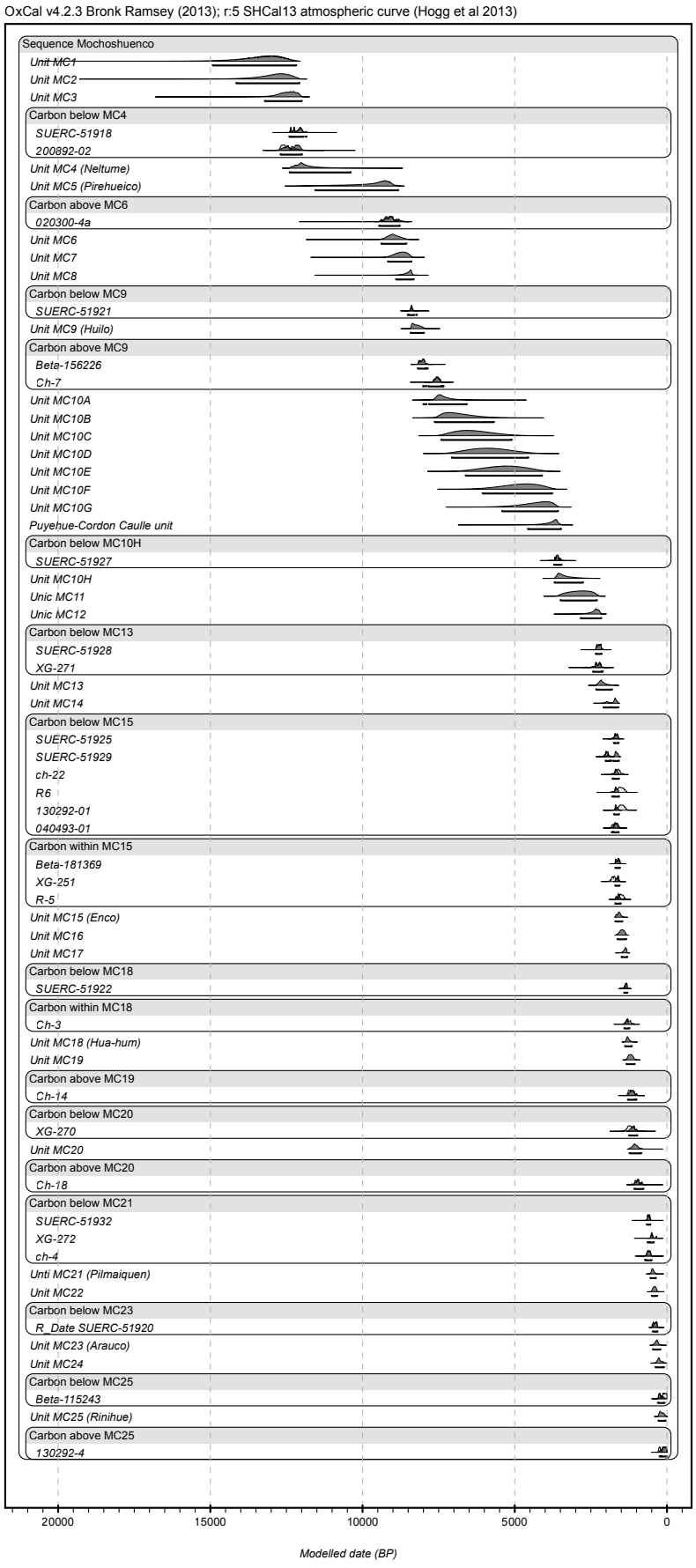

Figure A.2: Probability distributions for the radiocarbon dates and explosive units defined in Chapter 2 and Table A.5 and outputted from the OxCal script given in A.1. The black bar shows the 2σ range

A.4 Isopach and Isopleth data

Measurements for the largest preserved deposits were take in both proximal and distal locations. Measurements of deposit thickness and maximum clast size of pumice, scoria and lithics were made where possible. The maximum clast size was determined from the geometric mean of the three axes of each of the five largest clasts at an outcrop. The geometric mean of these five measurements gives the maximum clast estimate. In early field seasons (1998 to 2006), we determined the maximum clast size by measuring only the maximum diameter of the five largest, most spherical clasts. These averages and thickness measurements are presented in Table A.6. The complete dataset, which additionally included all axes measurements and the mean of each clast, is available in the supplementary material from Rawson et al. (2015; 10.1016/j.jvolgeores.2015.04.003) and (http://figshare.com/authors/Harriet_Rawson/663416); both are open access.

Isopach and Isopleth data

Outcrop	Latitude	Longitude	MP (cm)	ML (cm)	Th (cm)	Chemistry
MC4 (Neltume)						
302-01	-39.84	-72.03	5.3	2.7		yes
130120-13	-39.65	-71.91	2.5	0.7	300	yes
130130-05	-39.79	-72.10	3.2	1.6	186	yes
130130-03	-39.87	-71.90	1.8	0.6	8	yes
130130-02	-39.86	-71.90	3.3	2.2		yes
130116-09	-39.90	-71.91	1.9	1.3	10	yes
130106-08	-39.85	-72.11	5.4		50	yes
130108-06	-39.84	-71.94	3.0	1.7	20	yes
130207-01	-39.81	-71.65	1.2	0.5	14	yes
130108-05	-39.85	-71.92	5.2	3.2	145	yes
130120-16	-39.59	-72.02	2.3	0.6	250	yes
130122-02	-39.82	-71.90	4.1	1.4		yes
130127-03	-39.61	-72.16	1.9		18	yes
120313-03	-39.51	-71.86	0.8			yes
120313-07	-39.57	-72.08	2.1		120	yes
130106-05	-39.94	-72.11	5.0		27	yes
130111-09	-39.85	-71.90	5.0	2.8	112	yes
010300-1	-39.81	-71.98	14.0	4.2	>450	yes
CLD051	-39.51	-71.86	0.8			yes
CLD055	-39.57	-72.08	2.1		120	yes
CLD060	-39.46	-71.82	0.7		47	yes
CLD163	-39.46	-71.53	0.4		27	yes
CLD168	-39.50	-71.55	0.6		10	yes
CLD175	-39.56	-71.56	0.7		25	yes
CLD182	-39.45	-71.55	0.4		5	yes
CLD153	-40.23	-71.95				yes
030114-1	-39.35	-71.98	1.5		63	yes
030114-2	-39.38	-71.58	0.4		8	yes
030114-4	-39.50	-71.55	0.4		11	yes
040114-1	-39.49	-72.58	1.5		50	yes
040114-2	-39.53	-72.07	2.7		175	yes
040114-3	-39.59	-72.02	4.7		150	yes
120114-13	-39.99	-71.93	3.5		10	yes
150114-7	-39.81	-71.97	7.3	1.2	450-600	yes
150114-12	-39.87	-72.13	5.5		60	yes
130120-11	-39.72	-71.93	2.7	0.8		no
130122-03	-39.82	-71.91	3.2	1.3		no
130121-07	-39.80	-71.86	3.2			no
130121-07	-39.80	-71.88	3.1	1.5		no
130121-04	-39.79	-71.89	3.3	0.9		no
130127-02	-39.82	-72.04	4.7	2.1		no
130127-01	-39.81	-72.03	5.6	1.9	300	no
130118-01	-39.83	-72.04	3.7	1.3	500	no
130118-02	-39.81	-72.08	3.7	1.4		no
130118-05	-39.80	-72.10	2.5	0.8	150	no

Isopach and Isopleth data

Outcrop	Latitude	Longitude	MP (cm)	ML (cm)	Th (cm)	Chemistry
130111-07	-39.84	-72.02	4.3	3.2		no
116-03	-39.87	-72.12			14	no
116-05	-39.86	-72.11			22	no
116-08	-39.84	-72.11			103	no
130118-02	-39.81	-72.08	3.7	1.4		no
090406-4	-39.82	-72.00			600	no
130120-01	-39.81	-71.98	5.6	1.8		no
130120-02	-39.81	-71.97	3.3	0.9	100	no
130120-07	-39.81	-71.97	3.8	1.3		no
130120-06	-39.80	-71.95	4.0	2.3	200	no
130120-05	-39.80	-71.96	4.7	1.4	205	no
130120-04	-39.80	-71.96	3.5	0.7	170	no
130120-03	-39.81	-71.97	4.5	2.2	400	no
130120-08	-39.79	-71.96	3.7	1.9		no
130120-09	-39.75	-71.95	4.0	0.8		no
119-03	-39.71	-71.90				no
130120-12	-39.68	-71.91	1.6	0.2		no
119-04	-39.63	-71.92	1.6			no
130120-14	-39.63	-71.92	2.8	1.0	200	no
130120-15	-39.61	-71.91	2.2	0.7		no
130127-08	-39.57	-72.08	1.6	0.4		no
130127-07	-39.57	-72.08	2.1	0.6	125	no
130127-06	-39.57	-72.09	1.6	0.4	118	no
130127-05	-39.57	-72.09	1.7	0.4	95	no
130110-05	-39.56	-72.09	1.9	0.3	110	no
130110-04	-39.55	-72.10	1.5	0.3		no
130110-03	-39.56	-72.10	1.7	0.4	123	no
130110-06	-39.57	-72.12	1.6	0.3	70	no
130127-04	-39.58	-72.14	1.4		17	no
130118-08	-39.63	-72.16	1.0		15	no
130118-07	-39.75	-72.17			40	no
130118-06	-39.78	-72.12	2.0	0.5	96	no
117-01	-39.65	-71.92	3.3			no
030300-01	-39.88	-71.95	>8	>2.5	>160	no
090406-02	-39.85	-72.03			300	no
090406-03	-39.82	-71.97			600	no
160114-01	-39.83	-72.04			800	no
160114-03	-39.79	-72.10	8.0	3.8	200	no
160114-04	-39.78	-72.12	3.5	2.1		no
160114-05	-39.77	-72.14			33	no
MC5 (Pirehueico)						
130207-01	-39.81	-71.65	3.4	1.1	17	yes
130207-03	-39.83	-71.63	3.9		17	yes
130207-10	-39.86	-71.47	2.9	0.6	40	yes
130207-12	-39.86	-71.47	2.9	0.6	80	yes
130203-01	-40.03	-71.34	2.2			yes

Isopach and Isopleth data

Outcrop	Latitude	Longitude	MP (cm)	ML (cm)	Th (cm)	Chemistry
130207-06	-39.82	-71.56	3.0		15	yes
130107-05	-39.98	-71.92			140	yes
130117-06	-39.94	-71.84	3.3	1.2	300	yes
130207-08	-39.84	-71.51	3.2		25	yes
110114-03	-39.92	-71.53		5	1400	yes
120114-13	-39.99	-71.93	4.5		42	yes
130114-01	-39.99	-71.93	4.0		145	yes
100114-03	-39.92	-71.87			40	yes
130207-02	-39.82	-71.64	3.7			no
130207-04	-39.82	-71.61	3.3		18	no
130207-09	-39.85	-71.48	3.0	0.6		no
130207-13	-39.89	-71.41	2.5	0.5		no
130207-14	-39.89	-71.38	3.1	0.5		no
130207-15	-39.91	-71.30	2.0	0.5		no
170399-02	-39.79	-71.66	2.0			no
170399-01	-39.78	-71.71	2.5			no
020300-02	-40.01	-71.80	3.0	0.7	>50	no
020300-03	-39.99	-71.82	8.0		46	no
100114-06	-39.96	-71.87			130	no
130114-03	-39.92	-71.83		4	150	no
020300-04	-39.97	-71.86			83	no
030300-02	-39.96	-71.87			100	no
030300-04	-39.96	-71.89			265	no
0303005	-39.92	-71.83	25	10.5	230	no
MC9 (Huilo)						
130107-05	-39.98	-71.92	4.0	1.2	185	yes
130117-08	-39.95	-71.84	2.7	0.6	220	yes
130126-04	-39.88	-71.95	4.2	1.8		yes
130126.06	-39.87	-71.96	4.9	2.7		yes
130106-05	-39.94	-72.11	3.0		13	yes
140114-05	-39.88	-71.92			45	yes
130114-01	-39.99	-71.93	4.8		300	yes
150114-07	-39.81	-71.97	4.9	2.7	30	yes
110114-01	-39.92	-71.99			500-1000	yes
110114-02	-39.92	-71.99	25.0	6.50	900	yes
120114-03	-39.88	-71.95	6.9		80	yes
120114-13	-39.99	-71.93	7.5	4.50	166	yes
100114-05	-39.97	-71.86	4.7		330	yes
100114-03	-39.99	-71.82	3.6		100	yes
120114-06	-39.87	-71.96	8.0	5.5	225	yes
220198-02	-39.98	-71.83			210	yes
010300-01	-39.81	-71.98	5.0	3.0	30	yes
030300-03	-39.96	-71.87			300	yes
130111-07	-39.84	-72.02	4.8	1.3	41	no
130120-06	-39.80	-71.95	3.7	0.5		no
130120-03	-39.81	-71.97	2.9	0.4	20	no

Isopach and Isopleth data

Outcrop	Latitude	Longitude	MP (cm)	ML (cm)	Th (cm)	Chemistry
130120-04	-39.80	-71.96	2.0		29	no
130120-05	-39.80	-71.96	2.3		20	no
130120-02	-39.81	-71.97	2.1	0.5	26	no
130122-03	-39.82	-71.91	2.4	0.9	30	no
130121-07	-39.80	-71.86	2.7	0.6	35	no
130121-05	-39.80	-71.88	1.7		30	no
130121-04	-39.79	-71.89	1.8	0.3	38	no
130119-02	-39.97	-71.86	2.5	0.5	230	no
130119-01	-39.96	-71.87	3.3	0.8	100	no
130207-03	-39.83	-71.63	1.4			no
130207-04	-39.82	-71.61			20	no
130207-01	-39.81	-71.65	1.0		25	no
020300-2	-40.01	-71.78	4.0	1.3	90	no
030300-01	-39.88	-71.95	>11	>4	190	no
030300-05	-39.92	-71.83	7.0	3.0	130	no
060406-07	-39.98	-71.92			130	no
070406-01	-39.98	-71.92			250	no
090406-02	-39.85	-72.03			<40	no
090406-03	-39.82	-71.97	4.0	2.2	30	no
MC15C (Enco)						
130117-04	-39.95	-71.85	2.9	2.3	110	yes
130130-03	-39.87	-71.90	3.2	2.2		yes
130131-06	-39.94	-71.88	2.9			yes
121-01	-40.03	-71.87	4.1		70	yes
302-03	-39.88	-71.92			15	yes
115-03	-39.96	-71.90			190	yes
115-01	-39.87	-71.91			12	yes
020300-02	-40.01	-71.78			50	yes
100114-02	-39.99	-71.81	4.8	3.2	110	yes
080114-06	-39.90	-71.97			45	yes
150114-04	-39.96	-71.90			160	yes
130108-01	-39.87	-71.89	4.0	3.7	22	no
130108-03	-39.87	-71.91	4.8	3.6	21	no
130108-08	-39.88	-71.92			15	no
130111-09	-39.85	-71.90	3.2		8	no
130111-10	-39.85	-71.89	2.2			no
130115-01	-39.87	-71.92	2.4			no
130115-02	-39.87	-71.92	2.8		10	no
130115-04	-39.88	-71.92	2.7	3.3	14	no
130115-06	-39.88	-71.91	3.4	2.1	19	no
130115-07	-39.88	-71.92	3.0			no
130115-08	-39.87	-71.92	2.9		8.5	no
130115-09	-39.87	-71.92	2.5		5	no
130116-04	-39.89	-71.91	3.9	3.3	25	no
130116-07	-39.89	-71.90	5.0	2.7	26	no
130116-09	-39.90	-71.91	3.3	4.1	25	no

Isopach and Isopleth data

Outcrop	Latitude	Longitude	MP (cm)	ML (cm)	Th (cm)	Chemistry
130116-10	-39.87	-71.91	3.2	2.8	15	no
130117-05	-39.94	-71.84	2.2	2.6	20	no
130121-04	-39.79	-71.89	1.7			no
130121-07	-39.80	-71.86	1.5		3	no
130121-08	-39.80	-71.86	2.0		4	no
130121-09	-39.86	-71.91	2.5		9	no
130121-11	-39.87	-71.91	2.9		9	no
130121-12	-39.86	-71.89	3.1		13	no
130129-07	-39.98	-71.92	2.8		30	no
130129-10	-39.95	-71.90	4.2	1.4	210	no
130130-01	-39.85	-71.89	2.0	1.5	6	no
130131-02	-39.91	-71.93	4.2	3.5	45	no
130131-04	-39.90	-71.89	3.5	3.7		no
130131-05	-39.90	-71.90	4.3	3.0	50	no
226-04	-39.88	-71.92			17	no
226-01	-39.87	-71.90	4.1		15	no
080406-04	-39.88	-71.92			20	no
070406-04	-39.96	-71.90			160	no
090406-07	-39.87	-71.89			20	no
100406-01	-39.85	-71.96			10	no
080114-02	-39.87	-71.96			>150	no
100114-03	-39.99	-71.82	4.1		80	no
120114-06	-39.87	-71.96			80	no
140114-02	-39.85	-71.90			7	no
MC18 (Hua-Hum)						
130107-06	-40.00	-71.93	4.9	1.4	>40	yes
130119-03	-40.01	-71.77	1.8		15	yes
130129-07	-39.98	-71.92	3.4		80	yes
130119-08	-39.98	-71.86	1.6		10	yes
130108-03	-39.87	-71.91	1.5	0.8	20	yes
124-02	-39.90	-71.96			13	yes
229-02	-39.89	-71.96			48	yes
302-03	-39.88	-71.92			20	yes
130116-01	-40.00	-71.93	1.3	0.7	15	yes
130117-01	-39.92	-71.90			5	yes
130117-03	-39.95	-71.86	1.4		7	yes
130131-04	-39.90	-71.89	1.6			yes
130126-01	-39.90	-71.97			34	yes
130117-02	-39.95	-71.87	0.8		9	yes
130112-02	-40.23	-71.95	2.5	0.8	9.5	yes
020300-01	-40.01	-71.77	4.1		15	yes
080114-06	-39.90	-71.97	2.7	1.3	50	yes
120114-11	-39.99	-71.93	5.0		10	yes
090114-02	-40.02	-71.94	7.1	3.6	66	yes
115-01	-39.87	-71.91			30	no
226-01	-39.87	-71.90			>30	no

Isopach and Isopleth data

Outcrop	Latitude	Longitude	MP (cm)	ML (cm)	Th (cm)	Chemistry
130108-01	-39.87	-71.89	0.4		15	no
130108-08	-39.88	-71.92			16	no
130115-01	-39.87	-71.92	0.5		15	no
130115-02	-39.87	-71.92	0.7		16	no
130115-04	-39.88	-71.92	0.9		13	no
130115-05	-39.87	-71.91	1.7			no
130115-06	-39.88	-71.91	0.8		15	no
130115-07	-39.88	-71.92	1.5		>20	no
130116-04	-39.89	-71.91	0.9		15	no
130116-05	-39.88	-71.91	0.9	0.9	16	no
130116-06	-39.88	-71.90	1.2		35	no
130116-10	-39.87	-71.91	1.8		36	no
130117-05	-39.94	-71.84	1.2		8	no
130117-07	-39.95	-71.84	0.9		6	no
130119-06	-40.00	-71.80	1.6		10	no
130119-09	-39.98	-71.86	2.1		11	no
130119-10	-39.88	-71.94	1.1		15	no
130126-04	-39.88	-71.95			20	no
130131-04	-39.90	-71.89	1.5		20	no
130131-05	-39.90	-71.90	1.8			no
130121-09	-39.86	-71.91			8.5	no
230198-1	-40.07	-71.71	2.0		11	no

Table A.6: The maximum pumice (MP), maximum lithic (ML) and thickness (Th) measurements at both proximal and distal localities for the five largest fall deposits: MC4 (Neltume), MC5 (Pirehueico), MC9 (Huilo), MC15C (Enco) and MC18 (Hua-Hum). The 'chemistry' column corresponds to whether glass and/or oxide analyses were used to confirm, which eruption produced the deposit

A.5 Fe–Ti oxides

Within this section further details are given on how the Fe partitioning was calculated and the temperature and oxygen fugacity estimates from Fe–Ti oxide pairs.

A.5.1 Fe partitioning calculations in Fe–Ti oxides

EMP analyses assign all Fe to FeO*. To account for the Fe oxidation state (i.e., to convert FeO* to FeO and Fe_2O_3) so that the stoichiometry is correct the equations of Droop (1987) were used.

	oxygen total (OT)	cation total (CT)
ilmenite	3	2
magnetite	4	3

cation sum (CS) = Ti + Al + Fe + Mn + Mg + Ca (all in wt. % from EMP)

other cations (OC) = (CS – Fe) x (CT/CS) *Fe is wt.% from EMP*

Fe^{3+} = 2 x OT x (1 - (CT/CS)) x (CT/CS)

Fe^{2+} = CT - OC - Fe^{3+}

FeO = (FeO* x Fe^{2+}) / (Fe^{2+} + Fe^{3+})

Fe_2O_3 = (1.1113 x FeO* x Fe^{3+}) / (Fe^{2+} + Fe^{3+})

A.5.2 Temperature and oxygen fugacity

Using the method of Ghiroso and Evans (2008) the temperature and oxygen fugacity of the magma was estimated. These estimates are presented in Table A.7.

Temperature and Oxygen Fugacity estimates

Temperature (°C)	$\log_{10}fO_2$ (relative to NNO)	$\log_{10}fO_2$	Touching Pair?
MC2			
889	-0.12	-12.21	Yes
894	-0.11	-12.11	No
875	-0.22	-12.58	No
885	-0.11	-12.28	No
848	-0.59	-13.47	No
865	-0.45	-13.00	No
876	-0.19	-12.53	No
MC3			
907	0.08	-11.69	Yes
916	0.07	-11.54	Yes
917	0.11	-11.48	Yes
902	0.03	-11.83	Yes
905	0.12	-11.68	Yes
916	0.14	-11.47	Yes
911	0.12	-11.58	Yes
906	0.07	-11.72	Yes
898	0.10	-11.83	Yes
897	0.0	-11.95	No
907	0.12	-11.65	No
912	0.04	-11.64	No
893	-0.01	-12.03	No
911	-0.05	-11.75	No
903	0.09	-11.75	No
897	0.00	-11.95	No
901	0.09	-11.79	No
915	0.07	-11.55	No
886	-0.06	-12.21	No
MC4 (Neltume)			
898	0.08	-11.85	Yes
900	0.07	-11.82	Yes
898	0.01	-11.92	Yes
886	-0.04	-12.19	Yes
897	0.05	-11.90	Yes
903	0.08	-11.76	Yes
903	0.14	-11.70	Yes
881	-0.14	-12.38	Yes
892	-0.04	-12.08	Yes
895	-0.03	-12.01	Yes
901	0.09	-11.79	Yes
867	-0.24	-12.75	Yes

Temperature and Oxygen Fugacity estimates

Temperature (°C)	$\log_{10}fO_2$ (relative to NNO)	$\log_{10}fO_2$	Touching Pair?
885	-0.14	-12.31	Yes
901	0.01	-11.87	Yes
890	-0.04	-12.12	Yes
885	-0.07	-12.24	Yes
872	-0.12	-12.53	Yes
884	0.03	-12.16	Yes
908	0.14	-11.61	Yes
906	0.01	-11.78	Yes
889	-0.07	-12.16	Yes
889	-0.11	-12.20	Yes
892	-0.05	-12.09	Yes
894	-0.08	-12.08	Yes
875	-0.19	-12.55	Yes
871	-0.21	-12.64	Yes
907	0.12	-11.65	Yes
874	-0.18	-12.55	Yes
885	-0.06	-12.23	Yes
898	0.11	-11.82	Yes
898	0.11	-11.82	Yes
893	0.00	-12.02	Yes
900	0.09	-11.80	Yes
908	0.04	-11.71	Yes
902	0.10	-11.76	No
883	-0.11	-12.32	No
880	-0.07	-12.33	No
885	-0.12	-12.29	No
879	-0.17	-12.45	No
885	0.04	-12.13	No
886	-0.07	-12.22	No
875	-0.09	-12.45	No
895	0.07	-11.91	No
887	-0.13	-12.26	No
878	-0.11	-12.41	No
883	-0.17	-12.38	No
882	-0.14	-12.36	No
886	-0.12	-12.27	No
882	-0.09	-12.31	No
896	0.06	-11.91	No
898	0.11	-11.82	No
875	-0.15	-12.51	No
881	-0.17	-12.41	No
879	-0.18	-12.46	No
881	-0.21	-12.45	No
886	-0.02	-12.17	No
858	-0.17	-12.85	No

Temperature and Oxygen Fugacity estimates

Temperature (°C)	$\log_{10}fO_2$ (relative to NNO)	$\log_{10}fO_2$	Touching Pair?
866	-0.20	-12.73	No
864	-0.19	-12.76	No
876	-0.11	-12.45	No
891	-0.06	-12.12	No
893	-0.05	-12.07	No
887	-0.07	-12.20	No
874	-0.17	-12.54	No
884	-0.12	-12.31	No
863	-0.15	-12.74	No
880	-0.12	-12.38	No
899	0.01	-11.90	No
861	-0.07	-12.69	No
888	-0.04	-12.15	No
899	0.08	-11.83	No
897	-0.02	-11.97	No
886	0.05	-12.10	No
878	0.00	-12.30	No
892	0.05	-11.99	No
896	0.12	-11.85	No
897	0.10	-11.85	No
887	-0.10	-12.23	No
913	0.24	-11.42	No
880	-0.09	-12.35	No
888	0.01	-12.10	No
909	0.06	-11.67	No
874	-0.22	-12.59	No
887	-0.08	-12.21	No
872	-0.23	-12.64	No
887	-0.09	-12.22	No
885	-0.09	-12.26	No
878	-0.16	-12.46	No
880	-0.14	-12.40	No
877	-0.05	-12.37	No
879	-0.05	-12.33	No
853	-0.06	-12.84	No
888	-0.06	-12.17	No
883	-0.09	-12.30	No
894	-0.05	-12.05	No
879	-0.04	-12.32	No
881	-0.04	-12.28	No
872	-0.15	-12.56	No
897	0.06	-11.89	No
878	-0.10	-12.40	No
873	-0.20	-12.59	No
878	-0.07	-12.37	No

Temperature and Oxygen Fugacity estimates

Temperature (°C)	$\log_{10}fO_2$ (relative to NNO)	$\log_{10}fO_2$	Touching Pair?
890	0.06	-12.02	No
890	-0.07	-12.15	No
885	-0.11	-12.28	No
912	0.05	-11.63	No
908	-0.16	-11.91	No
891	-0.04	-12.10	No
893	-0.05	-12.07	No
880	-0.12	-12.38	No
885	-0.10	-12.27	No
908	0.05	-11.70	No
879	-0.12	-12.40	No
867	-0.19	-12.70	No
890	-0.15	-12.23	No
876	-0.20	-12.54	No
875	-0.07	-12.43	No
882	-0.11	-12.33	No
868	-0.13	-12.62	No
903	0.06	-11.78	No
898	0.09	-11.84	No
884	-0.01	-12.20	No
905	0.11	-11.69	No
890	0.04	-12.04	No
904	0.12	-11.70	No
903	0.13	-11.71	No
903	0.13	-11.71	No
910	0.15	-11.56	No
898	0.12	-11.81	No
899	0.07	-11.84	No
905	0.14	-11.66	No
898	0.08	-11.85	No
MC5 (Pirehueico)			
898	0.45	-11.48	Yes
892	0.43	-11.61	Yes
897	0.44	-11.51	Yes
901	0.41	-11.47	Yes
905	0.46	-11.34	Yes
904	0.46	-11.36	Yes
887	0.46	-11.67	Yes
920	0.52	-11.02	Yes
912	0.47	-11.21	Yes
894	0.38	-11.62	Yes
916	0.56	-11.05	Yes
917	0.56	-11.03	Yes
878	0.44	-11.86	Yes

Temperature and Oxygen Fugacity estimates

Temperature (°C)	$\log_{10}fO_2$ (relative to NNO)	$\log_{10}fO_2$	Touching Pair?
909	0.52	-11.21	Yes
910	0.46	-11.25	Yes
904	0.46	-11.36	Yes
881	0.60	-11.64	Yes
902	0.41	-11.45	Yes
897	0.54	-11.41	Yes
913	0.44	-11.22	Yes
913	0.52	-11.14	Yes
900	0.45	-11.44	Yes
900	0.40	-11.49	Yes
913	0.50	-11.16	Yes
922	0.48	-11.02	Yes
929	0.61	-10.77	Yes
903	0.43	-11.41	Yes
916	0.53	-11.08	Yes
896	0.54	-11.43	Yes
904	0.44	-11.38	Yes
905	0.51	-11.29	Yes
877	0.31	-12.01	Yes
889	0.37	-11.72	Yes
898	0.46	-11.47	Yes
905	0.54	-11.26	Yes
900	0.52	-11.37	Yes
906	0.36	-11.43	Yes
914	0.54	-11.10	Yes
913	0.59	-11.07	Yes
907	0.49	-11.28	Yes
892	0.41	-11.63	Yes
917	0.52	-11.07	Yes
916	0.50	-11.11	Yes
911	0.55	-11.15	Yes
917	0.55	-11.04	Yes
894	0.51	-11.49	Yes
916	0.63	-10.98	Yes
904	0.48	-11.34	Yes
909	0.54	-11.19	Yes
902	0.50	-11.36	Yes
899	0.41	-11.50	Yes
904	0.51	-11.31	Yes
889	0.44	-11.65	Yes
901	0.61	-11.27	Yes
902	0.39	-11.47	Yes
900	0.43	-11.46	Yes
896	0.54	-11.43	Yes
909	0.49	-11.24	Yes

Temperature and Oxygen Fugacity estimates

Temperature (°C)	$\log_{10}fO_2$ (relative to NNO)	$\log_{10}fO_2$	Touching Pair?
915	0.51	-11.11	Yes
902	0.50	-11.36	Yes
902	0.41	-11.45	Yes
933	0.51	-10.80	Yes
912	0.49	-11.19	Yes
904	0.42	-11.40	Yes
898	0.47	-11.46	Yes
906	0.46	-11.33	Yes
920	0.54	-11.00	Yes
916	0.54	-11.07	Yes
919	0.58	-10.97	Yes
897	0.41	-11.54	Yes
895	0.42	-11.56	No
893	0.52	-11.50	No
905	0.52	-11.28	No
893	0.45	-11.57	No
890	0.46	-11.62	No
897	0.47	-11.48	No
914	0.58	-11.06	No
888	0.51	-11.60	No
899	0.44	-11.47	No
901	0.46	-11.42	No
926	0.50	-10.93	No
891	0.49	-11.57	No
896	0.49	-11.48	No
902	0.63	-11.23	No
901	0.47	-11.41	No
904	0.50	-11.32	No
915	0.50	-11.12	No
900	0.53	-11.36	No
883	0.43	-11.78	No
910	0.53	-11.18	No
880	0.51	-11.75	No
890	0.49	-11.59	No
902	0.54	-11.32	No
904	0.56	-11.26	No
902	0.48	-11.38	No
884	0.46	-11.73	No
892	0.33	-11.71	No
886	0.27	-11.88	No
902	0.58	-11.28	No
901	0.57	-11.31	No
890	0.41	-11.67	No
883	0.38	-11.83	No
927	0.64	-10.78	No

Temperature and Oxygen Fugacity estimates

Temperature (°C)	$\log_{10}fO_2$ (relative to NNO)	$\log_{10}fO_2$	Touching Pair?
870	-0.05	-12.50	No
902	0.50	-11.36	No
906	0.51	-11.28	No
888	0.45	-11.66	No
898	0.50	-11.43	No
900	0.50	-11.39	No
895	0.46	-11.52	No
918	0.61	-10.96	No
894	0.48	-11.52	No
891	0.46	-11.60	No
890	0.44	-11.64	No
894	0.61	-11.39	No
908	0.62	-11.13	No
892	0.46	-11.58	No
903	0.48	-11.36	No
907	0.50	-11.27	No
928	0.54	-10.86	No
907	0.45	-11.32	No
904	0.33	-11.49	No
901	0.51	-11.37	No
897	0.41	-11.54	No
901	0.57	-11.31	No
903	0.47	-11.37	No
912	0.53	-11.15	No
905	0.52	-11.28	No
923	0.62	-10.86	No
886	0.47	-11.68	No
908	0.47	-11.28	No
897	0.42	-11.53	No
913	0.47	-11.19	No
916	0.50	-11.11	No
MC6			
929	0.43	-10.95	Yes
919	0.35	-11.20	Yes
933	0.48	-10.83	Yes
909	0.37	-11.36	Yes
936	0.50	-10.76	Yes
933	0.44	-10.87	Yes
908	0.34	-11.41	Yes
923	0.36	-11.12	No
MC7			
924	-0.32	-11.79	Yes
923	-0.43	-11.91	Yes

Temperature and Oxygen Fugacity estimates

Temperature (°C)	$\log_{10}fO_2$ (relative to NNO)	$\log_{10}fO_2$	Touching Pair?
925	-0.36	-11.81	No
MC9 (Huilo)			
934	0.50	-10.79	Yes
928	0.50	-10.90	Yes
939	0.58	-10.63	Yes
944	0.53	-10.60	Yes
934	0.61	-10.68	Yes
933	0.49	-10.82	Yes
939	0.54	-10.67	Yes
933	0.54	-10.77	Yes
941	0.58	-10.60	Yes
942	0.60	-10.56	Yes
938	0.54	-10.69	Yes
947	0.60	-10.47	Yes
945	0.64	-10.47	Yes
935	0.58	-10.70	Yes
928	0.54	-10.86	Yes
943	0.58	-10.56	Yes
932	0.50	-10.83	Yes
941	0.57	-10.61	Yes
933	0.52	-10.79	Yes
929	0.50	-10.88	Yes
933	0.56	-10.75	Yes
924	0.51	-10.96	Yes
936	0.55	-10.71	Yes
941	0.54	-10.64	Yes
934	0.50	-10.79	Yes
918	0.41	-11.16	Yes
942	0.57	-10.59	Yes
930	0.49	-10.87	Yes
935	0.57	-10.71	Yes
934	0.52	-10.77	Yes
933	0.54	-10.77	Yes
937	0.54	-10.70	Yes
935	0.52	-10.76	Yes
937	0.54	-10.70	Yes
939	0.56	-10.65	Yes
938	0.56	-10.67	Yes
949	0.64	-10.40	Yes
949	0.60	-10.44	Yes
933	0.54	-10.77	Yes
934	0.47	-10.82	Yes
948	0.61	-10.45	Yes
945	0.56	-10.55	Yes

Temperature and Oxygen Fugacity estimates

Temperature (°C)	$\log_{10}fO_2$ (relative to NNO)	$\log_{10}fO_2$	Touching Pair?
944	0.56	-10.56	Yes
926	0.50	-10.93	Yes
934	0.56	-10.73	Yes
928	0.50	-10.90	Yes
935	0.58	-10.70	Yes
926	0.49	-10.94	Yes
921	0.48	-11.04	Yes
921	0.44	-11.08	Yes
930	0.50	-10.86	Yes
930	0.51	-10.85	Yes
931	0.49	-10.86	Yes
937	0.57	-10.67	Yes
933	0.52	-10.79	Yes
938	0.53	-10.70	Yes
940	0.55	-10.64	Yes
933	0.53	-10.78	Yes
947	0.61	-10.46	Yes
933	0.50	-10.81	Yes
923	0.50	-10.98	Yes
933	0.53	-10.78	Yes
950	0.63	-10.39	Yes
925	0.53	-10.92	Yes
907	0.41	-11.36	Yes
940	0.59	-10.60	Yes
940	0.50	-10.69	Yes
923	0.48	-11.00	Yes
916	0.47	-11.14	Yes
939	0.49	-10.72	No
935	0.50	-10.78	No
924	0.46	-11.01	No
932	0.56	-10.77	No
914	0.43	-11.21	No
939	0.55	-10.66	No
929	0.56	-10.82	No
948	0.64	-10.42	No
932	0.53	-10.80	No
940	0.61	-10.58	No
937	0.58	-10.66	No
941	0.57	-10.61	No
940	0.57	-10.62	No
921	0.52	-11.00	No
920	0.50	-11.04	No
935	0.52	-10.76	No
933	0.48	-10.83	No
926	0.50	-10.93	No

Temperature and Oxygen Fugacity estimates

Temperature (°C)	$\log_{10}fO_2$ (relative to NNO)	$\log_{10}fO_2$	Touching Pair?
935	0.51	-10.77	No
919	0.47	-11.08	No
920	0.43	-11.11	No
922	0.47	-11.03	No
921	0.48	-11.04	No
947	0.50	-10.57	No
930	0.47	-10.89	No
941	0.60	-10.58	No
940	0.60	-10.59	No
936	0.55	-10.71	No
953	0.64	-10.33	No
936	0.57	-10.69	No
935	0.56	-10.72	No
933	0.58	-10.73	No
954	0.65	-10.31	No
939	0.65	-10.56	No
942	0.59	-10.57	No
918	0.50	-11.07	No
924	0.50	-10.97	No
928	0.58	-10.82	No
934	0.59	-10.70	No
932	0.54	-10.79	No
936	0.54	-10.72	No
939	0.56	-10.65	No
941	0.57	-10.61	No
927	0.48	-10.94	No
934	0.52	-10.77	No
941	0.55	-10.63	No
941	0.53	-10.65	No
945	0.59	-10.52	No
928	0.49	-10.91	No
944	0.56	-10.56	No
930	0.52	-10.84	No
934	0.52	-10.77	No
935	0.54	-10.74	No
938	0.56	-10.67	No
926	0.48	-10.95	No
939	0.56	-10.65	No
927	0.50	-10.92	No
938	0.53	-10.70	No
936	0.53	-10.73	No
932	0.56	-10.77	No
942	0.57	-10.59	No
932	0.54	-10.79	No
931	0.52	-10.83	No

Temperature and Oxygen Fugacity estimates

Temperature (°C)	$\log_{10}fO_2$ (relative to NNO)	$\log_{10}fO_2$	Touching Pair?
930	0.45	-10.91	No
922	0.49	-11.01	No
933	0.53	-10.78	No
941	0.55	-10.63	No
933	0.50	-10.81	No
935	0.53	-10.75	No
931	0.52	-10.83	No
921	0.48	-11.04	No
928	0.55	-10.85	No
925	0.48	-10.97	No
936	0.53	-10.73	No
925	0.47	-10.98	No
938	0.53	-10.70	No
924	0.50	-10.97	No
935	0.55	-10.73	No
939	0.57	-10.64	No
934	0.55	-10.74	No
931	0.54	-10.81	No
948	0.58	-10.48	No
939	0.53	-10.68	No
939	0.54	-10.67	No
933	0.50	-10.81	No
931	0.53	-10.82	No
923	0.48	-11.00	No
939	0.54	-10.67	No
935	0.55	-10.73	No
929	0.52	-10.86	No
932	0.53	-10.80	No
940	0.54	-10.65	No
929	0.48	-10.90	No
934	0.52	-10.77	No
941	0.57	-10.61	No
919	0.44	-11.11	No
937	0.52	-10.72	No
927	0.51	-10.91	No
920	0.46	-11.08	No
945	0.56	-10.55	No
927	0.50	-10.92	No
929	0.53	-10.85	No
945	0.58	-10.53	No
929	0.55	-10.83	No
934	0.52	-10.77	No
922	0.49	-11.01	No
951	0.62	-10.39	No
931	0.59	-10.76	No

Temperature and Oxygen Fugacity estimates

Temperature (°C)	$\log_{10}fO_2$ (relative to NNO)	$\log_{10}fO_2$	Touching Pair?
935	0.55	-10.73	No
934	0.49	-10.80	No
925	0.54	-10.91	No
932	0.55	-10.78	No
930	0.52	-10.84	No
942	0.61	-10.55	No
MC12			
934	-0.37	-11.66	Yes
958	-0.21	-11.10	Yes
932	-0.40	-11.73	Yes
922	-0.47	-11.97	Yes
941	-0.27	-11.45	Yes
914	-0.49	-12.13	Yes
927	-0.45	-11.87	Yes
932	-0.39	-11.72	Yes
952	-0.27	-11.26	Yes
940	-0.28	-11.47	Yes
911	-0.49	-12.19	Yes
926	-0.44	-11.87	No
934	-0.40	-11.69	No
937	-0.29	-11.53	No
924	-0.45	-11.92	No
942	-0.31	-11.47	No
932	-0.41	-11.74	No
921	-0.46	-11.98	No
945	-0.34	-11.45	No
913	-0.47	-12.13	No
930	-0.42	-11.78	No
905	-0.50	-12.30	No
923	-0.40	-11.88	No
964	-0.13	-10.92	No
957	-0.16	-11.07	No
951	-0.16	-11.17	No
935	-0.29	-11.57	No
921	-0.27	-11.79	No
945	-0.29	-11.40	No
924	-0.42	-11.89	No
917	-0.39	-11.98	No
904	-0.49	-12.31	No
938	-0.33	-11.56	No
928	-0.42	-11.82	No
949	-0.37	-11.41	No
919	-0.47	-12.02	No
929	-0.26	-11.64	No

Temperature and Oxygen Fugacity estimates

Temperature (°C)	$\log_{10}fO_2$ (relative to NNO)	$\log_{10}fO_2$	Touching Pair?
933	-0.36	-11.67	No
927	-0.36	-11.78	No
951	-0.15	-11.16	No
918	-0.42	-11.99	No
909	-0.49	-12.22	No
941	-0.30	-11.48	No
MC13			
932	0.53	-10.80	Yes
932	0.52	-10.81	Yes
924	0.51	-10.96	Yes
938	0.56	-10.67	Yes
935	0.56	-10.72	Yes
932	0.53	-10.80	Yes
932	0.52	-10.81	Yes
924	0.51	-10.96	Yes
934	0.57	-10.72	Yes
943	0.57	-10.57	Yes
937	0.57	-10.67	Yes
930	0.53	-10.83	Yes
928	0.56	-10.84	No
931	0.53	-10.82	No
947	0.53	-10.54	No
933	0.53	-10.78	No
928	0.56	-10.84	No
931	0.53	-10.82	No
920	0.47	-11.07	No
937	0.58	-10.66	No
943	0.59	-10.55	No
MC17			
961	0.12	-10.72	Yes
946	-0.07	-11.16	No
MC18B (Hua-Hum)			
979	0.44	-10.11	Yes
963	0.43	-10.38	Yes
960	0.40	-10.46	Yes
951	0.40	-10.61	Yes
940	0.30	-10.89	Yes
938	0.19	-11.04	Yes
944	0.33	-10.79	Yes
948	0.40	-10.66	No
971	0.49	-10.19	No

Temperature and Oxygen Fugacity estimates

Temperature (°C)	$\log_{10}fO_2$ (relative to NNO)	$\log_{10}fO_2$	Touching Pair?
965	0.49	-10.29	No
952	0.40	-10.59	No
965	0.43	-10.35	No
973	0.45	-10.20	No
955	0.37	-10.57	No
947	0.29	-10.78	No
942	0.27	-10.89	No
956	0.38	-10.54	No
952	0.40	-10.59	No
953	0.27	-10.70	No
MC20			
966	0.62	-10.14	Yes
954	0.54	-10.42	Yes
955	0.54	-10.40	Yes
953	0.55	-10.42	Yes
964	0.60	-10.19	Yes
974	0.54	-10.09	Yes
957	0.49	-10.42	Yes
958	0.56	-10.33	Yes
947	0.56	-10.51	Yes
983	0.50	-9.99	No
957	0.53	-10.38	No
962	0.52	-10.31	No
962	0.56	-10.27	No
951	0.57	-10.44	No
956	0.54	-10.38	No
971	0.59	-10.09	No
963	0.59	-10.22	No
963	0.56	-10.25	No
970	0.63	-10.07	No

Table A.7: The temperature and oxygen fugacity estimates for the Mocho-Choshuenco tephra units defined in Chapter 2. Determined using Fe–Ti oxide pairs and the method of Ghiorso and Evans (2008). NNO is the Ni-Ni-O buffer. These measurements are plotted in Fig. 2.7

A.6 Further methodology from Chapter 3

Chapter 3 was formatted for publication in Geology. Due to the tight restriction on article length most of the methodology was included in supplementary material, which is presented below.

A.6.1 Methodology for estimating effusive volumes/rates and composition

The age, composition and area covered by the effusive products are poorly constrained. Prior estimates of the pre-caldera edifice volume (160 km^3) and $^{40}Ar/^{39}Ar$ dates for the oldest exposed lavas (∼350 ka; Moreno and Lara, 2007) give an average effusion rate of ∼0.5 km^3/kyr. We cannot determine how rates of effusive activity may have changed on shorter timescales. The whole rock composition of the effusive products range from 52 to 68 wt% SiO_2, with a dominance of andesitic magmas (Moreno and Lara, 2007).

A.6.2 Methodology for estimating cumulate masses and magma supply rates

To estimate the cumulate masses, we assume that evolved melts formed by fractional crystallisation of a mafic parent (Fig. A.3A., One unit that has been influenced by mixing is highlighted in a pink dashed ellipse; Rawson et al., 2015). To estimate the cumulate fraction we use three proxies. Firstly (1) we also assume that the glass (melt) composition is a proxy for magma composition (the magmas are almost aphyric (Rawson et al., 2015), and that potassium concentration is a proxy for the amount of crystallisation (there is no evidence of potassium-bearing minerals crystallising at Mocho-Choshuenco, so potassium can be assumed to behave incompatibly). With these assumptions, the fraction of cumulates (Φ) can be approximated by 1- $[C_0/C_L] = \Phi$, where C_0 is the potassium concentration in the source, and C_L is the potassium concentration for the erupted magma. The average K_2O composition for each eruption was used to estimate Φ for each eruption. The cumulate masses can be constrained well for the explosive

deposits as they have a well-determined composition and volume (Fig. A.3B, C). As the composition, age and area covered by the effusive products is poorly constrained, an assumed potassium composition is used; andesitic effusive magmas are dominant (Moreno and Lara, 2007), so a mid-andesitic potassium composition is used. As the composition of the primary melt entering the crust is unknown, we estimate the cumulate volumes using three initial potassium compositions; the most primitive melt analysed at Mocho-Choshuenco (Mg# 50), the primary melt composition of MORB (Mg# 70; e.g., Workman and Hart, 2005), and a value between these two end members (Mg# 60), as primary arc melts additionally comprise a fluid and/or melt component from the subducting slab, so are probably less mafic than MORB (e.g., Grove et al., 2012). To determine primary melt potassium composition we back-project to the Mg#s (Fig. A.3.D) using the glass analyses of Rawson et al. (2015). For the second proxy (2) we take the primary melt as having a SiO_2 of 50 wt.% and assume Zr behaves perfectly incompatible, rather than K_2O. The whole rock data (presented in Chapter 4 and Appendix A.7) is used as only major element concentrations were determined for the glass analyses. The same method and assumptions as proxy 1 are then used to estimate the melt fraction (Φ). The third proxy (3) utilises the experimentally determined curve of melt fraction versus SiO_2 constructed by Nandedkar et al. (2014) and Caricchi and Blundy (2015). This curve is determined for a primary magma with 3 wt.% water, 50 wt.% SiO_2 that undergoes crystal fractionation at 0.7 GPa. The average SiO_2 glass compositions are used to measure, from the curve, the corresponding melt fraction (Φ) for each deposit.

Cumulate masses were estimated by multiplying Φ (fraction of cumulate by mass) by the corresponding masses for the explosive products and effusive magmas. Masses of explosive products were calculated by Rawson et al. (2015); for the effusive magmas, a density of 2650 kg/m^3 was assumed. From these mass estimates, we determine the magma supply rate required to sustain the eruptive fluxes; magma supply rate = [the mass of (effusive melt and corresponding cumulate + explosive melt and corresponding cumulate)]/duration of phase (in kyr). For clearer comparison with the eruption rates (given as km^3/kyr) the estimated magma supply rate is given as a volume by using an assumed density of 2830 kg/m^3 (the primary magma density estimated by Kay et al.,

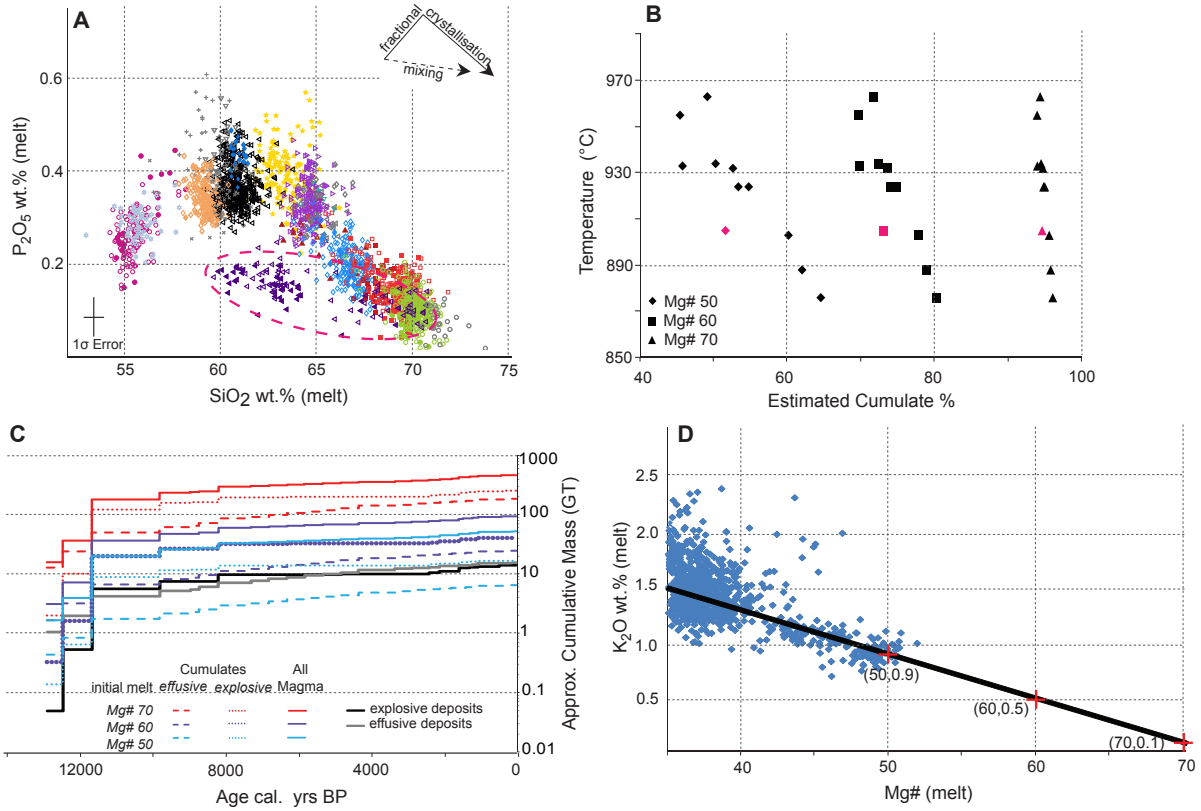

Figure A.3: (A) Major element glass composition (anhydrous) for the different tephra units from Mocho-Choshuenco. The different colours and/or symbols represent the data from different eruptions. P_2O_5 vs. SiO_2 illustrates clearly how fractional crystallisation is the dominant process generating the breadth of magmas. The unit that clearly experienced mixing is purple and circled with a pink dashed line. This unit is highlighted with a pink symbol in B and Fig. 3.1 (B) The temperature estimate plotted against the estimated fraction of cumulates (Φ) forming from the three initial melts. (C) The cumulate masses estimated for the extrusive and explosive eruptions. The total of these three estimates is given by All magma trend. (D) Glass analyses (from Rawson et al., 2015) used to estimate K_2O content by back-projecting to Mg# 50, 60 and 70

1992). The percentage of magma that erupts = 100 * (effusive + explosive mass)/[the mass of (effusive melt and corresponding cumulate + explosive melt and corresponding cumulate)]. If we further assume all melt reaches the surface, all intrusive rocks are formed of cumulates, no primary melt fully crystallises and the Phase 3 system is in equilibrium then the magma supply rate during phase 3 approximates the magma flux into the crust (i.e., ~17 km^3/kyr for a primary melt with Mg# 70; Table A.8)

	Explosive eruption rate (km^3/kyr)	% of magma erupted (by mass)			Primary melt supply (GT/kyr)			Primary melt supply (km^3/kyr)		
		Mg# 50	Mg# 60	Mg# 70	Mg# 50	Mg# 60	Mg# 70	Mg# 50	Mg# 60	Mg# 70
Phase 1	2.2	50	27	6	8	14	69	2.7	4.8	24.2
Phase 2	0.1	71	39	8	2	3	17	0.7	1.2	6.2
Phase 3	2.0	65	36	7	6	10	48	2.0	3.5	17.1
Average	1.3	56	31	6	5	9	45	1.7	3.1	15.8

	Explosive eruption rate (km^3/kyr)	% of magma erupted (by mass)		Primary melt supply (GT/kyr)		Primary melt supply (km^3/kyr)	
		Zr vs. SiO_2	Experiment	Zr vs. SiO_2	Experiment	Zr vs. SiO_2	Experiment
Phase 1	2.2	12	20	8	13	4.6	3
Phase 2	0.1	58	58	2	2	0.8	0.8
Phase 3	2.0	19	26	8	6	2.9	2.1
Average	1.3	18	26	8	6	2.8	1.9

Table A.8: Summary of how the explosive eruption rate, % of magma erupted and primary melt supply ($\approx$ magma flux into the crust for phase 3) vary between eruptive phases for different primary melts. Top table is the estimates assuming proxy 1. Bottom table is the estimates assuming proxy 2 (Zr vs. SiO_2) and proxy 3 (experiment).

Preservation issues mean that all estimates in Table A.8 should be treated a minimum values. Due to erosion, compaction and burial all tephra deposit volumes underestimate the true volume erupted, with Phase 1 volumes underestimated to the greatest extent and Phase 3 the least. Therefore despite the eruption flux estimated for Phase 3 being slightly larger than Phase 1 the true value of Phase 1 is anticipated to be significantly larger than Phase 3. Unfortunately no studies currently exist to quantify this.

A.6.3 Further methodology for determining eruption flux and magma storage timescales in Fig. 3.2.

In Fig. 3.2 we plot the eruption flux through time to illustrate our hypothesis that eruption fluxes were low in syn-glacial times, elevated in Phase 1 and low in Phase 2. This takes into account both the effusive and explosive deposits. However, as the resolution of the effusive deposits is not sufficient on the timescales considered this is assumed constant. Therefore variations in the eruption flux are a result of changes in the explosive behaviour. To construct the eruption flux:

1. The age of each tephra deposit is given by the age probability distribution from Bayesian analysis (Rawson et al., 2015). Therefore rather than a single age there is a range of ages for the deposits with some being more probable than others. The probabilities (i.e., area enclosed by the curve) all sum to one.

2. For each deposit we scale the area enclosed to the deposit mass.

3. This scaled area is then divided into 0.5 kyr bins for each deposit to smooth the flux.

4. The areas (mass/kyr) for all deposits are then summed (within each 0.5 kyr bin) and a curve is drawn through the mid-point value for each bin to give the approximate magma flux.

We further plot the approximate magma storage time. This is constructed by:

1. Using the method above (points 1-3) and scaling by the erupted, and corresponding cumulate, mass (see Section A.6.2 for details on how these masses were estimated). A primary melt composition of Mg# 60 is assumed (proxy 1).

2. These estimates, which are placed in 0.5 kyr bins, are then subtracted from an

assumed magma supply rate from the mantle. This gives an approximation of the stored magma mass ($\sim$ stored magma volume).

3. As $\tau \sim V/F$ (V is the stored magma volume and F is the eruptive flux) the magma timescales will follow the same general trend.

4. The plot is illustrated qualitatively, rather than quantitatively, due to the sensitivity to the assumed primary melt composition and magma supply rate from the mantle; these two parameters are still poorly constrained.

A.6.4 Estimation of stress change with depth

To estimate the depth-varying difference in lithospheric stress between the last glacial maximum and post-glacial times (due to ice unloading) we use Darwin's theory (1907-16) for the deformation of an elastic half-space by a periodic load:

$$\sigma = 2\rho g h \frac{2\pi z}{\lambda_w} e^{\frac{-2\pi z}{\lambda_w}}$$

$$\sigma_{max} \text{ occurs at } z = \frac{\lambda_w}{2\pi}$$

For southern Chile we use an ice thickness (h) of 1 km, an ice cap width (λ_w) of 100 km, and an ice density (ρ) of 917 kg/m^3 (e.g., Porter, 1981; Watt et al., 2013a). The lithospheric stress (σ) will increase when a load is present (i.e., due to a glacier during a glacial period). The stress-difference represents the difference in the lithospheric stress as a result of this loading. Fig. A.4, a plot of the stress-difference ($\Delta\sigma$) vs. depth (z) illustrates how the stress difference decays rapidly below 16 km (the depth of maximum stress-difference ($\Delta\sigma_{max}$)) and is <1 MPa at depths >70 km. For an ice sheet of the same thickness estimated to have covered Iceland at the last glacial maximum (λ_w = 400km with all other parameters the same; Geirstdóttir et al., 2000; Maclennan et al., 2002), the maximum stress difference is at 64 km and is <1 MPa at depths >280 km. Therefore the size of the ice sheet and crustal thickness is likely to be an important control on whether there is an appreciable increase in mantle melting during deglaciation. Alternatively it may imply the crust additionally has an inelastic viscous part that causes the response of the magmatic system to lag being glacial unloading (e.g., Jellinck et al., 2014).

Part of this change in stress may be accommodated by faults. There is a major strike slip fault that runs north-south to the west of the volcanic arc called the Liquiñe-Ofqui

Fault Zone (LOFZ). The magnitude, nature and age of past seismic activity along the LOFZ is poorly constrained. For example, despite being regarded as a strike slip fault, no significant Quaternary horizontal offsets have been documented (Lara et al., 2008). However, unloading of ice will cause a change in the vertical stress direction and so would be accommodated by thrust, rather than strike slip fault motion. Vertical displacement (i.e., thrust motion) along the LOFZ has been inferred from relief and changes in the river network. Part of this is speculated to have occurred during the Holocene, potentially caused by isostatic rebound after deglaciation (Lara et al., 2008). Therefore potentially the LOFZ accommodated part of this estimated stress difference.

It should be noted that in terms of directly influencing eruptive behaviour the only volcanic activity the LOFZ is through to directly control are the cinder cones that lie along its trace, which have been proposed to occur due to unclamping of the fault (e.g., Puyuhuapi). There is no clear evidence that it has a direct influence on the major stratovolcanoes, which are the focus of our study.

Although we assume a uniform ice thickness of 1 km and unloading of the ice at 18 kyr there is uncertainty in both of these measurements. Ice thickness measurements are challenging to constrain, are often based on models and vary with topography; thicknesses would be greatest within valleys and thinnest on steep topography. Furthermore, although the glacier equilibrium line is estimated at $\sim$ 1 km below present levels (e.g., Porter, 1981) detailed field mapping in mountain valleys estimate a minimum ice thicknesses at this latitude nearer 0.3 km (unpublished fieldwork by SERNAGEOMIN). To account for this uncertainty we estimate the stress difference with depth for both these ice thicknesses (Fig A.4). Fig A.4 highlights how ice thickness has an important control on the magnitude of depth-varying difference in lithospheric stress; however, even with the lower estimate of ice thickness (0.3 km) the stress change is of the same order of magnitude involved in dyke formation (Rubin, 1995). Pollen and sedimentological studies in Lago Puyehue (ca. 90 km south of Mocho-Choshuenco; Bertrand et al., 2008) indicate that deglaciation was complete by $\sim$14.75 kyr BP, therefore ice retreat (i.e., unloading) occurred over $\sim$3.25 kyr i.e., unloading was not instantaneous. Furthermore, there is uncertainty in the estimate of the onset of deglaciation ($\sim$18 kyr BP at Mocho-Choshuenco). This estimate

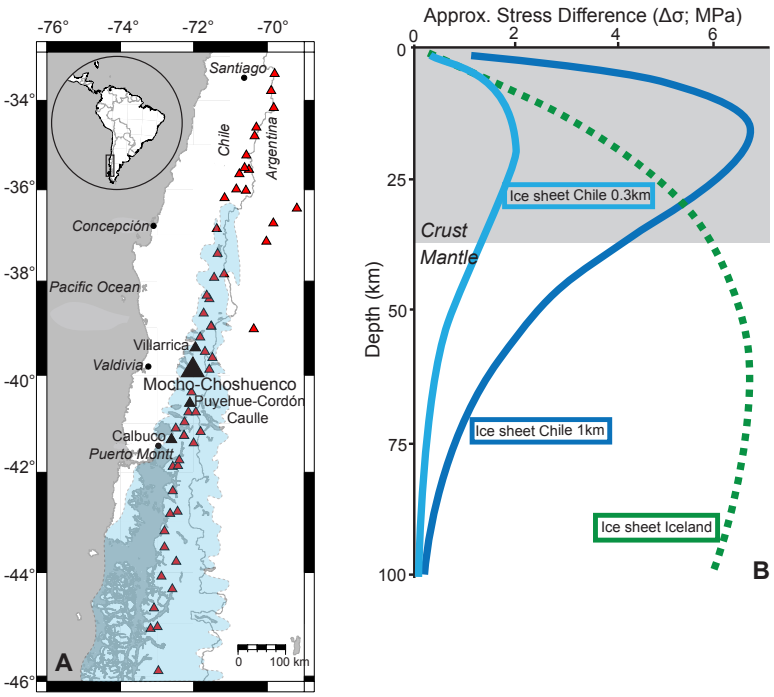

Figure A.4: (A) Map of the Southern Volcanic Zone (SVZ). Volcanoes that have known Holocene activity are marked with red triangles. Mocho-Choshuenco, Villarrica, Puyehue-Cordón Caulle and Calbuco are labelled and marked with black triangles. The extent of the ice sheet during the Llanquihue glaciation is shaded in blue and adapted from Watt et al. (2013a). (B) Plot of the stress difference between the last glacial maximum and after deglaciation versus depth in the lithosphere for an ice sheet of the size estimated for Chile (dark blue 1 km thick and light blue 0.3 km thick ice sheet; i.e., the maximum and minimum thickness estimated for the ice sheet at this latitude) and Iceland (green; 1 km thick)

is constrained from radiocarbon in lake cores, which have significant errors as a result of reservoir effects, and moraines, which represent the greatest ice extent, and not necessarily the onset of deglaciation. The time lag observed between the onset of deglaciation and the first volcanic activity may indicate that deglaciation occurred more recently than prior estimates suggest.

A.7 Whole Rock Method and Analyses

Within this section further details are given on the methodology for major and trace element whole rock analyses. Analyses were obtained for 120 tephra samples taken from Mocho-Choshuenco. The major and trace element compositions are presented in Table A.9.

A.7.1 Whole rock methodology

Major and trace element whole rock analyses were carried out; majors were analysed by X-ray fluorescence spectrometry (XRF) in the Department of Geology, University of Leicester and traces by Inductively Coupled Plasma-Mass Spectroscopy (ICP-MS; solution nebulised on a Thermo Finnigan Element 2 Sector-Field ICP-MS) at the Department of Earth Sciences, University of Oxford.

Most samples were crushed in an agate pestle and mortar. 13 samples were, due to their hardness, crushed in a marble pestle and mortar. An internal check of this methodology highlights no contamination was gained from this method versus the primary method of using just an agate pestle and mortar. All samples were powdered in an agate ball mill. For major analyses approximately 5 g of sample was dried at 110°C and the Loss on Ignition (LOI) was determined by heating at 800-900°C in a furnace for 2 hours. After LOI determination, 0.6 g of sample was homogenised and fused with 3 g of a fine grained, eutectic mixture of lithium metaborate and lithium tetraborate in platinum crucibles. The fusion beads were analysed by XRF along with a selection of secondary standards (BHVO-2, AGV-2, BH-1, WS-1, BCS375, BCS376, MRG-1, JP-1, BCS372/1) that were chosen to bracket the elemental compositions of the unknowns.

For trace analyses, 0.1 g of non-dried powder was digested in HF and HNO_3 at 110°C for 24 hours. Samples were dried and twice redissolved in HNO_3 at 110°C. Final dissolution was in 3.75 ml of HNO3 and ∼4 ml of Milli-Q at 110°C for 12 hours. This final solution was diluted to a volume of 15 ml with Milli-Q. U.S. Geological Survey standards BHVO-2 and AGV-2 were additionally dissolved to verify the results for the unknown samples. For ICP-MS analyses, 20 μml of the sample solution was used for majors (Y,

Zr, Nb, Mo, Pb, P, Sc, V, Cr, Co, Ni, Cu, Zn, Ga, Rb, Sr, Ba, Ce) and 200 μml of the sample solution for trace (Th, U, Cs, La, Pr, Nd, Sm, Eu, Gd, Tb, Dy, Ho, Er, Tm, Yb, Lu, Hf, Ta) analysis. Each sample, major and trace runs, had 200 $_{m}u$ml of an internal standard (I.S.; comprises Rh and Re), which was used to normalise and correct for any drift in the instrument during the run. This solution was diluted with 1780 μml (major and trace run) with HNO_3. In addition to these solutions 18 spikes, per run, were made to correct for matrix affects. Samples for the spikes were chosen so that they bracket the elemental compositions of the unknowns. Six spikes were made for three samples each run. These spikes were made up of 200 μml of I.S., 20 μml (major) or 200 μml (trace) sample solution and varying amounts of a standard, which when diluted with the HNO_3 made up to a 2000 μml solution. The standard comprised of 5 elements that check the sensitivity of low, medium and high molecular mass elements and if there is any oxide or double charged molecules forming in the solution. A quality control (Q.C.; solution of standard and HNO_3) sample was prepared and analysed for each run to check the calibration (i.e., acts as a secondary standard). Blanks were digested alongside the samples and analysed for each run too to detect any potential contamination of samples. Further internal checks were done by running the same sample, powder and solution twice. From all these checks we estimate the total trace element error as approximately 10% of the measurement.

Unit		MC20			MC18 (Hua-Hum)				MC15D (Enco)			MC15C (Enco)	
Sample	124_02F	116_10E	130126_01Dii	130126_01Di	302_03Ci	130126_01B	130129_07A	130107_06A	130106_01B	130131_07A	130108_03G	302_03B	130130_03F
SiO_2	61.95	62.07	63.59	63.24	60.71	60.90	60.92	61.67	57.58	58.22	59.83	59.83	59.98
TiO_2	1.12	1.06	1.04	1.06	1.10	1.14	1.09	1.11	1.18	1.25	1.23	1.25	1.23
Al_2O_3	16.71	16.68	16.45	16.51	17.44	16.88	17.20	16.56	17.79	16.91	16.71	16.75	16.59
Fe_2O_3	6.03	5.66	5.50	5.60	6.57	6.88	6.25	6.26	8.15	8.55	7.90	8.04	7.66
MnO	0.16	0.16	0.16	0.16	0.16	0.16	0.16	0.16	0.16	0.17	0.17	0.18	0.18
MgO	1.89	1.70	1.63	1.70	2.10	2.23	1.86	1.73	2.87	2.73	2.45	2.44	2.27
CaO	4.60	4.23	4.15	4.28	4.81	5.22	4.49	4.33	6.74	6.26	5.50	5.44	5.15
Na_2O	5.27	5.28	5.50	5.48	5.00	5.05	5.12	5.12	4.38	4.65	4.81	4.92	4.99
K_2O	1.41	1.49	1.56	1.53	1.37	1.43	1.48	1.56	1.11	1.16	1.27	1.25	1.33
P_2O_5	0.42	0.37	0.36	0.38	0.36	0.37	0.40	0.38	0.27	0.29	0.32	0.32	0.35
LOI	0.52	1.53	0.26	0.25	1.52	0.16	1.26	1.04	0.14	0.06	0.06	0.17	0.41
Y	39.52	38.58	36.32	37.56	35.97	32.87	40.19	39.14	31.22	33.18	35.38	36.38	37.29
Zr	185.07	186.14	176.42	184.52	185.09	169.96	213.55	196.02	130.14	135.91	146.21	150.77	158.74
Nb	5.31	5.31	4.96	5.13	5.97	5.36	6.63	5.58	3.47	3.58	3.96	3.98	4.24
Mo	1.50	1.50	1.43	1.48	1.43	1.27	1.56	1.57	1.04	1.15	1.19	1.24	1.29
Pb	17.12	17.16	16.24	16.77	17.41	14.89	18.68	17.98	12.83	13.19	14.25	14.35	15.01
P	Over range	Over range	1691	Over range	1852	1801	Over range	Over range	1371	1441	1569	1591	1763
Sc	22.75	20.68	18.92	20.19	23.73	22.68	21.84	22.29	29.55	31.39	28.47	29.27	27.72
V	80.52	63.53	52.73	57.98	108.58	115.21	86.14	91.40	200.07	219.92	159.74	163.14	137.64
Cr	1.66	0.85	0.18	0.17	2.30	0.25	1.48	1.33	11.94	3.82	2.20	0.90	0.93
Co	8.07	6.68	5.30	5.89	10.29	10.48	9.10	9.51	18.30	18.11	14.47	15.27	13.42
Ni	Below DL	Below DL	Below DL	Below DL	1.24	Below DL	Below DL	Below DL	7.34	2.84	1.35	Below DL	Below DL
Cu	6.37	6.55	4.65	4.42	12.82	10.90	10.93	20.75	35.35	41.68	26.78	26.85	21.68
Zn	112.26	104.79	97.50	102.62	103.16	101.66	106.52	104.14	105.18	111.41	109.21	111.12	108.65
Ga	24.28	23.00	21.30	22.46	24.02	21.88	23.74	23.00	24.05	23.97	23.42	23.85	23.74
Rb	37.69	36.99	35.74	34.04	35.00	30.30	37.00	38.35	27.43	28.86	31.15	31.36	33.68
Sr	528	474	430	454	494	481	499	435	540	493	474	479	460
Ba	548	535	511	532	514	491	582	548	396	403	436	440	466
Ce	50.68	49.04	46.62	47.78	52.37	46.03	58.88	52.14	34.55	36.48	38.89	41.71	41.57
Th	4.17	4.33	4.49	4.29	4.76	4.55	4.83	4.50	3.25	3.43	3.93	3.85	4.20
U	1.20	1.26	1.31	1.26	1.35	1.30	1.38	1.33	0.96	1.01	1.14	1.13	1.21
Cs	2.52	2.63	2.80	2.64	2.64	2.50	2.49	2.65	2.00	2.11	2.35	2.32	2.46
La	20.35	20.43	20.70	20.03	22.45	21.99	24.26	21.15	14.76	15.31	17.11	17.28	18.31
Pr	6.62	6.39	6.62	6.44	6.94	6.61	7.41	6.67	4.78	4.99	5.65	5.62	6.09
Nb	30.15	30.36	30.31	29.36	28.34	29.80	33.84	31.75	21.75	22.92	25.01	26.48	27.14
Sm	6.98	7.35	7.29	7.02	6.75	6.69	7.84	7.74	5.47	5.94	6.36	6.40	6.75
Eu	2.07	2.04	2.05	2.04	1.90	2.02	2.11	1.95	1.70	1.74	1.87	1.87	2.00
Gd	7.31	7.46	7.48	7.17	6.69	7.19	7.95	7.78	5.70	5.98	6.64	6.99	7.06
Tb	1.17	1.16	1.18	1.16	1.00	1.10	1.23	1.20	0.93	0.98	1.06	1.11	1.12
Dy	7.08	7.22	7.21	6.97	6.40	6.94	7.46	7.48	5.87	6.40	6.64	6.87	6.99
Ho	1.46	1.49	1.50	1.41	1.36	1.39	1.53	1.53	1.19	1.28	1.40	1.40	1.49
Er	4.28	4.27	4.43	4.08	3.94	4.11	4.49	4.59	3.55	3.75	4.07	4.18	4.42
Tm	0.61	0.61	0.62	0.61	0.57	0.57	0.66	0.64	0.51	0.56	0.58	0.58	0.64
Yb	4.01	4.03	4.16	3.90	3.86	3.90	4.24	4.25	3.37	3.51	4.00	3.95	4.16
Lu	0.62	0.61	0.65	0.60	0.57	0.58	0.67	0.65	0.49	0.52	0.58	0.58	0.63
Hf	4.96	5.20	5.42	5.22	4.90	5.16	5.73	5.44	3.73	3.91	4.34	4.36	4.89
Ta	0.31	0.30	0.34	0.30	0.32	0.31	0.38	0.32	0.20	0.21	0.23	0.23	0.25

Unit	MC15C	MC15B (Enco)		MC14		MC12				MC10G	MC10D		MC9 (huilo)
Sample	115_04E	229_02C	115_01F	115_04Cii	115_04Ci	130111_09A	130111_12Aii	130111_12Ai	229_02A	115_03I	115_03E	115_03F	130126_06Ai
SiO_2	59.73	57.44	59.39	57.25	57.25	56.43	57.66	58.15	61.06	47.24	48.25	46.36	65.18
TiO_2	1.24	1.29	1.26	1.34	1.34	1.14	1.14	1.14	1.10	1.16	1.11	1.21	0.88
Al_2O_3	16.35	17.12	16.29	17.24	17.24	18.06	18.01	17.99	17.05	21.55	21.57	22.18	15.63
Fe_2O_3	7.77	8.88	8.13	8.87	8.87	7.37	7.33	7.29	6.93	10.49	10.05	10.80	4.56
MnO	0.18	0.18	0.17	0.19	0.19	0.17	0.17	0.17	0.17	0.13	0.13	0.12	0.16
MgO	2.30	2.74	2.53	2.47	2.47	1.34	1.41	1.40	1.44	4.50	4.47	4.08	1.19
CaO	5.29	6.23	5.53	5.53	5.53	3.53	3.68	3.69	3.79	8.12	7.82	7.61	3.14
Na_2O	5.21	4.52	4.98	4.51	4.51	4.54	4.66	4.74	5.13	2.67	2.67	2.52	4.99
K_2O	1.31	1.13	1.27	1.15	1.15	1.47	1.49	1.52	1.64	0.44	0.45	0.36	2.35
P_2O_5	0.33	0.26	0.31	0.32	0.32	0.35	0.36	0.37	0.36	0.21	0.18	0.20	0.25
LOI	0.02	0.23	0.08	1.16	1.16	5.69	4.25	3.99	2.18	3.49	3.52	4.65	1.65
Y	37.06	37.00	35.03	36.46	36.58	49.39	46.29	46.58	45.14	20.95	22.03	20.50	48.32
Zr	157.67	147.81	147.50	153.25	153.87	247.70	231.17	235.63	225.50	101.99	95.35	103.58	234.00
Nb	4.21	3.76	3.97	3.95	3.93	6.04	5.73	5.83	5.61	2.92	2.21	3.00	5.37
Mo	1.29	1.25	1.22	1.17	1.18	1.64	1.63	1.70	1.72	0.51	0.50	0.40	2.09
Pb	15.24	15.07	14.14	13.90	14.23	20.97	22.25	22.80	21.06	8.90	8.78	9.55	22.53
P	1639	1468	1536	1514	1554	1711	1781	1800	1766	954	799	898	1233
Sc	27.77	35.59	28.64	29.49	30.63	26.37	25.11	24.70	23.42	34.94	32.78	33.45	18.57
V	136.32	254.17	163.35	179.38	186.20	64.57	56.48	53.33	52.05	281.82	259.23	265.68	42.90
Cr	0.78	2.89	0.75	3.31	3.46	2.15	2.26	1.08	1.35	73.97	58.61	69.70	0.18
Co	12.99	20.80	14.50	15.98	16.02	9.39	8.09	7.68	7.71	29.80	28.46	27.31	4.64
Ni	Below DL	2.31	Below DL	Below DL	Below DL	Below DL	Below DL	Below DL	Below DL	37.21	31.86	31.86	0.01
Cu	22.74	41.92	23.76	24.76	25.96	28.79	20.50	19.54	18.38	76.20	70.86	77.00	8.93
Zn	113.04	127.24	110.60	103.82	106.57	105.90	106.59	108.92	112.13	66.09	67.08	58.24	100.90
Ga	23.51	27.30	23.23	23.19	24.32	23.96	25.03	25.44	24.42	24.14	23.26	24.09	22.24
Rb	33.47	32.14	31.90	29.26	29.94	39.25	38.53	39.08	42.01	10.03	10.33	7.46	58.97
Sr	466	538	470	440	446	344	360	358	379	514	469	500	337
Ba	465	440	432	394	410	510	513	523	562	203	186	182	630
Ce	41.56	38.90	38.21	39.37	40.64	54.85	54.44	54.58	55.58	25.68	21.84	23.32	53.66
Th	4.21	3.58	3.90	4.22	4.18	6.29	6.52	6.82	6.28	2.92	2.36	2.85	6.52
U	1.23	1.04	1.14	1.23	1.20	1.83	1.78	1.87	1.73	0.71	0.66	0.67	1.94
Cs	2.53	2.09	2.34	2.32	2.24	3.01	2.92	3.16	3.14	0.73	0.86	0.59	4.65
La	18.97	15.44	17.70	17.55	17.24	25.26	22.94	23.81	22.60	10.72	10.36	11.19	23.00
Pr	6.07	5.09	5.75	5.67	5.75	7.83	7.70	7.83	7.44	3.62	3.54	3.68	7.43
Nb	26.52	23.08	24.51	26.50	26.82	36.79	35.44	36.05	36.05	18.56	17.97	18.93	33.54
Sm	6.81	6.14	6.22	6.64	6.69	8.96	8.79	8.90	9.28	4.40	4.57	4.62	8.21
Eu	1.97	1.78	1.83	1.95	2.01	2.36	2.32	2.34	2.34	1.44	1.43	1.41	2.08
Gd	7.32	6.39	6.58	7.02	7.26	9.27	9.08	9.19	9.10	4.63	4.73	4.55	8.87
Tb	1.14	1.00	1.02	1.13	1.15	1.42	1.47	1.42	1.45	0.74	0.74	0.72	1.39
Dy	7.19	6.47	6.62	7.29	7.30	9.24	9.06	9.43	8.97	4.53	4.87	4.68	8.92
Ho	1.48	1.31	1.33	1.47	1.47	1.83	1.84	1.85	1.87	0.89	0.94	0.90	1.79
Er	4.29	3.96	4.07	4.32	4.35	5.40	5.39	5.61	5.61	2.73	2.86	2.62	5.35
Tm	0.62	0.56	0.58	0.62	0.63	0.78	0.79	0.80	0.77	0.37	0.41	0.38	0.78
Yb	4.23	3.82	3.80	4.20	4.12	5.24	5.24	5.25	5.22	2.51	2.59	2.44	5.32
Lu	0.61	0.57	0.58	0.64	0.62	0.79	0.80	0.79	0.79	0.35	0.42	0.37	0.81
Hf	4.66	3.95	4.28	4.58	4.67	7.06	6.76	6.96	6.80	3.03	3.08	3.24	6.78
Ta	0.25	0.20	0.24	0.24	0.25	0.37	0.33	0.33	0.35	0.18	0.14	0.20	0.32

Unit	MC9 (Huilo)							MC5 (Pirehueico)					
Sample	130107_05Hii	130107_05Hi	130107_05G	130107_05F	130107_05E	130111_04A	130107_05D	130107_05Jii	130107_05Iii	130107_05Ii	130107_05L	130107_05K	130107_05Jib
SiO_2	62.80	63.24	62.22	62.71	63.13	52.98	63.91	63.71	61.56	62.85	64.40	62.92	62.80
TiO_2	0.89	0.88	0.90	0.87	0.84	1.23	0.80	0.75	0.80	0.75	0.77	0.78	0.78
Al_2O_3	16.73	16.63	16.73	16.85	16.91	22.73	16.31	16.39	18.01	17.14	17.50	17.00	17.49
Fe_2O_3	4.88	4.87	5.05	4.68	4.53	6.86	4.31	4.90	4.50	4.20	4.28	4.44	4.36
MnO	0.17	0.18	0.17	0.16	0.15	0.19	0.16	0.14	0.14	0.14	0.15	0.14	0.14
MgO	1.29	1.29	1.34	1.18	1.09	1.15	1.11	1.69	1.13	1.06	1.08	1.18	1.06
CaO	3.35	3.37	3.42	3.17	3.01	2.73	3.04	4.02	2.97	2.91	2.98	3.03	2.97
Na_2O	5.05	5.08	4.92	4.91	4.99	3.62	5.25	5.23	5.07	5.32	5.42	5.28	5.17
K_2O	1.57	1.58	1.51	1.56	1.61	1.01	1.68	1.76	1.64	1.73	1.80	1.74	1.74
P_2O_5	0.24	0.25	0.25	0.25	0.27	0.28	0.22	0.17	0.26	0.25	0.25	0.27	0.25
LOI	3.05	2.70	3.36	3.70	3.61	7.08	3.27	0.95	4.01	3.68	1.48	3.28	3.22
Y	43.73	42.36	42.51	42.93	40.60	49.02	41.54	36.92	41.18	41.81	38.85	51.00	44.29
Zr	206.09	201.45	201.36	207.75	214.47	258.70	204.73	196.97	241.38	238.13	222.34	280.03	235.76
Nb	5.24	5.10	5.09	5.24	5.31	6.28	5.15	4.77	5.75	5.66	5.35	6.69	5.67
Mo	1.52	1.51	1.45	1.51	1.51	1.16	1.58	1.85	1.52	1.66	1.57	2.02	1.61
Pb	20.37	19.58	19.69	20.59	21.33	24.50	20.36	19.24	22.76	22.79	20.63	26.62	22.86
P	1220	1229	1221	1212	1283	1281	1078	841	1255	1230	1119	1644	1243
Sc	19.04	18.18	19.15	17.84	16.46	24.25	16.70	17.85	15.63	14.94	14.52	19.59	15.96
V	48.69	47.79	52.85	38.92	33.25	64.01	33.02	88.91	42.03	39.21	38.25	59.86	40.70
Cr	0.34	0.15	0.56	0.44	0.20	1.17	0.40	12.65	1.84	0.87	1.15	2.53	1.18
Co	4.63	4.54	4.95	3.48	2.90	5.69	3.09	9.23	3.91	3.48	3.44	5.53	3.65
Ni	Below DL	Below DL	Below DL	Below DL	Below DL	Below DL	Below DL	7.26	Below DL	Below DL	Below DL	1.83	Below DL
Cu	4.77	4.80	4.57	3.71	3.48	5.90	3.60	20.26	6.56	5.78	5.77	12.34	9.29
Zn	112.19	110.06	107.59	104.13	98.91	81.91	103.22	88.77	100.99	92.89	81.70	106.78	92.89
Ga	23.22	23.08	23.15	23.64	22.61	27.45	22.81	21.99	22.37	22.05	20.74	26.12	22.24
Rb	44.15	37.67	42.97	43.98	44.24	25.43	42.59	46.65	43.05	47.07	44.93	57.93	46.68
Sr	372	366	372	365	342	262	343	358	407	373	327	429	394
Ba	668	655	668	668	621	376	609	591	753	666	579	754	672
Ce	51.27	50.24	49.57	50.45	48.03	60.09	48.92	47.41	55.28	54.73	54.31	66.12	52.65
Th	5.40	5.51	5.42	5.61	5.77	6.81	5.58	6.18	7.30	7.19	7.32	7.22	7.33
U	1.57	1.60	1.57	1.61	1.64	1.98	1.66	1.77	1.95	1.94	1.93	1.89	1.99
Cs	4.73	4.67	4.80	4.73	4.27	2.00	4.12	3.60	3.47	3.66	3.71	3.56	3.49
La	21.25	21.26	20.70	20.62	21.13	24.97	20.50	21.45	23.09	23.55	23.35	22.83	22.35
Pr	6.72	6.75	6.59	6.68	6.68	8.19	6.49	6.48	6.96	7.16	7.31	7.10	7.15
Nb	28.99	30.27	31.56	30.74	30.10	37.51	29.99	28.04	31.39	31.24	30.40	32.10	33.44
Sm	7.05	7.45	7.85	7.27	7.06	8.85	7.34	6.62	7.34	7.38	7.03	7.40	7.89
Eu	1.79	1.84	2.03	1.92	1.83	2.37	1.95	1.71	1.97	1.94	1.96	1.96	1.99
Gd	7.43	7.56	8.22	8.01	7.64	9.30	7.64	6.60	7.59	7.20	7.61	7.79	8.03
Tb	1.17	1.26	1.29	1.27	1.23	1.49	1.19	1.06	1.25	1.21	1.20	1.20	1.28
Dy	7.37	7.65	7.91	7.88	7.37	9.46	7.51	6.64	7.75	7.46	7.39	7.50	7.84
Ho	1.53	1.62	1.67	1.62	1.56	1.90	1.56	1.41	1.59	1.59	1.55	1.60	1.68
Er	4.61	4.87	5.09	4.88	4.51	5.72	4.77	4.33	4.85	4.66	4.60	4.71	5.00
Tm	0.68	0.68	0.74	0.72	0.69	0.85	0.69	0.63	0.71	0.68	0.67	0.69	0.73
Yb	4.41	4.76	4.84	4.96	4.57	5.60	4.66	4.28	4.78	4.79	4.56	4.70	4.86
Lu	0.68	0.73	0.72	0.75	0.68	0.87	0.72	0.63	0.74	0.72	0.69	0.72	0.78
Hf	5.42	5.83	5.89	6.05	6.08	7.26	5.96	5.72	7.18	6.75	6.67	6.53	6.89
Ta	0.28	0.30	0.32	0.33	0.32	0.39	0.30	0.30	0.36	0.38	0.35	0.35	0.36

Unit	MC5 (Pirehueico)	MC4 (Neltume)											
Sample	130207_10A	130111_02Bi	130130_05Biii	130130_05ciii	130111_02Bii	130130_05Di	130130_05Dii	130130_05Ci	130130_05Cii	130130_05Biv	130130_05Bii	130130_05Bi	130130_05A
SiO_2	56.79	52.66	52.16	57.80	51.52	56.90	56.79	53.95	55.01	58.41	59.03	63.13	64.33
TiO_2	0.90	1.24	1.27	1.18	1.12	0.89	0.89	0.84	0.87	0.83	0.73	0.77	0.69
Al_2O_3	21.09	17.65	17.59	17.29	18.86	20.52	20.56	23.05	22.38	19.78	20.38	21.74	21.22
Fe_2O_3	4.99	10.38	10.74	8.65	9.90	5.74	5.69	5.20	5.36	5.03	4.46	4.75	4.34
MnO	0.16	0.18	0.17	0.17	0.16	0.15	0.15	0.17	0.16	0.15	0.17	0.14	0.14
MgO	1.06	4.29	4.47	3.06	4.66	1.41	1.36	0.71	0.86	0.96	0.65	0.66	0.58
CaO	2.78	8.88	8.78	6.27	9.88	3.29	3.20	2.22	2.41	2.66	2.06	2.15	1.95
Na_2O	4.55	3.78	3.70	4.31	3.37	4.47	4.46	3.64	3.94	4.45	4.36	4.58	4.81
K_2O	1.37	0.64	0.59	1.14	0.52	1.35	1.36	1.30	1.34	1.48	1.64	1.73	1.89
P_2O_5	0.23	0.15	0.15	0.26	0.13	0.24	0.23	0.21	0.22	0.22	0.17	0.17	0.15
LOI	5.83	0.46	0.65	0.66	0.26	5.10	5.23	8.14	7.10	6.08	6.44	6.60	6.57
Y	41.07	21.23	21.62	31.72	18.77	37.40	36.54	56.73	49.78	57.13	55.54	53.75	51.02
Zr	259.93	71.60	71.20	106.77	58.77	284.12	292.65	346.24	329.80	298.12	319.11	318.33	330.39
Nb	6.33	1.78	1.75	4.22	1.47	7.45	7.58	8.64	8.42	7.81	8.37	8.24	8.51
Mo	1.39	0.61	0.59	0.93	0.51	1.52	1.49	1.55	1.62	1.63	1.76	1.63	1.78
Pb	24.76	7.32	7.47	12.72	5.79	25.20	25.86	30.90	29.70	27.45	30.38	28.90	29.53
P	1001	727	733	1340	620	1131	1064	953	999	1151	806	738	640
Sc	16.48	40.05	40.66	29.07	39.22	20.27	20.53	18.56	19.07	19.41	16.45	15.16	15.09
V	41.07	357.57	373.55	219.39	340.27	83.80	83.89	34.38	42.12	33.51	18.45	17.86	15.53
Cr	1.19	28.47	27.14	14.42	44.04	3.05	3.14	1.46	1.71	0.83	0.28	0.41	0.59
Co	4.25	29.53	30.83	20.70	30.83	6.76	7.46	3.71	4.30	3.65	2.53	2.09	1.88
Ni	Below DL	Below DL	Below DL	8.48	Below DL	Below DL	Below DL	Below DL	Below DL	Below DL	1.32	Below DL	Below DL
Cu	5.85	65.10	82.19	41.90	68.28	12.11	11.26	9.58	8.75	6.72	6.79	6.23	6.01
Zn	68.59	104.80	103.43	105.90	92.03	77.25	75.53	60.49	63.67	82.27	76.69	69.38	69.26
Ga	25.11	23.78	23.08	23.48	23.23	25.87	25.96	27.07	26.37	27.59	26.36	24.67	25.37
Rb	33.24	14.73	13.34	28.98	12.11	35.98	35.63	33.27	33.90	41.76	43.02	41.71	46.71
Sr	307	592	575	489	628	350	340	227	255	327	248	230	221
Ba	453	248	220	375	202	476	486	420	428	515	523	510	542
Ce	58.94	21.48	20.04	39.70	17.06	55.83	57.71	73.94	69.33	62.44	68.53	61.88	63.88
Th	8.27	1.55	1.50	3.66	1.30	7.77	7.67	9.62	9.33	7.48	9.11	8.89	9.14
U	2.45	0.50	0.49	1.02	0.41	2.24	2.21	2.73	2.67	2.27	2.66	2.54	2.61
Cs	2.61	1.14	0.98	2.78	0.92	2.54	2.55	2.39	2.48	2.82	3.16	3.05	3.28
La	24.83	8.12	8.51	17.29	6.97	19.76	20.46	33.00	29.36	31.43	35.16	32.92	30.90
Pr	8.01	2.92	3.02	5.53	2.55	6.75	6.74	10.18	9.59	9.32	9.99	9.80	9.42
Nb	36.64	14.57	14.06	23.50	13.06	31.60	29.90	46.29	40.41	37.15	38.90	40.71	37.05
Sm	8.72	3.74	3.76	5.90	3.44	7.68	7.51	10.84	9.28	8.63	8.94	9.11	8.53
Eu	2.20	1.38	1.35	1.76	1.24	2.06	1.97	2.41	2.19	2.07	1.95	1.91	1.94
Gd	8.64	4.30	4.10	6.09	3.73	7.67	7.36	10.55	9.42	8.58	8.99	9.42	8.37
Tb	1.40	0.67	0.65	0.98	0.60	1.23	1.19	1.73	1.48	1.36	1.42	1.53	1.36
Dy	8.78	4.21	4.28	6.16	3.92	7.93	7.84	10.67	9.69	8.66	9.22	9.63	8.65
Ho	1.81	0.88	0.86	1.24	0.78	1.59	1.56	2.23	1.96	1.81	1.88	1.98	1.78
Er	5.50	2.54	2.48	3.66	2.32	4.81	4.58	6.74	5.86	5.55	5.93	6.19	5.45
Tm	0.82	0.35	0.34	0.51	0.33	0.71	0.68	1.00	0.88	0.80	0.87	0.91	0.84
Yb	5.74	2.36	2.30	3.40	2.10	5.02	4.80	6.70	6.14	5.57	5.92	6.15	5.76
Lu	0.85	0.35	0.36	0.48	0.31	0.76	0.74	1.01	0.91	0.81	0.88	0.94	0.87
Hf	8.15	2.25	2.19	3.09	1.87	8.29	8.29	9.97	8.93	7.36	8.50	9.08	8.85
Ta	0.40	0.11	0.11	0.25	0.10	0.46	0.45	0.56	0.53	0.41	0.49	0.53	0.51

Unit	MC4 (Neltume)							MC3			MC1	
Sample	117_01B	130108_05A	130120_16Aii	130120_16Aiiib	130111_01A	130120_16Ai	130120_16Aiiia	130108_05Ciii	130108_05Ci	130108_05Cii	130116_11E	115_01A
SiO_2	57.94	60.65	65.71	67.89	67.09	64.01	67.89	52.03	55.00	58.77	51.38	52.00
TiO_2	0.66	0.75	0.54	0.64	0.60	0.58	0.64	1.04	0.97	0.89	1.39	1.40
Al_2O_3	21.19	18.49	15.67	16.40	15.78	16.28	16.40	20.82	19.36	17.05	18.20	18.15
Fe_2O_3	4.22	4.69	3.31	3.85	3.62	3.72	3.85	8.76	8.08	7.66	9.41	9.41
MnO	0.11	0.15	0.13	0.14	0.14	0.13	0.14	0.13	0.14	0.16	0.16	0.16
MgO	0.50	1.00	0.61	0.87	0.80	0.80	0.87	2.53	2.58	2.99	4.99	5.09
CaO	1.62	2.80	1.98	2.58	2.49	2.47	2.58	5.38	5.68	6.21	9.09	9.09
Na_2O	4.10	4.69	5.17	5.46	5.64	4.85	5.46	3.28	3.84	4.39	3.38	3.67
K_2O	1.65	1.64	2.17	2.12	2.14	1.97	2.12	0.82	1.00	1.29	1.34	1.38
P_2O_5	0.10	0.20	0.11	0.15	0.15	0.12	0.15	0.21	0.19	0.15	0.50	0.50
LOI	7.80	5.01	4.16	3.16	1.74	5.05	3.16	4.97	3.34	0.74	0.19	0.11
Y	45.84	46.54	42.83	42.52	42.70	41.30	61.35	32.86	31.19	31.52	29.21	28.88
Zr	350.02	267.02	261.42	245.08	244.59	251.45	352.53	190.02	178.11	152.34	216.97	216.91
Nb	8.69	7.10	6.84	6.51	6.47	6.56	9.46	4.80	4.49	3.87	14.12	14.09
Mo	1.52	1.62	2.04	1.94	2.05	1.85	2.83	0.83	0.96	1.25	1.35	1.41
Pb	25.97	25.48	24.37	22.50	22.39	22.88	32.48	16.07	16.19	13.89	38.71	10.84
P	451	986	567	736	734	594	1076	954	916	763	Over range	Over range
Sc	14.96	17.82	12.22	13.64	13.14	13.33	19.78	31.67	29.88	30.14	30.68	30.27
V	29.23	37.98	10.27	20.45	15.63	26.00	29.82	172.83	167.98	193.47	251.01	254.84
Cr	2.60	1.44	0.12	0.69	0.36	2.14	1.02	24.32	21.06	19.84	82.13	85.43
Co	3.14	4.08	1.66	2.58	2.09	2.98	3.67	15.51	15.63	19.49	29.76	30.42
Ni	Below DL	Below DL	Below DL	Below DL	Below DL	Below DL	Below DL	Below DL	Below DL	Below DL	32.33	35.04
Cu	15.42	9.01	3.74	4.66	3.80	8.31	6.64	48.38	46.00	53.81	70.68	73.99
Zn	67.76	89.48	84.17	86.59	91.05	82.36	126.58	69.23	78.95	98.27	93.70	92.49
Ga	18.18	24.76	21.36	21.54	22.07	21.74	31.36	23.51	23.22	22.15	21.55	21.93
Rb	42.37	43.90	59.32	56.75	59.47	55.78	82.29	20.34	25.73	33.52	32.06	32.31
Sr	193	318	245	293	311	288	432	335	394	397	795	807
Ba	491	561	738	683	691	763	Over range	284	356	416	547	558
Ce	57.55	56.79	57.76	56.25	55.99	55.45	80.04	34.31	35.78	36.08	69.29	69.28
Th	9.95	8.11	7.70	6.97	6.81	7.27	6.98	5.26	5.24	4.40	5.01	4.98
U	2.00	2.37	2.20	2.01	2.03	2.09	2.02	1.32	1.34	1.32	1.31	1.31
Cs	3.09	3.33	5.48	4.80	4.34	6.31	4.90	1.59	1.91	2.42	1.33	1.41
La	29.24	27.00	25.06	24.09	24.33	24.39	24.89	19.00	18.38	16.16	32.46	33.43
Pr	7.96	8.00	7.45	7.22	7.29	7.17	7.44	5.87	5.70	4.80	9.10	9.00
Nb	33.12	34.35	32.25	29.75	30.23	30.44	30.15	28.05	25.63	22.41	41.72	40.73
Sm	7.59	8.01	7.21	6.80	7.18	7.34	7.11	6.58	6.10	5.53	8.21	8.15
Eu	1.78	1.67	1.66	1.71	1.69	1.65	1.76	1.76	1.75	1.59	2.39	2.26
Gd	7.36	8.32	7.50	6.83	7.01	7.17	7.25	6.81	6.43	5.79	7.42	7.12
Tb	1.18	1.30	1.22	1.15	1.16	1.17	1.18	1.07	1.03	0.94	1.07	1.01
Dy	7.61	8.56	7.63	6.99	7.21	7.43	7.48	7.29	6.65	6.14	6.30	6.54
Ho	1.56	1.76	1.59	1.50	1.48	1.55	1.50	1.43	1.33	1.22	1.22	1.20
Er	4.78	5.32	4.86	4.47	4.57	4.70	4.67	4.35	4.00	3.68	3.52	3.51
Tm	0.70	0.79	0.72	0.66	0.68	0.72	0.69	0.62	0.57	0.52	0.49	0.47
Yb	4.94	5.26	4.99	4.64	4.63	4.80	4.63	4.08	3.94	3.70	3.16	3.17
Lu	0.73	0.81	0.75	0.70	0.71	0.72	0.72	0.62	0.59	0.55	0.49	0.47
Hf	9.59	7.60	7.43	6.47	6.54	7.12	6.70	5.73	5.58	4.56	5.59	5.36
Ta	0.54	0.45	0.43	0.39	0.40	0.40	0.38	0.33	0.31	0.25	0.85	0.85

Unit	Fui Cones												
Sample	130107_01A	130120_06A	130130_04A	130130_02D	130107_01B	130111_08A	226_05A	130108_03C*	130108_02A	130108_08C	130108_03D	130107_02B	130122_02A
SiO_2	49.62	43.54	48.92	49.17	45.97	51.36	50.96	50.21	52.21	52.02	52.15	55.07	55.14
TiO_2	1.20	1.11	1.19	1.27	1.39	1.10	1.49	1.29	1.29	1.49	1.57	1.11	0.96
Al_2O_3	18.18	22.88	18.27	18.65	19.76	17.61	17.25	20.22	19.03	17.39	18.18	17.32	19.51
Fe_2O_3	9.98	10.57	10.20	10.01	10.96	9.40	11.14	10.18	9.99	11.12	11.00	9.09	7.99
MnO	0.16	0.13	0.17	0.17	0.16	0.15	0.17	0.17	0.16	0.18	0.18	0.16	0.14
MgO	7.19	4.80	7.80	7.15	7.69	7.55	4.31	3.53	3.57	4.36	3.36	4.49	2.47
CaO	7.87	7.40	8.16	8.46	7.50	8.90	8.00	8.47	7.99	8.18	6.81	7.91	5.30
Na_2O	2.79	2.41	2.62	3.25	2.65	2.91	3.77	3.29	3.54	3.74	3.61	3.90	3.77
K_2O	0.85	0.31	0.76	0.95	0.72	0.77	0.64	0.61	0.78	0.66	0.91	0.88	1.09
P_2O_5	0.34	0.14	0.29	0.39	0.43	0.33	0.31	0.23	0.22	0.30	0.29	0.21	0.18
LOI	2.01	7.07	1.76	0.68	2.91	-0.06	1.05	2.10	1.47	0.73	2.05	-0.20	3.36
Y	24.09	17.47	23.07	22.63	24.69	21.24	28.18	24.16	26.03	28.26	33.00	24.45	33.58
Zr	157.85	91.92	161.40	166.69	174.63	82.84	101.37	100.31	108.36	100.49	147.28	94.43	186.31
Nb	9.94	2.14	9.67	11.24	12.34	6.59	2.93	2.38	2.71	2.94	3.73	2.55	4.83
Mo	0.83	0.74	0.62	0.92	0.84	1.32	0.70	0.67	0.83	0.74	1.04	0.84	1.08
Pb	13.84	8.98	9.28	14.30	15.01	6.34	9.04	9.44	11.01	8.82	12.49	9.62	16.88
P	1589	602	1270	1790	Over range	1511	1516	969	1112	1516	1380	1017	817
Sc	27.94	29.83	26.66	28.00	29.50	27.90	42.63	35.30	37.06	44.42	41.53	32.18	28.15
V	192.57	262.78	171.41	212.04	220.46	225.63	386.64	310.55	336.80	393.61	371.03	250.56	170.09
Cr	199.65	65.77	213.54	168.74	203.01	274.79	10.75	25.13	25.56	11.69	13.60	53.98	20.69
Co	41.76	29.60	41.73	40.69	43.04	37.54	29.28	24.64	25.72	29.89	25.89	27.34	15.75
Ni	139.41	44.89	123.23	114.19	125.15	134.16	Below DL	Below DL	Below DL	Below DL	Below DL	32.53	Below DL
Cu	63.69	67.32	61.26	59.34	53.15	9.55	51.01	82.81	88.83	49.12	109.49	44.49	50.74
Zn	93.14	57.55	92.83	95.83	77.65	77.37	104.92	76.33	92.59	105.59	98.58	98.26	80.56
Ga	20.60	23.65	20.46	20.94	21.67	19.15	24.60	22.67	24.32	24.62	25.38	21.84	22.83
Rb	23.43	6.46	41.13	20.62	14.63	14.58	15.47	13.32	19.11	15.93	22.79	22.09	28.88
Sr	883	428	781	Over range	792	707	552	485	518	560	457	516	344
Ba	878	132	441	825	626	468	261	219	297	264	320	329	365
Ce	64.32	19.14	52.24	67.87	66.39	44.95	28.35	28.23	31.61	28.11	36.21	28.12	36.30
Th	7.92	2.01	3.76	8.56	8.57	4.18	2.32	3.57	3.81	2.25	3.88	2.88	5.07
U	1.90	0.57	0.94	1.82	1.92	0.82	0.73	0.93	0.98	0.70	1.07	0.83	1.36
Cs	2.14	0.56	1.04	1.27	0.89	0.47	1.19	1.18	1.42	1.19	1.72	1.59	1.99
La	31.23	7.58	24.10	31.84	32.64	22.66	12.93	13.54	13.43	12.08	15.60	12.29	18.02
Pr	8.13	2.78	7.03	8.13	8.79	6.04	4.30	4.55	4.29	4.05	5.30	3.99	5.45
Nb	34.24	13.42	31.00	35.03	37.12	26.47	21.63	22.32	20.19	19.92	26.19	17.95	25.64
Sm	6.73	3.52	6.34	6.98	7.21	5.44	5.59	5.42	5.16	4.98	6.47	4.60	6.15
Eu	1.97	1.15	1.91	2.04	2.22	1.65	1.72	1.68	1.57	1.63	1.93	1.49	1.66
Gd	5.91	3.69	5.78	5.79	6.43	5.04	5.91	5.72	5.48	5.17	6.80	4.99	6.33
Tb	0.82	0.60	0.85	0.84	0.90	0.73	0.90	0.90	0.84	0.80	1.08	0.79	1.01
Dy	4.97	3.81	5.06	5.05	5.25	4.70	6.01	5.79	5.42	5.38	7.10	4.77	6.54
Ho	0.96	0.75	0.97	0.96	1.01	0.89	1.19	1.19	1.07	1.08	1.43	1.02	1.32
Er	2.74	2.21	2.80	2.73	2.96	2.53	3.47	3.59	3.22	3.19	4.25	2.89	3.93
Tm	0.38	0.31	0.38	0.38	0.41	0.35	0.48	0.51	0.47	0.45	0.59	0.42	0.58
Yb	2.55	2.11	2.56	2.50	2.71	2.29	3.15	3.17	3.02	2.90	3.89	2.75	3.98
Lu	0.39	0.31	0.39	0.36	0.40	0.35	0.49	0.49	0.45	0.42	0.59	0.39	0.59
Hf	3.92	2.79	4.21	4.21	4.44	2.58	3.15	3.41	3.44	2.87	4.58	2.87	5.57
Ta	0.62	0.13	0.60	0.68	0.79	0.39	0.17	0.17	0.17	0.16	0.23	0.16	0.31

Unit	Fui Cones												
Sample	130108_01C	130115_03B	227_01A	130121_10A	130116_03A	130108_08Bii	130107_02C	130129_04A	130107_02D	130116_02A	130115_04A	130108_01G	124_06Ai
SiO_2	53.67	54.20	55.10	50.08	53.78	56.01	55.06	56.33	54.59	56.48	56.35	56.80	57.02
TiO_2	1.52	1.51	1.11	1.16	1.54	1.47	1.10	1.27	1.09	1.45	1.41	1.40	1.45
Al_2O_3	17.66	17.19	17.59	18.00	17.55	16.55	17.44	17.71	17.57	16.59	17.04	16.96	16.40
Fe_2O_3	10.35	10.49	9.22	9.66	10.47	9.96	9.09	9.01	9.17	9.84	9.54	9.58	9.82
MnO	0.18	0.19	0.16	0.16	0.18	0.18	0.16	0.17	0.16	0.18	0.19	0.20	0.17
MgO	3.29	3.31	4.86	7.41	3.12	3.17	4.64	2.91	4.86	3.12	2.83	2.85	3.24
CaO	6.84	6.95	7.97	8.90	6.52	6.72	7.86	7.16	8.04	6.65	6.06	6.10	6.88
Na_2O	3.84	3.92	3.88	3.25	3.90	4.18	3.82	4.33	3.78	4.21	4.46	4.45	4.35
K_2O	1.01	1.04	0.83	0.91	1.07	1.20	0.90	1.00	0.84	1.22	1.08	1.09	1.23
P_2O_5	0.29	0.30	0.21	0.31	0.30	0.30	0.20	0.25	0.20	0.30	0.30	0.30	0.30
LOI	1.44	0.81	-0.15	0.16	1.66	0.34	-0.16	0.10	-0.16	0.10	0.77	0.70	-0.31
Y	33.07	34.10	24.17	22.97	36.13	34.70	24.61	30.73	24.46	36.79	36.23	34.78	36.05
Zr	148.60	147.65	92.86	149.08	161.23	147.06	94.08	119.85	93.99	156.19	146.41	141.06	150.29
Nb	3.72	3.77	2.44	8.36	4.00	3.79	2.52	3.00	2.38	4.08	3.66	3.54	3.85
Mo	1.13	1.11	0.84	0.90	1.12	1.16	0.83	0.99	0.82	1.21	1.12	1.11	1.21
Pb	12.96	13.10	9.49	12.44	14.12	13.07	9.20	10.90	9.44	14.01	12.61	12.39	13.02
P	1476	1496	961	1460	1494	1421	1027	1198	1003	1453	1446	1413	1424
Sc	37.84	38.84	30.89	28.70	38.56	34.83	32.91	31.29	33.35	34.84	33.98	32.41	35.26
V	342.17	346.16	251.27	223.19	320.41	300.22	254.94	258.95	257.04	301.06	247.53	239.11	309.29
Cr	12.38	11.96	64.87	192.18	9.90	9.39	64.06	4.12	66.13	8.88	0.27	0.55	9.39
Co	24.75	26.09	28.65	38.80	23.86	22.85	29.40	20.66	29.71	22.78	20.24	19.37	22.98
Ni	Below DL	Below DL	39.55	127.97	Below DL	Below DL	44.15	Below DL	42.64	Below DL	0.42	Below DL	Below DL
Cu	101.85	110.44	62.13	63.23	97.84	91.41	65.21	45.32	64.43	94.67	37.20	36.73	101.73
Zn	104.79	109.28	99.62	88.82	106.67	110.40	99.36	106.53	98.63	113.39	113.74	109.75	112.50
Ga	24.40	25.12	21.91	20.34	24.26	22.88	22.34	23.32	22.31	23.21	24.07	23.26	23.23
Rb	25.71	26.85	21.74	19.84	27.67	30.97	21.96	25.21	21.68	32.82	27.33	27.06	33.23
Sr	462	479	507	901	445	441	511	492	518	459	461	443	467
Ba	367	381	311	782	375	403	321	342	311	429	378	374	425
Ce	36.32	38.86	27.12	60.23	40.03	39.01	27.10	31.81	27.02	40.70	38.16	36.20	39.84
Th	4.15	4.17	2.44	7.33	4.53	4.37	2.67	3.02	2.59	4.43	3.62	3.65	4.21
U	1.15	1.20	0.72	1.71	1.30	1.27	0.80	0.91	0.78	1.30	1.07	1.13	1.21
Cs	1.94	2.01	1.50	1.60	2.04	2.39	1.57	1.92	1.54	2.42	2.02	2.08	2.48
La	16.27	16.96	11.20	28.63	17.54	17.05	11.89	13.96	11.79	18.25	15.81	16.60	17.19
Pr	5.26	5.56	3.59	7.39	5.66	5.55	3.79	4.46	3.84	5.92	5.26	5.37	5.45
Nb	24.65	25.22	17.98	32.95	27.63	26.97	17.30	23.16	17.64	28.12	26.81	24.82	25.45
Sm	6.46	6.35	4.66	6.50	6.90	6.60	4.40	5.78	4.45	7.08	6.68	6.28	6.35
Eu	1.88	1.92	1.43	1.85	1.97	1.93	1.41	1.87	1.46	1.98	2.09	1.90	1.77
Gd	6.66	6.68	4.89	5.82	7.39	7.17	4.89	6.29	4.97	7.39	7.20	6.99	6.79
Tb	1.04	1.09	0.76	0.80	1.16	1.12	0.73	1.02	0.76	1.14	1.14	1.07	1.07
Dy	6.73	6.78	4.93	4.94	7.31	7.24	4.80	6.42	4.94	7.23	7.48	7.00	6.61
Ho	1.32	1.38	0.98	0.96	1.46	1.45	0.99	1.30	1.00	1.45	1.49	1.42	1.37
Er	4.02	4.00	2.92	2.68	4.28	4.21	2.81	3.88	3.01	4.25	4.39	4.07	3.97
Tm	0.57	0.57	0.41	0.38	0.61	0.60	0.39	0.54	0.41	0.61	0.62	0.61	0.57
Yb	3.67	3.80	2.72	2.46	4.01	3.94	2.69	3.70	2.78	4.08	4.28	3.96	3.72
Lu	0.56	0.56	0.42	0.38	0.61	0.60	0.41	0.54	0.42	0.61	0.64	0.59	0.57
Hf	4.55	4.42	2.94	3.76	4.76	4.54	2.73	3.93	2.98	4.92	4.67	4.21	4.32
Ta	0.23	0.22	0.15	0.53	0.25	0.23	0.15	0.19	0.16	0.25	0.22	0.22	0.23

Unit	Fui Cones											Ranquil Cone
Sample	130108_08Bi	124_01A	130116_03B	130116_08B	124_06Aii	121_04A	130122_04A	116_10Aii	116_10Ai	130122_06A	302_03A	120_03A
SiO_2	56.01	54.99	54.71	57.34	57.02	59.32	59.67	60.71	61.28	60.87	58.05	55.67
TiO_2	1.47	1.46	1.12	1.35	1.45	0.87	1.25	1.21	1.23	1.21	1.36	1.37
Al_2O_3	16.55	16.62	17.57	16.60	16.40	17.25	16.47	16.46	16.50	16.34	17.12	16.33
Fe_2O_3	9.96	10.25	9.25	9.22	9.82	7.10	7.96	7.63	7.69	7.39	9.00	10.36
MnO	0.18	0.18	0.16	0.18	0.17	0.13	0.18	0.17	0.17	0.18	0.17	0.18
MgO	3.17	3.59	4.82	2.85	3.24	3.42	2.47	2.31	2.30	2.19	2.79	3.60
CaO	6.72	7.60	8.00	6.42	6.88	6.27	5.53	5.22	5.17	5.07	5.73	7.38
Na_2O	4.18	4.06	3.80	4.59	4.35	4.19	4.95	5.05	5.16	5.11	4.34	4.12
K_2O	1.20	1.07	0.86	1.14	1.23	0.95	1.28	1.37	1.30	1.37	1.04	1.02
P_2O_5	0.30	0.27	0.21	0.27	0.30	0.19	0.32	0.33	0.33	0.33	0.29	0.26
LOI	0.34	0.08	0.02	0.20	-0.31	0.04	0.16	0.19	0.04	-0.04	0.34	0.13
Y	36.64	32.36	25.13	35.63	35.81	21.61	35.13	37.69	39.42	37.97	35.93	31.68
Zr	156.07	132.00	98.10	138.55	150.64	11.75	147.04	162.26	165.79	160.53	140.30	125.85
Nb	4.02	3.32	2.56	3.51	3.91	3.16	3.96	4.31	4.34	4.35	3.53	3.08
Mo	1.21	1.06	0.84	1.13	1.24	1.00	1.22	1.88	1.77	1.34	1.11	1.03
Pb	13.64	11.78	9.44	12.31	13.34	11.59	14.70	19.26	16.00	15.08	13.62	11.41
P	1485	1364	1039	1367	1433	1002	1598	1703	1670	1720	1447	1224
Sc	36.13	40.18	32.49	33.69	35.46	23.08	28.63	28.02	28.26	27.90	35.01	36.43
V	321.85	361.14	251.91	246.48	313.62	188.55	164.01	144.16	145.25	123.36	251.87	341.13
Cr	10.10	14.05	67.16	0.22	9.66	21.00	0.85	1.08	0.91	0.43	0.23	11.90
Co	24.31	26.12	29.46	19.70	23.19	21.21	14.55	13.55	13.69	12.35	20.01	26.47
Ni	Below DL	Below DL	39.04	Below DL	Below DL	19.28	Below DL	Below DL	Below DL	Below DL	Below DL	Below DL
Cu	96.97	122.51	56.41	43.65	103.57	34.15	27.23	22.44	24.78	14.65	44.90	113.97
Zn	115.61	114.16	98.21	114.91	114.21	93.50	108.21	111.94	117.38	111.69	117.53	114.54
Ga	24.14	23.84	21.57	23.66	22.92	22.20	23.45	24.13	24.08	24.10	24.48	23.20
Rb	33.08	27.69	21.23	28.71	33.51	29.11	31.57	36.96	35.97	35.10	27.74	26.49
Sr	462	502	502	475	473	480	482	477	474	471	473	507
Ba	418	388	313	397	430	295	447	473	486	483	386	380
Ce	40.86	35.33	26.79	36.53	39.71	30.25	38.85	42.26	43.20	42.56	36.70	35.12
Th	4.35	3.69	2.70	3.49	4.25	3.60	3.93	4.19	4.09	4.34	3.70	3.71
U	1.26	1.08	0.78	1.04	1.24	0.95	1.16	1.22	1.19	1.26	1.09	1.09
Cs	2.42	2.08	1.54	2.21	2.53	0.95	2.33	2.66	2.48	2.62	2.21	1.98
La	17.87	15.35	11.79	15.59	17.80	13.97	16.66	17.92	17.67	18.86	16.59	14.65
Pr	5.72	5.03	3.83	5.12	5.75	4.18	5.41	5.85	5.93	6.20	5.58	4.66
Nb	27.60	23.39	17.83	23.95	26.21	17.24	25.32	25.79	28.55	26.98	26.29	23.16
Sm	6.74	5.77	4.48	6.14	6.53	4.01	6.10	6.63	7.09	6.78	6.79	5.83
Eu	1.96	1.73	1.44	1.83	1.89	1.20	1.87	1.92	2.09	1.94	2.06	1.76
Gd	7.37	6.29	4.96	6.78	7.06	4.19	6.42	6.73	7.65	7.12	7.09	6.19
Tb	1.14	0.98	0.77	1.05	1.09	0.65	1.04	1.10	1.19	1.12	1.15	0.95
Dy	7.30	6.41	4.86	6.73	6.78	4.01	6.49	6.94	7.48	7.08	7.38	6.22
Ho	1.50	1.30	1.00	1.35	1.41	0.82	1.34	1.42	1.52	1.47	1.49	1.26
Er	4.36	3.82	2.89	3.98	4.14	2.44	4.01	4.23	4.61	4.37	4.56	3.61
Tm	0.62	0.53	0.42	0.59	0.59	0.35	0.56	0.61	0.66	0.62	0.62	0.51
Yb	4.09	3.55	2.84	3.84	3.95	2.33	3.84	3.95	4.38	4.18	4.39	3.67
Lu	0.61	0.54	0.41	0.59	0.58	0.35	0.57	0.59	0.65	0.63	0.62	0.53
Hf	4.86	3.93	2.94	4.08	4.55	0.84	4.25	4.61	4.91	4.59	4.53	3.72
Ta	0.24	0.21	0.16	0.20	0.23	0.22	0.24	0.25	0.28	0.27	0.22	0.19

Unit	Tumba Buey			
Sample	130109_07A	130109_01Aii	130109_07B	130109_01Ai
SiO_2	59.19	60.72	61.16	60.72
TiO_2	1.18	1.11	1.12	1.11
Al_2O_3	16.94	16.68	16.76	16.68
Fe_2O_3	7.66	6.75	6.73	6.75
MnO	0.16	0.16	0.16	0.16
MgO	2.57	2.16	2.15	2.16
CaO	5.83	5.12	5.06	5.12
Na_2O	4.77	5.03	5.06	5.03
K_2O	1.30	1.47	1.51	1.47
P_2O_5	0.34	0.36	0.36	0.36
LOI	0.14	0.48	-0.00	0.48
hline				
Y	34.20	35.74	36.58	35.70
Zr	170.76	187.14	189.36	187.50
Nb	5.38	5.89	6.00	5.91
Mo	1.31	1.39	1.44	1.40
Pb	15.43	16.90	16.44	17.06
P	1837	Over range	1866	1833
Sc	28.46	23.90	23.34	24.06
V	183.75	126.25	122.04	123.07
Cr	0.68	0.20	0.74	0.17
Co	15.55	11.43	11.21	11.13
Ni	Below DL	Below DL	Below DL	Below DL
Cu	24.05	10.79	13.89	10.67
Zn	108.55	104.01	106.64	103.20
Ga	24.52	23.25	23.08	23.46
Rb	32.59	35.59	36.03	35.46
Sr	562	514	506	509
Ba	492	538	550	543
Ce	47.25	51.38	52.29	50.32
Th	4.07	4.58	4.67	4.56
U	1.14	1.32	1.33	1.31
Cs	2.26	2.56	2.57	2.54
La	20.46	22.57	24.28	22.42
Pr	6.43	6.93	7.50	6.83
Nb	27.35	29.08	32.37	30.29
Sm	6.59	6.78	7.23	7.14
Eu	1.88	1.89	2.14	2.02
Gd	6.49	6.73	7.66	7.35
Tb	1.02	1.06	1.15	1.12
Dy	6.16	6.63	7.14	6.92
Ho	1.28	1.30	1.49	1.43
Er	3.85	3.95	4.41	4.17
Tm	0.53	0.58	0.62	0.59
Yb	3.56	3.76	4.05	4.00
Lu	0.53	0.57	0.61	0.60
Hf	4.59	5.09	5.58	5.19
Ta	0.29	0.32	0.37	0.35

Table A.9: Major and trace element whole rock analyses. All major analyses are in wt. % and trace analyses in ppm. Below DL means the concentration was below the detection limit and Over Range means the concentration was above the detection limit of the mass spectrometer.